UNIVERSITY OF SOUTHAMPTON
FACULTY OF ENGINEERING AND THE ENVIRONMENT

AIRBUS NOISE TECHNOLOGY CENTRE

Aerodynamic and Aeroacoustic Modelling of Engine Fan Broadband Noise

by

Fernando Gea-Aguilera

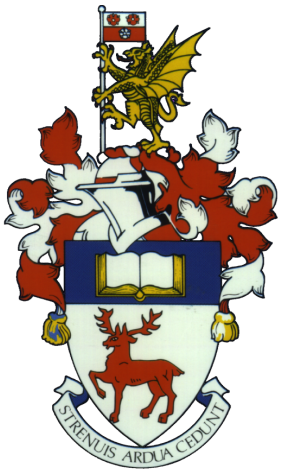

Thesis for the degree of Doctor of Philosophy

March 2017

UNIVERSITY OF SOUTHAMPTON

ABSTRACT

FACULTY OF ENGINEERING AND THE ENVIRONMENT
AIRBUS NOISE TECHNOLOGY CENTRE

Doctor of Philosophy

AERODYNAMIC AND AEROACOUSTIC MODELLING OF ENGINE FAN BROADBAND NOISE

by Fernando Gea-Aguilera

This thesis investigates simplified but representative configurations of the fan wake-OGV interaction noise, which is a major source of engine fan broadband noise during take-off and landing. To this end, Computational AeroAcoustics (CAA) simulations are performed by using the Linearised Euler Equations (LEEs) and synthetic turbulence methods.

An advanced digital filter method is presented to generate divergence-free synthetic turbulence with explicit control on the resulting turbulence spectrum. The method, which is based on the Random Particle-Mesh (RPM) method and synthetic eddy methods, is able to produce two- and three-dimensional fluctuating velocity fields of homogeneous isotropic and anisotropic turbulence. It is also shown that similar levels of simulation accuracy can be achieved by using digital filter and Fourier mode methods. Nevertheless, the advanced digital filter method provides enhanced performance in terms of computational cost (up to 3.9 times faster for two-dimensional simulations in this study).

CAA simulations using the advanced digital filter method are performed to improve current understanding of leading edge noise from single aerofoils. For example, the method is used to examine the distortion of turbulent structures in the leading edge region. Furthermore, a comparison between numerical and experimental noise measurements in open-jet wind tunnel experiments indicate that the advanced digital filter method is capable of reproducing experimental results with an accuracy to within 3 dB. This thesis also presents a parameter study to assess the effects of moderately anisotropic turbulence, as occurs in the fan wakes, on leading edge noise from single aerofoils.

Finally, fan wake modelling assumptions, such as cyclostationary variations in turbulent kinetic energy and integral length scale, are investigated using a cascade of thin aerofoils. Results indicate that broadband noise mainly depends on the circumferentially-averaged spectrum that is perceived by the cascade, and not on the instantaneous features of the fan wakes. A parameter study on cascade noise using isotropic turbulence is also included in this thesis, where variations in the vane count, aerofoil thickness, camber, mean flow Mach number, stagger angle, and inter-vane spacing are investigated. It is confirmed that the flat plate assumption provides sufficient accuracy for the frequency range in which engine fan broadband noise is relevant.

Contents

List of Figures

List of Tables

Declaration of Authorship

I, FERNANDO GEA-AGUILERA, declare that this thesis and the work presented in it are my own and have been generated by me as the result of my own original research.

AERODYNAMIC AND AEROACOUSTIC MODELLING OF ENGINE FAN BROADBAND NOISE

I confirm that:

1. This work was done wholly or mainly while in candidature for a research degree at this University;
2. Where any part of this thesis has previously been submitted for a degree or any other qualification at this University or any other institution, this has been clearly stated;
3. Where I have consulted the published work of others, this is always clearly attributed;
4. Where I have quoted from the work of others, the source is always given. With the exception of such quotations, this thesis is entirely my own work;
5. I have acknowledged all main sources of help;
6. Where the thesis is based on work done by myself jointly with others, I have made clear exactly what was done by others and what I have contributed myself;
7. Either none of this work has been published before submission, or parts of this work have been published as:

    - F. Gea-Aguilera, J. Gill, and X. Zhang, "Synthetic Turbulence Methods for Computational Aeroacoustics Simulations of Leading Edge Noise", *submitted to Computers and Fluids*, 2016.
    - F. Gea-Aguilera, X. Zhang, X. Chen, J. Gill, and T. Nodé-Langlois, "Synthetic Turbulence Methods for Leading Edge Noise Predictions," in *21st AIAA/CEAS Aeroacoustics Conference*, no. AIAA 2015-2670, Dallas, Texas, 2015.

- F. Gea-Aguilera, J. Gill, X. Zhang, X. Chen, and T. Nodé-Langlois "Leading Edge Noise Predictions using Anisotropic Synthetic Turbulence," in *22nd AIAA/CEAS Aeroacoustics Conference*, no. AIAA 2016-2840, Lyon, France, 2016.
- F. Gea-Aguilera, J. Gill, X. Zhang, and T. Nodé-Langlois, "Turbulence-Cascade Interaction Noise Using an Advanced Digital Filter Method," in *23rd International Congress on Sound and Vibration*, no. 328, Athens, Greece, 2016.
- F. Gea-Aguilera, J. Gill, X. Zhang, and T. Nodé-Langlois, "Fan Wake Modelling for Computational Aeroacoustic Simulations of Turbulence-Cascade Interaction Noise," in *Greener Aviation*, no. 113, Brussels, Belgium, 2016.
- F. Gea-Aguilera, J. Gill, D. Angland, and X. Zhang, "Wavy Leading Edge Airfoils Interacting with Anisotropic Turbulence," in *23rd AIAA/CEAS Aeroacoustics Conference*, no. AIAA 2017-3370, Denver, Colorado, 2017.

Signed: .....

Date: .....

Acknowledgements

I would like to thank my supervisor, Professor Xin Zhang, for his advice, patience, support, and guidance throughout the duration of my Ph.D. studies. Thanks also go to Dr. David Angland and Dr. Xiaoxian Chen for their additional support. I would also like to thank my mentor, Dr. James Gill, for his time and invaluable discussions on leading edge noise and computational aeroacoustics. Thanks must also go to Thomas Nodé-Langlois for providing technical feedback during regular meetings with Airbus.

This research has been possible thanks to financial support from Innovate UK, as part of the wHole AiRcraft Multidisciplinary nOise desigN sYstem (HARMONY) project, and the University of Southampton through the Airbus Noise Technology Centre (ANTC). The IRIDIS 4 High Performance Computing Facility and IT services at the University of Southampton are also acknowledged in the completion of this work.

I am also grateful to Professor Phillip Joseph for providing access to the analytical cascade model used in this thesis and technical feedback through internal reviews. I would also like to thank my colleagues from the Institute of Sound and Vibration Research (ISVR), Chaitanya Paruchuri and Thomas Hainaut, for the interesting discussions during HARMONY meetings.

During the course of my Ph.D., I have made a lot of new friends: Edu, Jaime, Rafa, Sonia, Javi, Jesús, Tim, Ravish, Meng, Fuyang, Ryu, Sylvain, Daryl, Andreas, Vincenzo, Markus, Nicolas, Toni, Alex, Manuel, ... Thanks go to all of you for the great moments that we shared, for the laughs and coffee breaks, and definitely for making easier my stay in Southampton. I would also like to thank all members of the futsal society at the University of Southampton for the nice trainings and football games that we played together.

Last but not least, I would like to thank my parents for being always there and for their unconditional support throughout my life.

Nomenclature

Abbreviations

1cFm	One-component Fourier mode method
2cFm	Two-component Fourier mode method
ANTC	Airbus Noise Technology Centre
APE	Acoutic Perturbation Equation
CAA	Computational AeroAcoustics
CFD	Computational Fluid Dynamics
CFL	Courant-Friedrichs-Lewy
CROR	Contra-Rotating Open Rotor
DNS	Direct Numerical Simulation
EPNL	Effective Perceived Noise Level
FAR	Federal Aviation Regulation
FFT	Fast Fourier Transform
FW-H	Ffowcs Williams and Hawkings
HARMONY	wHole AiRcraft Multidisciplinary nOise desigN sYstem
ICAO	International Civil Aviation Organization
IGV	Inlet Guide Vane
ISVR	Institute of Sound and Vibration Research
LEE	Linearised Euler Equation
LES	Large Eddy Simulation
OAPWL	OverAll sound PoWer Level
OGV	Outlet Guide Vane
PIV	Particle Image Velocimetry
PPW	Points Per Wavelength
PSD	Power Spectral Density
PWL	sound PoWer Level
RANS	Reynolds-Averaged Navier-Stokes
RDT	Rapid Distortion Theory

RPM	Random Particle-Mesh
SDT	Source Diagnostic Test
SNGR	Stochastic Noise Generation and Radiation
SPL	Sound Pressure Level

Greek Letters

α	Stagger angle
α_{bz}	Damping strength of a buffer zone
β	Prandtl-Glauert factor (= $\sqrt{1 - M_\infty^2}$)
β_{bz}	Exponent in the damping function of a buffer zone
$\Delta k_y'$	Auxiliary term in the calculation of the transverse wavenumber step
Δk_j	Wavenumber step of k_j
Δt	Time step in CAA simulation
Δx, Δy, Δz	Grid spacing in x-, y-, and z-directions, respectively
Δ_e	Eddy spacing or separation between eddy centres
δ_{ij}	Kronecker delta
Δ_{LE}	Minimum cell size in the leading edge region
ϵ_p	Direction of rotation of the pth eddy (± 1)
γ	Heat capacity ratio
$\Gamma(.)$	Gamma function
γ_{ij}^2	Magnitude-squared coherence function between ith and jth signals
κ_c	Filter cut-off wavenumber
Λ	Integral length scale for isotropic turbulence
Λ_w	Integral length scale in the fan wakes
$\boldsymbol{\kappa}_0 = (\kappa_x, \kappa_y, \kappa_z)$	Acoustic wavenumber
$\boldsymbol{\sigma} = (\sigma_x, \sigma_y)$	Unit vector in two-component Fourier mode method
η	Vector potential
Ω	Rotation speed
μ_h	hydrodynamic reduced frequency
μ_a	Acoustic reduced frequency
ω	Angular frequency (= $2\pi f$)
ϕ	Random phase term in Fourier mode methods
Φ_{ij}	Velocity spectrum of turbulence
ψ	Inner angle of mesh cell
ρ'	Fluctuating density
ρ_{tar}'	Target fluctuating density within buffer zones
ρ_0	Mean flow density
σ_e	Correction term for calculation of effective angle of attack

τ	Separation between two instants
θ	Far-field observer angle
θ'	Auxiliary angle in shear layer correction
Θ_1, Θ_2, Θ_3	Auxiliary terms in analytical flat plate theory
θ_c	Far-field observer angle with shear layer correction
ε	Turbulence dissipation
ε_{ijk}	Levi-Civita symbol
ζ	Auxiliary term in shear layer correction

Roman Letters

$\mathcal{U}$	White noise signal in RPM method
$\mathcal{U}_p$	Weighted white noise signal for pth eddy or particle
$\mathbf{e}_j$	Unit vector in the jth spatial direction
$\mathbf{k} = (k_x, k_y, k_z)$	Vortical wavenumber
$\mathbf{n}$	Unit normal vector
$\mathbf{r}_p = (r_p, r_p, r_p)$	Separation between a point in the flow field and the eddy centre ($= \mathbf{x} - \mathbf{x}_p$)
$\mathbf{t}$	Unit tangent vector
$\mathbf{u}' = (u'_x, u'_y, u'_z)$	Fluctuating velocity, velocity disturbances
$\mathbf{u}'_p$	Fluctuating velocity of the pth eddy
$\mathbf{u}'_s$	Point in the source region where turbulence is injected
$\mathbf{u}'_{tar}$	Target fluctuating velocity within buffer zones
$\mathbf{U}_0$	Mean flow velocity
$\mathbf{x} = (x, y, z)$	Cartesian coordinates, point in the flow field
$\mathbf{x}_p$	Centre or location of the pth eddy
C	Integer number used in the transverse wavenumber discretisation
$\mathcal{E}$	Error between E_{tar} and E_{sum}
$\mathcal{L}$	Non-dimensional unsteady loading term of a flat plate
$\mathcal{P}$	Sound power spectra
$\mathcal{P}_l$	Modal sound power
$\mathcal{P}_{ref}$	Reference sound power ($= 1 \times 10^{-12}$ W)
i	Imaginary unit, $\mathrm{i}^2 = -1$
$A(\theta, M_\infty)$	$= \sqrt{1 - M_\infty^2 \sin^2\theta}$
A_w	Distribution of turbulent kinetic energy in the fan wakes
A_p	Exponential term of the pth anisotropic Gaussian eddy
AoA	Angle of attack
b	Aerofoil semi-chord ($= c/2$)
c	Aerofoil chord
c_∞	Speed of sound

$C_{ij}(r)$	Two-point correlation of the vector potential
d	Aerofoil semi-span
E	Energy spectrum
E_f	Fresnel integral
E_{ij}	One-dimensional spectrum (of velocity fluctuations in the ith and jth-directions)
E_{sum}	Energy spectrum from Gaussian superposition
E_{tar}	Target energy spectrum
f	Frequency
$F(\theta, M_\infty)$	Integration term in sound power calculation for single aerofoils
$f(M_\infty)$	Phase correction factor in analytical flat plate theory
$f(r)$	Longitudinal correlation function
G	Spatial or temporal filter in RPM method
$g(r)$	Transverse (or lateral) correlation function
H	Vertical distance from noise source to far-field observer
h	Half-jet vertical length
$H_m^{(2)}$	mth order Hankel function of the second kind
h_w	Semi-wake width of the fan wakes
J_m	mth order ordinary Bessel functions of the first kind
k'	Wavenumber at the maximum of the energy spectrum
k_c	Constant in the von Kármán energy spectrum (= $[\sqrt{\pi}\Gamma(5/6)]/[\Lambda\Gamma(1/3)]$)
K_w	Turbulent kinetic energy in the fan wakes
l	Order of the acoustic mode in the circumferential direction, or duct mode
$l_{ij}^{(k)}$	Integral length scale of the ith and jth velocity components in the kth spatial direction
l_a	Axial length scale in axisymmetric turbulence ($l_a = l_{11}^{(1)}$)
l_t	Transverse length scales in axisymmetric turbulence ($l_t = l_{22}^{(2)} = l_{33}^{(3)}$)
l_x	Streamwise length scale in anisotropic Gaussian turbulence ($l_x = l_{11}^{(1)}$)
l_y	Transverse length scale in anisotropic Gaussian turbulence ($l_y = l_{22}^{(2)}$)
l_z	Spanwise length scale in anisotropic Gaussian turbulence ($l_z = l_{33}^{(3)}$)
L_{bz}	Length or width of a buffer zone
L_{ref}	Reference Length (= 1 m)
L_{span}	Spanwise extent (or width) of three-dimensional CAA domain
M_∞	Freestream Mach number (= U_∞/c_∞)
N, M	Number of Fourier modes used to discretise k_x, and k_y, respectively
N_r	Number of independent realisations in two-component Fourier mode method
n_w	Number of fan wakes within the CAA domain
P	Number of particles or eddies in the source region
p'	Fluctuating pressure

p'_c	Fluctuating pressure with shear layer correction
p'_{tar}	Target fluctuating pressure within buffer zones
p_0	Mean flow pressure
p_{ref}	Reference pressure ($= 2 \times 10^{-5}$ N.m^{-2})
$Q_l^{\pm}$	Non-dimensional modal power response function
R	Radius of a wrapped aerofoil cascade
r	Separation between two points in the flow field
r_0	Far-field observer distance
r_e	Eddy radius
$R_{ij}(r)$	Two-point velocity correlation
r_{LE}	Leading edge radius of an aerofoil
$R_l^{\pm}$	Cascade response function
s	Inter-vane spacing
$S(\mu_h)$	Sears function
S_k	Mesh skewness
S_{pp}	Pressure spectral density
t	Time
T_w	Period of the fan wakes
t_A	Maximum aerofoil thickness
u'_0	Characteristic velocity term of anisotropic eddies
u'_a	Root-mean-square fluctuating velocity in the axial direction
u'_t	Root-mean-square fluctuating velocity in the transverse direction
$u'_{rms,b}$	Root-mean-square fluctuating velocity of background turbulence
$u'_{rms,w}$	Root-mean-square fluctuating velocity of wake turbulence
U_∞	Freestream speed
U_{ref}	Reference Speed ($= 1$ m.s^{-1})
V_s	Source region where synthetic turbulence is injected

Subscripts

$_\infty$	Freestream variable
$_{max}$	Maximum
$_{min}$	Minimum
$_{ref}$	Reference variable
$_{rms}$	Root-mean-square

Superscripts

$^{(2D)}$	Two-dimensional turbulence
$^{(3D)}$	Three-dimensional turbulence
*	Complex conjugate

$^{\pm}$	Upstream (+) and downstream (-)

Symbols

$\langle . \rangle$	Ensemble average operator
$\|\|.\|\|$	Magnitude (or modulus) of a vector
ln(.)	Natural logarithm
Re {.}	Real part operator
∇	Gradient operator
$\nabla \cdot$	Divergence operator
$\nabla \times$	Curl operator
$\otimes$	Convolution operator
$\overline{(.)}$	Time average
$\widehat{(.)}$	Variable in wavenumber or frequency domain
mod(a,b)	Remainder of a divided by b

Chapter 1

Introduction

Over the past few decades, commercial aviation has experienced a large increase in the number of passengers and goods transported. This expansion has been accompanied by a reduction in fuel costs, which has helped to develop emerging economies and accelerate economic globalisation. Furthermore, air traffic is forecast to grow in the coming years [1]. In order to ensure sustainable development, the growth of commercial aviation must be associated with a reduction in its environmental impact. The aerospace industry is committed to reducing carbon emissions, which contribute to the greenhouse effect, and noise pollution, which may be disturbing for the community on the ground, especially in populated areas near airports. Both carbon emissions and noise pollution have adverse effects on the environment and could potentially affect human health [2, 3].

Airworthiness authorities are becoming increasingly strict in terms of noise pollution. Stringent targets have been set in Europe [4] for noise reduction by 2050, which aims to reduce perceived aircraft noise by 65% in comparison to the baseline year 2000. Furthermore, the International Civil Aviation Organization (ICAO) has implemented noise-related charges for airports experiencing noise problems [5]. Consequently, several airports have already implemented constraints in terms of night flight slots, which could affect intercontinental flights and the growth of commercial aviation. A notable example of these local regulations is the Quota Count system developed by the United Kingdom government to reduce noise emissions of London airports over night [6].

The operating conditions and phase of flight determine the main noise sources of the aircraft, which are shown in Figure 1.1a. During take-off, the engines have to provide the aircraft with enough thrust to fly. Consequently, jet noise and fan noise are important contributors to the overall acoustic level during this phase of flight. Airframe noise due to unsteady flows generated around high-lift devices, such as flaps and slats, and landing gear becomes more relevant during landing. Nevertheless, the contribution of the engine noise to the overall acoustic level remains dominant [7].

According to the Federal Aviation Regulation (FAR36) [8] and the ICAO Annex 16 [9], the standard metric for aircraft certification in terms of noise pollution is the Effective Perceived Noise Level (EPNL, in units of EPNdB), which takes into account tones, duration, and overall noise level. Figure 1.1b shows a schematic representation of the sound measurement locations for aircraft noise certification. The EPNL is calculated from sound measurements at two different locations during take-off, one at the *sideline* position with the engines at full power and another one at the *cut-back* position with engines at 80% of full power. Additional noise measurements are taken at the *approach* position with engines at 50% of full power.

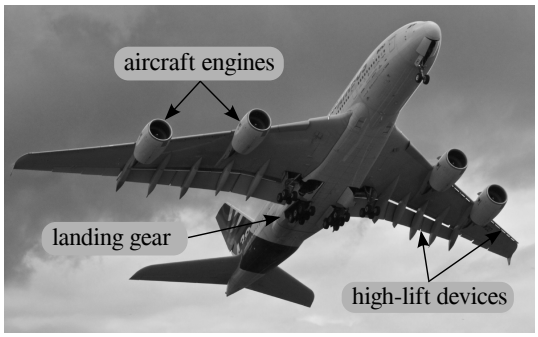

(a) Sources of noise in a commercial aircraft. Image reproduced with permission of the rights holder, James Gill.

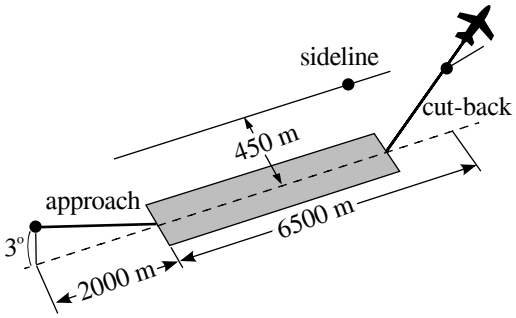

(b) Sound measurements for noise certification.

Figure 1.1: Aircraft noise certification.

An improved understanding of engine noise is necessary to meet noise certification requirements for the next generation of commercial aircraft. Engine noise is characterised by both tonal and broadband noise, which can be produced in different parts of the engine, such as the fan, compressor, combustion chamber, turbine, and nozzle. In the 60's, jet noise produced by turbojet-powered aircraft was the dominant source of noise. This was mainly caused by the turbulent mixing between the jet and the external flow around the nacelle. Today, modern turbofan engines have significantly reduced jet noise by shielding the hot stream with a cold bypass exhaust stream and by increasing the bypass ratio. Thus, fan noise has become the biggest challenge when attempting to reduce engine noise during take-off and approach, as the compressor and turbine stages remain quieter than the fan stage [10, 11]. Figure 1.2 shows the main sources of noise in a turbofan engine and a comparison of the relative sound PoWer Level (PWL) from different components of the engine.

Contra-Rotating Open Rotors (CRORs) have been established as a promising alternative to ultra-high bypass turbofan engines for the next aircraft generation. CRORs are expected to reduce both fuel consumption and carbon emissions. Turbofan engines and CRORs share several noise sources, however, the absence of a nacelle around the CROR blades makes it more difficult to fulfil the community noise regulations.

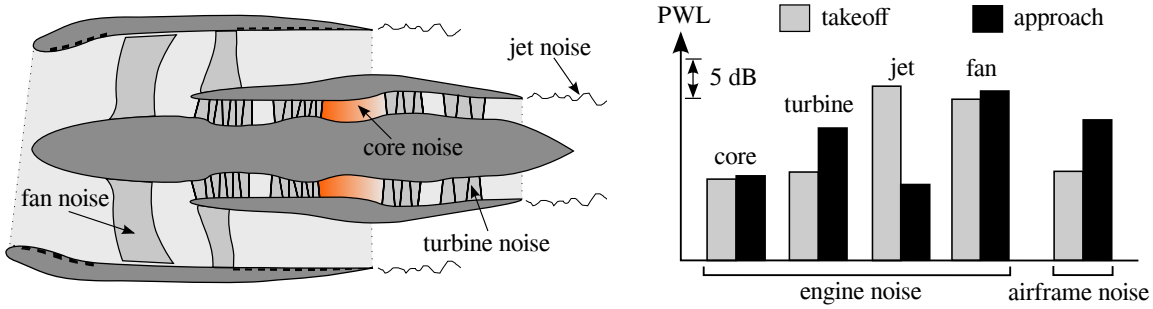

(a) Cross-section of a turbofan engine.

(b) Relative PWL from different components of an aircraft. Data obtained from Astley *et al.* [7].

Figure 1.2: Schematic of a turbofan engine and main sources of noise.

1.1 Engine Fan Broadband Noise

Early research studies to reduce fan noise focused on diminishing tonal noise, since the human hearing response[1] is particularly sensitive to certain frequencies. Tones arise from the Blade Passing Frequency (BPF) of the fan blades and its harmonics, from buzz saw tones caused by supersonic fan blade tips [12], and from interaction tones due to the interaction of the fan wake velocity deficit and the Outlet Guide Vanes (OGVs) [13]. Tonal noise behaves more deterministically than broadband noise, which has allowed an effective reduction of fan tonal noise over the past few decades and has highlighted the importance of fan broadband noise.

Engine fan broadband noise is generated by the interaction of any source of turbulence with fan blades or OGVs, which may cause *aerofoil self-noise* and *leading edge noise,* as shown in Figure 1.3.

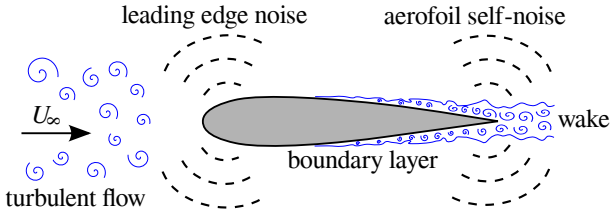

Figure 1.3: Sources of broadband noise from a single aerofoil.

- **Aerofoil self-noise** is a noise mechanism inherent in all aerofoils, as it is generated by the interaction of the fan blades and OGVs with turbulence from their own boundary layer and wake. Trailing edge noise is a common type of aerofoil self-noise, which is generated as the turbu-

[1] The human hearing range is between 20 Hz and 20 kHz.

lent boundary layer passes over the aerofoil trailing edge. Further details on various aerofoil self-noise mechanisms can be found in the work of Brooks *et al.* [14].

- **Leading edge noise.** The interaction of oncoming turbulence with the fan blades and OGVs generates dipole-like sound that radiates from the aerofoil leading edge. Leading edge noise, also known as turbulence-aerofoil interaction noise, can be caused due to turbulence generated at the engine intake, boundary layer on the casing, and fan wakes, as shown in Figure 1.4.

  – **Turbulence ingestion noise**. Turbulence ingested through the fan intake interacts with the leading edge of the fan blades, which produces broadband noise. The flow acceleration in the axial direction at the fan intake causes turbulence to show high levels of anisotropy, with turbulence length scales that are significantly larger in the engine axial direction when compared to the lateral directions [15, 16]. The importance of the turbulence ingestion noise depends on the location of the engine on the aircraft (under the wings, near the tail, etc.). This is because installation effects, such as wing wakes and airframe boundary layer, have an impact on the quality of the air ingested by the engine.

  – **Boundary layer-fan tip interaction noise**. Broadband noise also arises from the interaction of the fan blade tips with the boundary layer along the outer casing. This source of noise is notably affected by the fan tip clearance and the high turbulence intensity and anisotropy within the boundary layer [17]. The fan tip interaction also produces strong sheared flows in the fan wake near the outer casing that affects the fan wake-OGV interaction noise.

  – **Fan wake-OGV interaction noise**, also known as rotor wake-stator interaction noise. Broadband noise is generated from the interaction of the fan wakes with the OGVs, Inlet Guide Vanes (IGVs) of the compressor, and a splitter section between them. However, the contributions of the splitter section and the IGVs are considered small. This source of noise is influenced by the characteristics of the turbulence in the fan wakes, such as high turbulence intensity and moderate anisotropy [17, 18], and OGV design parameters, such as aerofoil thickness and camber.

Ganz *et al.* [17] ran a series of experiments to quantify the individual contribution of different broadband noise sources in a 18-inch fan rig. From their experiment, it is seen that the fan wake-OGV interaction noise is the greatest contributor to the engine fan broadband noise. Therefore, a good understanding of the main factors that influence leading edge noise is required for effective noise prediction and reduction in turbofan engines. Additionally, leading edge noise is also relevant in CRORs, helicopter rotors, and wind turbines.

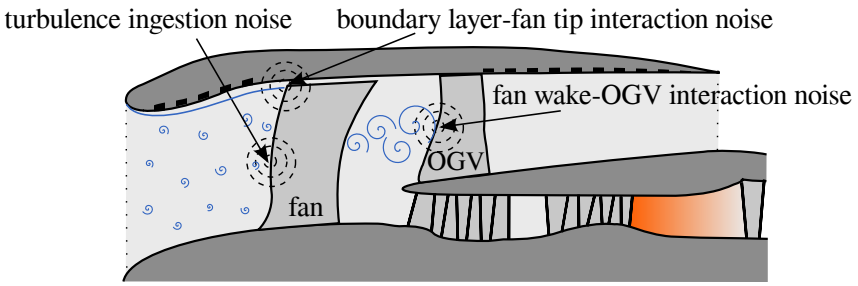

Figure 1.4: Sources of leading edge noise in a turbofan engine.

1.2 Context and Thesis Aims

Today, the scientific community is working on developing approaches to provide major aircraft manufacturers with aeroacoustic predictions of the entire aircraft. This is the final goal of the wHole AiRcraft Multidisciplinary nOise desigN sYstem (HARMONY) programme, in collaboration between Rolls-Royce, Airbus, Bombardier, the University of Southampton, and the University of Cambridge. The HARMONY programme, which is supported by Innovate UK, includes a work package on fan broadband noise modelling. The present Ph.D. thesis was conducted within this framework at the Airbus Noise Technology Centre in the University of Southampton.

The main objective of the present thesis is to develop computationally affordable methods to improve understanding and noise prediction capabilities of engine fan broadband noise. Particularly, this thesis focuses on the numerical modelling of the aerodynamics and aeroacoustics of simplified but representative cases of the fan wake-OGV interaction noise and its underlying noise mechanism, the leading edge noise.

Although Direct Numerical Simulations (DNS) and Large Eddy Simulations (LES) could potentially be used in aeroacoustic studies, the computational cost is currently prohibitive in an industrial context, where high Reynolds numbers are often required and high frequencies need to be computed for the noise predictions [19, 20]. Typical Computational Fluid Dynamics (CFD) simulations using the Reynolds-Averaged Navier-Stokes (RANS) equations are time independent, and therefore they are not suitable for aeroacoustic simulations [21]. Promising broadband noise predictions have been obtained recently by using a Lattice-Boltzmann solver to investigate complex fan-OGV configurations at a reasonable computational cost [22, 23]. Nevertheless, DNS, LES, and Lattice-Boltzmann simulations have difficulty in evaluating the contribution of independent noise sources, which may mask the relative influence of the noise source under investigation due to variations in design parameters. Therefore, DNS, LES, and Lattice-Boltzmann solvers are not convenient for large parameter studies that could potentially enhance the current understanding of leading edge noise, and they are not suit-

able to assess the influence of classic modelling assumptions, such as isotropic/anisotropic turbulence, uniform/non-uniform mean flows, etc.

This thesis presents an extensive Computational AeroAcoustics (CAA) study on turbulence interacting with aerofoils and cascades, which allows for a fundamental understanding of leading edge noise. Numerical simulations involve the use of synthetic turbulence methods to reproduce the statistics of oncoming turbulence, such as the fan wakes, and an in-house high-order CAA code that solves the Linearised Euler Equations (LEEs) to model sound generation and propagation. The LEEs are a simplified set of governing equations in which viscosity and non-linear terms are neglected, and constitute an affordable numerical approach to perform leading edge noise simulations.

1.3 Literature Review

This section presents a literature review on synthetic turbulence methods (see Section 1.3.1), leading edge noise from single aerofoils (see Section 1.3.2), and fan wake-OGV interaction noise (see Section 1.3.3). A brief summary of the literature review is presented at the end of each section to highlight the key results and conclusions.

1.3.1 Synthetic Turbulence for CAA applications

The total flow velocity can be split into mean flow ($\mathbf{U}_0$) and fluctuating velocity ($\mathbf{u}'$). The fluctuating velocity can be generated in numerical simulations by a synthetic turbulence method to reproduce the key features of realistic turbulent flows. For example, synthetic turbulence methods are used in DNS and LES to initialise the fluctuating velocity field and as a turbulent inflow generator. Additionally, synthetic turbulence can be used in CAA simulations to model the vortical disturbances in the full or linearised Euler equations. In order to avoid additional sources of noise related to the turbulent inflow, the fluctuating velocity is normally assumed to be divergence-free in CAA simulations. The characteristics of some methods developed for LES, such as divergence-free fluctuating velocity, make them suitable for CAA simulations and have also been considered here.

The purpose of this literature review is to provide a broad overview of existing techniques to produce synthetic turbulence, and is not restricted to the area of leading edge noise predictions. Synthetic turbulence methods can be classified into three different categories depending on how the turbulent velocity field is generated. Thus, it is possible to distinguish between methods based on Fourier modes, synthetic eddies, and filtering random data.

Methods Based on Fourier Modes

Methods based on Fourier modes generate a fluctuating velocity field through a summation of weighted sinusoidal functions. Therefore, the resulting turbulent field is periodic and contains a discrete number of frequencies. Increasing the number of modes leads to a well-defined spectral content, but it also increases the computational expense. Despite these potential limitations, Fourier mode methods have become very popular over the past decades due to their simple implementation in numerical codes and their facility for reproducing a target turbulence spectrum.

The use of Fourier modes to generate a stochastic velocity field was proposed by Kraichnan [24] in 1970, when studying the scalar diffusion of fluid particles. The method generates divergence-free velocity fluctuations through a summation of harmonic functions that produce a Gaussian energy spectrum. This type of isotropic spectrum is often used in synthetic turbulence methods, despite the fact that Gaussian spectra are centred at a certain wavenumber and cannot account properly for the energy contained at high frequencies. Karweit *et al.* [25] modified Kraichnan's method [24] to reproduce the von Kármán energy spectrum, which provides a better description of the spectral content in the inertial subrange. In this method, the amplitude of the modes is proportional to the square root of the energy spectrum. Based on Kraichnan's work [24], Smirnov *et al.* [26] generated anisotropic turbulence through a scaling and orthogonal transformation of the velocity correlation tensor. This technique, which was developed for LES applications, produces a fluctuating velocity field that is not completely divergence-free in cases that consider highly anisotropic turbulence. In order to account for non-Gaussian energy spectra, Huang *et al.* [27] proposed to generate several independent velocity fields following the approach of Smirnov *et al*. [26]. The superposition of all the flow fields matches a target isotropic energy spectrum. Recently, Castro *et al.* [28] introduced a number of parameters to better control the statistical properties of the anisotropic velocity generated by the method of Huang *et al.* [27]. Further developments were performed by Batten *et al.* [29], who proposed a Cholesky decomposition of the Reynolds stress tensor to characterise the amplitude of Fourier modes. Yu and Bai [30] proposed the use of a vector potential in Fourier mode methods. Thus, the fluctuating velocity is obtained by taking the curl of the vector potential, $\mathbf{u}' = \nabla \times \boldsymbol{\eta}$, which ensures the divergence-free condition. Alternatively, Patruno and Ricci [31] revisited the method of Castro *et al.* [28] and proposed some corrections to include Taylor's frozen turbulence assumption [32] and an explicit control over the resulting anisotropic turbulence spectra.

In the area of CAA simulations, Béchara *et al.* [33] included a random phase term in the definition of the fluctuating velocity field. This method, which was applied to jet noise predictions using the LEEs, is known as Stochastic Noise Generation and Radiation (SNGR). In a later revision of the SNGR technique, Bailly *et al*. [34, 35] introduced both a convection term and an angular frequency term in the definition of each Fourier mode. These allowed the convection of vortical disturbances by

a mean flow to be included in the study. Billson *et al.* [36] modelled the time correlation by using a hybrid approach. The method combines the generation of a turbulent field according to Béchara *et al.* [33] with a time filter to achieve an exponential decorrelation. In a later work, Billson *et al.* [37] adapted the transformation of Smirnov *et al.* [26] to include anisotropy in the Reynolds stress tensor and length scales when using a SNGR-based method [33, 35].

Fourier mode methods have also been applied to study leading edge noise using CAA solvers. For example, Clair *et al.* [38] used a one-component Fourier mode method that was based on the method of Bailly *et al.* [34, 35]. The method was able to reproduce the isotropic fluctuating velocity field that is perpendicular to the aerofoil chord, as proposed by Amiet for flat plates [39]. The method was extended in a later work to deal with more realistic fan-OGV configurations in an annular duct [40]. Recently, Gill *et al.* [41] included the streamwise and spanwise velocity fluctuations to address leading edge noise predictions using Fourier modes.

Methods Based on Synthetic Eddies

Stochastic turbulent flows can be generated by a summation of eddies with different shapes, such as Gaussian or Mexican-Hat profiles. Each eddy introduces a velocity field around its centre, which vanishes far from it. In contrast with Fourier mode methods, the resulting turbulent flow is not periodic and has a continuous spectral density.

An early work in the area of LES was performed by Sergent [42], who used the vorticity field to characterise two-dimensional velocity fluctuations at the inflow plane. Jarrin *et al.* [43, 44] developed a fully three-dimensional synthetic eddy method that is able to reproduce the Reynolds stress tensor by using a similar reconstruction as in Lund *et al.* [45]. However, the resulting velocity field is not divergence-free. Poletto *et al.* [46] adapted the method of Jarrin *et al.* [43, 44] to generate a divergence-free turbulent flow from a vorticity vector. This method is able to produce anisotropic turbulence by using eddies with different amplitude and length scales in each spatial direction. Similarly, Sescu and Hixon [47] used the vector potential to define the fluctuating velocity field introduced by synthetic eddies with Gaussian, Wavelet, and Mexican-Hat profiles. After taking the curl of the vector potential, the resulting velocity perturbation is divergence-free. However, the method was not designed to explicitly reproduce a target energy spectrum.

Using an Euler-based solver, Kim and Haeri [48] adapted the method of Sescu and Hixon [47] to study turbulence-aerofoil interaction noise from three-dimensional flat plates with wavy leading edges. The von Kármán energy spectrum was reconstructed via superposition of synthetic eddies with different profiles under certain constraints. The method required the optimisation of 15 constraint

parameters, and the generation of 8 random numbers for the specification of the size and amplitude of each eddy, among others.

Methods Based on Digital Filters

Digital filter methods generate fluctuating velocity fields by applying spatial and temporal filters to stochastic data fields, such as white noise signals. As in synthetic eddy methods, the resulting turbulent flow is not periodic and presents a broadband spectral content.

Careta *et al.* [49] proposed to generate stochastic turbulent flows from a vector potential that was defined by filtering white noise signals. The Langevin equation was used to model the spatio-temporal evolution of the white noise signals. The method was able to accurately reproduce two-dimensional divergence-free turbulent flows with well-defined energy spectra and correlation functions. For LES simulations, Klein *et al.* [50] proposed to generate stochastic turbulent flows directly from a summation of filters applied to a series of random data. Anisotropic turbulence can be reproduced by using filters with different lengths in each spatial direction. However, the resulting turbulent flow is not divergence-free. A detailed description of how to calculate the coefficients of the filters was presented by di Mare *et al.* [51].

Digital filter methods have also been used in CAA simulations. Ewert *et al.* [52, 53] extended previous works of Careta *et al.* [49] and Klein *et al.* [50] to develop the Random Particle-Mesh (RPM) method. Divergence-free velocity fluctuations are defined by taking the curl of the vector potential, which is defined by applying spatio-temporal filters to white noise signals. Although the RPM method was originally developed to realise Gaussian energy spectra, Siefert and Ewert [54] and Wohlbrandt *et al.* [55] showed that non-Gaussian energy spectra can also be obtained through a superposition of Gaussian spectra. The RPM method can generate anisotropic flows by using the transformation of Smirnov *et al.* [26]. Alternatively, Siefert and Ewert [54] proposed to use a hierarchy of filters to account for anisotropy in the Reynolds stress tensor and length scales. The RPM method is often used along with the Acoustic Perturbation Equations (APEs) [56], which are more stable for propagating acoustic waves but do not support vortical disturbances. Therefore, an auxiliary mesh is required to evaluate the velocity disturbances computed by the RPM method when using the APEs. This technique has been used to study airframe noise [52] and trailing edge noise [57], among others. Cozza *et al.* [58] modified the RPM method to follow an Eulerian approach while using the APEs and a temporal filter based on previous work by Billson *et al.* [36]. A similar technique was presented by Mesbah [59] for jet noise predictions using the LEEs.

In the area of leading edge noise predictions, Dieste and Gabard [60] derived exact expressions for the filters that can reproduce two-dimensional Liepmann and von Kármán isotropic energy spectra

for a RPM-based method. Synthetic turbulence was directly evaluated on the surface of a flat plate and imposed through a wall boundary condition in a LEE solver for the noise propagation. In order to account for the distortion of the turbulent structures around thick aerofoils, Wohlbrandt *et al.* [61] tested a number of numerical implementations using the RPM method. Among them, the use of a buffer zone in the source region where synthetic turbulence was computed, was found to provide consistent noise results in a LEE solver. In order to reduce the number of grid points on which the velocity fluctuations need to be computed, Kim *et al.* [62] proposed two types of inflow boundary condition for a RPM-based method to inject the synthetic turbulence at the edges of the computational domain. One of them follows the radiation boundary condition of Tam *et al.* [63]. The other one is based on the characteristic waves of the Euler equations proposed by Giles [64].

Summary of Previous Work on Synthetic Turbulence Methods

Several synthetic turbulence methods, such as Fourier mode, digital filter, and synthetic eddy methods, have been used to study leading edge noise in CAA simulations [38, 41, 48, 61]. Initial work in the field preferred Fourier mode methods, which can be seen as a natural extension of methods to inject single harmonic gusts in CAA simulations. However, Fourier mode methods can be computationally expensive when a large number of modes are required, which is often the case for three-dimensional simulations with high-frequency resolution [41]. Digital filter and synthetic eddy methods are often considered to provide a more realistic description of the turbulent flow, since the resulting fluctuating velocity field has a continuous spectral density and is not periodic. Nevertheless, it remains unclear which type of method is the most suitable for accurate leading edge noise predictions at an acceptable computational cost. A direct comparison between various synthetic turbulence methods would be beneficial to highlight their advantages and limitations in practical cases.

To date, the majority of CAA studies on leading edge noise are restricted to two-dimensional simulations using isotropic synthetic turbulence [60, 61, 62], and few attempts have been made to use fully three-dimensional turbulence [38, 40, 41, 48]. Fully three-dimensional works are often restricted to simplified representations of isotropic turbulence, such as modelling only the upwash velocity fluctuations [38, 40]. Although there are methods that are able to synthesise anisotropic turbulence, they usually present difficulties to realise divergence-free anisotropic turbulence in a simple manner and to provide explicit control on the resulting turbulence spectra, as required for leading edge noise predictions.

Alternatively, synthetic turbulence methods developed for LES applications that are divergence-free could potentially be used in CAA simulations. However, these methods usually focus on reproducing the one-point velocity correlations, such as the Reynolds stress tensor, and not on reproducing a target energy spectrum [26, 47, 50].

1.3.2 Turbulence-Aerofoil Interaction Noise

The following literature review includes relevant analytical, experimental, and numerical studies, in which the modelling assumptions and aerofoil geometry effects on broadband noise are highlighted. Details on the experimental or computational setup and potential limitations are also provided.

Analytical Studies

Initially, analytical works focused on calculating the aerodynamic response of a harmonic gust interacting with a single flat plate at zero angle of attack, $AoA = 0^{o}$. Sears [65] calculated the two-dimensional aerofoil response to parallel sinusoidal gusts and Filotas [66] extended the analysis to include skewed sinusoidal gusts in compressible flow. Figure 1.5 shows both parallel and skewed gusts impinging on a flat plate.

For low-frequency gusts, Amiet [67] derived the unsteady lift of a flat plate for compressible flows by following the similarity rules given by Graham [68]. These rules state that the aerofoil response due to a harmonic gust can be associated with either a parallel gust in a compressible flow (supercritical gust) or a skewed gust in an incompressible flow (subcritical gust), depending on a mathematical relationship between the Mach number and wavenumber components of the gust. For high-frequency gusts, Amiet [69] separated the effects of the leading edge and the trailing edge by considering semi-infinite flat plates. The resulting expression for the unsteady lift of a flat plate in a subsonic compressible flow shows that compressibility effects are particularly important at high frequencies.

Amiet [39] studied the unsteady response of a three-dimensional flat plate to derive analytical expressions for the acoustic power spectrum due to oncoming turbulence. Following a Fourier mode decomposition, the oncoming turbulence was described by a summation of skewed gusts that were convected by a uniform mean flow as frozen turbulence [32]. Since velocity fluctuations that are perpendicular to the flat plate are responsible for the unsteady lift, only the upwash velocity spectrum was included in the analytical model of Amiet [39]. In a recent work, Blandeau *et al.* [70] adapted Amiet's model [39] to study leading edge noise from a flat plate using two-dimensional Green's functions for the far-field sound propagation.

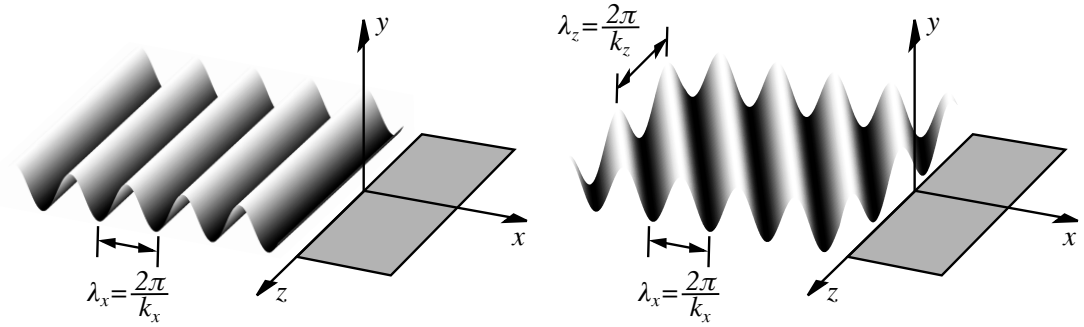

(a) Parallel gust with $k_x \neq 0$ and $k_z = 0$.

(b) Skewed gust with $k_x \neq 0$ and $k_z \neq 0$.

Figure 1.5: Harmonic gusts with fluctuating velocity perpendicular to a flat plate.

In order account for the thickness effects on leading edge noise, semi-analytical corrections to flat plate theories [71, 72, 73] and asymptotic approximations [74] have been proposed. For symmetric thick aerofoils, Gershfeld [71] obtained leading edge noise predictions by means of shape-dependent Green's functions. Additionally, Gershfeld [71] showed that the flat plate solution can be corrected to account for aerofoil thickness effects on the noise by using an exponential scaling law, $\exp(-\pi f t_A / U_\infty)$, where f is the frequency, t_A is the maximum aerofoil thickness, and U_∞ is the freestream speed. Such a correction term implies that leading edge noise decreases as the aerofoil thickness increases. Moreau *et al.* [72] proposed both camber and thickness corrections to produce leading edge noise predictions of aerofoils with realistic geometry. The camber correction assumes that the aerofoil mean line is an arc. This leads to a change in the noise radiation pattern, which increases on the pressure side and decreases on the suction side. Following Hunt's work [75], Moreau *et al.* [72] proposed a thickness correction that was based on the distorted velocity spectrum in the leading edge region of a NACA 0012 aerofoil, and showed that the effect of aerofoil thickness is to reduce the noise at high frequencies. Using rapid distortion theory, Santana *et al.* [73] modified the von Kármán spectrum to account for a stronger decay at high frequencies. The re-defined von Kármán spectrum was introduced in the analytical model of Amiet [39] to improve the accuracy of the noise predictions from a NACA 0012 aerofoil. A discussion on the limitations of analytical models for both leading and trailing edge noise was presented by Roger and Moreau [76]. Potential extensions to account for the effects of thickness and angle of attack on the noise were also discussed.

Glegg and Devenport [77] used a panel method to obtain the unsteady aerofoil response and leading edge noise predictions of realistic aerofoils. The noise predictions were only valid for aerofoils in incompressible flows, and were limited to low frequencies due to the assumption of acoustically compact aerofoils. This panel method was also used by Devenport *et al.* [78] to study leading edge noise from aerofoils with realistic geometry. For isotropic turbulence, aerofoil thickness was found to decrease noise levels at relatively high frequencies, whereas the effect of angle of attack on the noise

was nearly negligible. In contrast, a significant increase in noise levels with increasing angle of attack was reported when testing anisotropic turbulence for leading edge noise predictions of a NACA 0015 aerofoil. An increase of up to 10 dB was found at $AoA = 12^{o}$ in comparison with the $AoA = 0^{o}$ baseline, when turbulence was moderately stretched in the streamwise direction. This result highlights the importance of including anisotropy for accurate leading edge noise predictions.

Experimental Studies

In 1976, Paterson and Amiet [79] performed far-field noise measurements of a NACA 0012 aerofoil in an open-jet anechoic wind tunnel. The experiment tested two different geometric angles of attack, $AoA = 0^{o}$ and 8^{o}, and mean flow speeds ranging from 40 m/s to 165 m/s. Nearly isotropic turbulence was generated by placing a grid upstream of the jet exit. Noise measurements were performed by placing a microphone array outside the jet in the mid-span plane, such that sound scattering and refraction occurred as the acoustic waves passed through the jet shear layer. Experimental data were treated to remove the background noise and compared with Amiet's theory [39], which was adapted to account for the shear layer refraction [80, 81]. Broadband noise results showed that the angle of attack introduces a measurable but small increase in the noise spectra, of about 1 dB at all frequencies and observer locations. Nevertheless, the role of the angle of attack in leading edge noise predictions is difficult to quantify experimentally. This is because open-jet wind tunnels produce a deviation of the jet as it passes over the aerofoil, which decreases the effective angle of attack that is perceived by the aerofoil. Additionally, aerofoil thickness was found to reduce noise levels at high frequencies when compared to the flat plate prediction.

Using a similar experimental setup as in Paterson and Amiet's work [79], Moreau *et al.* [72] compared experimental noise measurements of a 3% thick flat plate with Amiet's analytical model [39]. Noise levels were found to be within 3 dB for most frequencies. Additionally, the geometric angle of attack was varied between 0^{o} and 15^{o} for different thick aerofoils with no significant change in noise levels. In a later work, Moreau and Roger [82] found leading edge noise as the dominant noise mechanism of single aerofoils interacting with turbulence for low and mid-range frequencies, up to a few kHz, whereas aerofoil self-noise becomes relevant at significantly higher frequencies and angles of attack.

In order to minimise the jet deflection of aerofoils placed at incidence, Staubs [83] performed a series of experiments in a half-open jet wind tunnel with enclosed test section. The upper and lower walls were treated acoustically to reduce sound reflections, whereas the lateral walls were made of Kevlar panels, which allow acoustic waves to pass through with minimal attenuation. The experiment included aerofoils with different chord, thickness, leading edge radius, camber, and angle of attack interacting with grid-generated turbulence. Results showed that aerofoil thickness effects on the noise

depend on the leading edge radius and the overall thickness, among others. Additionally, it was suggested that the effect of angle of attack becomes more important when the aerofoil chord (c) is large in comparison to the integral length scale (Λ).[2] Further analysis of the experimental results was presented by Devenport *et al.* [78], where noise measurements were compared with the panel method approach of Glegg and Devenport [77]. The effect of the angle of attack was found to be small, less than 2 dB at $AoA = 12^{\circ}$, for symmetric aerofoils with 12% and 15% maximum thickness and Λ/c of 0.403 and 0.134, respectively.

Hutcheson *et al.* [84] measured leading edge noise from a number of NACA 0015 aerofoils with various Λ/c on aerofoils placed at incidence. For aerofoils with small Λ/c, the effects of angle of attack on the noise were nearly negligible, with an increase of 2 dB for angles of attack below $AoA = 15^{\circ}$. However, an increase of about 2 dB every 4° was reported for aerofoils with $\Lambda/c \geq 1$. This result contrasts with the previous work of Staubs [83]. Additionally, Roger and Moreau [76] compared experimental measurements of leading edge noise from a number of works, and suggested that the noise reduction due to aerofoil thickness scales proportionally with the ratio t_A/Λ.

Turbulence-aerofoil interaction noise was also examined on a NACA 65(12)-10 aerofoil with small Λ/c by Gruber [85]. As in previous works, aerofoil thickness was found to reduce broadband noise at high frequencies in comparison with the flat plate prediction. However, the angle of attack was found to reduce leading edge noise by about 4 dB for a geometric $AoA = 15^{\circ}$ and mean flow speed 20 m/s. Such a noise reduction was associated with of the lack of homogeneity in turbulence across the test section, which varies the properties of the turbulence perceived by the aerofoil at non-zero angle of attack. In the same open-jet wind tunnel facility [86], Chaitanya *et al.* [87] performed an extensive parameter study on the effects of leading edge radius, Mach number, and camber on leading edge noise. Noise reductions were achieved by increasing the leading edge radius of thin aerofoils, whereas noise levels were unaffected by variations of camber of up to 8% on aerofoils with $t_A/c = 0.06$. Particle Image Velocimetry (PIV) measurements were performed around the aerofoil leading edge to investigate noise reduction mechanisms related to variations in the turbulent flow. Aerofoils with sharp leading edge were found to produce stronger transverse velocity fluctuations than aerofoils with a blunt leading edge.

[2] In this thesis, the following notation is used for the integral length scales

$$l_{ij}^{(k)} = \int_0^{\infty} \frac{\langle u_i'(\mathbf{x} + r\mathbf{e}_k) u_j'(\mathbf{x}) \rangle}{\langle u_i'(\mathbf{x}) u_j'(\mathbf{x}) \rangle} \mathrm{d}r,$$

where u_i' represents the ith fluctuating velocity component, r is the separation between two points in the kth direction, $\mathbf{e}_k$ is a unit vector in the kth direction, and $\langle . \rangle$ is the ensemble average operator. Therefore, $l_{ij}^{(k)}$ is the integral length scale of the ith and jth fluctuating velocity components in the kth spatial direction. For isotropic turbulence, $l_{11}^{(1)}/l_{22}^{(1)} = l_{11}^{(1)}/l_{33}^{(1)} = 2$ and $l_{11}^{(1)} = l_{22}^{(2)} = l_{33}^{(3)} = \Lambda$.

Although there are few experimental studies that are intended for leading edge noise predictions using anisotropic turbulence, grid-generated turbulence in wind tunnel facilities normally presents a certain level of anisotropy. For example, Paterson and Amiet [79] reported a streamwise-to-transverse integral length scale ratio, $l_{11}^{(1)}/l_{22}^{(1)}$, of approximately 1.25, whereas $l_{11}^{(1)}/l_{22}^{(1)} = 2$ is expected for isotropic turbulence [88]. Unlike experiments using grid-generated turbulence, Olsen and Wagner [89] tested a number of symmetric aerofoils at zero angle of attack interacting with a jet shear layer, where anisotropy is more pronounced. The study showed a notable reduction in noise levels at high frequencies, which is consistent with findings in experiments using nearly isotropic turbulence. Hall *et al.* [90] measured the noise from thick aerofoils with various leading edge geometries interacting with anisotropic turbulence from a boundary layer. The scaling law of Gershfeld [71] (to predict the effects of aerofoil thickness on the noise) showed an acceptable agreement with experimental results, despite the fact that the scaling law was initially intended for aerofoils interacting with isotropic turbulence. Recently, Geyer *et al.* [91] tested a NACA 0012 aerofoil placed close to the nozzle exit, where anisotropy occurs and turbulence intensity is high.

Numerical Studies

Early numerical works focused on noise predictions of gust-aerofoil interaction. Parallel and skewed harmonic gusts were used to show the effects of aerofoil thickness and angle of attack on the noise directivity [92, 93]. Recently, Gill *et al.* [94] used a multi-frequency gust approach in a LEE solver to assess mean flow modelling assumptions, and to study the effects of aerofoil thickness and leading edge radius on the noise at higher frequencies than previous works. Noise predictions using inviscid and viscous mean flows were found to be in good agreement at low and mid-frequencies, with small discrepancies at high frequencies. This result suggests a negligible role of viscosity on leading edge noise predictions. In contrast, simulations using a uniform mean flow produced an over-prediction of the noise levels at high frequencies. This was associated with the lack of gust distortion in the vicinity of the aerofoil leading edge when a uniform mean flow is assumed. Recently, Kim *et al.* [95] used a RPM-based method to assess aerofoil thickness effects using inviscid mean flows with isotropic turbulence, and achieved similar conclusions as in the previous work of Gill *et al.* [94] using harmonic gusts.

Deniau *et al.* [96] tested several LES approaches to reproduce experimental measurements of a NACA 65(12)-10 aerofoil by means of a one-component Fourier mode method that only accounts for the upwash velocity fluctuations. However, simulations included additional noise sources, such as trailing edge noise and installation effects, and acoustic data were contaminated by recirculation bubbles on the aerofoil pressure side. Using a similar turbulence description, Clair *et al.* [38] extended the investigation to assess the effects of leading edge serrations on the noise from a NACA 65(12)-

10 aerofoil by means of an Euler equation solver. Simulations using a uniform mean flow showed a slower noise decay at high frequencies when compared to the viscous mean flow solution, which is consistent with the findings of Gill *et al.* [94]. Similar conclusions were reached by Hainaut *et al.* [97], who performed LEE simulations of a NACA 65(12)-10 aerofoil by using stochastic vorticity sources to locally inject a one-component fluctuating velocity field. This method was also used to show that the aerofoil response remains unaffected by variations in the integral length scale. Additionally, Gill [98] concluded that the noise reduction due to aerofoil thickness at high frequencies is not sensitive to variations in the integral length scale when assuming isotropic turbulence. Recently, Hainaut *et al.* [99] extended a synthetic turbulence method based on stochastic vorticity sources to generate two-component fluctuating velocity fields. This method was used to examine the distortion of the turbulent flow in the leading edge region of various aerofoil geometries, as this is believed to be responsible for aerofoil geometry effects on leading edge noise.

Gill *et al.* [41] performed leading edge noise predictions using Fourier mode methods with one, two, and three fluctuating velocity components in LEE simulations. The transverse velocity fluctuations were identified as the main contributors to the noise generation, whereas the chordwise and spanwise velocity disturbances had minor effects for symmetric aerofoils at zero angle of attack. This finding may help to reduce the number of components to be used in CAA simulations and, therefore, decrease the computational expense. The effects of camber and angle of attack on the noise was found to be negligible in the presence of isotropic turbulence. However, Gill *et al.* [41] suggested that anisotropic turbulence could play a significant role in the leading edge noise of aerofoils at non-zero angle of attack after examination of the aerofoil-gust response function.

Summary of Previous Work on Turbulence-Aerofoil Interaction Noise

Leading edge noise from single aerofoil configurations has been studied from analytical [39, 71], experimental [72, 78, 79, 87], and computational perspectives [38, 41, 95]. However, analytical models often assume flat plates, and the noise prediction of real geometry aerofoils is done by semi-analytical corrections [71, 72] or asymptotic solutions [74]. The distortion of the turbulent structures in the leading edge region has been modelled analytically by means of rapid distortion theory [72, 73], and has been highlighted as a major noise reduction mechanism of thick aerofoils in CAA simulations using harmonic gusts [94, 95]. Initial work on the distortion of the upwash turbulence spectrum has recently been presented by Hainaut *et al.* [99], and PIV of the turbulent flow in the leading edge region has been shown by Chaitanya *et al.* [87].

To date, variations in leading edge noise due to isotropic turbulence interacting with real geometry aerofoils are well understood. An increase in aerofoil thickness produces a significant reduction in the noise levels at high frequencies [41, 79, 87, 95], whereas changes in angle of attack and camber

produce minor effects on the noise levels [41, 72]. However, few works have addressed the effects of anisotropic turbulence on leading edge noise [78, 90], despite the typical anisotropic features of turbulence in the engine intake [15, 16] and fan wakes [18]. Experimental noise measurements in open-jet wind tunnels are also affected by a certain degree of anisotropy [79].

1.3.3 Turbulence-Cascade Interaction Noise

Analytical Studies

The majority of turbulence-cascade interaction noise models are based on a two-step approach, which follows a similar derivation as in Amiet's work [39] for the leading edge noise of a flat plate. Firstly, the unsteady cascade response due to harmonic perturbations is calculated through aerodynamic relationships. Secondly, the acoustic power is obtained through a weighted sum of all harmonics according to the spectral density of the upwash velocity fluctuations.

Smith [100] modelled the interaction of small amplitude sinusoidal wakes with a two-dimensional flat plate cascade by means of the LEEs. The mean flow was aligned with the flat plate cascade such that there were no steady loads acting on the vanes. Furthermore, lean and sweep effects were neglected, and only the stagger angle was specified as an input (see Figure 1.6). Cheong *et al.* [101] extended the harmonic gust analysis of Smith [100] via Fourier decomposition to reproduce the isotropic Liepmann spectrum. The acoustic power spectrum showed a different behaviour for low and high frequencies. At low frequencies, the acoustic interaction between neighbouring blades results in a small sensitivity to the vane count. In contrast, the power spectrum was reported to scale with the number of vanes at high frequencies, showing that cascade effects were negligible. Similar results were found by Blandeau *et al.* [70]. Additionally, a similar level of agreement was reported between the model of Cheong *et al.* [101] and the three-dimensional model proposed by Hanson [102] when compared to available experimental data. This result suggests that oblique gusts and three-dimensional effects might play a secondary role in the prediction of the acoustic power spectrum. Jenkins [103] adapted the original formulation of Cheong *et al.* [101] to be used with both CFD and experimental input data from the fan wakes.

Several sources of leading edge noise, such as turbulence ingestion noise and rotor wake-stator interaction noise, were included in the analytical model of Ventres *et al.* [104]. Noise predictions were computed from two-dimensional flat plate response functions applied at different radii, as in linear cascades. This technique, which is known as the strip theory approximation, can account for radial variations in the oncoming turbulence, stagger angle, and inter-vane spacing, among others. Additionally, three-dimensional propagation in an infinite hard-walled duct was included by means of the Green's function for an annular duct. Nallasamy and Envia [105] extended the model of Ventres

et al. [104] to extract input data of the fan wakes from CFD simulations. Noise predictions from the analytical model were in reasonable agreement with experimental measurements taken from the 22-inch Source Diagnostic Test (SDT) fan rig of the NASA Glenn Research Centre [106, 107, 108, 109].

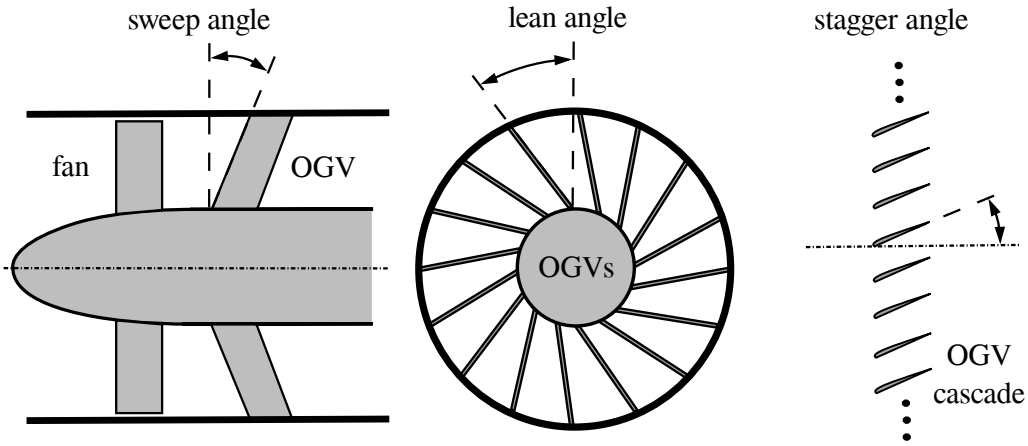

Figure 1.6: Schematic representation of sweep, lean, and stagger angles. Fan-stator and bypass duct cross-section (left), front view of the stator (centre), and unwrapped stator at the mid-span section (right).

Hanson [102] developed a broadband noise model based on previous models by Hanson and Horan [110] and Glegg [111]. The latter provides the acoustic response of a fully three-dimensional gust interacting with a rectilinear flat plate cascade with unloaded vanes. Thus, the model of Hanson [102] accounts for lean and sweep effects on the acoustic power spectrum. Sweep alone was found to be more effective than the lean alone in terms of broadband noise reduction, since swept vanes lead to a reduction in the chordwise Mach number that is perceived by the vanes.

Alternatively, Posson *et al.* [112] developed a broadband noise prediction model to account for both turbulence ingestion and rotor wake-stator interaction noise. The method is based on previous works by Ventres *et al.* [104], Nasallamy and Envia [105], and Hanson [102]. Results were validated using experimental results from the SDT fan rig. Acoustic power spectra were found to be highly sensitive to the input turbulence spectra through a comparison between isotropic and anisotropic turbulence using the axisymmetric spectra of Kerschen and Gliebe [113]. For example, turbulence stretched in the engine axial direction shifts the maximum noise level towards lower frequencies and reduces the noise by up to 16 dB at high frequencies. Based on the model of Posson *et al.* [112], Grace [114] proposed a low-order method for the computation of the fan wake-OGV interaction noise downstream of the OGVs that was vetted on several cases from the SDT fan rig. Experimental and CFD data were used to compute the turbulence statistics of the fan wakes, which were then fitted by the isotropic Liepmann spectra. The turbulence length scale was found to be a key parameter in the shape of the

resulting noise spectra. Similar conclusions were also achieved by Ju *et al.* [115] when assessing the influence of the integral length scale in background and wake turbulence separately.

A different type of approach, to account for the three-dimensional cascade without using strip theory, has been proposed by Atassi *et al.* [116, 117, 118]. The model solves the LEEs for an annular unloaded cascade and includes the effect of swirling mean flow, which was shown to have an effect on acoustic mode propagation through the bypass duct.

Although the majority of established cascade models are based on the flat plate assumption, there have been some attempts to include aerofoil geometry effects on the noise. For example, Evers and Peake [119] extended the flat plate model of Hanson and Horan [110] to account for small thickness, camber and angle of attack. The model consists of an asymptotic solution for the prediction of upstream acoustic power in non-uniform mean flow. Aerofoil geometry was found to have a reduced effect on broadband noise, with variations in noise spectra of up to 2 dB. Recently, Grace [120] tested an asymptotic gust response method [74] to include aerofoil geometry effects in a low-order model for the prediction of exhaust cascade noise. Although the approach was restricted to small vane geometry variations, which might not be representative of realistic OGV designs, the flat plate assumption was found to be sufficiently accurate.

Experimental Studies

One of the most relevant works on fan noise was performed by Ganz *et al.* [17] in the Boeing 18-inch fan rig. The experiment focused on quantifying the contribution of several noise sources by testing a fan stage with three different tip clearances that was mounted with or without a stator. Three different stator configurations with various vane chords and solidities were used in the experiment, each of them located at two different axial locations. Fan tip clearance was found to influence fan tip vortices in the wake, where the turbulence intensity was found to be the highest. In contrast, turbulence intensity in the mid-span region was the lowest. The isotropic von Kármán spectrum gave good representation of the circumferentially-averaged turbulence spectra in this region. The fan wake-OGV interaction noise was identified as the dominant source of broadband noise. Additionally, the fan blades were found to scatter and shield upstream-travelling pressure waves.

A comprehensive characterisation of the noise mechanisms involved in the fan system was performed at the SDT fan rig [106, 107, 108, 109]. A 22-inch turbofan engine was tested in an anechoic low speed wind tunnel at a freestream Mach number of 0.1, which is representative of landing and take-off conditions. Tests included two different fan designs with 22 blades each, one of them with a 10 % higher blade tip speed, and three stator vanes with 54, 26, and 26-swept guide vanes. Anisotropic axisymmetric turbulence was reported in experimental measurements of fan wakes, especially close

to the trailing edge of the fan blades [18]. Increasing fan tip clearance was found to produce a small increase in noise levels. The swept guide vanes produced a measurable reduction in both tonal and broadband noise, although the low-count vane produced a cut-on BPF tone.

To reduce the number of noise sources under study, Posson and Roger [121] measured the rear-arc acoustic power from grid-generated turbulence interacting with two different stator vanes within an annular duct. The experiment was designed to provide benchmark results for the validation of cascade analytical models, such as those of Posson *et al.* [112] and Grace [114]. The oncoming turbulence was assumed to be isotropic and convected by a nearly uniform flow upstream of the OGVs. Therefore, the swirl due to an eventual fan was neglected. Lean and sweep angles were small enough to be neglected in analytical models.

Experimental measurements from a large scale fan rig were used by Jenkins (see Chapter 8 in Reference [103]) as a benchmark for aerodynamic and aeroacoustic studies of turbofan engines. The experiment included one fan blade configuration and three different OGV designs placed at two different axial locations. Furthermore, an acoustically treated intake was installed in the fan system. Hotwire measurements in all three spatial directions near the OGV leading edge were performed to extract aerodynamic information from the fan wakes at different radial locations. Forward-arc noise measurements were taken from a microphone array within the anechoic chamber. Rear-arc noise measurements were derived from a set of microphones placed on the wall of the bypass duct. Experimental acoustic data were used for comparison with the two-dimensional cascade model of Jenkins [103].

Numerical Studies

LES and RANS simulations are often performed to extract turbulence statistics from the fan wakes. For example, Nallasamy and Envia [105] used a RANS code with a modified $K-\varepsilon$ turbulence model to predict the turbulence statistics required as an input for an analytical model of turbulence-cascade interaction noise. Similarly, Grace [114] extracted CFD data from simulations of the SDT fan rig that were used in a low-order cascade model. Sescu [122] computed the fan wakes by using a synthetic eddy method to reproduce the unsteady velocity field of the fan wakes in the experiment of the SDT fan rig [18]. Other computational methods, such as that by Olausson and Eriksson [123], combine both RANS and LES with synthetic fluctuations to generate turbulent wakes.

Initial CAA studies in the field of turbulence-cascade interaction noise focused on modelling the interaction of single-frequency gusts with cascades. For example, Namba and Schulten (see Category 4 in Reference [124]) proposed a three-dimensional benchmark case in which the fan wakes were modelled by a discrete sum of harmonic gusts. Results were discussed by using Smith's model [100] and Tyler and Sofrin's rule [13]. Another benchmark case was proposed by Envia (see Category 3,

Problem 2 in Reference [125]) using a quasi two-dimensional cascade configuration with a realistic OGV geometry. At the inlet plane, three harmonic gusts were introduced and convected downstream by the mean flow. Sound Pressure Level (SPL) measurements were provided at different locations for validation purposes. Recently, Chaitanya *et al.* [126] investigated the effects of vane geometry in two-dimensional simulations using a harmonic gust decomposition in a linearised Navier-Stokes equation solver. A parameter study that was performed at a fixed frequency showed small effects on cascade noise due to aerofoil thickness, camber, angle of attack, and swirl in the mean flow.

Using a synthetic turbulence method based on a summation of Fourier modes, Polacsek *et al.* [40] performed three-dimensional LEE simulations of a single flat OGV passage with isotropic turbulence that only included the upwash velocity fluctuations. Unsteady data from the CAA calculation were used as an input for a FW-H solver, which modelled the sound propagation within a duct with uniform mean flow. Such a CAA method was applied to reproduce experimental results from Posson and Roger [121] and a swirling mean flow configuration investigated by Atassi and Vinogradov [117].

Dieste (see Chapter 6 in Reference [127]) modelled cyclostationary variations in the turbulent kinetic energy of the fan wakes using two-dimensional synthetic turbulence. The method was validated for broadband noise predictions using a single flat plate. Based on Dieste's work [127], Wohlbrandt *et al.* [128] adapted the RPM method in a LEE solver to reproduce two-dimensional fan wakes with Gaussian spectra and different modelling assumptions, such as cyclostationary variations in the turbulent kinetic energy and integral length scale. However, modelling the turbulent kinetic energy of the fan wakes was found to have a limited effect on turbulence-cascade interaction noise, and the effect of the integral length scale was inconclusive for the tested cases. The approach presented some computational limitations. For example, turbulence was only injected in a small region of the CAA domain to reduce the computational expense, such that only a few OGVs interacted with the fan wakes, and spurious noise reflections were identified in the CAA domain.

Lattice-Boltzmann simulations have also been proposed for fan broadband noise predictions [22, 23, 129]. This approach is able to simulate complex turbofan engine configurations while including several noise sources simultaneously. Preliminary simulations of the active noise control fan rig [130] were performed as a benchmark towards complex turbofan noise predictions including fan and jet noise [129]. Recently, the SDT experimental results were accurately reproduced [22], and installation effects were also addressed [23]. To increase the accuracy of the noise predictions, a trip needed to be used on the fan blade surface to recover the correct turbulence intensity in the fan wakes.

Summary of Previous Work on Turbulence-Cascade Interaction Noise

The majority of analytical models of turbulence-cascade interaction noise use the flat plate assumption to model the vane geometry [101, 102, 112]. Asymptotic methods, such as those by Evers

and Peake [119] and Grace [120], have been proposed to study the effects of small variations in aerofoil thickness, camber, and angle of attack. However, the study of Evers and Peake [119] was restricted to the computation of upstream noise spectra, and Grace [120] highlighted the difficulty of using asymptotic methods for single aerofoils in cascade models. Fan rig experiments have shown the effects of lean and sweep angles on cascade noise [17, 107], but an experimental parameter study on the effects of vane geometry would be expensive, impractical, and affected by several noise sources acting simultaneously. Recently, CAA simulations using harmonic gusts have been performed to study vane geometry effects on cascade noise [126]. An extension to fully broadband noise predictions using CAA simulations would be beneficial to gain a more detailed insight into engine fan noise.

Analytical models often assume isotropic turbulence to model the fan wakes statistics. However, analytical models are quite sensitive to the input turbulence spectrum, particularly to the turbulence length scales [112, 114, 115]. Unlike classic analytical models, CAA simulations using synthetic turbulence can be used to accurately reproduce the fan wake statistics. For example, Dieste [127] modelled the circumferential distribution of the turbulent kinetic energy, and Wohlbrandt *et al.* [128] included variations in the integral length scale. However, the effects of modelling the turbulent kinetic energy on broadband noise were evaluated for single flat plate configurations [127], and the effects of cyclostationary variations in the integral length scale were inconclusive for the tested cascade configurations [128]. Furthermore, previous CAA works were restricted to Gaussian spectra in order to reduce the computational cost [127, 128], whereas the von Kármán spectrum has been found to provide a good representation of the spectral content in the fan wakes at the mid-span [17].

1.4 Original Contributions

The original contributions of this thesis are summarised as follows:

- **Presentation of the advanced digital filter method to generate two- and three-dimensional isotropic/anisotropic synthetic turbulence**. The resulting turbulent flow is obtained from a superposition of divergence-free eddies, which act as spatial filters. The advanced digital filter method provides explicit control over the resulting isotropic/anisotropic turbulence spectra, as required for leading edge noise predictions. Additionally, the accuracy and performance of the advanced digital filter method has been compared to synthetic turbulence methods based on a summation of Fourier modes.

- **Improvement of current understanding of leading edge noise**. This thesis investigates various aspects that influence leading edge noise, such as the distortion of the streamwise and transverse velocity spectra in the leading edge region, the unsteady pressure response on the surface of thick aerofoils, and strongly sheared mean flows with jet configurations, as occurs in

open-jet wind tunnel experiments. Strong distortions of the turbulent flows occur in the vicinity of the leading edge, in a region within 2% of the aerofoil chord for symmetric aerofoils at $AoA = 0^{o}$ and 6^{o}. It has been found that the distortion of the upwash velocity spectrum follows the trends predicted by rapid distortion theory. The unsteady pressure response on the aerofoil surface is weaker as the aerofoil thickness increases, especially at high frequencies, which explains the far-field noise reduction due to aerofoil thickness. Furthermore, leading edge noise predictions using a gradient term suppression in the LEEs were shown to provide satisfactory results in the presence of a jet. Nevertheless, leading edge noise is not significantly affected by the aerofoil mean loading in CAA simulations.

- **Effects of anisotropy on turbulence-aerofoil interaction noise**. A CAA study is performed to assess the effects of anisotropic turbulence on leading edge noise from various single aerofoil configurations. The study includes variations in the streamwise-to-transverse length scale ratio between 0.33 and 3, which is representative of the anisotropy in the fan wakes. Noise reduction at high frequencies due to aerofoil thickness shows similar trends for both isotropic and moderately anisotropic turbulent flows. However, the effects of anisotropic turbulence on the PWL spectra become more evident at high frequencies for aerofoil configurations at non-zero angle of attack.

- **Influence of fan wake modelling assumptions on turbulence-cascade interaction noise**. Various fan wake modelling assumptions, such as isotropic turbulence with von Kármán spectra and cyclostationary variations in the turbulent kinetic energy and integral length scale, are investigated in two-dimensional cascade configurations. Numerical noise results are compared to analytical predictions using the cascade model of Cheong *et al.* [101]. Results indicate that cyclostationary variations in the turbulent kinetic energy shift the amplitude of the PWL spectra, whereas variations in the integral length scale affect the slope of the PWL spectra. Overall, broadband noise mainly depends on the circumferentially-averaged turbulence spectra that are perceived by the OGV cascade, and is independent of the instantaneous statistics of the fan wakes. Therefore, isotropic turbulence with the spectral content of the fan wakes is sufficient for accurate cascade noise predictions.

- **Effects of OGV design parameters on turbulence-cascade interaction noise**. Broadband noise spectra are examined systematically upstream and downstream of the cascade for several configurations, including variations in vane count, thickness, mean flow Mach number, camber, stagger angle, and inter-vane spacing. A modal spectral decomposition is performed to study the contribution of cut-on 'duct modes' to the PWL spectra by means of mode-frequency maps. Variations in OGV design parameters lead to significant variations in the cut-on modes and modal spectral distributions. However, their effect on the PWL spectra is normally below 2 dB, which confirms the suitability of the flat plate assumption for the prediction of OGV noise.

1.5 Outline of Contents

The current work is organised as follows.

- Chapter 2 focuses on the development and analysis of synthetic turbulence methods that are suitable for leading edge noise predictions. An advanced digital filter method is presented for two-dimensional simulations using isotropic turbulence. Alternatively, one- and two-component Fourier mode methods are also developed. The advantages and limitations of the methods are discussed.

- Chapter 3 investigates leading edge noise from two-dimensional single aerofoils by means of synthetic turbulence methods presented in Chapter 2. Variations in aerofoil thickness, Mach number, and angle of attack are analysed. To improve current understanding of leading edge noise, the distortion of the velocity spectra in the stagnation region is examined for each aerofoil configuration, the spectral content of the unsteady pressure on the aerofoil surface is investigated, and the PWL spectra and directivity plots are given in the far-field.

- In Chapter 4, the advanced digital filter method is extended to realise fully three-dimensional isotropic turbulence. The method is applied to reproduce experimental measurements of leading edge noise in open-jet wind tunnels. Alternatively, a low-cost approach is explored to perform accurate noise predictions of experimental data from two-dimensional CAA simulations.

- In Chapter 5, the advanced digital filter method is adapted to realise two- and three-dimensional anisotropic turbulence using eddies with various length scales in different spatial directions. A parameter study is performed to assess potential effects of moderately anisotropic turbulence on leading edge noise from single aerofoils. To this end, thick aerofoils at various mean flow Mach numbers and angles of attack are investigated.

- Chapter 6 presents an extensive study on turbulence-cascade interaction noise. The advanced digital filter method is adapted to reproduce the statistics of the fan wakes with various modelling assumptions, such as cyclostationary variations in turbulent kinetic energy and integral length scales. The effects of fan wake modelling assumptions on cascade noise are investigated. Finally, a parameter study is presented to review cascade geometry effects on broadband noise using isotropic turbulence.

- Finally, a summary of the main conclusions and suggestions for future research are provided in Chapter 7.

Chapter 2

Synthetic Turbulence Methods

The present chapter describes the CAA methodology that is used throughout this thesis, focusing on the generation of synthetic turbulence with the statistics and spectral content of the oncoming turbulence. The correct modelling of the turbulence is essential for accurate leading edge noise predictions, and therefore, the choice of a synthetic turbulence method might have an impact on the quality of the resulting noise predictions. To date, methods based on a summation of Fourier modes [38, 41], digital filters [61, 95], and synthetic eddies [48] have been used in CAA solvers for the prediction of turbulence-aerofoil interaction noise. However, a direct comparison between different types of synthetic turbulence methods has not been performed yet, and it remains unclear what the advantages and limitations of each method are for leading edge noise predictions. In this chapter, three different synthetic turbulence methods have been developed for leading edge noise predictions. Among them, an advanced digital filter method, and one- and two-component Fourier mode methods. To simplify the development of the different methods, purely two-dimensional isotropic turbulence is assumed in this chapter.

The advanced digital filter method combines the advantages of the RPM method [52, 60], for the mathematical background, and synthetic eddy methods [43, 47, 48], for the numerical implementation. This allows the generation of non-periodic turbulence without explicitly filtering white noise signals, and gives a significant reduction in the number of constraint parameters and random numbers involved in comparison to previous methods. The reconstruction of a target isotropic energy spectrum is achieved by defining a new eddy profile from a superposition of Gaussian eddies.

Fourier mode methods are based on a superposition of harmonic gusts whose amplitude is modulated by a target isotropic energy spectrum, as in previous works by Clair *et al.* [38] and Gill *et al.* [41]. The one-component Fourier mode method only models the upwash velocity disturbances. The

two-component Fourier mode method and the advanced digital filter method consider both streamwise and transverse velocity disturbances.

The present chapter is organised as follows. The characteristics of the CAA solver that is used in this thesis are detailed in Section 2.1. The governing equations of the advanced digital filter method are presented in Section 2.2. One- and two-component Fourier mode methods are presented in Section 2.3. Finally, synthetic turbulence methods developed in this chapter are validated for leading edge noise predictions in Section 2.4, where numerical results of a NACA 0001 aerofoil are compared with the analytical solution for a flat plate. Section 2.4 also includes details on the CAA mesh generation, numerical setup, and modelling assumptions. Further comparison of the advantages and limitations of the different synthetic turbulence methods is presented in Chapter 3, where more challenging configurations of turbulence-aerofoil interaction noise are examined.

2.1 Computational Aeroacoustic Solver

The present thesis uses a high-order finite difference CAA code that has been developed within the University of Southampton and used in prior CAA studies [131, 132, 133]. Synthetic turbulence methods are implemented in the CAA code, which solves the LEEs to compute the noise generation and propagation from the interaction of turbulence with aerofoils. All CAA simulations used the IRIDIS-4 high performance computing facility at the University of Southampton.

2.1.1 Linearised Euler Equations

The CAA code solves the LEEs in the time domain. The flow variables are separated into mean and fluctuating components such that density, pressure, and velocity are split as

$$\rho_0 + \rho', \quad p_0 + p', \quad \mathbf{U}_0 + \mathbf{u}', \tag{2.1}$$

respectively, where the subscript '$_0$' represents the mean flow components, and the fluctuating components are indicated by the superscript '′'. The mean flow velocity, $\mathbf{U}_0 = (U_{0,x}, U_{0,y}, U_{0,z})$, can be obtained from CFD simulations, and the fluctuating velocity, $\mathbf{u}' = (u'_x, u'_y, u'_z)$, is modelled by a synthetic turbulence method. The LEEs in non-conservative form can be written as

$$\frac{\partial \rho'}{\partial t} + \mathbf{U}_0 \cdot \nabla \rho' + \mathbf{u}' \cdot \nabla \rho_0 + \rho_0 \nabla \cdot \mathbf{u}' + \rho' \nabla \cdot \mathbf{U}_0 = -\frac{c_\infty}{L_{ref}} \sigma_{bz} (\rho' - \rho'_{tar}), \tag{2.2}$$

$$\frac{\partial \mathbf{u}'}{\partial t} + (\mathbf{u}' \cdot \nabla)\mathbf{U}_0 + (\mathbf{U}_0 \cdot \nabla)\mathbf{u}' + \frac{\nabla p'}{\rho_0} - \frac{\nabla p_0}{\rho_0^2} \rho' = -\frac{c_\infty}{L_{ref}} \sigma_{bz} (\mathbf{u}' - \mathbf{u}'_{tar}), \tag{2.3}$$

$$\frac{\partial p'}{\partial t} + \mathbf{U}_0 \cdot \nabla p' + \mathbf{u}' \cdot \nabla p_0 + \gamma \left(p_0 \nabla \cdot \mathbf{u}' + p' \nabla \cdot \mathbf{U}_0 \right) = -\frac{c_\infty}{L_{ref}} \sigma_{bz} \left(p' - p'_{tar} \right), \tag{2.4}$$

where $\gamma = 1.4$ is the heat capacity ratio, $c_\infty = 340\,\mathrm{m/s}$ is the speed of sound, $L_{ref} = 1\,\mathrm{m}$ is the reference length, and σ_{bz} is the damping function of the buffer zones (see Section 2.1.4), which is added to the right hand side of the LEEs as a source term. The target fluctuating variables, ρ'_{tar}, p'_{tar}, and $\mathbf{u}'_{tar}$, are normally set to zero when solving the LEEs. It should be noted that the LEEs can propagate acoustic, vortical, and entropy waves. In CAA simulations of leading edge noise, synthetic turbulence corresponds to vortical waves that interact with the aerofoil surface to generate acoustic waves. This process is assumed to be isentropic, and Equation 2.2 can be replaced by the relationship $\rho' = p'/c_\infty^2$ to reduce the computational expense of the CAA simulations.

2.1.2 Numerical Schemes

The LEEs are solved by using a 4th-order pentadiagonal compact spatial scheme [134] and a 4-6 stage Runge-Kutta time marching scheme with low dispersion and dissipation [135]. The numerical solution is filtered after each time step by a compact low-pass filter with variable cut-off wavenumber, $\kappa_c = 0.88\pi$ [136]. Thus, the CAA code is able to propagate vortical disturbances without significant dispersion and dissipation errors with 8 Points Per Wavelength (PPW). The Courant-Friedrichs-Lewy (CFL) number is lower than 0.6 in all the simulations presented in this thesis to ensure numerical stability.

2.1.3 Slip-Wall Boundary Condition

The absence of viscous terms in the LEEs prevents the flow from creating a boundary layer on the aerofoil surface, where a slip-wall boundary condition is applied. Therefore, the velocity is tangent to the aerofoil surface, and the normal component of the velocity is set to zero, which corresponds to the hard-wall assumption. This implies that $\mathbf{u}' \cdot \mathbf{t} \neq 0$ and $\mathbf{u}' \cdot \mathbf{n} = 0$, where $\mathbf{t}$ and $\mathbf{n}$ are the local tangent and normal vectors, respectively. Additionally, the pressure acts perpendicularly to the aerofoil surface such that the fluctuating pressure is exerted in the direction of the local normal vector.

2.1.4 Non-Reflective Boundary Condition

Implicit buffer zones, as defined by Gill *et al.* [137], are used to damp acoustic waves that reach the edges of the CAA domain by applying an exponential ramp function

$$\sigma_{bz}(x') = \begin{cases} \alpha_{bz}\left(1 - \frac{L_{bz}-x'}{L_{bz}}\right)^{\beta_{bz}} & \text{if } x' \in [0,\, L_{bz}], \\ 0 & \text{otherwise.} \end{cases} \tag{2.5}$$

Here, L_{bz} denotes the length of the buffer zone, α_{bz} controls the strength of the damping, β_{bz} determines the shape of the damping function, and x' represents the distance from the edge of the CAA domain. Optimal values to damp acoustic waves are $\alpha_{bz} = 6$ and $\beta_{bz} = 2$ [137]. However, a higher α_{bz} is required to damp vortical waves before reaching the edges of the computational domain, which may cause numerical instabilities. In the CAA simulations presented in this thesis, α_{bz} varies between 30 and 50, and $\beta_{bz} = 2$. These values allow an effective damping of acoustic and vortical waves without producing strong reflections that could affect the accuracy of the noise predictions.

2.2 Synthetic Turbulence Using an Advanced Digital Filter Method

The advanced digital filter method uses the mathematical background of the RPM method [52, 60] to reduce the number of constraint parameters and random numbers involved in the turbulence synthesis, and a numerical implementation strategy based on synthetic eddy methods [43, 47, 48], which allows the generation of non-periodic turbulence without explicitly filtering white noise signals. This significantly simplifies the numerical implementation of the method in comparison with previous works in the field, and reduces the computational cost. A superposition of Gaussian eddies is used to define a new eddy profile that can reproduce a target energy spectrum, such as the von Kármán spectrum, which is useful to extend the energy content to higher frequencies than can be reached by a single Gaussian spectrum. Although Dieste and Gabard [60] derived the exact equations of the spatial filters for two-dimensional von Kármán and Liepmann spectra, a superposition of Gaussian spectra is preferred here. This is because the equations of the filters for the non-Gaussian spectra go beyond the simplicity of the exponential function that defines a Gaussian filter, and they are tailored to a specific energy spectrum, which is a less generic option. Since the current development is based on previous derivations for the RPM method, a complete derivation of the governing equations are presented in Appendix A.

2.2.1 Gaussian Energy Spectra

The fluctuating velocity field in a source region, V_s, can be written as [52, 60]

$$\mathbf{u}'(\mathbf{x},t) = \nabla \times \int_{V_s} G(\mathbf{x}-\mathbf{x}_s)\mathcal{U}(\mathbf{x}_s,t)\mathrm{d}\mathbf{x}_s, \tag{2.6}$$

where G is the spatial filter, $\mathbf{x}$ is a point in the flow field, $\mathbf{x}_s$ is a point within the source region, and $\mathcal{U} = (\mathcal{U}_1, \mathcal{U}_2, \mathcal{U}_3)$ is the white noise field. When discretising Equation 2.6, the fluctuating velocity field can be written as the contribution of P small particles or eddies that define the whole source region where the turbulence is prescribed, i.e., $V_s = \sum_{p=1}^{p=P} V_{s,p}$. Each eddy introduces a fluctuating velocity field, $\mathbf{u}'_p = (u'_{x,p}, u'_{y,p}, u'_{z,p})$, around its centre that vanishes far from it, thus acting as a spatial filter. For a two-dimensional turbulent flow, the white noise field is reduced to a single term, $\mathcal{U} = (0, 0, \mathcal{U})$. Therefore, the resulting velocity field is calculated as

$$u'_x(\mathbf{x},t) = \sum_{p=1}^{P} u'_{x,p} = \sum_{p=1}^{P} \frac{\partial}{\partial y} G(\mathbf{x}-\mathbf{x}_p)\mathcal{U}_p, \tag{2.7a}$$

$$u'_y(\mathbf{x},t) = \sum_{p=1}^{P} u'_{y,p} = -\sum_{p=1}^{P} \frac{\partial}{\partial x} G(\mathbf{x}-\mathbf{x}_p)\mathcal{U}_p, \tag{2.7b}$$

where $\mathbf{x}_p$ is the centre of the pth eddy, and $\mathcal{U}_p$ represents the white noise term weighted over the portion of source region that corresponds to each eddy, $V_{s,p}$,

$$\mathcal{U}_p = \int_{V_{s,p}} \mathcal{U}(\mathbf{x}_s,t)\mathrm{d}\mathbf{x}_s. \tag{2.8}$$

Using the white noise properties for frozen turbulence [52] (also, see Equations A.3a-A.3c in Appendix A), it is possible to show that the mean value and the variance of the white noise term are $\langle \mathcal{U}_p \rangle = 0$ and $\langle \mathcal{U}_p^2 \rangle = \Delta_e^2$, respectively, where $\langle . \rangle$ is the ensemble average operator and Δ_e is a constant that represents the separation between eddy centres for uniformly distributed eddies in the source region, as shown in Figure 2.2. Therefore, $\mathcal{U}_p$ can be obtained from a normal distribution with zero mean and standard deviation Δ_e. A novelty of the current digital filter formulation is to rewrite the velocity field introduced by each eddy as

$$u'_{x,p}(\mathbf{x}) = \epsilon_p \Delta_e \frac{\partial}{\partial y} G(\mathbf{r}_p), \tag{2.9a}$$

$$u'_{y,p}(\mathbf{x}) = -\epsilon_p \Delta_e \frac{\partial}{\partial x} G(\mathbf{r}_p), \tag{2.9b}$$

where $\mathbf{r}_p = \mathbf{x} - \mathbf{x}_p$, and ϵ_p randomly takes the value ± 1, which satisfies $\langle \epsilon_p \rangle = 0$. In this derivation, the white noise term that is usually found in RPM methods is replaced by $\epsilon_p \Delta_e$, which is less demanding from a computational perspective and accelerates the convergence of the turbulence statistics. This novel and efficient implementation highlights similarities between RPM and synthetic eddy methods. Thus, ϵ_p is a parameter that defines the direction of rotation for each eddy, and Δ_e controls the density of eddies that are introduced through the injection plane. Consequently, all eddies have the same amplitude, and the only difference between them is the direction of rotation.

The isotropic energy spectrum is linked to the spatial filter in wavenumber space [60] (also, see derivation in Appendix A) by

$$E^{(2D)}(k) = 4\pi^3 k^3 \hat{G}(k)^2, \tag{2.10}$$

where k is the overall wavenumber, and the Fourier transform[3] of the spatial filter is defined as

$$\hat{G}(k) = \frac{1}{4\pi^2} \int_{-\infty}^{+\infty} G(\mathbf{r}_p) \exp\left[-\mathrm{i}\mathbf{k} \cdot \mathbf{r}_p\right] \mathrm{d}\mathbf{r}_p. \tag{2.11}$$

Since the target energy spectrum can be obtained from a superposition of Gaussian spectra, the equations of the fluctuating velocity are first derived according to the Gaussian spectrum proposed by Kraichnan [24]

$$E^{(2D)}(k) = \frac{2}{\pi^2} u'^2_{rms} \Lambda^4 k^3 \exp\left(-\frac{\Lambda^2 k^2}{\pi}\right), \tag{2.12}$$

where u'_{rms} is the root-mean-square of the turbulent velocity[4], and Λ is the integral length scale. Introducing Equation 2.12 into Equation 2.10 and performing the inverse Fourier transform, a single Gaussian filter in physical space takes the form

$$G(r_p) = \sqrt{\frac{2u'^2_{rms}}{\pi}} \exp\left(-\frac{\pi r_p^2}{2\Lambda^2}\right). \tag{2.13}$$

By substituting Equation 2.13 into Equations 2.9a and 2.9b, the two-dimensional fluctuating velocity field generated by a single Gaussian eddy can be expressed as

$$u'_{x,p}(\mathbf{x}) = -\sqrt{2\pi} \Delta_e \epsilon_p \left(y - y_p\right) \frac{u'_{rms}}{\Lambda^2} \exp\left(-\frac{\pi r_p^2}{2\Lambda^2}\right), \tag{2.14a}$$

$$u'_{y,p}(\mathbf{x}) = \sqrt{2\pi} \Delta_e \epsilon_p \left(x - x_p\right) \frac{u'_{rms}}{\Lambda^2} \exp\left(-\frac{\pi r_p^2}{2\Lambda^2}\right). \tag{2.14b}$$

[3] The convention for the Fourier transform adopted in this thesis is the same as in Pope [88].

[4] For isotropic turbulence, $u'_{rms} = \sqrt{\langle u'^2_x \rangle} = \sqrt{\langle u'^2_y \rangle} = \sqrt{\langle u'^2_z \rangle}$.

Figure 2.1 shows fluctuating velocity contours and magnitude of a two-dimensional Gaussian eddy according to Equations 2.14a and 2.14b.

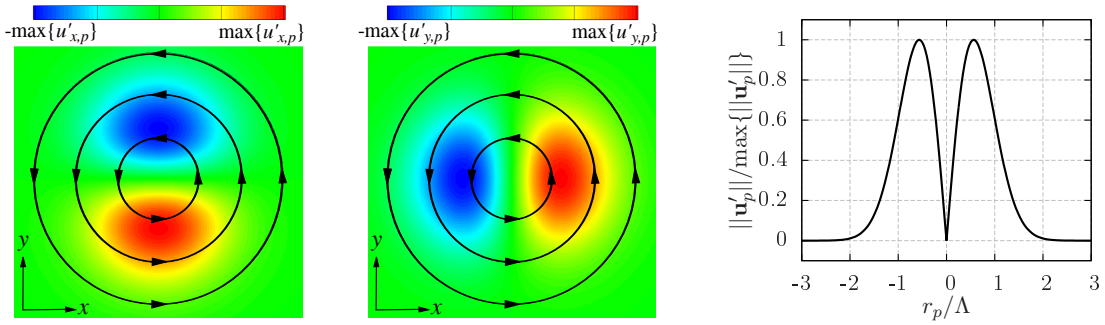

(a) $u'_{x,p}$ contours and streamlines. (b) $u'_{y,p}$ contours and streamlines. (c) Eddy cross-section.

Figure 2.1: Fluctuating velocity field of a two-dimensional Gaussian eddy.

The eddies are introduced into the CAA domain through a local injection plane and are convected by the mean flow as frozen turbulence. Figure 2.2 shows a schematic representation of the numerical implementation. The ability of the synthetic turbulence to realise the desired statistical properties relies on the maximum eddy radius, r_e, and the eddy spacing, Δ_e, which may be expressed as a function of the integral length scale. Dieste [127] suggested $r_e = 2.43\Lambda$ and $\Delta_e = \Lambda/6$ for Gaussian spectra. In the present work, a parameter study was performed to show that both r_e and Δ_e can take less demanding values without affecting the quality of the synthetic turbulence. Particularly, the target turbulence statistics are recovered provided that $r_e \geq 3\Lambda/2$ and $\Delta_e \leq \Lambda/2$. These new limiting values allow a reduction in the size and number of eddies injected into the CAA domain, which decreases the number of grid points on which synthetic turbulence must be computed. The complete parameter study is presented in Appendix B.

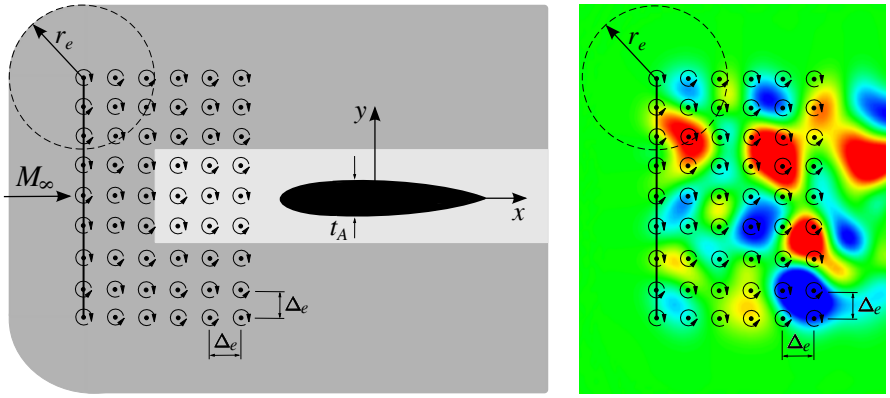

Figure 2.2: Synthetic eddies and injection plane parameters (r_e and Δ_e). Light grey background represents the region where the desired statistical properties are reproduced.

Validation cases were run in a computational domain with freestream Mach number $M_\infty = U_\infty/c_\infty = 0.3$ and a uniform grid spacing, 1.1×10^{-3} m. The spectral density of the velocity fluctuations was assessed by calculating one-dimensional spectra defined as

$$E_{ij}^{(2D)}(k_x) = 2\int_{-\infty}^{\infty} \Phi_{ij}^{(2D)}\left(k_x, k_y\right) \mathrm{d}k_y, \tag{2.15}$$

where the velocity spectrum, $\Phi_{ij}^{(2D)}$, is related to the energy spectrum of two-dimensional isotropic turbulence by

$$\Phi_{ij}^{(2D)}(\mathbf{k}) = \frac{E^{(2D)}(k)}{\pi k}\left(\delta_{ij} - \frac{k_i k_j}{k^2}\right). \tag{2.16}$$

It should be noted that for frozen turbulence, $E_{ij}(f) = 2\pi E_{ij}(k_x)/U_\infty$. Furthermore, the one-dimensional spectrum $E_{ij}(f)$ corresponds to the Power Spectral Density (PSD) of the velocity fluctuations in the ith and jth-directions. In this validation case, a total number of 1.1×10^4 velocity samples were obtained from a monitor point that was located at a distance larger than r_e downstream of the injection plane. Velocity samples were collected every 9 non-dimensional time steps, $\Delta t c_\infty/L_{ref} = 4 \times 10^{-4}$. The multitaper spectral analysis of Thomson [138] is used to calculate the spectral density of fluctuating velocity and pressure when using the advanced digital filter method.

Figure 2.3 shows analytical and numerical one-dimensional spectra to assess the effectiveness of the new limiting values for r_e and Δ_e. In both cases, numerical results closely match the analytical expressions. The small oscillations that can be observed in the numerical predictions are mainly related to the stochastic nature of the synthetic turbulence, which may require a larger number of samples for the spectra to converge at some frequencies, and errors induced by the spectral analysis tool to estimate the spectral density of the fluctuating velocity [138]. Despite a noticeable difference in the values for r_e and Δ_e used in Figure 2.3, the difference in computational time is less than 5% for the validation cases presented in this section. This is due to the implementation strategy, which identifies the grid points in the CAA domain that are affected by injection of eddies. Thus, the amplitude of the eddies acting on each grid point can be pre-evaluated and stored at the very beginning of the simulation to reduce the number of calculations per time step.

Although each eddy is divergence-free by definition, some spurious noise may appear around the injection plane as the eddies are superimposed onto the mean flow velocity. This spurious noise depends on the grid quality, r_e, and Δ_e . If the grid is not fine enough to smoothly reproduce the shape of the eddies, background noise is expected to be relatively high around the injection plane. This is related to the PPW requirement for the solver to convect vortical waves. In the CAA simulations presented in this section, 11 grid points were used along an eddy radius of $r_e = 3\Lambda/2$ to maintain a low level of spurious noise at high frequencies. This number of grid points per eddy radius is consistent with previous synthetic eddy methods. For example, Kim and Haeri [48] suggest that 10

cells should be used along an eddy radius. Additionally, if the eddies are truncated at a value close to $r_e = 3\Lambda/2$, where the normalised amplitude of the eddy is $\left\|\mathbf{u}'_p\right\| / \max\left\{\left\|\mathbf{u}'_p\right\|\right\} = 0.128$ (see Figure 2.1c), the derivatives $\partial u'_{x,p}/\partial x$ and $\partial u'_{y,p}/\partial y$ are not close to zero, which leads to a local infringement of the divergence-free condition. Nevertheless, the amplitude of these spurious pressure fluctuations is of the order of 10^3 times smaller than those due to the turbulence-aerofoil interaction in all simulations presented in this thesis.

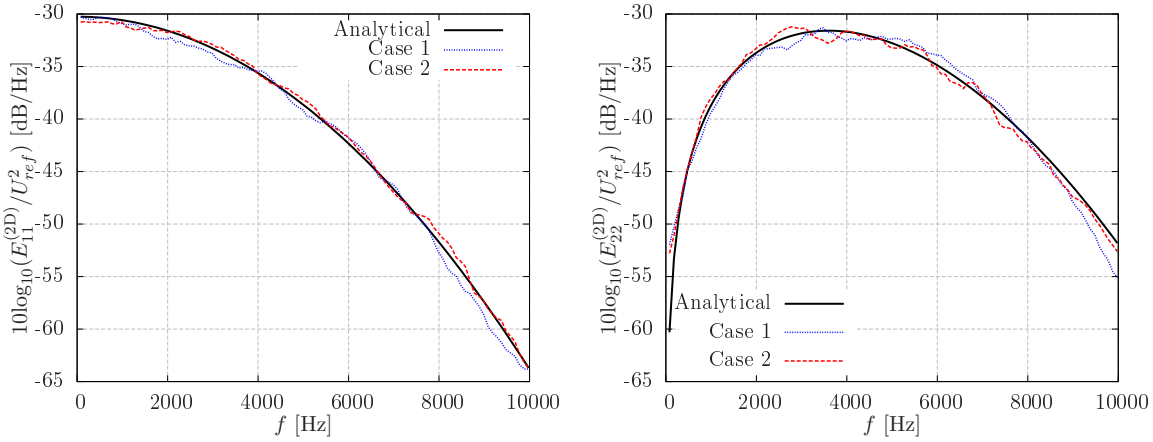

(a) Streamwise, $U_{ref} = 1$ m/s.

(b) Transverse, $U_{ref} = 1$ m/s.

Figure 2.3: One-dimensional Gaussian spectra of two-dimensional turbulence with $M_\infty = 0.3$, $u'_{rms}/U_\infty = 0.017$, and $\Lambda = 0.008$ m. *Case 1* corresponds to $r_e = 3\Lambda/2$ and $\Delta_e = \Lambda/2$, and *Case 2* corresponds to $r_e = 5\Lambda/2$ and $\Delta_e = \Lambda/6$.

Unlike previous works in this field [60, 61, 62], special boundary conditions are not required around the injection plane. This because the synthetic turbulence is not introduced at the boundaries of the CAA domain, and the levels of spurious noise are negligible for practical cases. The RPM method was initially developed for the APEs, which cannot propagate vortical waves, and required an auxiliary mesh in the source region for computing synthetic turbulence before being interpolated into the CAA domain [52]. The use of an auxiliary mesh increases the computational cost, but allows a better control of the synthetic turbulence. For example, it would be possible to include evolving turbulence by means of time decorrelation introduced by a Langevin equation, contrary to the frozen turbulence assumption.

2.2.2 Non-Gaussian Energy Spectra through Gaussian Superposition

An extension of the previous derivation for Gaussian spectra is developed here in order to match a target non-Gaussian energy spectrum within a certain wavenumber (or frequency) range. The main

idea is to define a new eddy profile from a superposition of N_e Gaussian eddies that have the same direction of rotation, ϵ_p, but different root-mean-square velocity, $u'_{rms,i}$, and integral length scale, Λ_i, for $i = 1, ..., N_e$. Thus, it is possible to define a digital filter from a summation of Gaussian filters in wavenumber space

$$\hat{G}_{sum}(k) = \sum_{i=1}^{N_e} \hat{G}_i(\Lambda_i, u'_{rms,i}, k), \tag{2.17}$$

where, according to Equations 2.10 and 2.12, each Gaussian filter is defined as

$$\hat{G}_i(\Lambda_i, u'_{rms,i}, k) = \frac{\Lambda_i^2}{\pi^2} \sqrt{\frac{u'^2_{rms,i}}{2\pi}} \exp\left(-\frac{\Lambda_i^2 k^2}{2\pi}\right). \tag{2.18}$$

Using Equations 2.10 and 2.17, the target energy spectrum (e.g. von Kármán, Liepmann, etc.) can be approximated by

$$E^{(2D)}_{sum}(k) = 4\pi^3 k^3 \hat{G}^2_{sum}(k) = 4\pi^3 k^3 \left[\sum_{i=1}^{N_e} \hat{G}_i(\Lambda_i, u'_{rms,i}, k)\right]^2. \tag{2.19}$$

Introducing Equation 2.18 into Equation 2.19, straightforward algebra shows that

$$E^{(2D)}_{sum}(k) = \frac{2k^3}{\pi^2} \sum_{i=1}^{N_e} \sum_{j=1}^{N_e} \sqrt{u'^2_{rms,i} u'^2_{rms,j}} \left(\Lambda_i \Lambda_j\right)^2 \exp\left[-\frac{k^2}{2\pi}\left(\Lambda_i^2 + \Lambda_j^2\right)\right]. \tag{2.20}$$

Thus, the fluctuating velocity field introduced by the pth eddy from the Gaussian superposition is

$$u'_{x,p}(\mathbf{x}) = -\sqrt{2\pi}\Delta_e \epsilon_p \left(y - y_p\right) \sum_{i=1}^{N_e} \frac{u'_{rms,i}}{\Lambda_i^2} \exp\left(-\frac{\pi r_p^2}{2\Lambda_i^2}\right), \tag{2.21a}$$

$$u'_{y,p}(\mathbf{x}) = \sqrt{2\pi}\Delta_e \epsilon_p \left(x - x_p\right) \sum_{i=1}^{N_e} \frac{u'_{rms,i}}{\Lambda_i^2} \exp\left(-\frac{\pi r_p^2}{2\Lambda_i^2}\right). \tag{2.21b}$$

The new eddy profile defined by Equations 2.21a and 2.21b requires a suitable set of parameters, $u'_{rms,i}$ and Λ_i for $i = 1, ..., N_e$, for the Gaussian superposition. These parameters can be obtained by minimising $\mathcal{E}(k) = |E_{tar}(k) - E_{sum}(k)|$ within the wavenumber range of interest, where $E_{tar}(k)$ is the target energy spectrum, such as the von Kármán or Liepmann spectrum. This optimisation is performed by finding a set of values for $u'_{rms,i}$ that satisfy the system of equations given by $\mathcal{E}(k'_i) = 0$, where $k'_i = \sqrt{3\pi/(2\Lambda_i^2)}$ for $i = 1, ..., N_e$. It should be noted that k'_i corresponds to the wavenumber of maximum energy for a Gaussian spectrum defined by Equation 2.12. Random combinations of k'_i are tested until $|10\log_{10}[E_{tar}(k)/E_{sum}(k)]| < 0.5$ dB within the whole wavenumber range under study.

Although there is not a unique set of parameters to reproduce a target energy spectrum, proposed values are given for all simulations presented in this thesis. In practical cases a total number of eddies, N_e, that ranges between 4 and 6 is sufficient to obtain a good representation of the target energy spectrum over a wide wavenumber (or frequency) range.

The Gaussian superposition methodology is used to reproduce the two-dimensional von Kármán energy spectrum, which is defined as

$$E^{(2D)}(k) = \frac{110 u'^2_{rms} \Lambda}{27\pi} \frac{\left(\frac{k}{k_c}\right)^4}{\left[1 + \left(\frac{k}{k_c}\right)^2\right]^{17/6}}, \tag{2.22}$$

where $k_c = [\sqrt{\pi}\Gamma(5/6)]/[\Lambda\Gamma(1/3)]$ with $\Gamma(.)$ as the Gamma function. In this case, an accurate representation of the von Kármán energy spectrum is obtained by using $N_e = 5$ different Gaussian eddies with the parameters given in Table 2.1.

ith Gaussian eddy	Λ_i [m]	$u'^2_{rms,i}$ [m^2/s^2]
1	2.524×10^{-2}	5.194×10^{-2}
2	1.401×10^{-2}	2.152×10^{-1}
3	7.285×10^{-3}	3.012×10^{-1}
4	3.023×10^{-3}	4.667×10^{-1}
5	2.238×10^{-3}	8.929×10^{-3}

Table 2.1: Parameters for Gaussian superposition to obtain the two-dimensional von Kármán spectrum with $M_\infty = 0.3$, $u'_{rms}/U_\infty = 0.017$, and $\Lambda = 0.008$ m.

Figure 2.4a shows the reconstructed von Kármán spectrum from a superposition of Gaussian spectra using Equation 2.20. Although only N_e Gaussian eddies are combined to define a new eddy profile, the resulting energy spectrum is obtained from the superposition of N_e^2 spectra, as a consequence of the double summation in Equation 2.20. This Gaussian superposition methodology helps to reduce the amplitude of the individual Gaussian eddies that are involved, and therefore the amplitude of potential background noise around the injection plane. Additionally, it can be seen in Figure 2.4a that the resulting energy spectrum from the superposition process (E_{sum}) only matches the target energy spectrum (E_{tar}) within a certain wavenumber range. This is because Gaussian spectra are centred at a single wavenumber and tend to zero quickly at high frequencies. Therefore, the total turbulent kinetic energy [88]

$$K = \int_0^{+\infty} E^{(2D)}(k) \mathrm{d}k, \tag{2.23}$$

is not completely recovered from the reconstructed energy spectrum. This is not a limitation for CAA simulations of leading edge noise, in which the mesh resolution is adjusted to propagate vortical and acoustic waves within a wavenumber (or frequency) range of interest. A good agreement between analytical and superposed energy spectra is found in Figure 2.4b, where $|10\log_{10}[E_{tar}(k)/E_{sum}(k)]| < 0.5\,\text{dB}$ for $k \in [46, 1071]\ \text{m}^{-1}$.

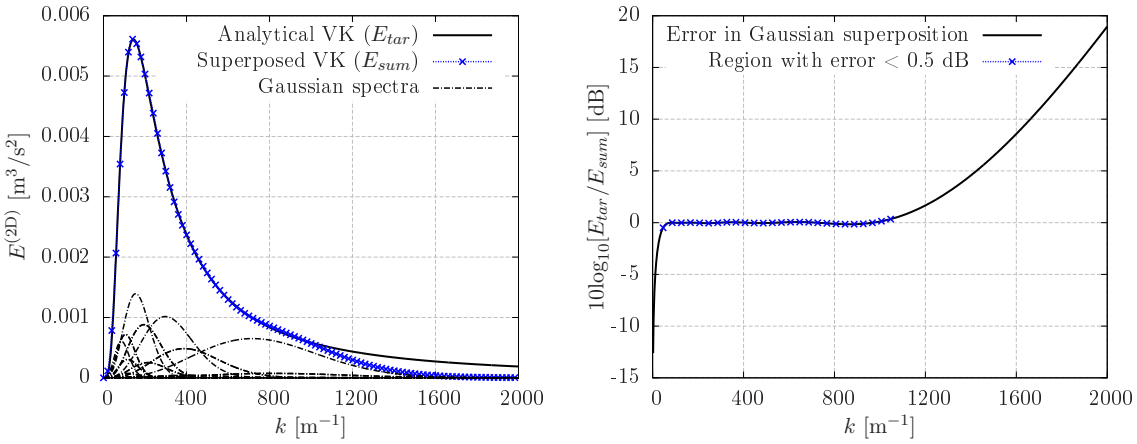

(a) Energy spectrum from Gaussian superposition.

(b) Error in Gaussian superposition.

Figure 2.4: Resulting spectrum from the Gaussian superposition and deviation from analytical von Kármán (abbreviated as VK) energy spectrum with $M_\infty = 0.3$, $u'_{rms}/U_\infty = 0.017$, and $\Lambda = 0.008\,\text{m}$. The parameters for the Gaussian superposition methodology are given in Table 2.1.

Note that the values of $u'^2_{rms,i}$ and Λ_i for $i = 1, ..., N_e$ that are given in Table 2.1 can be scaled to reproduce the two-dimensional von Kármán spectrum with a different turbulence intensity and integral length scale. Since the new eddies are obtained from a combination of several Gaussian eddies, limiting values to realise non-Gaussian energy spectra are based on the largest and smallest Gaussian eddies involved. Hence, $r_e \geq 3 \max\{\Lambda_i\}/2$ and $\Delta_e \leq \min\{\Lambda_i\}/2$ for $i = 1, ..., N_e$. Figure 2.5 shows one-dimensional spectra from numerical simulations using two sets of values for r_e and Δ_e. A good agreement was found for both combinations of parameters for frequencies up to 10 kHz.

2.3 Synthetic Turbulence Using Fourier Mode Summation

In this section, one- and two-component Fourier mode methods are presented to generate isotropic synthetic turbulence. These methods are developed here to realise a purely two-dimensional turbulent flow with the statistics of a target isotropic energy or velocity spectrum. The resulting turbulent flow is periodic in both time and space, and has a discrete number of frequencies, as is usual in Fourier mode methods.

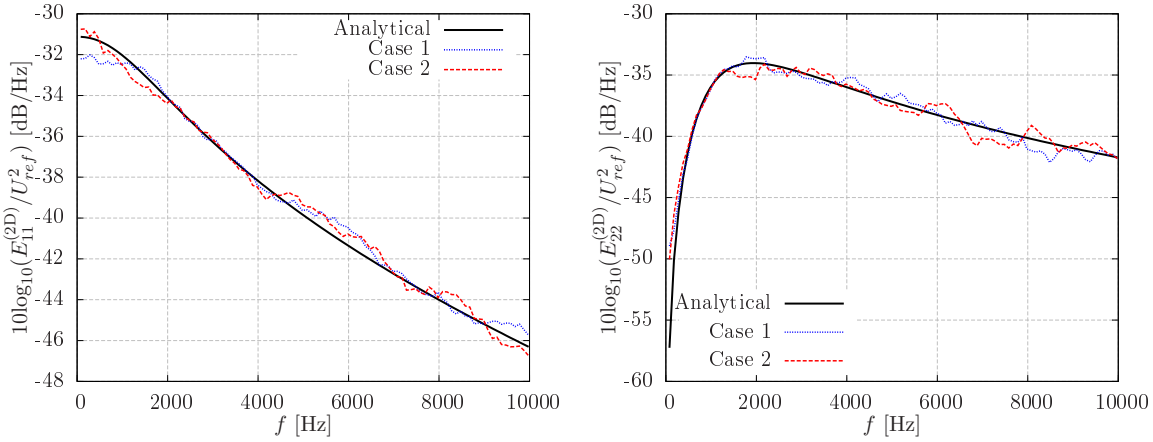

(a) Streamwise, $U_{ref} = 1$ m/s.

(b) Transverse, $U_{ref} = 1$ m/s.

Figure 2.5: One-dimensional von Kármán spectra of two-dimensional turbulence with $M_\infty = 0.3$, $u'_{rms}/U_\infty = 0.017$, and $\Lambda = 0.008$ m. *Case 1* corresponds to $r_e = 3\max\{\Lambda_i\}/2$ and $\Delta_e = \min\{\Lambda_i\}/2$, and *Case 2* corresponds to $r_e = 5\max\{\Lambda_i\}/2$ and $\Delta_e = \min\{\Lambda_i\}/6$, where the values for Λ_i are given in Table 2.1.

2.3.1 One-Component Turbulent Inflow

The fluctuating velocity field is described as a superposition of plane waves, whose amplitude is proportional to the square root of the transverse velocity spectrum. This synthetic turbulence method is a simplified version of previous works by Clair *et al.* [38] and Gill *et al.* [41] to generate purely two-dimensional turbulence. The fluctuating velocity field can be written as

$$u'_y(\mathbf{x},t) = \sum_{n=1}^{N} \sqrt{\Phi_{22}^{(2D)}(k_{x,n})\,\Delta k_{x,n}}\cos\left[k_{x,n}(x - U_\infty t) + \phi_n\right], \tag{2.24}$$

where N is the total number of modes, ϕ_n is a random phase term varying between 0 and 2π radians for the nth mode, $k_{x,n}$ is the streamwise wavenumber component, and $\Delta k_{x,n}$ is the streamwise wavenumber step. The velocity spectrum to be used in Equation 2.24 is obtained after integration over all transverse wavenumbers, k_y, as follows

$$\Phi_{22}^{(2D)}(k_x) = \int_{-\infty}^{+\infty} \Phi_{22}^{(2D)}\left(k_x, k_y\right) \mathrm{d}k_y. \tag{2.25}$$

A uniform distribution is used to discretise the streamwise wavenumber component. Since $k_x = 2\pi/\lambda_x$, the wavelengths are selected following the distribution $\lambda_{x,max}$, $\lambda_{x,max}/2$, $\lambda_{x,max}/3$, ..., $\lambda_{x,max}/N$, for the modes $n = 1, 2, ..., N$, respectively. Unlike methods based on digital filters and synthetic

eddies, the oncoming turbulence has a finite number of discrete frequencies, N, and is periodic around the largest wavelength, $\lambda_{x,max}$. Therefore, the Fast Fourier Transform (FFT) algorithm is used to calculate frequency spectra of the fluctuating velocity and pressure from simulations using Fourier mode methods.

2.3.2 Two-Component Turbulent Inflow

The method proposed by Bailly *et al.* [34, 35] was developed to reconstruct a three-dimensional energy spectrum based on the overall wavenumber such that the amplitude of each mode was proportional to $\sqrt{E^{(3D)}(k)\Delta k}$. However, the amplitude of the modes can be redefined in terms of the wavenumber components in each direction. This capability is particularly relevant for CAA simulations, since the mesh might have different spatial resolutions in each direction if the grid density is not homogeneous.

The derivation presented for two-dimensional turbulence allows for a complete control of the wavenumber components. For isotropic turbulence, the total turbulent kinetic energy can be obtained by integrating the energy spectrum or the velocity spectra as follows

$$K = \int_0^{+\infty} E^{(2D)}(k)\mathrm{d}k = \frac{1}{2}\int\int\int_{-\infty}^{+\infty} [\Phi_{11}^{(2D)}(\mathbf{k}) + \Phi_{22}^{(2D)}(\mathbf{k})]\mathrm{d}\mathbf{k}. \tag{2.26}$$

Introducing Equation 2.16 into Equation 2.26, straightforward algebra shows that Δk can be replaced by $\Delta k_x \Delta k_y / (\pi k)$ for the discrete integration of the energy spectrum. Consequently, the two-component turbulent inflow is defined as follows

$$\mathbf{u}'(\mathbf{x}, t) = \sum_{n=1}^{N} \sum_{\substack{m=-M \\ m\neq 0}}^{M} \sqrt{E^{(2D)}(k_{nm}) \frac{\Delta k_{x,n} \Delta k_{y,m}}{\pi k_{nm}}} \cos\left[k_{x,n}(x - U_\infty t) + k_{y,m} y + \phi_{nm}\right] \boldsymbol{\sigma}_{nm}, \tag{2.27}$$

where $N \times 2M$ is the total number of Fourier modes, ϕ_{nm} is the random phase term of the nth streamwise mode and mth transverse mode, $k_{nm} = \sqrt{k_{x,n}^2 + k_{y,m}^2}$ is the overall wavenumber component, $\Delta k_{x,n}$ and $\Delta k_{y,m}$ are related to the wavenumber discretisation, and $\boldsymbol{\sigma}_{nm}$ is a unit vector ($\|\boldsymbol{\sigma}_{nm}\| = 1$) that guarantees the divergence-free condition ($\boldsymbol{\sigma}_{nm} \cdot \mathbf{k} = 0$). For a purely two-dimensional flow, the components of the unit vector are given by $\sigma_{x,nm} = \pm k_{y,nm}/k$ and $\sigma_{y,nm} = \mp k_{x,nm}/k$.

Alternatively, the fluctuating velocity field defined in Equation 2.27 can also be written in terms of the velocity spectra by using Equation 2.16 as

$$u_x'(\mathbf{x}, t) = \sum_{n=1}^{N} \sum_{\substack{m=-M \\ m\neq 0}}^{M} \sqrt{\Phi_{11}^{(2D)}\left(k_{x,n}, k_{y,m}\right) \Delta k_{x,n} \Delta k_{y,m}} \cos\left[k_{x,n}(x - U_\infty t) + k_{y,m} y + \phi_{nm}\right], \tag{2.28a}$$

$$u'_y(\mathbf{x},t) = \sum_{n=1}^{N} \sum_{\substack{m=-M \\ m\neq 0}}^{M} \sqrt{\Phi_{22}^{(2D)}\left(k_{x,n}, k_{y,m}\right) \Delta k_{x,n} \Delta k_{y,m}} \cos\left[k_{x,n}\left(x - U_\infty t\right) + k_{y,m} y + \phi_{nm}\right]. \tag{2.28b}$$

The $k_{x,n}$ discretisation of the N modes follows the uniform distribution proposed for the one-component Fourier mode method (see Section 2.3.1). Following previous work by Béchara *et al.* [33], a logarithmic distribution has been adopted here for the $k_{y,m}$ discretisation of the $2M$ modes. Such a distribution allows for a good representation of the spectral content while minimising the number of modes in the transverse direction. Thus, the transverse wavenumber components are defined as

$$k_{y,m} = \frac{m}{|m|} \exp\left[\ln(k_{y,min}) + (|m| - 1)\Delta k'_y\right], \tag{2.29}$$

where ln() represents the natural logarithm, and the auxiliary term $\Delta k'_y$ is defined as

$$\Delta k'_y = \frac{\ln(k_{y,max}) - \ln(k_{y,min})}{M - 1}. \tag{2.30}$$

In this work, $k_{y,min} = 2\pi/\lambda_{x,max}$, and $k_{y,max} = 2\pi NC/\lambda_{x,max}$, where C is an integer number that defines the limit of integration for the energy spectrum in the transverse direction. The transverse wavenumber step, $\Delta k_{y,m}$, is obtained by following the rectangle method for numerical integration

$$\Delta k_{y,m} = \begin{cases} \dfrac{k_{y,m+1} - k_{y,m-1}}{2} & \text{if} \quad |m| = 2, ..., M-1, \\ \Delta k_{y,m} = \Delta k_{y,|m|+1} & \text{if} \quad |m| = 1, \\ \Delta k_{y,m} = \Delta k_{y,|m|-1} & \text{if} \quad |m| = M. \end{cases}$$

2.3.3 Numerical Implementation

Although different approaches exist to implement Fourier mode methods in CAA solvers, they all focus on injecting the fluctuating velocity field without producing spurious noise that may affect the accuracy of the noise predictions. For example, Clair *et al.* [38] used a turbulent inflow based on Tam's boundary conditions [139], and Kim [140] and Gill [98] opted for implicit and explicit buffer zones, respectively.

In this thesis, synthetic turbulence using Fourier modes is defined within implicit buffer zones at the edge of the CAA domain, where the mean flow is required to be uniform. This is done to prevent spurious sources of noise from appearing at the buffer zone exit. Gust-enforcing buffer zones that are used for Fourier mode methods damp density, pressure, and velocity fluctuations to a target solution

in the LEEs (see Equations 2.2-2.4). Particularly, ρ'_{tar} and p'_{tar} are set to zero, and $\mathbf{u}'_{tar}$ corresponds to the vortical disturbances defined by a Fourier mode method. Vortical disturbances are convected by the mean flow as frozen turbulence, as they leave the buffer zones.

Figure 2.6 shows a schematic representation of the buffer zone configuration for leading edge noise predictions of single aerofoils. In order to reduce the computational time, the fluctuating velocity field is initialised throughout the CAA domain at the beginning of the simulation, which helps to reduce the expense of the transitory state.

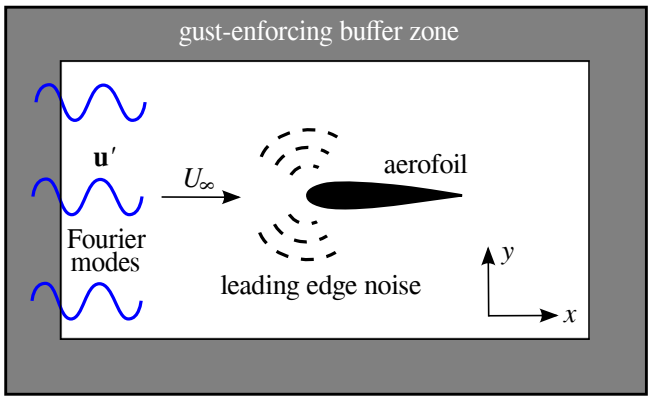

Figure 2.6: Buffer zone configuration for Fourier mode simulations.

2.4 Validation Case: Two-Dimensional NACA 0001 Aerofoil

In this section, the advanced digital filter method and Fourier mode methods are validated for leading edge noise predictions using a NACA 0001 aerofoil. Details on the CAA methodology are given, including modelling assumptions, CAA mesh, and input parameters that are required for the synthetic turbulence methods. Noise results are compared with far-field predictions from an analytical flat plate model.

2.4.1 Analytical Flat Plate Model

The key equations in the analytical model of Amiet [39] are reproduced in this section according to Blandeau *et al.* [70] for two-dimensional noise radiation. This model has been previously used for validation of analytical [78], numerical [38, 41, 60], and experimental [79] leading edge noise predictions from single aerofoils, and therefore it constitutes a well-established tool for validation purposes. Additionally, this flat plate model will be used in Chapter 3 to highlight aerofoil geometry effects on broadband noise. Figure 2.7 shows the reference frame for the flat plate model.

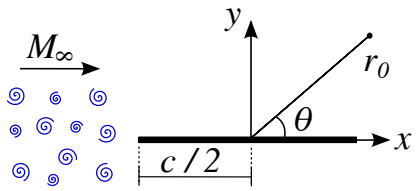

Figure 2.7: Reference frame and far-field observers for a two-dimensional flat plate.

According to Blandeau *et al.* [70], the pressure spectral density in the far-field is given by

$$S_{pp}^{(2D)}(r_0, \theta, \omega) = \frac{\pi \rho_\infty^2 b^2 \sin^2\theta U_\infty \kappa_0}{2 r_0 A(\theta, M_\infty)^3} |\mathcal{L}(\theta, k_x)|^2 \, \Phi_{22}^{(2D)}(k_x), \tag{2.31}$$

where $A(\theta, M_\infty) = \sqrt{1 - M_\infty^2 \sin^2\theta}$, $\kappa_0 = \omega / c_\infty$ is the acoustic wavenumber, $\omega = 2\pi f$ is the angular frequency, $b = c/2$ is the aerofoil semi-chord, r_0 is the far-field observer distance, and θ is the radiation angle. The non-dimensional unsteady loading term, $\mathcal{L}(\theta, k_x)$, is given at low acoustic reduced frequencies, $\mu_a = k_x M_\infty b / \beta^2 < \frac{\pi}{4}$, by [67]

$$\mathcal{L}_{low}(\theta, k_x) = \frac{1}{\beta} S(\mu_h) \exp\left[\mathrm{i}\mu_h f(M_\infty)\right] \left\{ J_0\left(\mu_a M_\infty \frac{\cos\theta}{A(\theta, M_\infty)}\right) - \mathrm{i} J_1\left(\mu_a M_\infty \frac{\cos\theta}{A(\theta, M_\infty)}\right) \right\},$$

where J_0 and J_1 are Bessel functions of the first kind, $\beta = \sqrt{1 - M_\infty^2}$ is the Prandtl-Glauert factor, $\mu_h = k_x b / \beta^2$ is the hydrodynamic reduced frequency, $f(M_\infty) = (1 - \beta)\ln(M_\infty) + \beta \ln(1 + \beta) - \ln(2)$ is a phase correction factor, and $S(\mu_h)$ represents the Sears function, which is defined by means of the Hankel functions of the second kind ($H_0^{(2)}$ and $H_1^{(2)}$),

$$S(\mu_h) = \frac{2}{\pi \mu_h \left[H_0^{(2)}(\mu_h) - \mathrm{i} H_1^{(2)}(\mu_h) \right]}.$$

At high acoustic reduced frequencies, $\mu_a > \frac{\pi}{4}$, the non-dimensional unsteady loading term $\mathcal{L}(\theta, k_x)$ is split into two contributions [69]

$$\mathcal{L}_{high}(\theta, k_x) = \mathcal{L}_1(\theta, k_x) + \mathcal{L}_2(\theta, k_x),$$

where $\mathcal{L}_1(\theta, k_x)$ corresponds to the main leading edge scattering half-plane problem,

$$\mathcal{L}_1(\theta, k_x) = \frac{\sqrt{2} E_f^*(2\Theta_1) \exp(\mathrm{i}\Theta_2)}{\pi \beta \sqrt{\mu_h (1 + M_\infty) \Theta_1}}, \tag{2.32}$$

which is corrected by the solution of the back scattering trailing edge problem,

$$\mathcal{L}_2(\theta, k_x) = \frac{\exp(\mathrm{i}\Theta_2)\left\{\mathrm{i}\left(1-\exp(-\mathrm{i}2\Theta_1)\right)+(1-\mathrm{i})\left[E_f^*(4\mu_a)-\sqrt{\frac{2}{1+\cos\theta/A(\theta,M_\infty)}}E_f^*(2\Theta_3)\exp(-\mathrm{i}2\Theta_1)\right]\right\}}{\pi\Theta_1\beta\sqrt{2\pi\mu_h(1+M_\infty)}}. \tag{2.33}$$

In Equations 2.32 and 2.33, the following terms have been introduced to simplify the notation

$$\Theta_1 = \mu_a\left(1-\frac{\cos\theta}{A(\theta,M_\infty)}\right),\ \Theta_2 = \mu_a\left(M_\infty-\frac{\cos\theta}{A(\theta,M_\infty)}\right)-\frac{\pi}{4},\ \Theta_3 = \mu_a\left(1+\frac{\cos\theta}{A(\theta,M_\infty)}\right), \tag{2.34}$$

and E_f^* represents the conjugate of the Fresnel integral, which is defined as

$$E_f^*(\Theta) = \frac{1}{\sqrt{2\pi}}\int_0^\Theta \frac{\exp(-\mathrm{i}\xi)}{\sqrt{\xi}}\mathrm{d}\xi.$$

The SPL in the far-field is then calculated as

$$\mathrm{SPL}(r_0,\theta,\omega) = 10\log\left(\frac{2S_{pp}(r_0,\theta,\omega)}{p_{ref}^2}\right), \tag{2.35}$$

where the reference pressure is $p_{ref} = 2\times10^{-5}\,\mathrm{N/m^2}$ and the factor 2 has been introduced to realise a one-sided spectrum. In order to measure the SPL at different frequencies in Hz, instead of rad/s, an additional 2π factor should be added to $S_{pp}(r_0,\theta,\omega)$ in Equation 2.35.

The $S_{pp}(r_0,\theta,\omega)$ at different observers over a circle of constant radius can be used to calculate the sound power from an aerofoil with unit span ($L_{ref} = 1\,\mathrm{m}$),

$$\mathcal{P}(\omega) = \frac{r_0 L_{ref}}{2\rho_\infty c_\infty}\int_0^{2\pi} S_{pp}(r_0,\theta,\omega)F(\theta,M_\infty)\mathrm{d}\theta, \tag{2.36}$$

where $F(\theta,M_\infty) = \beta^4 A(\theta,M_\infty)/(A(\theta,M_\infty)-M_\infty\cos\theta)^2$ as shown by Blandeau *et al.* [70]. It follows from Equation 2.36 that the sound power is independent of the observer distance. The sound power level takes the form

$$\mathrm{PWL}(\omega) = 10\log\left(\frac{2\mathcal{P}(\omega)}{\mathcal{P}_{ref}}\right), \tag{2.37}$$

where $\mathcal{P}_{ref} = 1\times10^{-12}\,\mathrm{W}$ is the reference power level.

2.4.2 Aerofoil Configuration and Modelling Assumptions

A NACA 0001 aerofoil at $M_\infty = 0.6$ and $AoA = 0^\mathrm{o}$ is chosen to validate leading edge noise predictions using different synthetic turbulence methods. For such a thin aerofoil, a uniform mean

flow can be assumed for comparison with an analytical flat plate model [94]. The aerofoil chord is set to $c = 0.15\,\text{m}$, which is of the order of the size of OGVs in modern turbofan engines. The freestream density is $\rho_\infty = 1.2\,\text{kg/m}^3$ throughout this thesis, unless otherwise stated.

In Sections 2.2 and 2.3, synthetic turbulence methods have been developed by assuming that the vortical disturbances are convected by the mean flow as frozen turbulence. This implies that the vortical disturbances are convected unchanged by the mean flow until reaching the leading edge region, and the frequency is related to the vortical wavenumber by $2\pi f = \mathbf{k}\cdot\mathbf{U}_0$. The frozen turbulence assumption has been shown to produce similar leading edge noise predictions to evolving turbulence [60]. Furthermore, this assumption is justified for turbofan engines, since the rate of change of the turbulent structures is slow compared to the time taken to pass over the stator blades.

In this thesis, leading edge noise predictions of single aerofoils in the far-field are performed by means of a time-domain Ffowcs-Williams and Hawkings (FW-H) solver, which is based on formulation 1A of Farassat and Succi [141, 142] and neglects quadrupole noise sources. The FW-H surface, in which the unsteady flow variables are collected, corresponds to the aerofoil surface. This is done to prevent vortical disturbances from passing through the FW-H surface, which may produce additional noise sources when quadrupole source terms are neglected in the FW-H formulation [143]. The sampling frequency is calculated by ensuring that at least 25 samples of unsteady variables are collected along a period of the smallest vortical wavelength being resolved. The FW-H solver assumes a uniform mean flow outside the collection surface, which is consistent with the assumption of uniform mean flow in the CAA simulation.

2.4.3 Mesh Generation

The size of structured CAA meshes used to study turbulence-aerofoil interaction usually extends to 6 or 8 chord lengths in all directions around the aerofoil. This CAA mesh size allows for the collection of unsteady pressure samples in the acoustic far-field and the convergence of the mean flow when solving the full Euler equations [38, 140]. In this thesis, the size of the mesh for LEE simulations of a NACA 0001 aerofoil can be reduced to less than 4 chords in all directions around the aerofoil. This is because the mean flow is uniform, and the FW-H surface for the far-field noise radiation corresponds to the aerofoil surface. This allows significant savings in the computational cost.

The CAA mesh was designed by using at least 8 PPW to convect vortical disturbances upstream of the aerofoil leading edge, as required by the CAA solver presented in Section 2.1, and it is able to accurately propagate frequencies of up to $f_{max} = 8000\,\text{Hz}$ at $M_\infty = 0.6$. If the grid spacing in the source or propagation region is uniform, then the required grid spacing can be estimated using the frozen turbulence assumption as $\Delta x = \Delta y = U_\infty/(f_{max}\text{PPW})$. In this work, the PPW requirement is

similar to that of Clair *et al.* [144] (10 PPW) when using a different CAA solver to propagate harmonic gusts. The mesh presents a C-shape topology around the aerofoil leading edge, and a rectangular structure with H-shape topology near the edges of the domain. The aerofoil surface is defined by 540 grid points, and the smallest cell is located at the leading edge. The non-dimensional time step is $\Delta t c_\infty / L_{ref} = 4 \times 10^{-6}$, which ensures that the CFL number is below 0.54 and guarantees the numerical stability of the simulations. Figure 2.8 shows the block topology around the NACA 0001 aerofoil and the structured mesh in the leading edge region. Since viscous effects on leading edge noise are neglected in this thesis, the boundary layer is not included in the mean flow solution and CAA mesh is not refined close to the wall. The width of the buffer zones is $L_{bz} = 1c$, which is sufficient to damp potential noise reflections for the configuration investigated. Further details on the CAA meshes, such as maximum skewness and minimum cell size, are given in Appendix C for representative configurations.

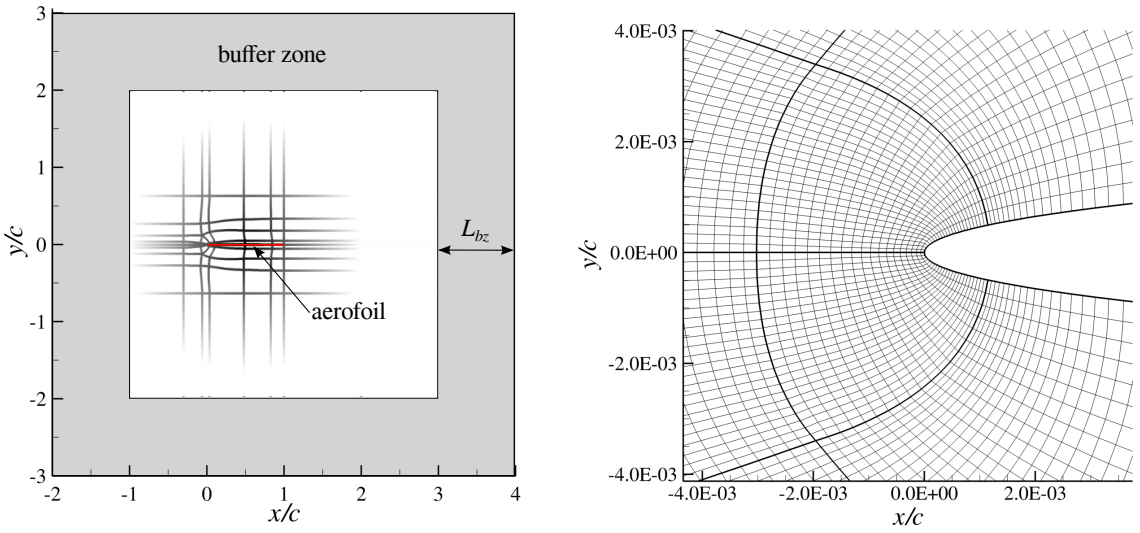

(a) Block topology around the aerofoil. A thick red line is used to highlight the location of the aerofoil.

(b) Mesh in the leading edge region.

Figure 2.8: Two-dimensional CAA mesh for a NACA 0001 aerofoil at $AoA = 0^o$.

2.4.4 Numerical Setup for Synthetic Turbulence Methods

Synthetic turbulence methods are used to generate purely two-dimensional turbulence with the von Kármán spectrum. The turbulence intensity and integral length scale are set to $u'_{rms}/U_\infty = 0.017$ and $\Lambda = 0.008$ m, respectively. In this thesis, integral length scales are small compared to the aerofoil chord, as is the case in typical fan wakes.

The advanced digital filter method uses $N_e = 5$ Gaussian eddies to define a new eddy shape that can reproduce the von Kármán spectrum. The parameters that are required for the Gaussian superposition are given in Table 2.2. Since the mean flow is uniform in the CAA domain, the eddies are not distorted by mean flow gradients in the vicinity of the leading edge. Consequently, the injection plane can be placed upstream of the aerofoil leading edge at a distance equivalent to the eddy radius, r_e. The transitory state in the advanced digital filter method lasts until the first set of eddies introduced within the CAA domain is convected past the aerofoil. Then, the simulation was run for a total number of 8.625×10^6 iterations, which corresponds to the propagation of approximately 10 periods of $\lambda_{x,max}$ according to Fourier mode methods. This value has been taken as a reference for a direct comparison with the results given by the two-component Fourier mode method, as explained below.

ith Gaussian eddy	Λ_i [m]	$u'^2_{rms,i}$ [m^2/s^2]
1	2.524×10^{-2}	2.077×10^{-1}
2	1.401×10^{-2}	8.608×10^{-1}
3	7.285×10^{-3}	1.205
4	3.023×10^{-3}	1.867
5	2.238×10^{-3}	3.566×10^{-2}

Table 2.2: Parameters for Gaussian superposition to obtain the two-dimensional von Kármán spectrum with $M_\infty = 0.6$, $u'_{rms}/U_\infty = 0.017$, and $\Lambda = 0.008$ m.

Table 2.3 presents the parameters that are required for the wavenumber discretisation using the one- and two-component Fourier mode methods, abbreviated as 1cFm and 2cFm, respectively. In both cases, there are $N = 100$ modes uniformly distributed in the x-direction, whose wavelengths range from $\lambda_{x,max} = 2.55$ m ($f = 80$ Hz) to $\lambda_{x,max}/N$ ($f = 8000$ Hz). Additionally, the two-component Fourier mode method requires $2M = 20$ modes that follow a logarithmic distribution in the y-direction. The transitory state of these simulations corresponds to the frozen propagation of the synthetic turbulence over a distance of $\lambda_{x,max}$. Then, each simulation was run for another whole period of the largest wavenumber, while unsteady data for the velocity and noise spectra calculations are collected. For the two-component Fourier mode method, averaging over several realisations is required to obtain converged velocity and noise spectra. This is because each $k_{x,n}$ (or frequency) is related to several $k_{y,m}$ that may lead to noise cancellation effects depending on the phase terms ϕ_{nm}, as can be inferred from Equation 2.27. Consequently, $N_r = 10$ independent simulations were performed, and individual velocity and noise spectra were averaged to obtained converged results. This strategy reduces the statistical error of the numerical results, which decreases proportionally to $\sqrt{1/N_r}$ [41].

	$\lambda_{x,max}$ [m]	N	M	C
1cFm	2.55	100	-	-
2cFm	2.55	100	10	3

Table 2.3: Parameters for the one- and two-component Fourier mode methods at $M_\infty = 0.6$.

Figure 2.9 shows contours of fluctuating vorticity magnitude and pressure for the different synthetic turbulence methods. Fluctuating pressure plots show the NACA 0001 aerofoil radiating as a multi-frequency dipole source, where the noise is generated at the leading edge. Furthermore, there are no fluctuating pressure waves approaching the aerofoil from the edges of the CAA domain, which indicates a satisfactory performance of the implicit buffer zones as a non-reflecting boundary condition.

The advanced digital filter method allows a local injection of the turbulent structures close to the aerofoil leading edge (see Figure 2.9e), whereas Fourier mode methods define the velocity disturbances throughout the CAA domain. For realistic simulations of open-jet wind tunnel experiments, a local turbulence injection can avoid the interaction of vortical disturbances with jet shear layers, which may produce instabilities in the LEEs [145]. Furthermore, injecting the turbulence locally can produce significant savings in computational cost. Figure 2.9e also shows a change in the size and amplitude of the turbulent structures downstream of the aerofoil compared to those upstream of the aerofoil. This is related to the grid stretching that is used downstream of the aerofoil in the CAA mesh, which reduces the grid density and dissipates small vortical disturbances.

2.4.5 Turbulent Velocity Spectra

A monitor point was placed at approximately $0.02c$ upstream of the aerofoil leading edge to control the quality of the oncoming turbulence in the CAA simulations. Figure 2.10 shows a comparison of one-dimensional velocity spectra from simulations using different synthetic turbulence methods. The one-component Fourier mode method, which only enforces $E_{22}^{(2D)}$, shows an agreement with the analytical result to within 1.5 dB. The same level of agreement is shown for $E_{11}^{(2D)}$ and $E_{22}^{(2D)}$ when using the advanced digital filter method. In contrast, numerical results from the two-component Fourier mode method show oscillations of up to 3.5 dB between the analytical and the numerical curves. These oscillations can be reduced by increasing the number of realisations, N_r, or by applying a smoothing technique to the curves.

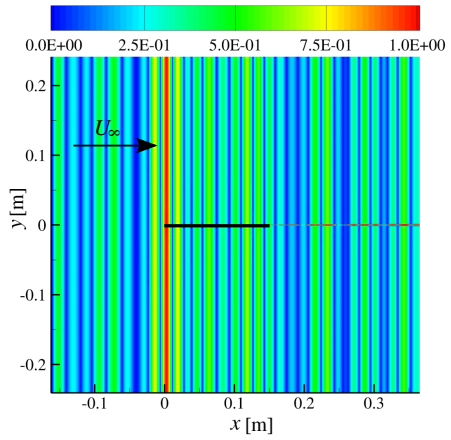

(a) One-component Fourier mode method. Contours of vorticity magnitude, $\|\nabla \times \mathbf{u}'\| / \max\{\|\nabla \times \mathbf{u}'\|\}$.

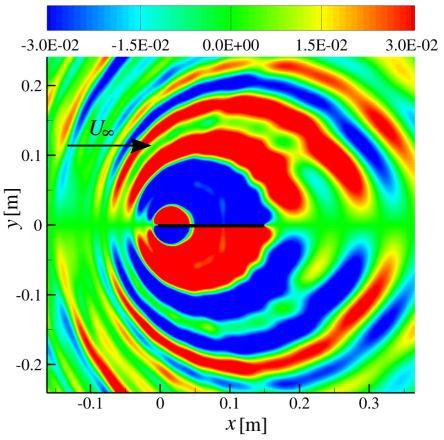

(b) One-component Fourier mode method. Contours of fluctuating pressure, $p'/\max\{p'\}$.

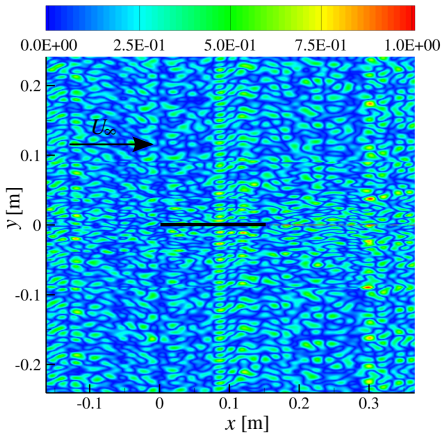

(c) Two-component Fourier mode method. Contours of vorticity magnitude, $\|\nabla \times \mathbf{u}'\| / \max\{\|\nabla \times \mathbf{u}'\|\}$.

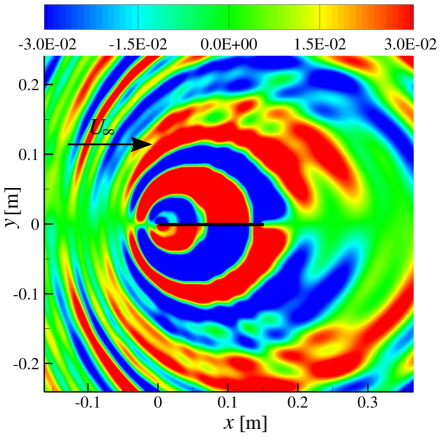

(d) Two-component Fourier mode method. Contours of fluctuating pressure, $p'/\max\{p'\}$.

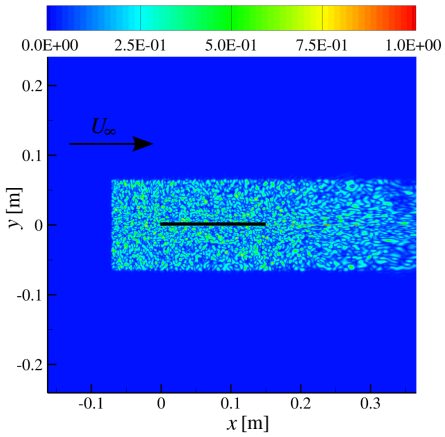

(e) Advanced digital filter method. Contours of vorticity magnitude, $\|\nabla \times \mathbf{u}'\| / \max\{\|\nabla \times \mathbf{u}'\|\}$.

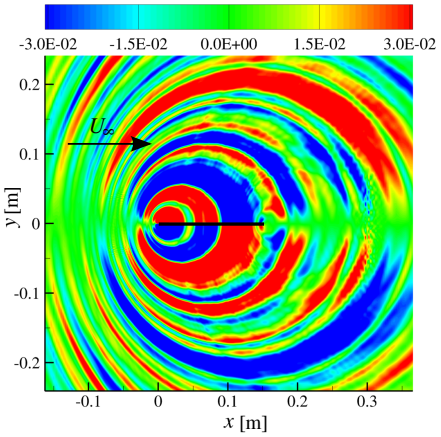

(f) Advanced digital filter method. Contours of fluctuating pressure, $p'/\max\{p'\}$.

Figure 2.9: Instantaneous contour plots of a NACA 0001 aerofoil at $M_\infty = 0.6$ (uniform mean flow). A thick black line is used to highlight the location of the aerofoil.

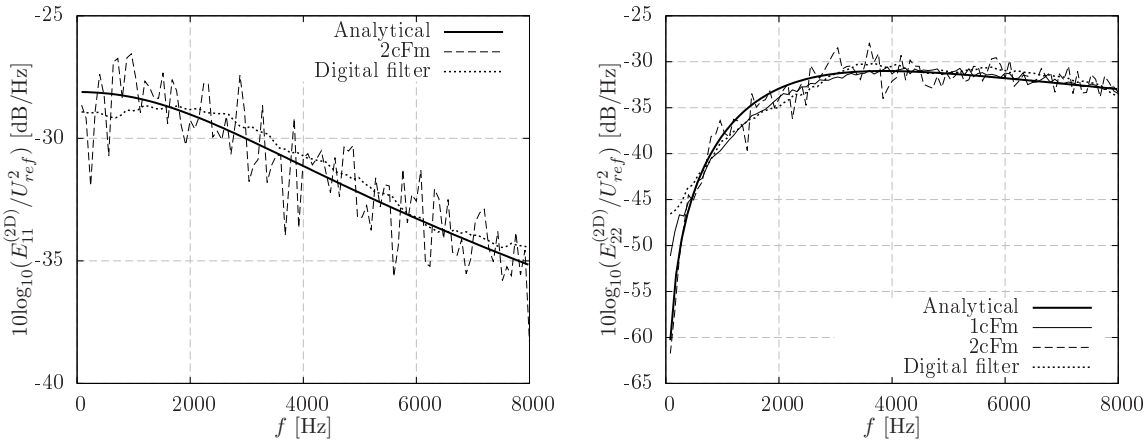

(a) Streamwise, $U_{ref} = 1$ m/s.

(b) Transverse, $U_{ref} = 1$ m/s.

Figure 2.10: One-dimensional von Kármán spectra of two-dimensional turbulence with $M_\infty = 0.6$, $u'_{rms}/U_\infty = 0.017$, and $\Lambda = 0.008$ m.

2.4.6 Far-Field Noise Spectra

A FW-H solver is used to yield an integral solution of the FW-H equation for far-field directivity. Far-field observers are placed at a distance of $r_0 = 100c$ from the aerofoil mid-chord, ranging from $\theta = 0^o$ to 360^o with an angle resolution of 1^o, according to the reference frame shown in Figure 2.7.

Figure 2.11 shows the PWL and SPL spectra. All synthetic turbulence methods that have been developed in this chapter provide noise predictions accurate up to 1.5 dB for most frequencies. Small discrepancies between analytical and numerical noise results are influenced by the convergence of the turbulence spectra (see Figure 2.10), particularly the spectrum that corresponds to the transverse velocity fluctuations ($S_{pp}^{(2D)} \propto \Phi_{22}^{(2D)}$ as can be seen in Equation 2.31).

Directivity plots are shown in Figure 2.12, where the location of the lobes and SPL levels are in good agreement for all the three synthetic turbulence methods. Nevertheless, the methods that include the streamwise velocity fluctuations over-predict the SPL at high observer angles, $\theta > 160^o$. This is believed to be associated with the interaction between streamwise disturbances and the cross-section of the NACA 0001 aerofoil. Such a noise mechanism is not included in the analytical model of a flat plate, since only the transverse velocity fluctuations contribute to the leading edge noise.

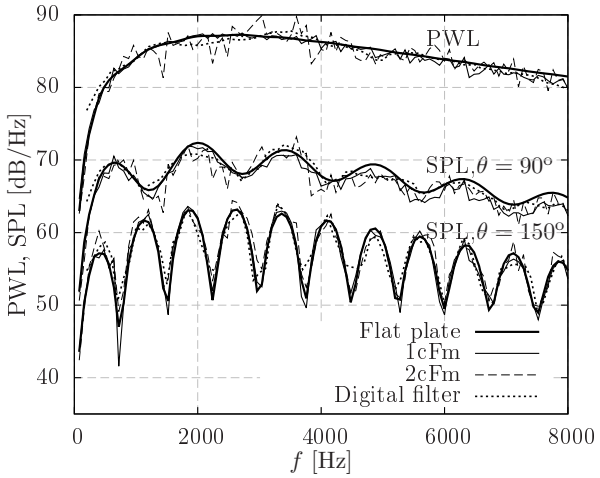

Figure 2.11: PWL and SPL spectra at $r_0 = 100c$ for a two-dimensional NACA 0001 aerofoil at $M_\infty = 0.6$.

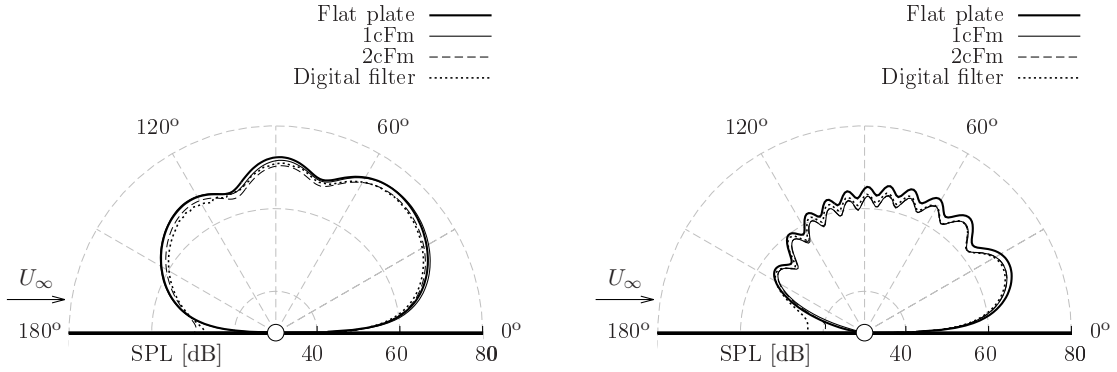

(a) $f = 2000$ Hz. (b) $f = 8000$ Hz.

Figure 2.12: Directivity plots at $r_0 = 100c$ for a two-dimensional NACA 0001 aerofoil at $M_\infty = 0.6$.

2.5 Summary

In this chapter, a CAA methodology that uses synthetic turbulence in a LEE solver has been presented for leading edge noise predictions. To date, synthetic turbulence based on a summation of Fourier modes, digital filters, and synthetic eddies have been used to study turbulence-aerofoil interaction noise. A direct comparison between several synthetic turbulence methods is required to identify what type of method is the most suitable for accurate noise predictions at a reduced computational expense. Based on previous works in the field, three different synthetic turbulence methods are fully

developed here to generate a two-dimensional fluctuating velocity field with the statistics of a target isotropic energy spectrum:

- **Advanced digital filter method**. This novel synthetic turbulence method combines the advantages of the RPM and synthetic eddy methods to reduce the number of constraint parameters and random numbers involved, and to avoid the generation and filtering of white noise signals in comparison with previous methods. The resulting turbulent field is able to match a target energy spectrum through a superposition of Gaussian eddies that define a new eddy profile. All eddies have the same size, shape, and amplitude, and the only difference between them is their direction of rotation, which accelerates the convergence of the turbulence statistics and simplifies the numerical implementation. Furthermore, optimised values to define the eddy radius ($r_e \geq 3\Lambda/2$) and the eddy spacing ($\Delta_e \leq \Lambda/2$) are found from a parameter study to increase the computational performance of the method.

- **One-component Fourier mode method**. This method generates transverse velocity fluctuations from a summation of parallel gusts, whose amplitude is proportional to the square root of a target velocity spectrum. This simple representation of the oncoming turbulence is based on the work of Amiet [39], in which the upwash velocity spectrum is used to compute the leading edge noise of a flat plate.

- **Two-component Fourier mode method**. Based on a summation of skewed gusts, this method generates a fluctuating velocity field that includes both streamwise and transverse components. This allows a more realistic representation of the oncoming turbulence than the one-component Fourier mode method.

An initial validation of the different types of synthetic turbulence methods highlights differences in the characteristics of the resulting turbulent flow. Methods based on Fourier modes generate a periodic fluctuating velocity field with a finite number of discrete frequencies. These methods inject the fluctuating velocity field throughout the CAA domain in order to meet the divergence-free condition. In contrast, the advanced digital filter method generates a turbulent flow from divergence-free synthetic eddies that are injected locally. The resulting turbulent flow is non-periodic and has a broadband spectrum. Differences between synthetic turbulence methods are summarised in Table 2.4.

	Turbulence spectrum	Periodicity of the turbulence	Turbulence injection
Fourier modes	Discrete	Periodic	Global buffer zones
Digital filters	Continuous	Non-periodic	Local injection plane

Table 2.4: Summary of differences between Fourier mode methods and digital filter methods.

Synthetic turbulence methods have been validated for leading edge noise predictions in CAA simulations of a NACA 0001 aerofoil. Noise results have been compared with a two-dimensional version of Amiet's model [70]. For a thin aerofoil at zero angle of attack, the accuracy of the noise predictions is related to the convergence of the velocity spectra. The one-component Fourier mode method and the advanced digital filter method provide velocity and noise spectra to within an accuracy of 1.5 dB. In contrast, results of the two-component Fourier mode method present a slower convergence than the advanced digital filter method for a similar simulation length. Oscillations of up to 3.5 dB are seen in velocity and noise spectra.

Chapter 3

Leading Edge Noise Predictions Using Isotropic Turbulence

In Chapter 2, two-dimensional isotropic synthetic turbulence was generated by using the advanced digital filter method (see Section 2.2) and Fourier mode methods (see Section 2.3). These methods were developed and validated for leading edge noise predictions using a NACA 0001 aerofoil. The present chapter examines a number of single aerofoil configurations to assess the accuracy and computational expense of digital filter and Fourier mode methods, including variations in freestream Mach number, aerofoil thickness, and angle of attack.

Additionally, this chapter presents an extensive characterisation of the unsteady flow field around the aerofoils to improve current understanding of noise reduction mechanisms due to realistic aerofoil geometry. To this end, averaged contours of fluctuating velocity and pressure fields are analysed in the near-field, the distortion of velocity spectra is examined in the leading edge region, and a spectral analysis of the unsteady pressure response on the aerofoil surface is also included. This information is straightforward to extract from numerical simulations, which can overcome limitations in data collection that occur in open-jet wind tunnel experiments. The PWL spectra and directivity plots are also computed in the far-field.

The present chapter is organised as follows. The aerofoil configurations investigated in this chapter are detailed in Section 3.1, including CAA mesh information, mean flow modelling assumptions, and input parameters for synthetic turbulence methods. The effects of aerofoil thickness and freestream Mach number on near- and far-field broadband noise are discussed in Section 3.2. Then, an angle of attack configuration is tested in Section 3.3. Finally, Section 3.4 presents a summary of the computational expense from digital filter and Fourier mode methods.

3.1 Aerofoil Configurations

NACA 4-digit aerofoils with 6 % and 12 % maximum thickness-to-chord ratios are tested at $AoA = 0^{o}$ with freestream Mach numbers $M_{\infty} = 0.3$ and 0.6. These aerofoils are representative of the thickness in OGVs ($t_A/c \sim 0.06$) and in the pylon of CRORs ($t_A/c \sim 0.12$). The aerofoil chord is set to $c = 0.15$ m. Additionally, the thicker aerofoil is tested at $M_{\infty} = 0.3$ and $AoA = 6^{o}$.

3.1.1 Mesh Generation

The CAA mesh for each configuration extends to $4c$ in all directions around the aerofoil mid-chord. All meshes were designed to propagate acoustic waves without dissipation up to chord-based reduced frequencies of $fc/U_{\infty} = 12$. Therefore, the frequency range covered for the CAA simulations in this chapter is similar to that in recent numerical works of leading edge noise. For example, the studies of Clair *et al.* [38] and Gill [98] were limited to frequencies lower than $fc/U_{\infty} = 12.5$, and simulations of Dieste and Gabard [60] were restricted to frequencies below $fc/U_{\infty} = 10$. Figure 3.1 shows the CAA mesh in the leading and trailing edge regions of a NACA 0012 aerofoil. Further details on the CAA meshes that are used in this thesis are given in Section 2.4.3 and Appendix C.

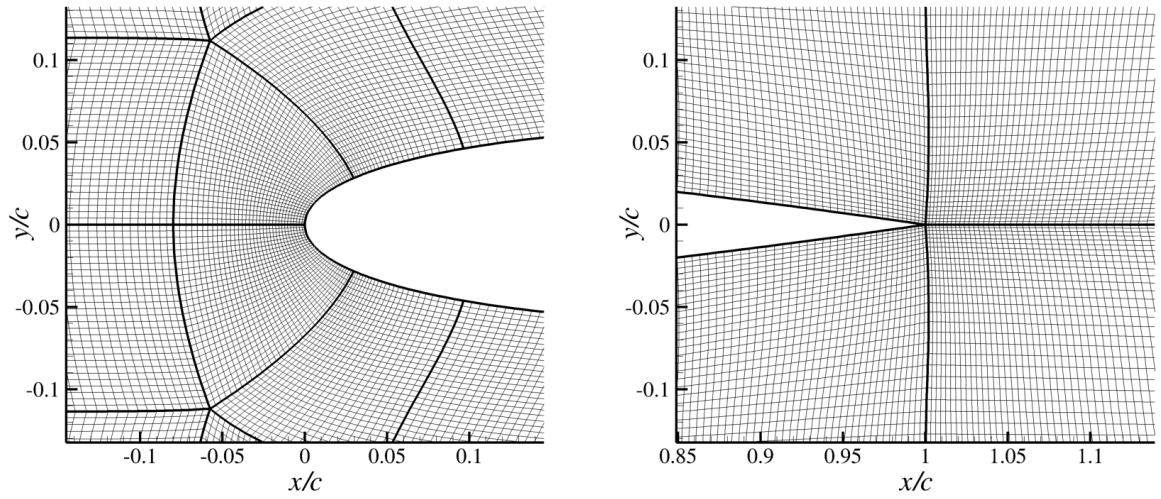

(a) Leading edge region.

(b) Trailing edge region.

Figure 3.1: Two-dimensional CAA mesh for a NACA 0012 aerofoil at $AoA = 0^{o}$.

Extending the study of leading edge noise to frequencies higher than $fc/U_{\infty} = 12$ might be unnecessary in practical cases. This is because aerofoil self-noise, which is not modelled in the CAA simulations in this thesis, is expected to be dominant at high frequencies. For example, Chaitanya *et*

al. [87] found that aerofoil self-noise was dominant for thickness-based frequencies $ft_A/U_\infty > 1$ in an anechoic wind tunnel experiment, which correspond to approximately $fc/U_\infty > 8.3$.

3.1.2 Inviscid Mean Flow Modelling

The assumption of uniform mean flow is valid for thin aerofoils at zero angle of attack, such as the NACA 0001 aerofoil that was examined in Section 2.4. However, Gill *et al.* [94] showed that as the aerofoil thickness increases, leading edge noise of aerofoils in uniform mean flows becomes over-predicted at high frequencies. This is because the distortion of the turbulent structures in the leading edge region is not modelled by a uniform mean flow simulation. Furthermore, viscosity was found to have a small effect on leading edge noise predictions when compared to inviscid solutions. Similar results were also reported by Clair *et al.* [38] and Hainaut *et al.* [97] when studying leading edge noise from a NACA 65(12)-10 aerofoil. Additionally, Clair *et al.* [38] found hydrodynamic instabilities and non-physical pressure fluctuations near the trailing edge when using a viscous mean flow, which was related to strong velocity gradients in the boundary layer region.

Consequently, steady inviscid mean flows have been adopted for the CAA simulations of thick aerofoils presented in this thesis. The inviscid mean flow is computed by using a second-order finite volume CFD solver (FLUENT v14.5). In the near-field, CFD and CAA meshes are similar. However, the CFD mesh extends to $20c$ in all directions around the aerofoil in order to reduce the influence of the boundary conditions on the mean flow solution. As the mean flow computation for each aerofoil configuration was converged, it was interpolated onto the CAA mesh.

3.1.3 Numerical Setup for Synthetic Turbulence Methods

In this chapter, digital filter and Fourier mode methods are used to generate synthetic turbulence with the statistics of the von Kármán spectrum defined by Equation 2.22 with $u'_{rms}/U_\infty = 0.017$ and $\Lambda = 0.008\,\text{m}$ ($\Lambda/c = 0.053$), which correspond to the same values that were used in Chapter 2. Therefore, the parameters for the Gaussian superposition to reproduce the von Kármán spectrum with the advanced digital filter method are given in Tables 2.1 and 2.2 for $M_\infty = 0.3$ and 0.6, respectively. The parameters required for the wavenumber discretisation in Fourier mode methods are given in Table 2.3 for $M_\infty = 0.6$. Simulations at $M_\infty = 0.3$ required the same number of Fourier modes with $\lambda_{x,max} = 1.275\,\text{m}$ and $C = 2$.

3.2 Effects of Aerofoil Thickness and Freestream Mach Number

This section presents a detailed characterisation of the unsteady flow surrounding NACA 0006 and NACA 0012 aerofoils at $AoA = 0^o$. CAA simulations were performed at two different freestream Mach numbers, $M_\infty = 0.3$ and 0.6. Although aerofoils at high Mach numbers cannot be tested in open-jet wind tunnel experiments due to the increase in jet noise, previous CAA studies reported some discrepancies between noise reduction due to aerofoil thickness at high frequencies for various Mach numbers [95, 98]. Aerofoil thickness effects on the near- and far-field broadband noise are examined here by using digital filter and Fourier mode methods to generate the oncoming turbulence.

3.2.1 Turbulence Distortion in the Leading Edge Region

The distortion of the turbulent structures in the leading edge region is believed to be responsible for the noise reduction of thick aerofoils at high frequencies. Previous works examined the distortion of harmonic gusts [94, 95] or were restricted to examine the distortion of the transverse velocity spectrum [73, 97]. This section provides a spectral analysis of both streamwise and transverse velocity spectra along the stagnation line.

When using the LEEs, the distortion of the turbulent structures is caused by variations in the mean flow velocity. Figure 3.2a shows the Mach number distribution at three different locations for NACA 0006 and NACA 0012 aerofoils. At 20% of the chord away from the leading edge ($x/c = -0.2$ and $y/c = 0$), M_x/M_∞ shows a small reduction in the streamwise Mach number of about 10% of the freestream value. Consequently, a small distortion of the turbulent structures would be expected at this location. Closer to the leading edge, the streamwise Mach number becomes strongly affected. A 50% reduction in M_x can be seen at $0.02c$ upstream of the NACA 0012 aerofoil leading edge, whereas this reduction is about 25% for the NACA 0006 aerofoil along the stagnation line. This suggests that the distortion of turbulent structures is expected to begin further upstream as the aerofoil thickness increases.

For Fourier mode methods, synthetic turbulence is prescribed within the buffer zones, where the mean flow is nearly uniform. The distance between the aerofoil leading edge and the buffer zone is approximately $3.5c$. However, the location of the turbulence injection plane should be studied for the advanced digital filter method. If the injection plane is excessively close to the leading edge, where strong mean flow gradients occur, turbulent structures could not have sufficient time to be distorted before impinging on the aerofoil. Consequently, the noise prediction would be affected by incorrect distortion of the oncoming turbulence. To overcome this issue, the injection plane is placed in a region where the mean flow is nearly uniform. The proposed distance is $r_{e,1} + c$ upstream of the leading edge, where $r_{e,1} = 5\max\{\Lambda_i\}/2$ according to the values for Λ_i given in Table 2.1. Therefore, the injection

plane of the advanced digital filter method is located at $x/c \approx -1.42$, as shown in Figure 3.2b. Closer locations of the injection plane are discussed in Section 3.2.2.

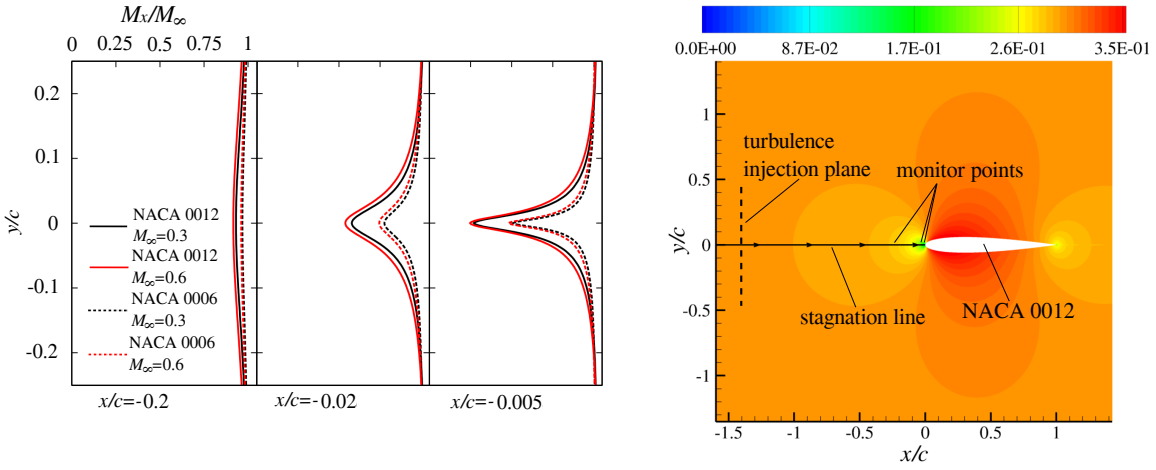

(a) M_x/M_∞ at different locations upstream of the aerofoil leading edge.

(b) Contours of Mach number around a NACA 0012 aerofoil ($M_\infty = 0.3$).

Figure 3.2: Mean flow distortion around aerofoils at $AoA = 0^o$ in the freestream.

Figure 3.3 shows contours of streamwise and transverse turbulence intensity around a NACA 0012 aerofoil using the advanced digital filter method. It can be seen that the streamwise turbulence intensity, $u'_{x,rms}/U_\infty$, decreases in the stagnation region. This is due to the reduction in M_x along the stagnation line and the cross-section of the aerofoil, which restricts velocity fluctuations in the x-direction. However, the transverse turbulence intensity, $u'_{y,rms}/U_\infty$, is increased in the stagnation region, as anticipated by Gill *et al.* [94] and Kim *et al.* [95] when examining the distortion of harmonic gusts. This result remains valid here for isotropic turbulence.

The decay in $u'_{x,rms}/U_\infty$ and the increase in $u'_{y,rms}/U_\infty$ along the stagnation line suggests that some kinetic energy in the streamwise disturbances is transferred into the transverse component. This process is accelerated near the aerofoil leading edge in a region within $0.02c$. Recently, experimental tests by Santana *et al.* [73] found that the strongest turbulence distortion occurs in a distance of the order of the leading edge radius[5]. This corresponds to $x/c \approx -0.016$ for a NACA 0012 aerofoil, which is consistent with the results shown in Figure 3.3.

[5]For a NACA 4-digit aerofoil, the leading edge radius is calculated as $r_{LE}/c = 1.1019\,(t_A/c)^2$.

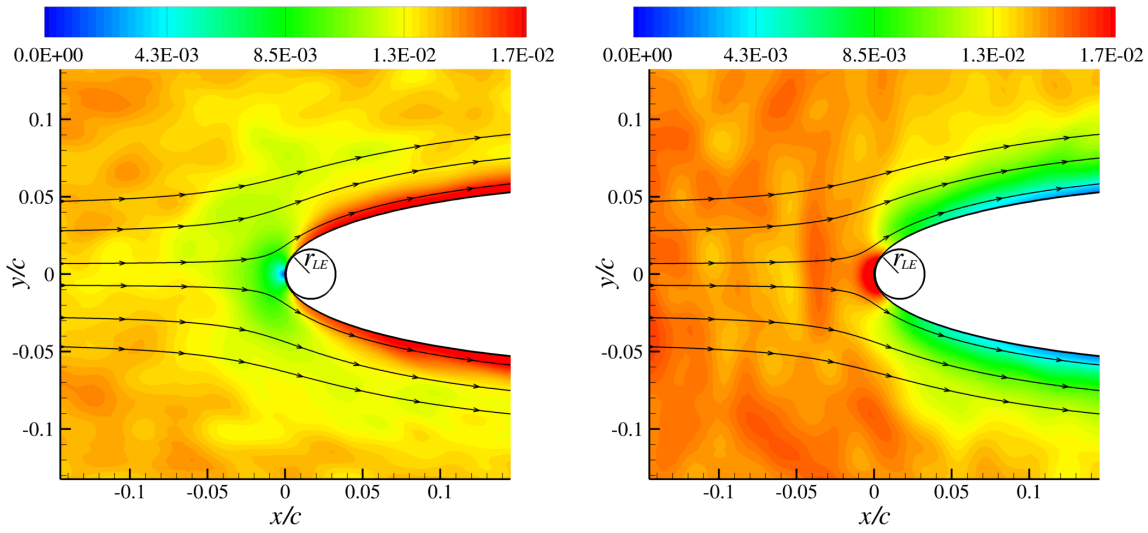

(a) Contours of $u'_{x,rms}/U_\infty$.

(b) Contours of $u'_{y,rms}/U_\infty$.

Figure 3.3: Contours of turbulence intensity and mean flow streamlines around a NACA 0012 aerofoil at $M_\infty = 0.3$ and $AoA = 0^o$. Turbulence intensities were calculated from 500 independent samples of fluctuating velocity fields using the advanced digital filter method. Note that r_{LE} represents the leading edge radius.

Figure 3.4 shows one-dimensional spectra near the NACA 0012 aerofoil at $M_\infty = 0.3$. All synthetic turbulence methods predict similar levels of distortion in the spectra. $E_{11}^{(2D)}$ drops about 3 dB at all frequencies, and the amplitude of $E_{22}^{(2D)}$ increases at low frequencies and decreases at high frequencies. This reduction at high frequencies is larger for the one-component Fourier mode method, which could be related to the lack of streamwise velocity fluctuations. Similar trends were reported by Hainaut *et al.* [99] in another CAA study that focused on the distortion of the transverse velocity spectrum, and by Hunt [75] when analysing the shape of the velocity spectra around a cylinder by means of the rapid distortion theory developed by Batchelor and Proudman [146]. The maximum value of $u'_{y,rms}/U_\infty$ in the stagnation region is associated with an increase in $E_{22}^{(2D)}(f)$ at low frequencies.

Both $E_{11}^{(2D)}$ and $E_{22}^{(2D)}$ present a reduction in the amplitude at high frequencies with respect to the prescribed spectra at the injection plane. It should be noted that the distortion of the turbulence spectra does not occur in the presence of a uniform mean flow. This explains the over-prediction in leading edge noise predictions at high frequencies when using uniform mean flows around thick aerofoils [38, 94, 97].

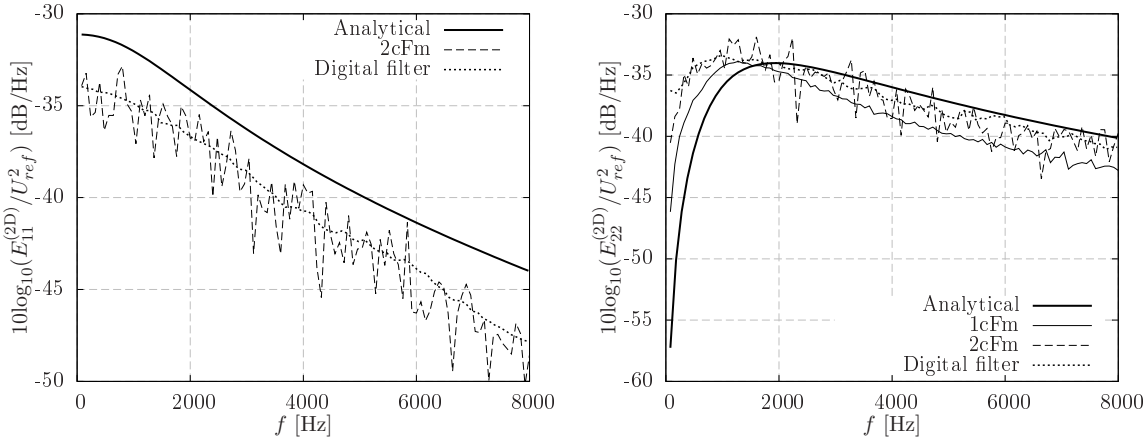

(a) Streamwise, $U_{ref} = 1$ m/s.

(b) Transverse, $U_{ref} = 1$ m/s.

Figure 3.4: One-dimensional spectra $0.02c$ upstream of the leading edge of a NACA 0012 aerofoil at $M_\infty = 0.3$ and $AoA = 0^o$.

Figure 3.5 shows differences between distorted and injected one-dimensional spectra for NACA 0006 and NACA 0012 aerofoils using the advanced digital filter method. Away from the leading edge, at $x/c = -0.2$, no significant distortions are appreciated for any of the aerofoils and freestream Mach numbers investigated, where $10\log_{10}(E_{ij}^{(2D)}/E_{ij,\infty}^{(2D)}) \approx 0$ dB. However, distortions in the turbulence spectra are noticeable at $x/c = -0.02$. These distortions are more pronounced and begin further upstream as the aerofoil thickness increases. For example, the averaged reduction in $E_{11}^{(2D)}$ is about 10 dB for the NACA 0012 aerofoil at $x/c = -0.005$, whereas a 5 dB reduction is observed for the NACA 0006 aerofoil at the same location. Nevertheless, the distortions of the spectra closely follow the same trends for each aerofoil geometry, and are weakly influenced by variations in the freestream Mach number. This result is consistent with the overlap of the distorted mean flows in Figure 3.2a.

Modifications in the velocity spectra have been proposed to better match experimental noise measurements using analytical models [72, 73]. These modifications aim to reproduce the distortions of the turbulence spectra in the presence of a thick aerofoil. Figure 3.5 also shows a modified isotropic von Kármán spectrum based on rapid distortion theory. Following the previous work of Santana *et al.* [73], the exponential term in the denominator of the isotropic von Kármán spectrum (see Equation 2.22) should be amended from 17/6 to 22/6 in order to follow the asymptotic slope reported by Hunt [75] at high frequencies. Thus, the modified energy spectrum in the vicinity of the leading edge takes the form

$$E^{(2D)}(k) = \frac{110 u_{rms}'^2 \Lambda}{27\pi} \frac{\left(\frac{k}{k_c}\right)^4}{\left[1 + \left(\frac{k}{k_c}\right)^2\right]^{22/6}}. \tag{3.1}$$

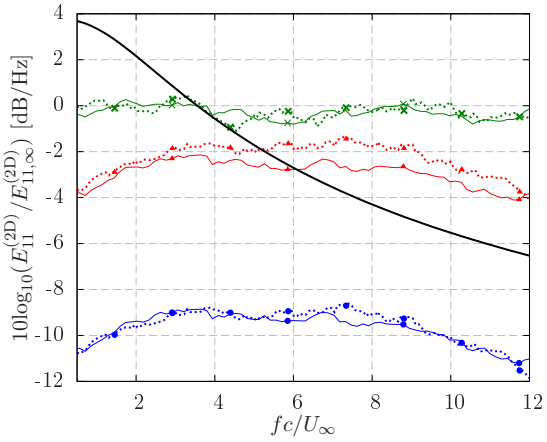

(a) Normalised $E_{11}^{(2D)}(f)$ for a NACA 0012 aerofoil.

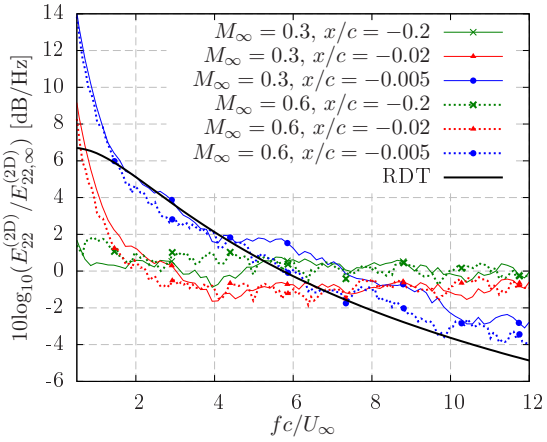

(b) Normalised $E_{22}^{(2D)}(f)$ for a NACA 0012 aerofoil.

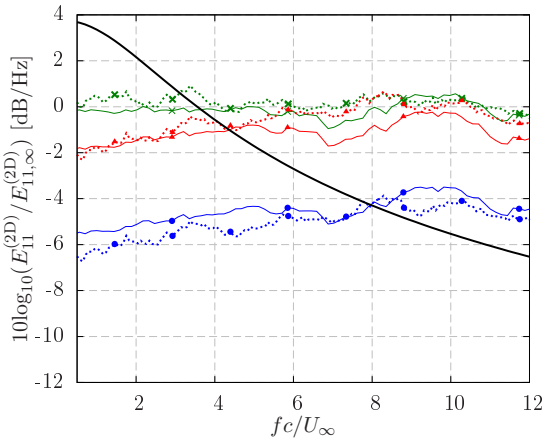

(c) Normalised $E_{11}^{(2D)}(f)$ for a NACA 0006 aerofoil.

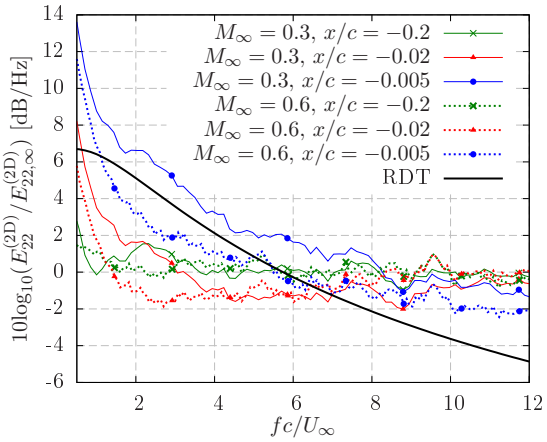

(d) Normalised $E_{22}^{(2D)}$ for a NACA 0006 aerofoil

Figure 3.5: Distortion of one-dimensional spectra using the advanced digital filter method. Numerical results are normalised with the upstream one-dimensional spectra, $E_{ij,\infty}^{(2D)}$, and compared to analytical results from rapid distortion theory, abbreviated as RDT.

The distorted energy spectrum in Equation 3.1 produces a redistribution of the energy in the velocity spectra, but it does not affect the total turbulent kinetic energy, which remains constant. The numerical $E_{22}^{(2D)}$ resembles the distorted analytical spectrum at $x/c = -0.005$, where the agreement is better than 2 dB for the NACA 0012 aerofoil over a large portion of the frequency range. The good agreement justifies the use of Equation 3.1 to improve analytical predictions of a NACA 0012 aerofoil, as done by Santana *et al.* [73]. However, a worse agreement is found between numerical and analytical distorted spectra for the NACA 0006 aerofoil. This suggests that a different modification of the energy spectrum might be required for each aerofoil geometry. Furthermore, the modified energy spectrum does not match the behaviour of $E_{11}^{(2D)}$ in the vicinity of the aerofoils. A modification in the slope of

the isotropic energy spectrum does not seem suitable for reproducing simultaneously the distortion of the streamwise and transverse velocity spectra. Nevertheless, leading edge noise predictions are not expected to be significantly affected by discrepancies in the streamwise velocity spectrum, since they are dominated by the transverse spectrum.

3.2.2 Location of the Turbulence Injection Plane

In the previous section, the injection plane of the advanced digital filter method was placed $r_{e,1} + c$ upstream of the aerofoil leading edge, where $r_{e,1} = 5\max\{\Lambda_i\}/2$ according to the values for Λ_i given in Table 2.1. At that location, the mean flow is nearly uniform and the turbulent structures have enough time to be distorted before reaching the aerofoil. However, the distortion of the turbulent structures occur in the vicinity of the aerofoil, which suggests that a closer location of the injection plane could be possible for leading edge noise predictions. This could potentially result in a reduction of the mesh size and the transitory state, and savings in the computational cost. To investigate this, a new location is considered for the injection plane in the CAA simulations of the NACA 0012 aerofoil at $M_\infty = 0.3$ and 0.6. The new location is $r_{e,2}$ upstream of the aerofoil leading edge, where $r_{e,2} = 3\max\{\Lambda_i\}/2$ according to the values for Λ_i given in Table 2.1, which corresponds to $x/c \approx -0.25$.

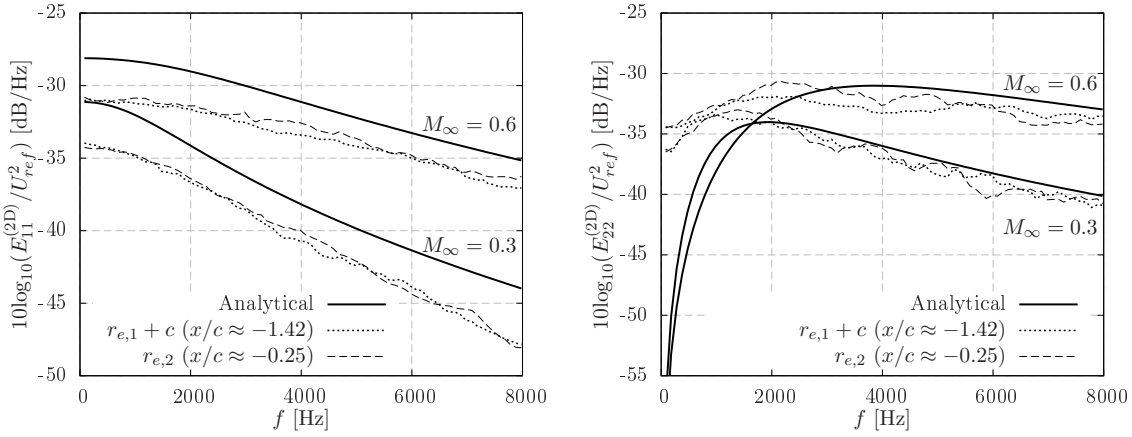

(a) Streamwise, $U_{ref} = 1$ m/s.

(b) Transverse, $U_{ref} = 1$ m/s.

Figure 3.6: One-dimensional spectra $0.02c$ upstream of the leading edge of a NACA 0012 aerofoil at $AoA = 0^o$ using the advanced digital filter method. The injection plane is placed at two different locations upstream of the aerofoil leading edge.

One-dimensional spectra using two different locations for the injection plane are presented in Figure 3.6. Results show that locations lead to similar distortions in the spectra and, consequently, similar noise predictions are expected. This implies that the injection plane can be placed at a distance

of $r_e \geq 3\max\{\Lambda_i\}/2$ upstream of the aerofoil leading edge in practical cases, even if the mean flow is not completely uniform at this location.

3.2.3 Near-Field Noise

The noise perceived in the far-field is a consequence of the noise generated and radiated from the near-field. This section examines the unsteady pressure field in the near-field from CAA simulations of thick aerofoils. The aim is to provide a better understanding of the leading edge noise in its origin.

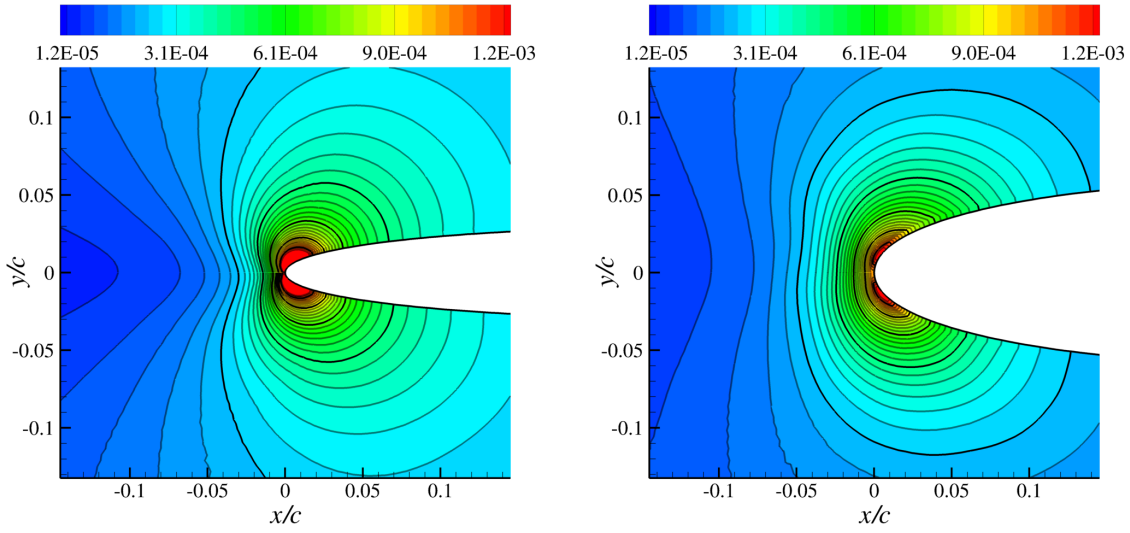

(a) NACA 0006 aerofoil.

(b) NACA 0012 aerofoil.

Figure 3.7: Contours of $p'_{rms}/\rho_\infty c_\infty^2$ around aerofoils at $M_\infty = 0.3$ and $AoA = 0^o$. Contour levels were calculated from 500 independent samples of fluctuating pressure fields using the advanced digital filter method.

Figure 3.7 shows contours of the root-mean-square fluctuating pressure around NACA 0006 and NACA 0012 aerofoils. In both cases, a maximum $p'_{rms}/\rho_\infty c_\infty^2$ is found on each side of the stagnation point, which is due to the symmetry in the aerofoil configuration and the dipole pattern that follows the leading edge noise. This result indicates that the noise is not radiated from the stagnation point, where the largest $u'_{y,rms}$ occurs (see Figure 3.3b). Furthermore, the noise source has slightly moved backwards from the leading edge. Nevertheless, this result is consistent with Amiet's theory [39], in which the maximum p'_{rms} is located exactly at the leading edge of the flat plate. Gill [98] reported a similar behaviour in p'_{rms} when examining the distortion of harmonic gusts around thick aerofoils. Overall, the NACA 0006 aerofoil produces a stronger aerofoil response than the NACA 0012 aerofoil, as can be inferred from the larger area with red contours in Figure 3.7. In contrast, the NACA 0012

aerofoil presents stronger $p'_{rms}/\rho_\infty c_\infty^2$ contours in the upstream direction along the stagnation line. This indicates that as the aerofoil thickness increases, noise radiated in the upstream direction becomes more important.

To study the relationship between the distorted turbulent structures and the unsteady pressure response on the aerofoil surface, the magnitude-squared coherence is defined as

$$\gamma^2_{u_i p}(f) = \frac{\left|S_{u_i p}(f)\right|^2}{S_{u_i u_i}(f) S_{pp}(f)}, \tag{3.2}$$

where $S_{u_i u_i}$ is the spectral density of the fluctuating velocity (u'_i) in the vicinity of the leading edge, S_{pp} is the spectral density of the fluctuating pressure (p') on the aerofoil surface, and $S_{u_i p}$ is the cross-spectral density between u'_i and p'. Figure 3.8 shows the coherence between velocity fluctuations collected at $x/c = -0.02$ along the stagnation line and pressure fluctuations on the surface of a NACA 0012 aerofoil at various locations.

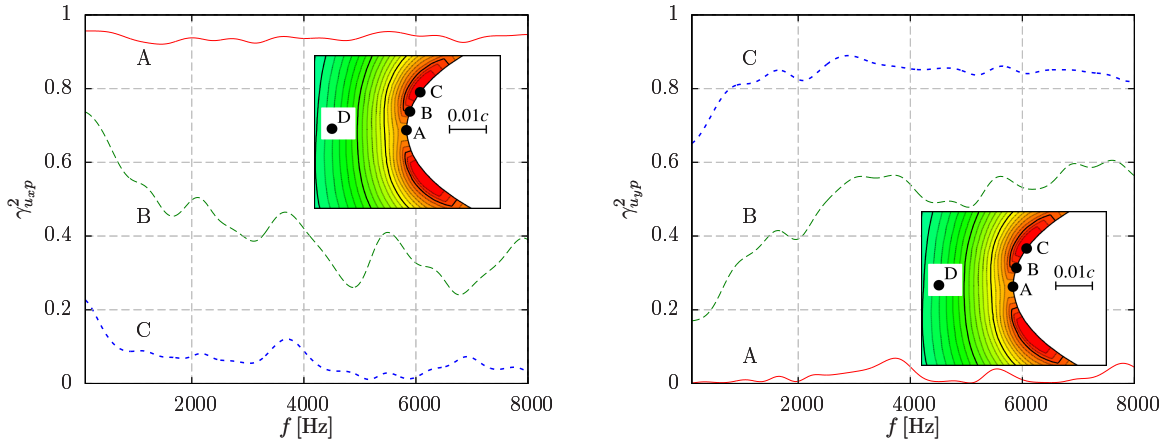

(a) Coherence between pressure fluctuations and streamwise velocity fluctuations.

(b) Coherence between pressure fluctuations and transverse velocity fluctuations.

Figure 3.8: Magnitude-squared coherence between pressure fluctuations at three different locations (A, B, and C) on the aerofoil surface and velocity fluctuations in the vicinity of the aerofoil leading edge (location D, $x/c = -0.02$ along the stagnation line). Results were obtained from the simulation of a NACA 0012 aerofoil at $M_\infty = 0.3$ and $AoA = 0^o$ using the advanced digital filter method. Inserted contour plots correspond to an enlarged view of $p'_{rms}/\rho_\infty c_\infty^2$ at the leading edge from Figure 3.7b.

The streamwise velocity fluctuations are mainly responsible for the noise radiated from the stagnation point (location A), as can be inferred from Figure 3.8, where $\gamma^2_{u_x p} \approx 0.95$ and $\gamma^2_{u_y p} \approx 0.05$ at all frequencies. Since the turbulence intensity in the streamwise direction is attenuated in the vicinity of the leading edge (see Figure 3.3a), this explains why the noise is not radiated from the stagnation point.

When moving away from the stagnation point (locations B and C), the transverse velocity fluctuations become increasingly coherent with the unsteady pressure response. The maximum in $p'_{rms}/\rho_\infty c_\infty^2$ (approximately at location C) is mainly due to the transverse fluctuating velocity component, as occurs for flat plates.

Contours of root-mean-square fluctuating pressure are useful to locate the noise source, but do not provide any information about its frequency content. Figure 3.9 shows the spectral decomposition of the unsteady pressure response along the aerofoil chord in terms of SPL. It can be seen that noise is mainly radiated from locations close to the aerofoil leading edge ($x/c < 0.2$) and low reduced frequencies ($fc/U_\infty < 4$). Thus, the maximum in $p'_{rms}/\rho_\infty c_\infty^2$ contours in Figure 3.9 is primarily caused by low frequencies. This result is consistent with the distorted turbulence spectra in the vicinity of the leading edge, where the transverse velocity spectrum undergoes a significant increase at low frequencies. When comparing results from both aerofoils, the SPL is lower for the thicker aerofoil, especially from the mid-chord at high frequencies. Therefore, the reduction of unsteady pressure fluctuations on the surface of thick aerofoils explains the well-known noise reduction due to aerofoil thickness at high frequencies in the far-field [78, 79, 94].

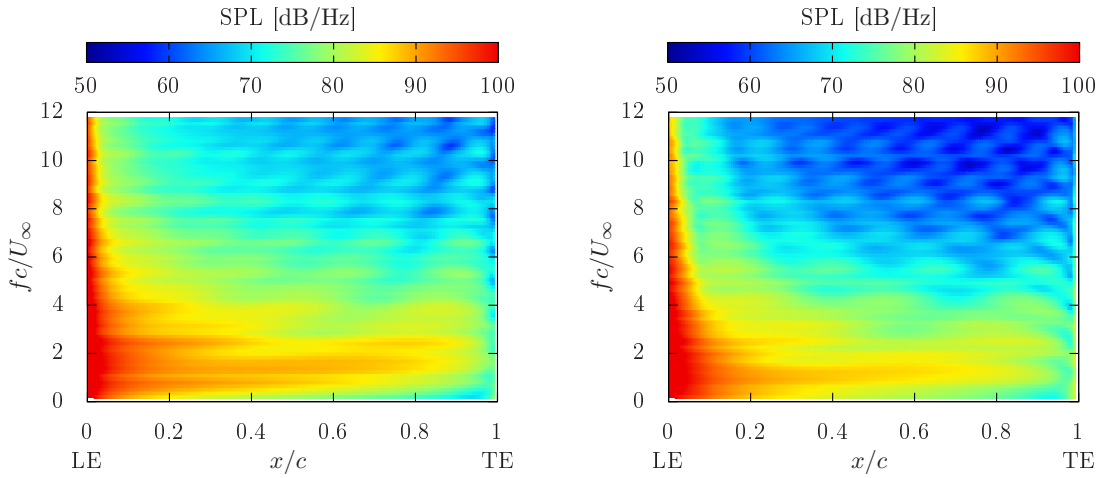

(a) NACA 0006 aerofoil.

(b) NACA 0012 aerofoil.

Figure 3.9: SPL spectra on the surface of aerofoils at $M_\infty = 0.3$ and $AoA = 0^o$ using the advanced digital filter method. Leading Edge (LE) and Trailing Edge (TE) correspond to $x/c = 0$ and $x/c = 1$, respectively.

Figure 3.10 shows fluctuating velocity and pressure contours of the NACA 0012 aerofoil simulations at $M_\infty = 0.3$. Although the unsteady pressure fields follow a dipole pattern as in Figure 2.9 for a NACA 0001 aerofoil at $M_\infty = 0.6$, convective amplification effects are less pronounced at low Mach numbers.

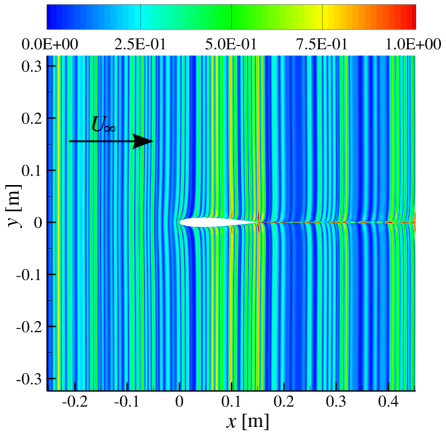

(a) One-component Fourier mode method. Contours of vorticity magnitude, $\|\nabla \times \mathbf{u}'\| / \max\{\|\nabla \times \mathbf{u}'\|\}$.

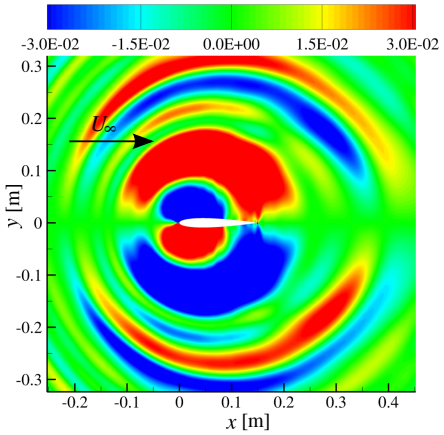

(b) One-component Fourier mode method. Contours of fluctuating pressure, $p'/\max\{p'\}$.

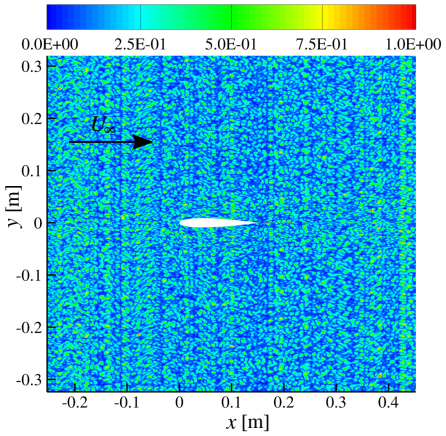

(c) Two-component Fourier mode method. Contours of vorticity magnitude, $\|\nabla \times \mathbf{u}'\| / \max\{\|\nabla \times \mathbf{u}'\|\}$.

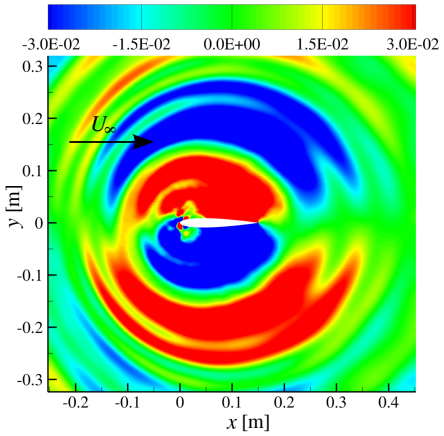

(d) Two-component Fourier mode method. Contours of fluctuating pressure, $p'/\max\{p'\}$.

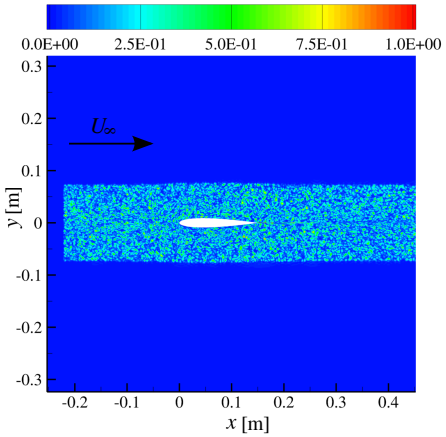

(e) Advanced digital filter method. Contours of vorticity magnitude, $\|\nabla \times \mathbf{u}'\| / \max\{\|\nabla \times \mathbf{u}'\|\}$.

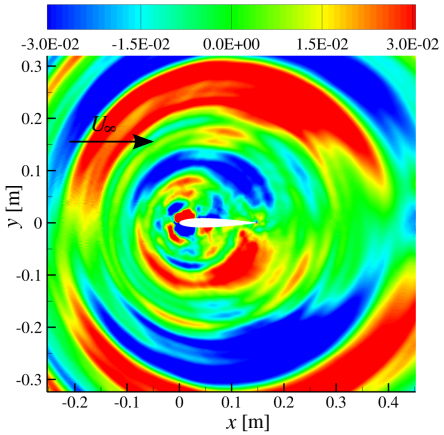

(f) Advanced digital filter method. Contours of fluctuating pressure, $p'/\max\{p'\}$.

Figure 3.10: Instantaneous contour plots of a NACA 0012 aerofoil at $M_\infty = 0.3$ (inviscid mean flow).

3.2.4 Far-Field Noise

Figure 3.11 shows the reference frame for far-field noise predictions of single aerofoil configurations. Far-field observers were placed at a distance of $r_0 = 100c$ from the aerofoil mid-chord, ranging from $\theta = 0^o$ to 180^o with an angle resolution of 1^o.

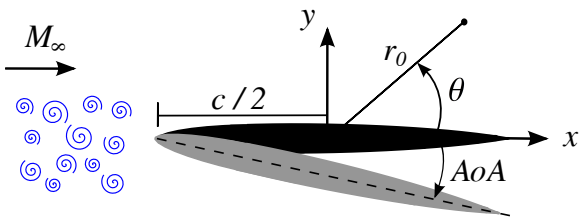

Figure 3.11: Reference frame for leading edge noise predictions in the far-field.

Figure 3.12 shows the PWL spectra for NACA 0006 and NACA 0012 aerofoils at $AoA = 0^o$ using digital filter and Fourier mode methods. Results agree with the findings reported in the literature. Noise reduction at a fixed frequency is more pronounced for thicker aerofoils at low Mach numbers, as shown experimentally by Paterson and Amiet [79] and numerically by Gill *et al.* [94], among others. For example, a NACA 0012 aerofoil at $M_\infty = 0.3$ produces a noise reduction of 8 dB at 8000 Hz, whereas a NACA 0006 aerofoil at $M_\infty = 0.6$ produces nearly the same PWL spectrum as a flat plate for frequencies up to 6000 Hz.

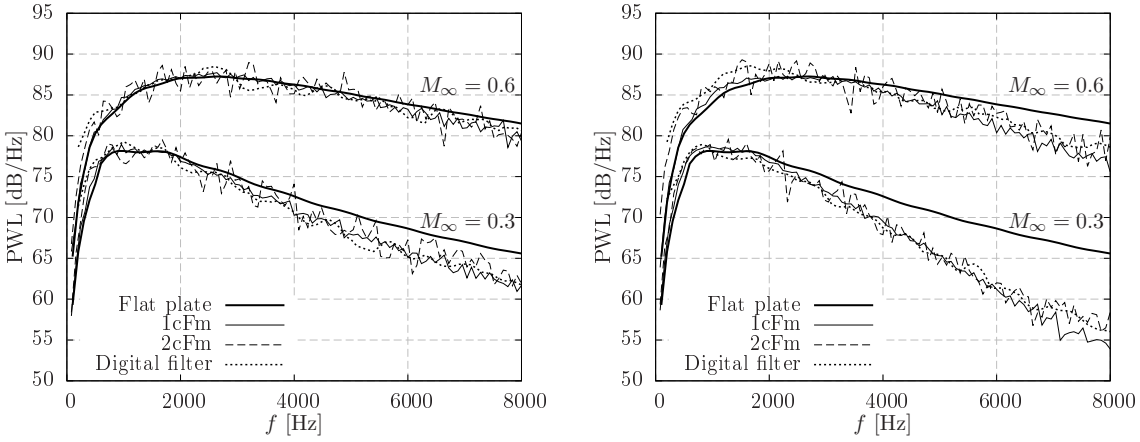

(a) NACA 0006 aerofoil.

(b) NACA 0012 aerofoil.

Figure 3.12: PWL spectra for NACA 0006 and NACA 0012 aerofoils at $AoA = 0^o$ and freestream Mach numbers $M_\infty = 0.3$ and 0.6.

For each case investigated in Figure 3.12, all three synthetic turbulence methods predict similar noise levels. Only for the NACA 0012 aerofoil simulations, an under-prediction of up to 3 dB is identified at frequencies above 6000 Hz for the one-component Fourier mode approach in comparison with the methods that include two components. This finding suggests that the streamwise velocity fluctuations could be necessary for simulations of thick aerofoils at high frequencies. Nevertheless, this small disagreement is close to the level of accuracy of the current method ($\sim$ 1.5 dB), which makes it difficult to draw further conclusions.

The noise reduction is quantified by calculating $\Delta\text{PWL} = \text{PWL}\,|_{\text{flat plate}} - \text{PWL}|_{\text{NACA aerofoil}}$. Figure 3.13a presents the ΔPWL spectra as a function of the chord-based reduced frequency, fc/U_∞. NACA aerofoils appear to be louder than a flat plate at low frequencies, $fc/U_\infty \leq 2$. This might be due to the streamwise velocity fluctuations interacting with the cross-section of the NACA aerofoils. Nevertheless, numerical noise predictions are not reliable at very low frequencies ($fc/U_\infty \approx 0$) due to the reduced physical time simulated and the limited number of time steps in numerical simulations to maintain an acceptable computational cost.

The noise reduction follows a linear increase in dB with fc/U_∞, which is more pronounced as the aerofoil thickness increases. For a given aerofoil geometry, ΔPWL is approximately the same at various Mach numbers and frequencies. This result could be explained by the normalised turbulent spectra shown in Figure 3.5, where the distortion of the turbulent structures in the vicinity of the leading edge was found to be weakly influenced by the Mach number. Additionally, the linear behaviour in the ΔPWL spectra from $fc/U_\infty = 1$ could be related to the quasi-linear decay of the transverse spectrum, $E_{22}^{(2D)}$, which corresponds to the dominant velocity component in the noise generation of aerofoils at $AoA = 0^o$. Previous experimental works also reported this linear behaviour in the noise reduction due to aerofoil thickness at high frequencies, such as those by Olsen and Wagner [89] and Chaitanya *et al.* [87]. Other works by Gill [98] and Kim *et al.* [95] using CAA solvers showed a dependency of the noise reduction on the freestream Mach number. Particularly, an earlier onset of noise reduction due to aerofoil thickness was observed at low Mach numbers ($M_\infty = 0.2$). This behaviour is not evident in ΔPWL spectra for the moderate and high Mach numbers considered in this chapter, $M_\infty = 0.3$ and 0.6.

It is well known that noise reduction at high frequencies depends on the overall thickness and leading edge radius [83, 87, 94], among others. Figure 3.13b presents the ΔPWL spectra as a function of the thickness-based reduced frequency, ft_A/U_∞. For the tested NACA 4-digit aerofoils, there is a good overlap of the ΔPWL spectra onto a single plot for the various thicknesses and Mach numbers, especially for $ft_A < 0.6$. This result is consistent with the CAA predictions of Gill [98] using synthetic turbulence based on a two-component Fourier mode method for aerofoil thicknesses ranging from $t_A/c = 0.02$ to 0.12 at $M_\infty = 0.5$.

Additionally, Figure 3.13b includes the scaling law proposed by Gershfeld [71] to account for aerofoil thickness effects on leading edge noise, which takes the form

$$\Delta\text{PWL} = 10\log_{10}[\exp(\pi\frac{ft_A}{U_\infty})] = \log_{10}[\exp(10\pi)]\frac{ft_A}{U_\infty}. \tag{3.3}$$

The noise reduction proposed by Gershfeld [71] is significantly over-predicted at high frequencies for the aerofoil configurations that have been investigated in this chapter. Alternatively, a representative estimation of ΔPWL for various thick aerofoils and freestream speeds can be obtained by using the linear least squares method to fit the CAA predictions. The best fit line for ΔPWL in dB is given by

$$\Delta\text{PWL} = -2.0857 + 8.6854\frac{ft_A}{U_\infty}. \tag{3.4}$$

There are a few differences between Gershfeld's correction [71] and Equation 3.4. The best fit line presents a lower slope than Gershfeld's correction [71] ($8.6854 < \log_{10}[\exp(10\pi)] \approx 13.6438$). Furthermore, $\Delta\text{PWL} < 0$ dB at $f = 0$ Hz in Equation 3.4. This is to account for a slight increase in noise at low frequencies due to aerofoil thickness. This implies that the best fit line is not valid close to the limit $t_A \to 0$, since the flat plate solution is not recovered ($\Delta\text{PWL} = 0$ dB for $t_A = 0$ m).

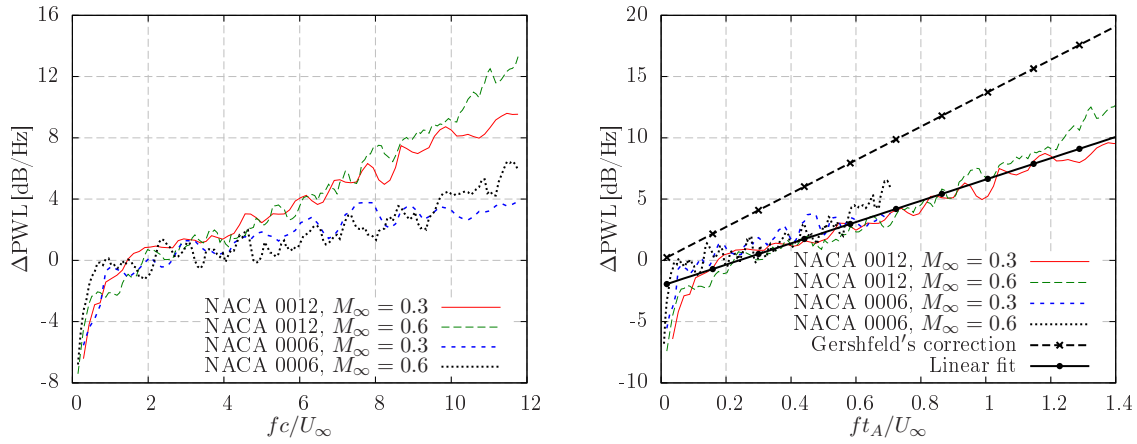

(a) ΔPWL as a function of fc/U_∞.

(b) ΔPWL as a function of ft_A/U_∞.

Figure 3.13: $\Delta\text{PWL} = \text{PWL}|_{\text{flat plate}} - \text{PWL}|_{\text{NACA aerofoil}}$ spectra for aerofoils at $AoA = 0^o$ using the advanced digital filter method.

Directivity plots of the NACA 0012 aerofoil are shown in Figure 3.14. Noise reduction at medium and high frequencies is mainly due to a decrease in SPL at downstream observer angles when compared with the flat plate solution. At high observer angles, the advanced digital filter method and the two-component Fourier mode method over-predict the noise levels. This is attributed to the streamwise velocity fluctuations and their interaction with the cross-section of the thick aerofoil. The lack

of this fluctuating velocity component could lead to a significant under-prediction of the noise at high frequencies, especially at upstream observer angles, as shown in Figure 3.14b at 8000 Hz.

For all synthetic turbulence methods, Figures 3.14b and 3.14d show a disagreement in the location of the lobes at acute upstream angles in comparison with the flat plate prediction. This could be related to the numerical treatment of the trailing edge in the CAA simulations. Although the Kutta condition is satisfied by the inviscid mean flow solution, the unsteady Kutta condition has not been explicitly imposed at the trailing edge. This might introduce small numerical errors in the location of upstream lobes. The numerical error is mainly relevant for thick aerofoils at high frequencies. Ayton *et al.* [147] estimated that the averaged error, including upstream and downstream observers, was below 2 dB for various frequencies. CAA simulations in this thesis have been shown to correctly predict the location of the lobes for thin aerofoils (for example, see Figure 2.12 for the NACA 0001 aerofoil).

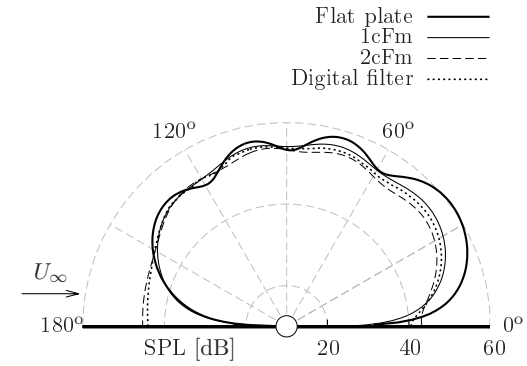

(a) $M_\infty = 0.3$, $f = 4000$ Hz ($fc/U_\infty \approx 5.88$).

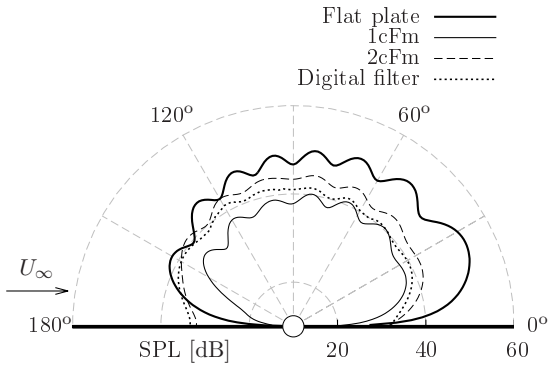

(b) $M_\infty = 0.3$, $f = 8000$ Hz ($fc/U_\infty \approx 11.76$).

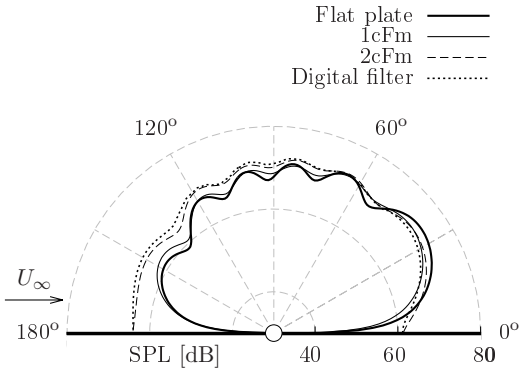

(c) $M_\infty = 0.6$, $f = 4000$ Hz ($fc/U_\infty \approx 2.94$).

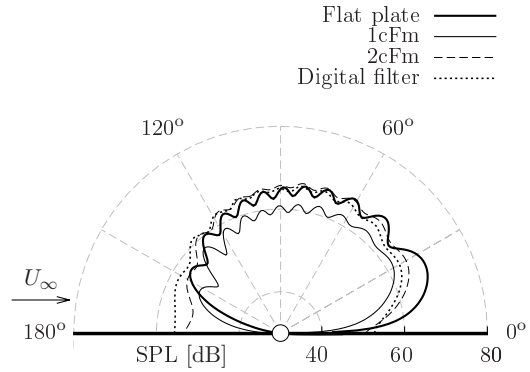

(d) $M_\infty = 0.6$, $f = 8000$ Hz ($fc/U_\infty \approx 5.88$).

Figure 3.14: Directivity plots at $r_0 = 100c$ for a NACA 0012 aerofoil at $AoA = 0^o$.

3.3 Effect of Angle of Attack

Aerofoils at non-zero angle of attack can be difficult to model in LEE solvers. This is because the angle of attack increases the velocity gradients in the leading edge region, which may cause the flow to become locally supersonic and the appearance of shocks. In this case, non-linear terms must be retained, and the full Euler equations could be required [148]. Additionally, the boundary layer detaches on the suction side at a high angle of attack. This phenomenon causes strong unsteady flows and vortex shedding around the trailing edge, which is an additional source of noise that cannot be modelled by the current CAA methodology.

In this section, the suitability of synthetic turbulence methods to study angle of attack is assessed on a NACA 0012 aerofoil at $M_\infty = 0.3$ and $AoA = 6^o$. This configuration has been chosen to study an aerofoil at a moderate angle of attack in which the mean flow remains subsonic and leading edge noise is the dominant source of noise. The aerofoil has been rotated around the leading edge, which stays at the same location as in the zero angle of attack simulations.

3.3.1 Turbulence Distortion in the Leading Edge Region

Variations in the turbulence intensities around the aerofoil leading edge are shown Figure 3.15 for the angle of attack configuration. Strong distortions of the turbulent structures occur in a region within $0.02c$ from the aerofoil surface. The turbulence intensity in the x-direction decreases in the stagnation region, and the transverse component is amplified, as found for the aerofoil at $AoA = 0^o$ (see Figure 3.3). Additionally, Figure 3.15b shows that the maximum $u'_{y,rms}/U_\infty$ has moved slightly from the stagnation point towards the suction side, where the strongest mean flow acceleration is expected to occur.

Figure 3.16 shows one-dimensional spectra using different synthetic turbulence methods at $0.02c$ upstream of the aerofoil leading edge. At this location, initial distortions in the turbulence spectra were evident for the $AoA = 0^o$ configuration in Figure 3.4. It should be noted that this monitor point is no longer on the stagnation line, since the stagnation point shifts towards the pressure side of an aerofoil placed at non-zero angle of attack. The distortion of both $E_{11}^{(2D)}$ and $E_{22}^{(2D)}$ in the vicinity of a NACA 0012 aerofoil shows similar trends and levels at $AoA = 0^o$ and 6^o. This could potentially explain why the angle of attack has been reported to have a small effect on leading edge noise. Only for the one-component Fourier mode method a larger decay in $E_{22}^{(2D)}$ is found at all frequencies, which leads to an under-prediction of 3.5 dB at 8000 Hz in Figure 3.16b. This phenomenon is attributed to the lack of streamwise velocity disturbances, since the one-component Fourier mode method cannot benefit from a potential energy transfer from one velocity component to the other.

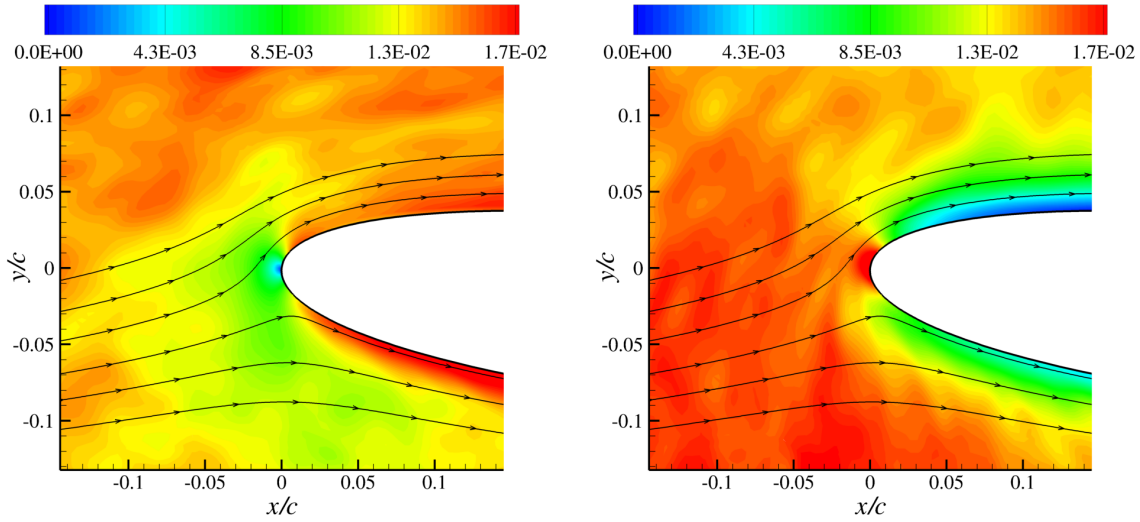

(a) Contours of $u'_{x,rms}/U_\infty$.

(b) Contours of $u'_{y,rms}/U_\infty$.

Figure 3.15: Contours of turbulence intensity and mean flow streamlines around a NACA 0012 aerofoil at $M_\infty = 0.3$ and $AoA = 6^o$. Turbulence intensities were calculated from 500 independent samples of fluctuating velocity fields using the advanced digital filter method.

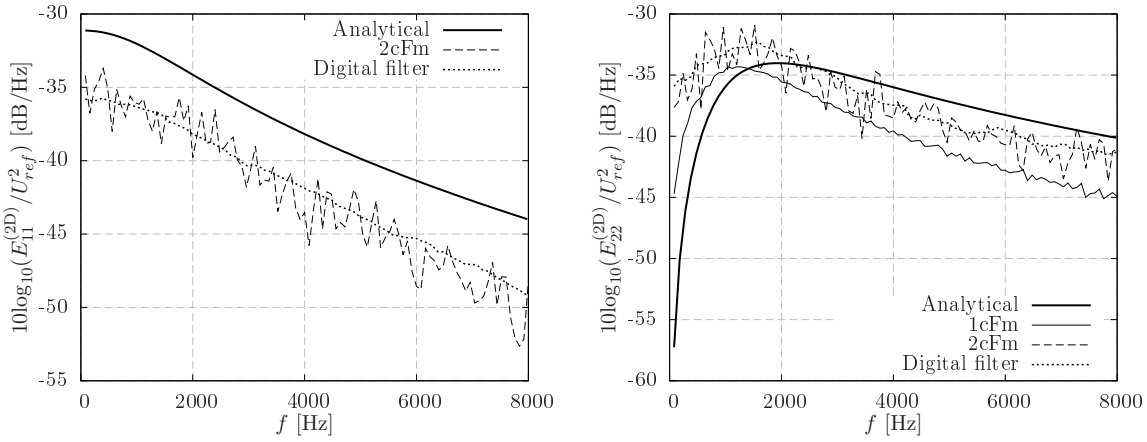

(a) Streamwise, $U_{ref} = 1$ m/s.

(b) Transverse, $U_{ref} = 1$ m/s.

Figure 3.16: One-dimensional spectra $0.02c$ upstream of the leading edge of a NACA 0012 aerofoil at $M_\infty = 0.3$ and $AoA = 6^o$.

3.3.2 Near-Field Noise

Contours of root-mean-square fluctuating pressure for a NACA 0012 aerofoil at $AoA = 6^o$ are shown in Figure 3.17. The angle of attack breaks down the symmetry in the noise radiation that was found for the $AoA = 0^o$ configuration. The noise radiates now from a single location that is placed on the suction side of the leading edge, as anticipated by Gill for harmonic gusts [98]. This contrasts with the NACA 0012 aerofoil at $AoA = 0^o$, where a maximum $p'_{rms}/\rho_\infty c_\infty^2$ was found on each side of the leading edge. Although the noise source concentrates on the suction side of the leading edge, lines of iso-contours indicate that noise radiated from the pressure side is larger in the near-field. Thus, far-field observers below the aerofoil are expected to be louder than those above the aerofoil.

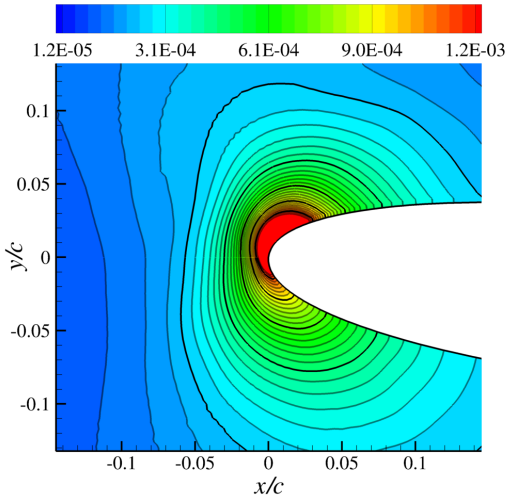

Figure 3.17: Contours of $p'_{rms}/\rho_\infty c_\infty^2$ around a NACA 0012 aerofoil at $M_\infty = 0.3$ and $AoA = 6^o$. Contour levels were calculated from 500 independent samples of fluctuating pressure fields using the advanced digital filter method.

The frequency content of the unsteady pressure on the aerofoil surface is analysed in Figure 3.18. The maximum $p'_{rms}/\rho_\infty c_\infty^2$ is still caused by fluctuating pressure in the leading edge region at low frequencies. However, there are some differences between pressure and suction sides. Close to the leading edge ($x/c < 0.3$), the suction side exhibits larger SPL at high frequencies ($fc/U_\infty > 6$). However, the SPL is larger on the pressure side for medium and low frequencies ($fc/U_\infty < 6$) along the aerofoil chord.

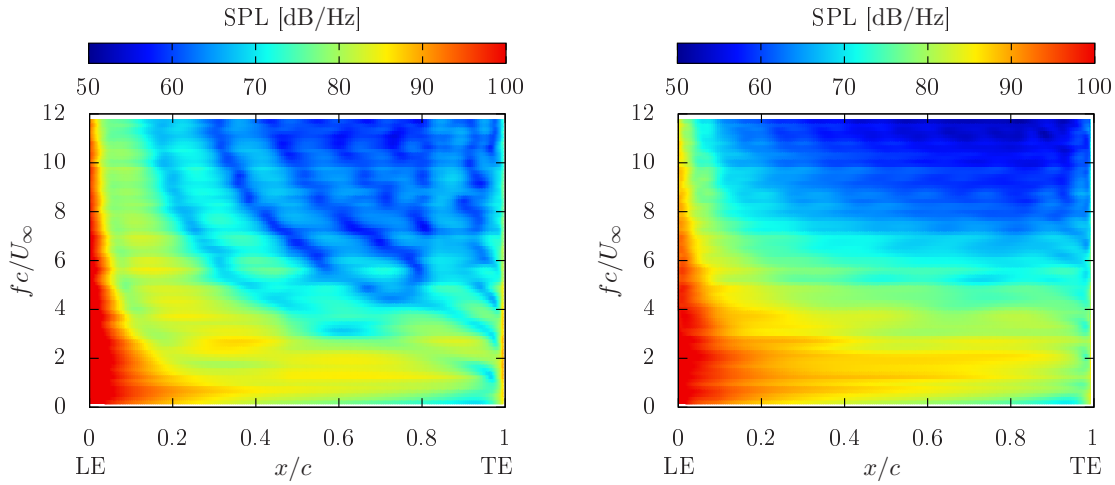

(a) Suction side.

(b) Pressure side.

Figure 3.18: SPL spectra on the surface of a NACA 0012 aerofoil at $M_\infty = 0.3$ and $AoA = 6^o$. Leading Edge (LE) and Trailing Edge (TE) correspond to $x/c = 0$ and $x/c = 1$, respectively.

3.3.3 Far-Field Noise

Figure 3.19 shows the PWL spectra from various synthetic turbulence methods. Both the advanced digital filter method and the two-component Fourier mode approach produce noise levels within 2 dB for most frequencies. This result confirms that CAA noise predictions are independent of the synthetic turbulence method employed, provided that both streamwise and transverse velocity components are included in the analysis. Consequently, the choice of a synthetic turbulence method relies on the computational expense, which is discussed in Section 3.4. The one-component Fourier mode approach under-predicts the PWL by more than 5 dB for frequencies above 4000 Hz in comparison with synthetic turbulence methods that include two fluctuating velocity components. As discussed by Gill *et al.* [41], this under-prediction of the noise levels is due to the lack of positive skewed gusts in the one-component Fourier mode method (modes with $k_y > 0$), which generate an increased gust response for aerofoils at $AoA > 0^o$. Furthermore, the under-prediction of the noise levels also agrees with the rapid decay of the transverse turbulence spectrum at high frequencies (see Figure 3.16b).

The PWL spectrum from the $AoA = 0^o$ configuration using the advanced digital filter method is also included in Figure 3.19 to highlight the small effect of the angle of attack, as found in previous experimental studies by Moreau *et al.* [72] and Devenport *et al.* [78], among others. Although the examination of the near-field unsteady field showed significant differences between aerofoils at $AoA = 0^o$ and 6^o, these differences are not translated into noticeable variations in the PWL spectra. It should be noted that the integral length scale-to-chord ratio is $\Lambda/c = 0.053$ in the present CAA

simulations, which is significantly below the threshold proposed by Hutcheson *et al.* [84] at which the effects of angle of attack on the noise could be relevant ($\Lambda/c \geq 1$).

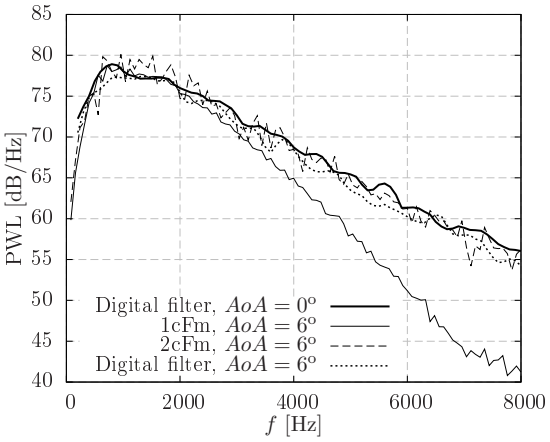

Figure 3.19: PWL spectra for a NACA 0012 aerofoil at $M_\infty = 0.3$ and $AoA = 6^o$.

Directivity plots of a NACA 0012 aerofoil at $AoA = 6^o$ are shown in Figure 3.20 at two different frequencies. The one-component Fourier mode method predicts the position of lobes correctly at 2000 Hz, with an under-prediction of about 5 dB at upstream observers. However, noise levels and directivity patterns at 8000 Hz are not correctly predicted. This result highlights the importance of the streamwise velocity fluctuations when predicting broadband noise from aerofoils at non-zero angle of attack. Additionally, synthetic turbulence methods with two fluctuating velocity components predict similar directivity plots.

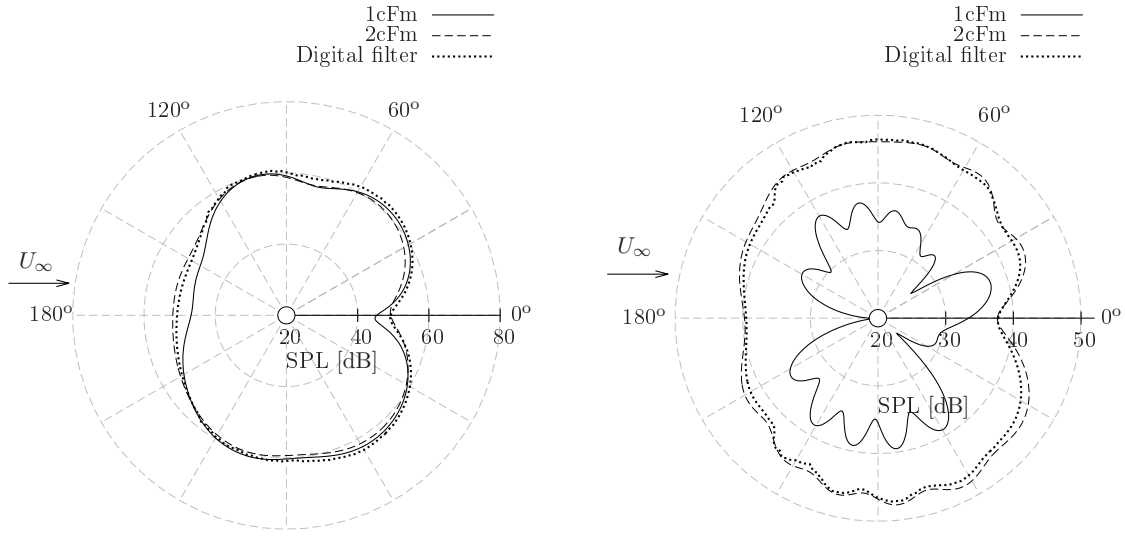

(a) $f = 2000$ Hz ($fc/U_\infty \approx 2.94$). (b) $f = 6000$ Hz ($fc/U_\infty \approx 8.82$).

Figure 3.20: Directivity plots for a NACA 0012 aerofoil at $M_\infty = 0.3$ and $AoA = 6^o$.

Although the PWL spectra are weakly affected by a moderate variation in angle of attack, directivity plots show some differences. For example, noise levels are slightly larger below the aerofoil, with an increase of up to 3 dB at some observer angles, in comparison with noise levels above the aerofoil for the frequencies examined.

3.4 Computational Expense

A comparison in terms of computational time from the different methods to synthesise turbulence is presented in this section. Since the conclusions of this comparison are similar for all the aerofoil configurations analysed, only data for the NACA 0012 aerofoil at $M_\infty = 0.3$ and $AoA = 0^o$ are presented. Table 3.1 shows the relative expense of the different methods. The same CAA mesh and number of processors were used for the simulations of the different synthetic turbulence methods. The number of time steps include both transitory state and data collection process.

The relative comparison shows that the one-component Fourier mode approach is the fastest approach, followed by the advanced digital filter method, which is 4.8 times slower in total. However, a single time step can be run faster with the advanced digital filter method. The difference in the total computational time arises from the total number of time steps that are required to obtain accurate noise predictions. The digital filter method, which produces a non-periodic turbulent inflow, requires a larger number of fluctuating velocity and pressure samples in order for the turbulence and noise spectra to converge. The transitory state in the advanced digital filter method lasts until the first set of eddies introduced within the CAA domain is convected past the aerofoil, which represents about 1.5 % of the total computational time.

	Time per time step [s]	No. time steps	Total expense [s]	Relative expense
1cFm	4.541×10^{-2}	84998	3860	1.0
2cFm	8.556×10^{-2}	849980	72721	18.8
Digital filter	4.177×10^{-2}	439657	18362	4.8

Table 3.1: Comparison of computational expense for a NACA 0012 aerofoil at $M_\infty = 0.3$ and $AoA = 0^o$. The CAA mesh has 821,010 grid points and 96 cores were used for all the simulations.

The two-component Fourier mode approach is the slowest method among those presented in this work. This is caused by two aspects. Firstly, the total number of Fourier modes in these simulations is $N \times 2M = 2000$, whereas only $N = 100$ modes are required for the one-component Fourier mode method. Secondly, 10 independent simulations were used to obtain converged noise results that are within 3 dB accuracy, and a transitory state has to be considered for each of them. In the simulations

using Fourier mode methods, the transitory state corresponds to the frozen propagation of the synthetic turbulence over a distance of $\lambda_{x,max}$. Then, each simulation was run for another whole period of the largest wavenumber involved, to collect the required unsteady data for the velocity and noise spectra calculations. Therefore, the transitory state represents 50% of the total computational time.

From the numerical results in Sections 3.2 and 3.3, it is concluded that similar noise predictions can be obtained from digital filter and Fourier mode methods, provided that both the streamwise and transverse velocity fluctuations are included in the simulation. Nevertheless, the digital filter method presents the best compromise to obtain accurate leading edge noise predictions, independently of the aerofoil configuration, in a reasonable computational time. This is because leading edge noise predictions using the advanced digital filter method are approximately 3.9 times faster than the two-component Fourier mode method.

Although a fair comparison has been presented in this section, variations in the numerical implementation, number of samples collected for the spectral analysis, number of modes included in Fourier mode simulations, number of realisations used to average results in the two-component Fourier mode method, and the transitory state, among others, could lead to changes in the computational cost.

3.5 Summary

In this chapter, two-dimensional leading edge noise predictions from the advanced digital filter method are compared to those provided by one- and two-component Fourier mode approaches. Various aerofoil configurations have been analysed, including variations in aerofoil thickness (NACA 0006 and NACA 0012 aerofoils), freestream Mach number ($M_\infty = 0.3$ and 0.6), and angle of attack ($AoA = 0^o$ and 6^o). The mean flow used for the LEEs was obtained from inviscid CFD simulations. In order to improve current understanding of leading edge noise, the unsteady flow in the leading edge region has been examined for the various configurations. Furthermore, the distorted turbulence spectra and unsteady pressure response on the aerofoil surface have been discussed in detail here. The main findings are summarised as follows:

- Distortions in the turbulent structures around an aerofoil begin at approximately $0.02c$ upstream of the leading edge, where initial distortions in the velocity spectra can be appreciated. This distance is of the order of magnitude of the leading edge radius for a NACA 0012 aerofoil, as anticipated by Santana *et al.* [73]. Therefore, the turbulence injection plane of the advanced digital filter method can be located r_e upstream of the aerofoil leading edge in practical cases.

- Turbulent structures have been examined in the stagnation region of thick aerofoils. In the streamwise direction, the turbulence intensity $u'_{x,rms}/U_\infty$ is damped, and the one-dimensional

spectrum $E_{11}^{(2D)}$ shows a uniform decay at all frequencies, with almost no change in shape. In the transverse direction, the turbulence intensity $u'_{y,rms}/U_\infty$ is significantly increased, and the one-dimensional spectrum $E_{22}^{(2D)}$ increases at low frequencies and decreases at high frequencies.

- The distortion of $E_{22}^{(2D)}$ in CAA simulations closely follows the trends and levels predicted by a modified von Kármán spectrum using rapid distortion theory.

- The distortion of the turbulence spectra in the leading edge region is weakly influenced by the freestream Mach number when plotted against chord-based reduced frequency, fc/U_∞. Furthermore, the distortion of the turbulence spectra mainly depends on the aerofoil geometry.

- Aerofoils at zero and non-zero angle of attack present similar distortions of the turbulence spectra in the leading edge region. This justifies the small effect of the angle of attack on leading edge noise.

- The coherence between distorted turbulent structures and unsteady pressure on the aerofoil surface has been investigated. For a thick aerofoil at zero angle of attack, the streamwise velocity fluctuations are the main contributors to the unsteady pressure at the stagnation point. However, the maximum p'_{rms} is mainly related to the transverse velocity fluctuations, as occurs for flat plates.

- The spectral analysis of the unsteady pressure response on the surface of NACA 0006 and NACA 0012 aerofoils indicates that the increase in p'_{rms} in the leading edge region is primarily caused by low frequencies. Additionally, the unsteady pressure response of high frequencies is weaker for the thicker aerofoil, which explains the far-field noise reduction at high frequencies due to aerofoil thickness.

- For a given NACA aerofoil, the $\Delta\text{PWL} = \text{PWL}\,|_{\text{flat plate}} - \text{PWL}|_{\text{NACA aerofoil}}$ spectrum scales linearly with the chord-based reduced frequency, fc/U_∞, for moderate and high Mach numbers. Furthermore, a good collapse onto a single trend has been found when plotting ΔPWL against thickness-based reduced frequency for $ft_A/U_\infty \leq 0.6$. These results provide further evidence of noise reduction scaling with the aerofoil thickness and the freestream speed (or Mach number), as recently discussed in numerical and experimental works [87, 98]. Additionally, a best fit line has been calculated to estimate ΔPWL as a function of ft_A/U_∞ using the least squares method.

- The one-component Fourier mode approach is the simplest and fastest synthetic turbulence method of those tested, and produces satisfactory noise predictions for symmetric aerofoils with moderate thickness ($t_A/c = 0.06$) at zero angle of attack. However, either the advanced digital filter method or the two-component Fourier mode approach is required when considering thick aerofoils ($t_A/c \geq 0.12$) and non-zero angle of attack.

- Similar predictions of leading edge noise can be obtained by using different synthetic turbulence methods, provided that both the transverse and the streamwise velocity fluctuations are included. However, two-dimensional simulations using the advanced digital filter method are about 3.9 times faster than the two-component Fourier mode method, and therefore, give enhanced computational performance.

Chapter 4

Numerical Predictions of Open-Jet Wind Tunnel Experiments

The aim of the present chapter is to develop a numerical methodology that is able to reproduce leading edge noise predictions from various aerofoil configurations and open-jet wind tunnel facilities. When studying aerofoils with large thickness ($t_A/c = 0.12$) or placed at incidence ($AoA = 6^{\circ}$) in Chapter 3, the advanced digital filter method was found to be advantageous over Fourier mode methods in terms of computational cost and simulation accuracy. However, numerical simulations were restricted to purely two-dimensional turbulence. Although this type of turbulence has extensively been used in a number of works [60, 61, 62], it cannot be employed to reproduce experimental noise measurements without applying some correction factors [57]. This is because the governing equations of purely two-dimensional turbulence differ from those of fully three-dimensional turbulence (see Chapter 10 in the work of Davidson [149]). Therefore, a turbulence spectrum correction needs to be applied to account for the shape of the three-dimensional velocity spectra. Additionally, the acoustic power decays as $1/r_0^2$ in a three-dimensional free field, whereas it decays as $1/r_0$ in case of a two-dimensional free field [57, 96].

In this chapter, two different approaches are proposed to perform numerical leading edge noise predictions that can be compared with experimental measurements. Firstly, the advanced digital filter method is extended to generate fully three-dimensional turbulence in Section 4.1. Then, the advanced digital filter method is adapted in Section 4.2 to realise a two-dimensional turbulent flow with the key statistics of three-dimensional turbulence. In Section 4.3, both numerical approaches are compared with leading edge noise measurements of a NACA 0012 aerofoil tested by Paterson and Amiet [79]. An experiment by Chaitanya *et al.* [87] is used in Section 4.4 to reproduce leading edge noise predictions from aerofoils with thickness ranging from $t_A/c = 0.06$ to 0.24. Finally, Section 4.5 includes

numerical simulations of a cambered NACA 65(12)-10 aerofoil at various angles of attack to reproduce experimental results from Fundamental Case 1 in the Fan Stage Broadband Noise Benchmarking Programme [97].

4.1 Three-Dimensional Advanced Digital Filter Method

This section presents an extension of the advanced digital filter method to produce fully three-dimensional isotropic turbulence. The resulting turbulent flow preserves the main characteristics of the two-dimensional version (see Section 2.2), such as being divergence-free, non-periodic, and containing broadband spectra. Realistic turbulence is useful when studying more generic cases in which three-dimensional effects are important, such as wavy leading edge aerofoils and aerofoils with taper or sweep.

4.1.1 Gaussian Energy Spectra

Following a similar development as described in Section 2.2.1, the three-dimensional energy spectrum is linked to the spatial filter in wavenumber space through (see Equation A.50 in Appendix A)

$$E^{(3D)}(k) = 32\pi^4 k^4 \hat{G}(k)^2, \tag{4.1}$$

where $k = \sqrt{k_x^2 + k_y^2 + k_z^2}$, and the isotropic Gaussian energy spectrum for a three-dimensional turbulent flow is defined, according to Kraichnan [24], as

$$E^{(3D)}(k) = \frac{4}{\pi^3} u_{rms}'^2 \Lambda^5 k^4 \exp\left(-\frac{\Lambda^2 k^2}{\pi}\right). \tag{4.2}$$

Introducing Equation 4.2 into Equation 4.1, the spatial filter in wavenumber space to realise a Gaussian energy spectrum takes the form

$$\hat{G}(k) = \sqrt{\frac{u_{rms}'^2 \Lambda^5}{8\pi^7}} \exp\left(-\frac{\Lambda^2 k^2}{2\pi}\right). \tag{4.3}$$

Taking the inverse Fourier transform of Equation 4.3, the three-dimensional spatial filter in physical space is given by

$$G(r_p) = \sqrt{\frac{u_{rms}'^2}{\pi\Lambda}} \exp\left(-\frac{\pi r_p^2}{2\Lambda^2}\right), \tag{4.4}$$

where $r_p = \sqrt{(x-x_p)^2 + (y-y_p)^2 + (z-z_p)^2}$ is the distance between a point in the flow field, (x, y, z), and the eddy centre, (x_p, y_p, z_p). When dealing with three components of the fluctuating velocity field, the RPM method [52] requires the filtering of three statistically independent white noise signals (see Equation 2.6), whose variances are

$$\left\langle \mathcal{U}_{i,p}^2 \right\rangle = \int_{V_{s,p}} \langle \mathcal{U}_i(\mathbf{x}_s, t) \mathcal{U}_i(\mathbf{x}_s, t) \rangle \, \mathrm{d}\mathbf{x}_s = \Delta_e^3,$$

for $i = 1, 2, 3$. Therefore, each $\mathcal{U}_{i,p}$ follows a normal distribution with zero mean and standard deviation $\Delta_e^{3/2}$. The direction of rotation of the pth eddy is now defined by three random numbers $\epsilon_{i,p}$ for $i = 1, 2, 3$, each of them randomly taking ± 1. This represents an advantage in comparison with the synthetic eddy method proposed by Kim and Haeri [48], in which 8 independent random numbers are required to compute each eddy.

The three-dimensional velocity field introduced by each Gaussian eddy takes the form

$$u'_{x,p}(\mathbf{x}) = \sqrt{\pi}\Delta_e^{3/2} \left[\epsilon_{2,p} \left(z - z_p \right) - \epsilon_{3,p} \left(y - y_p \right) \right] \frac{u'_{rms}}{\Lambda^{5/2}} \exp\left(-\frac{\pi r_p^2}{2\Lambda^2} \right), \tag{4.5a}$$

$$u'_{y,p}(\mathbf{x}) = \sqrt{\pi}\Delta_e^{3/2} \left[\epsilon_{3,p} \left(x - x_p \right) - \epsilon_{1,p} \left(z - z_p \right) \right] \frac{u'_{rms}}{\Lambda^{5/2}} \exp\left(-\frac{\pi r_p^2}{2\Lambda^2} \right), \tag{4.5b}$$

$$u'_{z,p}(\mathbf{x}) = \sqrt{\pi}\Delta_e^{3/2} \left[\epsilon_{1,p} \left(y - y_p \right) - \epsilon_{2,p} \left(x - x_p \right) \right] \frac{u'_{rms}}{\Lambda^{5/2}} \exp\left(-\frac{\pi r_p^2}{2\Lambda^2} \right). \tag{4.5c}$$

Figure 4.1a shows contours of fluctuating velocity magnitude from three-dimensional Gaussian eddies. A number of these eddies can be combined to realise isotropic turbulence that follows the three-dimensional Gaussian energy spectrum defined by Equation 4.2. To this end, the injection plane is extended in the z-direction, where eddies are injected with a uniform spacing of Δ_e along a distance of at least $2r_e$, as shown in Figure 4.1b. The normalised radius of a three-dimensional Gaussian eddy, r_e/Λ, is approximately the same as a two-dimensional Gaussian eddy. This is because the exponential terms in the equations that define the length of two- and three-dimensional eddies are similar. Consequently, the limiting values that are given in Appendix B remain valid, and the correct turbulence statistics are obtained provided that $r_e \geq 3\Lambda/2$ and $\Delta_e \leq \Lambda/2$.

For validation purposes, a cuboid-shaped CAA mesh has been designed to propagate vortical disturbances for frequencies up to 10 kHz. The mean flow is uniform at $M_\infty = 0.3$, and the parameters that define the Gaussian energy spectrum are $u'_{rms}/U_\infty = 0.017$ and $\Lambda = 0.008$ m. Figure 4.2 shows one-dimensional spectra from a monitor point downstream of the injection plane. Numerical results are in good agreement with the analytical expressions, since the averaged error is lower than 1.5 dB.

This validates the advanced digital filter method to generate fully three-dimensional synthetic turbulence.

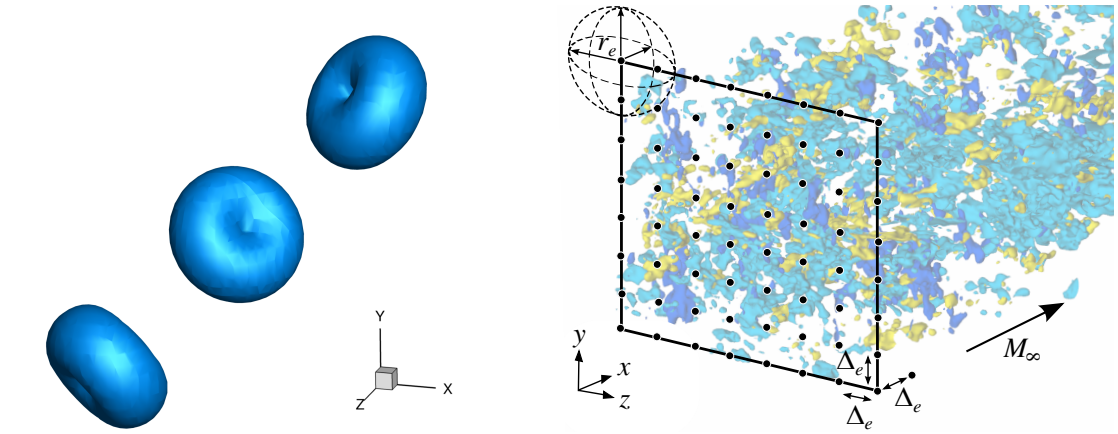

(a) Iso-contours of fluctuating velocity magnitude in single Gaussian eddies.

(b) Turbulence injection plane.

Figure 4.1: Implementation of three-dimensional advanced digital filter method.

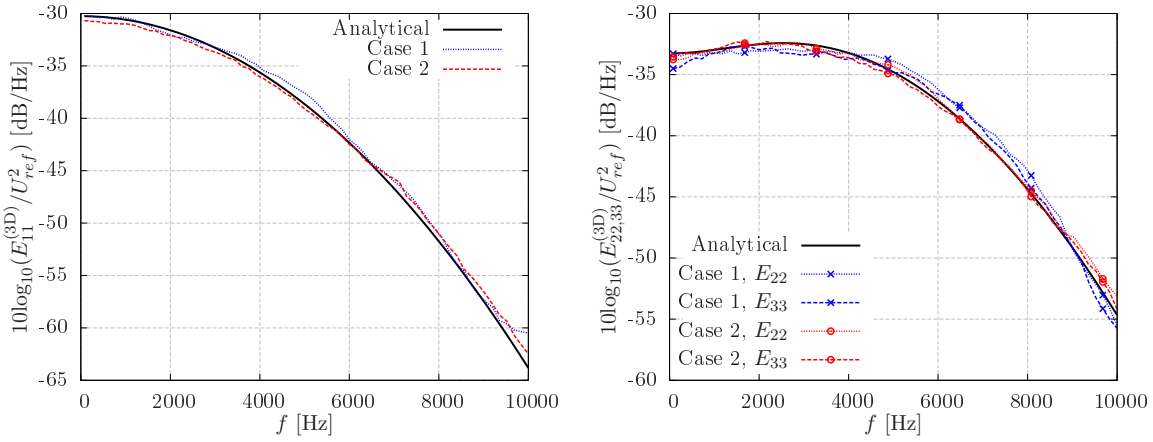

(a) Streamwise, $U_{ref} = 1$ m/s.

(b) Transverse and spanwise, $U_{ref} = 1$ m/s.

Figure 4.2: One-dimensional Gaussian spectra of three-dimensional turbulence with $M_\infty = 0.3$, $u'_{rms}/U_\infty = 0.017$, and $\Lambda = 0.008$ m. *Case 1* corresponds to $r_e = 3\Lambda/2$ and $\Delta_e = \Lambda/2$, and *Case 2* corresponds to $r_e = 5\Lambda/2$ and $\Delta_e = \Lambda/6$.

4.1.2 Non-Gaussian Energy Spectrum through Gaussian Superposition

A target non-Gaussian energy spectrum can be achieved by defining a new eddy profile from the superposition of several Gaussian eddies. Using Equation 4.1, the energy spectrum from a summation

of Gaussian filters is given by

$$E_{sum}^{(3D)}(k) = 32\pi^4 k^4 \left[\sum_{i=1}^{N_e} \hat{G}_i(\Lambda_i, u'_{rms,i}, k) \right]^2 . \tag{4.6}$$

Introducing Equation 4.3 for the spatial filter of each Gaussian eddy into Equation 4.6, the resulting energy spectrum is

$$E_{sum}^{(3D)}(k) = \frac{4k^4}{\pi^3} \sum_{i=1}^{N_e} \sum_{j=1}^{N_e} \sqrt{u'^2_{rms,i} u'^2_{rms,j} \Lambda_i^5 \Lambda_j^5} \exp\left[-\frac{k^2}{2\pi} \left(\Lambda_i^2 + \Lambda_j^2 \right) \right]. \tag{4.7}$$

In this case, the fluctuating velocity field introduced by the pth eddy from the Gaussian superposition takes the form

$$u'_{x,p}(\mathbf{x}) = \sqrt{\pi} \Delta_e^{3/2} \left[\epsilon_{2,p} \left(z - z_p \right) - \epsilon_{3,p} \left(y - y_p \right) \right] \sum_{i=1}^{N_e} \frac{u'_{rms,i}}{\Lambda_i^{5/2}} \exp\left(-\frac{\pi r_p^2}{2\Lambda_i^2} \right), \tag{4.8a}$$

$$u'_{y,p}(\mathbf{x}) = \sqrt{\pi} \Delta_e^{3/2} \left[\epsilon_{3,p} \left(x - x_p \right) - \epsilon_{1,p} \left(z - z_p \right) \right] \sum_{i=1}^{N_e} \frac{u'_{rms,i}}{\Lambda_i^{5/2}} \exp\left(-\frac{\pi r_p^2}{2\Lambda_i^2} \right), \tag{4.8b}$$

$$u'_{z,p}(\mathbf{x}) = \sqrt{\pi} \Delta_e^{3/2} \left[\epsilon_{1,p} \left(y - y_p \right) - \epsilon_{2,p} \left(x - x_p \right) \right] \sum_{i=1}^{N_e} \frac{u'_{rms,i}}{\Lambda_i^{5/2}} \exp\left(-\frac{\pi r_p^2}{2\Lambda_i^2} \right). \tag{4.8c}$$

The set of parameters $u'_{rms,i}$ and Λ_i for $i = 1, ..., N_e$ in Equation 4.7 are obtained by following a similar optimisation process as described in Section 2.2.2, with $k'_i = \sqrt{2\pi/\Lambda_i^2}$. This corresponds to the wavenumber of maximum energy in the Gaussian energy spectrum defined by Equation 4.2. As the new eddy profile is obtained from a superposition of Gaussian eddies, the limiting values to reproduce the desired statistical properties of a turbulent flow are $r_e \geq 3 \max\{\Lambda_i\}/2$ and $\Delta_e \leq \min\{\Lambda_i\}/2$.

The method is validated to reproduce the three-dimensional von Kármán spectrum, which is defined as

$$E^{(3D)}(k) = \frac{55 u'^2_{rms} \Lambda}{9\pi} \frac{\left(\frac{k}{k_c} \right)^4}{\left[1 + \left(\frac{k}{k_c} \right)^2 \right]^{17/6}}. \tag{4.9}$$

Proposed parameters for the three-dimensional Gaussian superposition are given in Table 4.1, which aims to reproduce the von Kármán spectrum with $M_\infty = 0.3$, $u'_{rms}/U_\infty = 0.017$ and $\Lambda = 0.008\,\text{m}$. It should be noted that only 10 parameters are required to reproduce the three-dimensional von Kármán spectrum if $N_e = 5$. A larger number of constraint parameters is normally required in synthetic eddy methods due to the use of different eddy profiles, among others. For example, 15 constraint parameters

are to be optimised in the synthetic eddy method of Kim and Haeri [48] to reproduce a similar turbulent flow. Figure 4.3 shows numerical and analytical one-dimensional spectra for the three-dimensional Gaussian superposition. An agreement to within 1 dB accuracy of analytical predictions is shown for a case with $r_e = 3\max\{\Lambda_i\}/2$ and $\Delta_e = \min\{\Lambda_i\}/2$, according to the parameters given in Table 4.1.

ith Gaussian eddy	Λ_i [m]	$u'^2_{rms,i}$ [m^2/s^2]
1	3.798×10^{-2}	1.111×10^{-2}
2	2.218×10^{-2}	1.246×10^{-1}
3	1.217×10^{-2}	2.730×10^{-1}
4	6.251×10^{-3}	3.135×10^{-1}
5	2.639×10^{-3}	4.567×10^{-1}

Table 4.1: Parameters for Gaussian superposition to obtain the three-dimensional von Kármán spectrum with $M_\infty = 0.3$, $u'_{rms}/U_\infty = 0.017$, and $\Lambda = 0.008$ m.

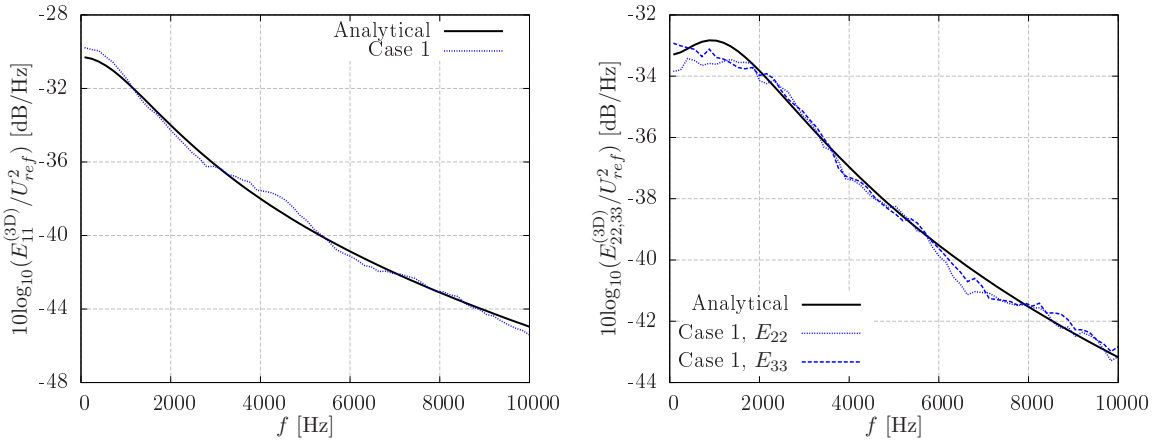

(a) Streamwise, $U_{ref} = 1$ m/s.

(b) Transverse and spanwise, $U_{ref} = 1$ m/s.

Figure 4.3: One-dimensional von Kármán spectra of three-dimensional turbulence with $M_\infty = 0.3$, $u'_{rms}/U_\infty = 0.017$, and $\Lambda = 0.008$ m. *Case 1* corresponds to $r_e = 3\max\{\Lambda_i\}/2$ and $\Delta_e = \min\{\Lambda_i\}/2$, where the values for Λ_i are given in Table 4.1.

4.2 Pseudo Three-Dimensional Turbulence

Fully three-dimensional CAA simulations are more expensive than two-dimensional CAA simulations from a computational perspective. This is due to an increased number of grid points in the CAA domain and the additional momentum equation in the LEEs that must be solved, among oth-

ers. This section presents an alternative low-cost approach that involves CAA simulations using two-dimensional synthetic turbulence with the key statistics of three-dimensional turbulence. This type of turbulence is referred to as 'pseudo three-dimensional turbulence' in this work. Then, unsteady data from the two-dimensional CAA simulation is combined with a three-dimensional FW-H solver for the far-field noise radiation.

In previous CAA studies of leading edge noise, simulations using purely two-dimensional turbulence applied some correction factors to compare numerical results with experimental measurements [97, 127]. For example, Dieste [127] found the correction factor for flat plates by comparing the two-dimensional pressure spectral density in the far-field, as given by Equation 2.31, and its three-dimensional version derived by Amiet [39]

$$S_{pp}^{(3D)}(r_0, \theta, \omega) = \frac{\pi \rho_\infty^2 b^2 d \sin^2\theta U_\infty \kappa_0^2}{r_0^2 A(\theta, M_\infty)^4} |\mathcal{L}(\theta, k_x)|^2 \, \Phi_{22}^{(3D)}(k_x, k_z = 0), \tag{4.10}$$

where d is the aerofoil semi-span, and $\Phi_{22}^{(3D)}(k_x, k_z = 0)$ is the three-dimensional velocity spectrum of the upwash disturbances with the spanwise wavenumber set to zero, $k_z = 0$. Thus, the correction term for flat plates takes the form

$$S_{pp}^{(3D)} = \frac{M_\infty k_x 2d}{r_0 \sqrt{1 - M_\infty^2 \sin^2\theta}} \frac{\Phi_{22}^{(3D)}(k_x, k_z = 0)}{\Phi_{22}^{(2D)}(k_x)} S_{pp}^{(2D)}. \tag{4.11}$$

Such a correction factor includes two different terms to amend $S_{pp}^{(2D)}$. The first fraction on the right hand side corresponds to a correction factor to account for the three-dimensional decay of sound and the aerofoil span. The second fraction on the right hand side is a correction factor for the transverse velocity spectrum. However, Equation 4.11 is inaccurate for thick aerofoils interacting with synthetic turbulence methods with two or three velocity components, since only the upwash velocity spectrum is included. This justifies the need for the numerical methodology presented in this section.

4.2.1 Numerical Methodology

The numerical methodology that is presented in this section produces accurate noise predictions at a reduced computational cost that can be compared with experimental measurements without applying correction factors for the shape of the velocity spectra and the far-field noise propagation.

According to the analytical model of Amiet [39], far-field noise at the mid-span plane is only affected by the upwash velocity spectrum with the spanwise wavenumber $k_z = 0$ (see Equation 4.10), if the span is much larger than the integral length scale. This assumption was employed by authors

such as Clair *et al.* [38] and Gill *et al.* [41] when using synthetic turbulence based on Fourier modes. The amplitude of each mode is proportional to the square root of the velocity or energy spectrum in Fourier mode methods, which makes it straightforward to set $k_z = 0$. In this case, Clair *et al.* [38] reported that a constant spanwise wavenumber step $\Delta k_z = \pi/d$ was necessary to recover the correct amplitude of the pressure spectral density. This section shows that the $k_z = 0$ assumption can also be made when using digital filter methods, provided that an amplitude scaling factor of π/d is applied to the pressure spectral density at all frequencies.

For two-dimensional isotropic turbulence, introducing Equation 2.16 into Equation 2.15, the one-dimensional spectrum of the transverse velocity fluctuations can be written as

$$E_{22}^{(2D)}(k_x) = 2\int_{-\infty}^{\infty} \frac{E^{(2D)}}{\pi k}\left(1 - \frac{k_y^2}{k^2}\right) \mathrm{d}k_y. \tag{4.12}$$

Similarly, for three-dimensional isotropic turbulence and assuming $k_z = 0$, $E_{22}^{(3D)}$ can be expressed as

$$E_{22}^{(3D)}(k_x, k_z = 0) = 2\int_{-\infty}^{\infty} \frac{E^{(3D)}}{4\pi k^2}\left(1 - \frac{k_y^2}{k^2}\right) \mathrm{d}k_y. \tag{4.13}$$

It is inferred from Equations 4.12 and 4.13 that if $E^{(2D)}$ takes the form of $E^{(3D)}/(4k)$, the resulting two-dimensional velocity spectra, $\Phi_{22}^{(2D)}(k_x, k_y)$, will follow the shape of $\Phi_{22}^{(3D)}(k_x, k_y, k_z = 0)$. The same reasoning applies to the streamwise fluctuating velocity component. Consequently, it is possible to realise a two-dimensional turbulent flow with the key statistics of the three-dimensional turbulence through a Gaussian superposition. To this end, $E_{sum}^{(2D)}$ in Equation 2.20 is set to reproduce $E^{(3D)}/(4k)$.

The pseudo three-dimensional turbulence is injected into a two-dimensional CAA domain, where unsteady data are collected on the aerofoil surface. Then, a three-dimensional aerofoil (or wing) with straight leading edge is generated by copying the unsteady data repeatedly in the spanwise direction over the full span. The configuration is shown in Figure 4.4.

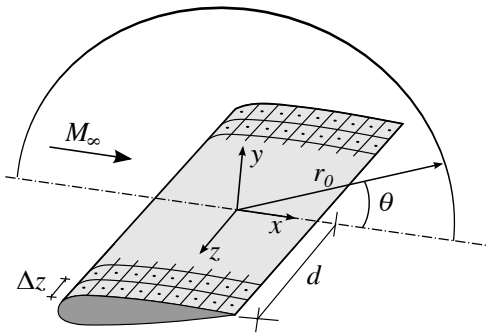

Figure 4.4: FW-H surface and far-field observer location.

By using a FW-H solver, the fluctuating pressure is radiated in a three-dimensional free field. It should be noted that all panels in the spanwise direction contain the same information, and are therefore radiating in phase. This assumption is suitable for aerofoils with straight leading edge since there is only one mode in the spanwise direction that affects the noise perceived by an observer at the mid-span plane in the far-field ($k_z = 0$). Furthermore, if the distance between two consecutive panels in the spanwise direction is much smaller than the distance to the far-field observer, the retarded time is approximately the same for all panels in the spanwise direction.

4.2.2 Validation Case: Three-Dimensional NACA 0001 Aerofoil

The numerical methodology of pseudo three-dimensional turbulence is validated in this section. To this end, leading edge noise from a NACA 0001 aerofoil is computed numerically and compared to the analytical prediction of Amiet [39], which is given by Equation 4.10. The same CAA mesh as in Section 2.4.3 is used in this validation case. Thus, the aerofoil chord is set to $c = 0.15\,\mathrm{m}$, and the grid resolution is sufficient to solve frequencies up to 8000 Hz in a uniform mean flow at $M_\infty = 0.6$.

The parameters for the Gaussian superposition are found by setting $E^{(2\mathrm{D})}_{sum}$ in Equation 2.20 to follow the shape of $E^{(3\mathrm{D})}/(4k)$ with $k_z = 0$, $u'_{rms}/U_\infty = 0.017$, and $\Lambda = 0.008\,\mathrm{m}$. Proposed parameters are given in Table 4.2.

ith Gaussian eddy	Λ_i [m]	$u'^2_{rms,i}$ [m^2/s^2]
1	3.618×10^{-2}	4.204×10^{-4}
2	2.029×10^{-2}	2.149×10^{-3}
3	1.091×10^{-2}	1.963×10^{-3}
4	5.524×10^{-3}	1.079×10^{-3}
5	2.199×10^{-3}	6.760×10^{-4}

Table 4.2: Parameters for Gaussian superposition to obtain a two-dimensional fluctuating velocity field with the statistics of the three-dimensional von Kármán spectrum, assuming $k_z = 0$ with $M_\infty = 0.6$, $u'_{rms}/U_\infty = 0.017$, and $\Lambda = 0.008\,\mathrm{m}$.

The pseudo three-dimensional turbulence is injected into a two-dimensional CAA domain containing a NACA 0001 aerofoil, and fluctuating velocity samples are collected for the validation of the turbulence statistics. Figure 4.5 illustrates one-dimensional spectra that are calculated near the aerofoil leading edge. A good agreement is found between numerical and analytical spectra, with the largest disagreement being about 1.5 dB.

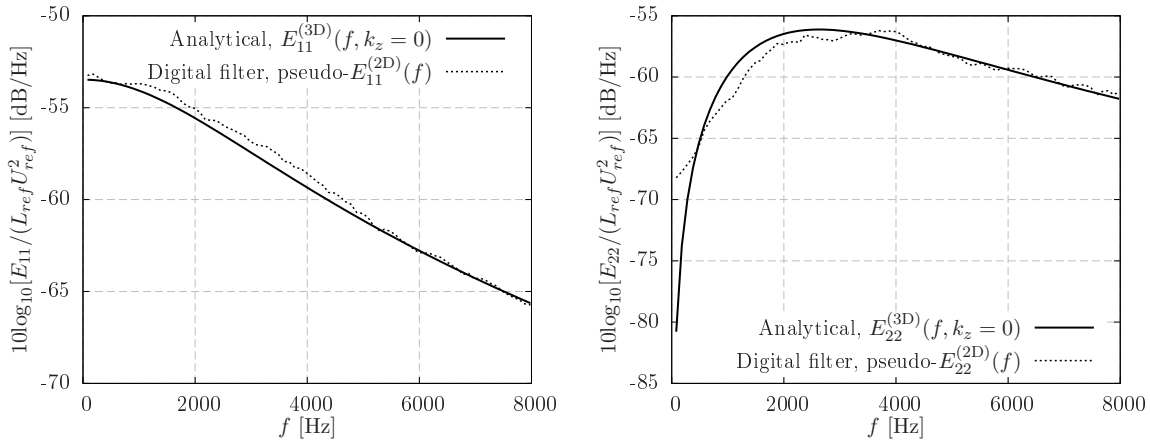

(a) Streamwise. (b) Transverse.

Figure 4.5: Analytical one-dimensional von Kármán spectra of three-dimensional turbulence with $M_\infty = 0.6$, $u'_{rms}/U_\infty = 0.017$, and $\Lambda = 0.008\,\text{m}$, in comparison with the corresponding numerical spectra using pseudo three-dimensional turbulence. Numerical spectra were obtained from a monitor point on the stagnation line, which is placed $0.02c$ upstream of the leading edge of a NACA 0001 aerofoil. The reference length and speed are $L_{ref} = 1\,\text{m}$ and $U_{ref} = 1\,\text{m/s}$, respectively.

Additionally, fluctuating pressure, density, and velocity samples are collected at 540 grid points on the aerofoil surface. Then, unsteady data are copied in the spanwise direction over the full span. Three different spanwise resolutions are tested, $d/\Delta z = 5,\ 15,\ 30$, where Δz is the spanwise length of the each panel in the FW-H solver, as shown in Figure 4.4. The aerofoil semi-span is assumed to be $d = 0.225\,\text{m}$ for the noise computation, which is similar to that of aerofoils tested by Gruber [85] and Chaitanya *et al.* [87] in open-jet wind tunnel experiments.

Figure 4.6a shows PWL and SPL spectra at different observer locations. For the PWL calculation, the sound power from three-dimensional aerofoils is computed in this thesis as

$$\mathcal{P}(\omega) = \frac{dr_0}{\rho_\infty c_\infty} \int_0^{2\pi} S_{pp}(r_0, \theta, \omega) F(\theta, M_\infty) \mathrm{d}\theta. \tag{4.14}$$

An under-prediction of about 2 dB is observed at all frequencies in Figure 4.6a when the spanwise resolution is $d/\Delta z = 5$. Nevertheless, noise results are weakly affected by the tested spanwise resolutions, and $d/\Delta z \geq 15$ is sufficient to generate a well-defined three-dimensional aerofoil with straight leading edge. In these cases, the agreement between analytical and numerical noise levels is better than 1.5 dB. Additionally, Figure 4.6b shows the directivity pattern at 8000 Hz, which corresponds to the highest frequency that has been computed for this validation case. The location and shape of the lobes and the noise levels closely follow those predicted by using the analytical model of Amiet [39].

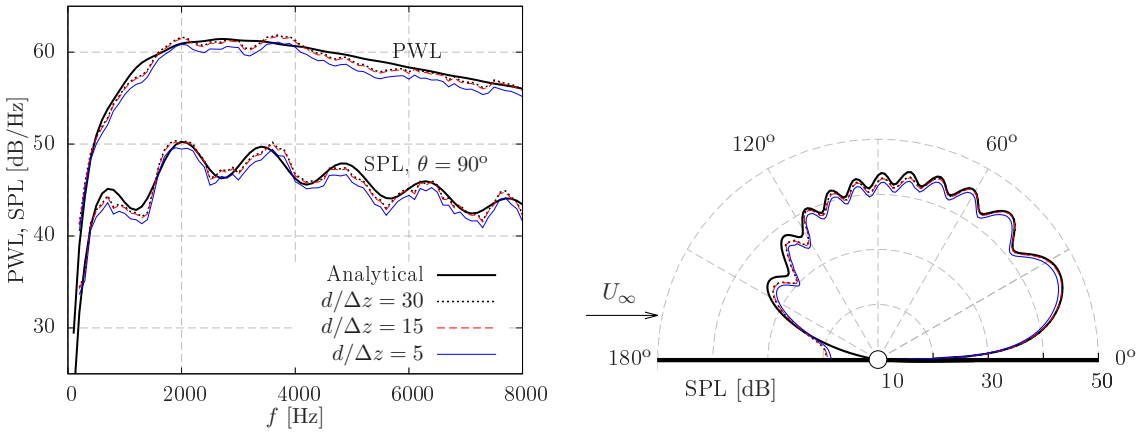

(a) PWL and SPL spectra.

(b) Directivity plot at $f = 8000$ Hz.

Figure 4.6: Noise predictions at $r_0 = 100c$ for a three-dimensional NACA 0001 aerofoil at $M_\infty = 0.6$.

4.3 Simulations of a NACA 0012 Aerofoil at Zero Angle of Attack

In this section, CAA simulations using fully and pseudo three-dimensional turbulence are performed to reproduce the experiment of Paterson and Amiet [79, 150]. The aim is to assess the advantages, limitations, and accuracy of each approach to perform leading edge noise predictions that can be compared with experimental measurements. Although a certain degree of anisotropy was found in the grid-generated turbulence, CAA simulations are performed by using isotropic synthetic turbulence for the comparison with experimental data.

4.3.1 Experimental Setup

Paterson and Amiet [79, 150] performed a series of aerodynamic and acoustic measurements on a NACA 0012 aerofoil at different mean flow speeds and angles of attack. Since the effect of the angle of attack was found to be small (below 2 dB at $AoA = 8^o$), the zero angle of attack configuration has been chosen here for the numerical analysis. The aerofoil chord and span were 0.23 m and 0.53 m, respectively. The experiment was conducted at mean flow speeds of 60 m/s, 90 m/s, and 120 m/s in the test section for frequencies up to 3000 Hz.

The isotropic von Kármán spectrum was found to be in good agreement with hotwire measurements across the test section. Consequently, the turbulence intensity was approximately equal for streamwise and transverse disturbances, which are presented in Table 4.3. Although the turbulence intensity was different for the various jet speeds tested, the integral length scale was nearly 0.03 m in

all cases. A microphone array was placed in the acoustic far-field, outside the jet shear layer, at 2.25 m from the aerofoil centreline in the mid-span plane. Figure 4.7 shows a schematic representation of the experimental setup.

U_∞	u'_{rms}/U_∞	Λ [m]
60 m/s	0.039	0.03
90 m/s	0.048	0.03
120 m/s	0.041	0.03

Table 4.3: Turbulence intensity and integral length scale for various jet speeds in the experiment of Paterson and Amiet [79].

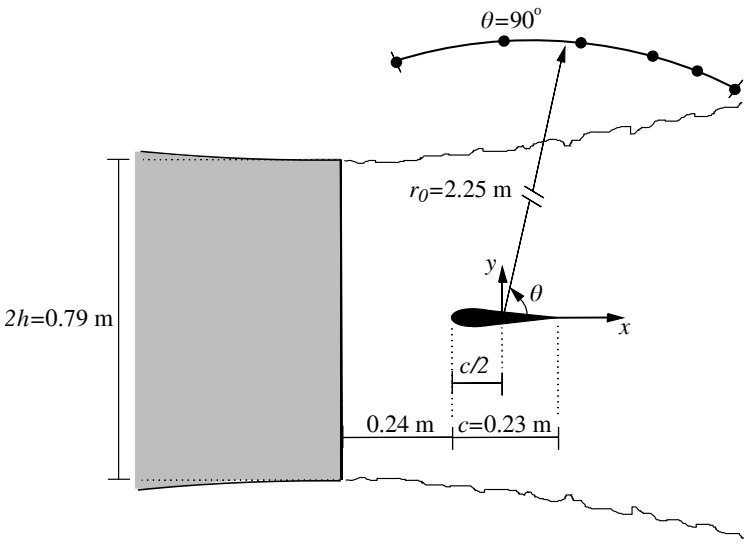

Figure 4.7: NACA 0012 aerofoil in the experimental setup of Paterson and Amiet [79].

The presence of strong mean flow gradients in the jet shear layer can produce numerical instabilities in CAA simulations [145]. To avoid this, an inviscid mean flow with no shear layer is used for the numerical simulations. This could lead to variations in aerofoil loading and pressure coefficient between the experiment and the CAA simulations. The effect of this assumption on the noise predictions is discussed in Section 4.5. It should also be noted that the experimental apparatus has not been included in the CAA simulations. Thus, installation effects, such as acoustic reflections with the jet nozzle, are neglected.

4.3.2 Numerical Setup for Fully Three-Dimensional Turbulence

Fully three-dimensional CAA simulations are challenging due to the associated increase in the computational cost. In order to minimise its impact, a three-dimensional mesh is generated by extruding a two-dimensional mesh in the spanwise direction. The mesh topology and grid details around the aerofoil are shown in Figure 4.8, and further details can be found in Appendix C.

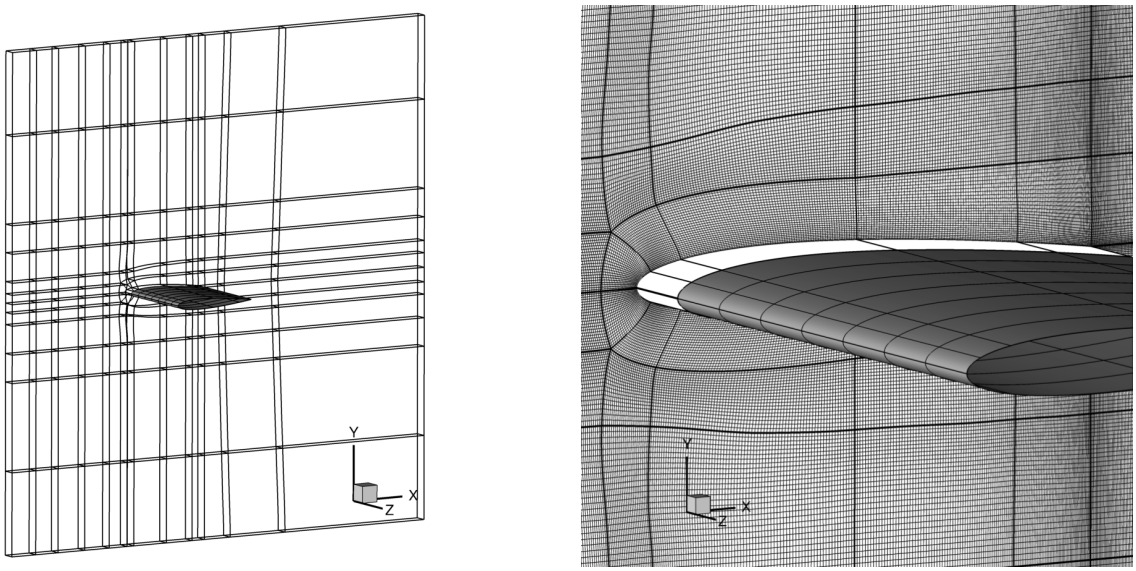

(a) Mesh topology and blocks.

(b) Mesh in the leading edge region.

Figure 4.8: Three-dimensional CAA mesh of a NACA 0012 aerofoil at $AoA = 0^{o}$.

The spanwise extent of the CAA domain is set to $L_{span} = 2r_e$, where $r_e = 3 \max\{\Lambda_i\}/2$ according to the values given in Table 4.4 for the Gaussian superposition using Equation 4.7. This corresponds to the minimum length to introduce a whole three-dimensional eddy without truncation, and ensures that the spanwise correlation of the velocity fluctuations is statistically zero for a spanwise separation equivalent to the width of the CAA domain. This numerical strategy allows the simulation of a wing with a reduced span, where the ratio between the wing span in the experiment and the width of the CAA mesh is $2d/L_{span} = 1.9$. Since the pressure spectral density is proportional to the semi-span (see Equation 4.10), numerical SPL predictions can be scaled by $10\log_{10}(2d/L_{span})$ to account for the full span of the real aerofoil. A similar strategy was adopted by Clair *et al.* [38] when performing three-dimensional CAA simulations with reduced span.

Periodic boundary conditions were used on the spanwise edges of the CAA domain. To this end, the injection plane has been extended in the spanwise direction to account for the truncation of the eddies that are close to the edges, and thus preserve the periodicity condition in the fluctuating velocity

field. This was achieved by generating *ghost* eddies on the opposite side of the injection plane in the spanwise direction, as shown in Figure 4.9. Each ghost eddy has the same characteristics, such as direction of rotation, as its corresponding eddy within the CAA domain. This ensures the continuity of the turbulent structures across the spanwise edges.

		$u'^2_{rms,i}$ [m^2/s^2]		
ith Gaussian eddy	Λ_i [m]	(U_∞ = 60 m/s)	(U_∞ = 90 m/s)	(U_∞ = 120 m/s)
1	9.284×10^{-2}	2.317×10^{-1}	7.898×10^{-1}	1.024
2	5.116×10^{-2}	4.064×10^{-1}	1.385	1.797
3	2.848×10^{-2}	3.968×10^{-1}	1.352	1.754
4	1.607×10^{-2}	3.147×10^{-1}	1.073	1.391
5	8.086×10^{-3}	2.435×10^{-1}	8.301×10^{-1}	1.077
6	5.333×10^{-3}	1.752×10^{-1}	5.971×10^{-1}	7.742×10^{-1}

Table 4.4: Parameters for Gaussian superposition to obtain the three-dimensional von Kármán spectrum with the turbulence intensity and integral length scale of Paterson and Amiet's experiment [79].

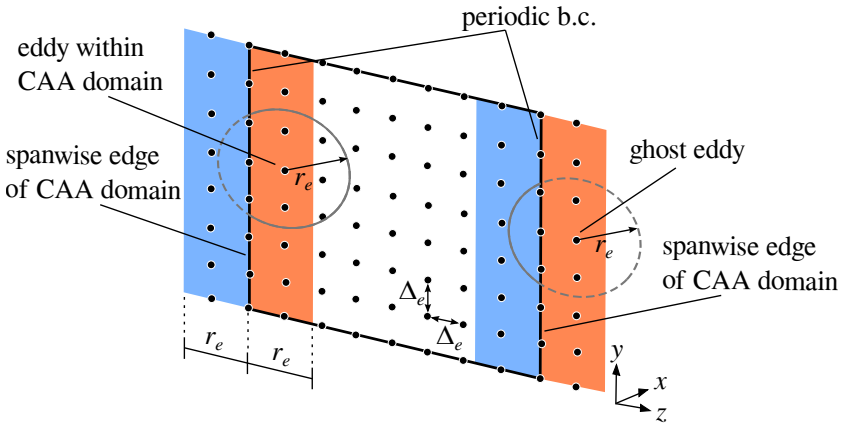

Figure 4.9: Three-dimensional injection plane with periodic boundary conditions (abbreviated as b.c.) for the advanced digital filter method.

Figure 4.10 shows instantaneous plots of the NACA 0012 aerofoil. Synthetic turbulence is introduced locally upstream of the aerofoil leading edge. As expected for isotropic turbulence, the size of the turbulent structures is similar in different spatial directions throughout the CAA domain. Contours of fluctuating pressure at the aerofoil mid-span plane exhibit the same dipole-like pattern as in purely two-dimensional CAA simulations (see Figure 3.10).

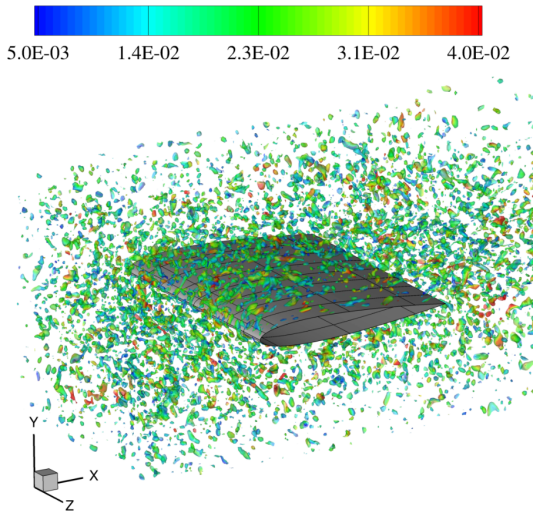

(a) Iso-contours of constant Q-criterion coloured by non-dimensional fluctuating velocity magnitude, $\|\mathbf{u}'\|/c_\infty$.

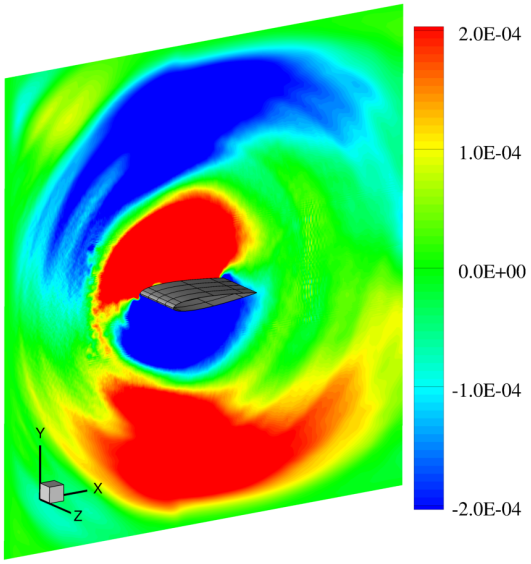

(b) Contours of non-dimensional fluctuating pressure at mid-span plane, $p'/\rho_\infty c_\infty^2$.

Figure 4.10: Instantaneous contour plots of a three-dimensional NACA 0012 aerofoil at $U_\infty = 60\,\mathrm{m/s}$ and $AoA = 0^\mathrm{o}$.

4.3.3 Numerical Setup for Pseudo Three-Dimensional Turbulence

Table 4.5 shows the parameters for the Gaussian superposition using pseudo three-dimensional turbulence. Since the integral length scale was approximately 0.03 m in all experimental configurations, the same values of Λ_i for $i = 1, ..., N_e$ are suitable to reproduce the von Kármán energy spectrum for different jet speeds.

		$u'^2_{rms,i}\,[\mathrm{m}^2/\mathrm{s}^2]$		
ith Gaussian eddy	Λ_i [m]	($U_\infty = 60\,\mathrm{m/s}$)	($U_\infty = 90\,\mathrm{m/s}$)	($U_\infty = 120\,\mathrm{m/s}$)
1	1.551×10^{-1}	2.751×10^{-4}	8.480×10^{-4}	9.950×10^{-4}
2	9.045×10^{-2}	3.015×10^{-3}	9.294×10^{-3}	1.090×10^{-2}
3	4.934×10^{-2}	4.425×10^{-3}	1.364×10^{-2}	1.601×10^{-2}
4	2.495×10^{-2}	2.468×10^{-3}	7.608×10^{-3}	8.927×10^{-3}
5	1.206×10^{-2}	9.319×10^{-4}	2.873×10^{-3}	3.371×10^{-3}
6	4.824×10^{-3}	5.173×10^{-4}	1.595×10^{-3}	1.871×10^{-3}

Table 4.5: Parameters for Gaussian superposition to obtain a two-dimensional fluctuating velocity field with the statistics of the three-dimensional von Kármán spectrum assuming $k_z = 0$, and with the turbulence intensity and integral length scale in the experiment of Paterson and Amiet [79].

4.3.4 Comparison with Experimental Results

Paterson and Amiet [79] compared their experimental measurements with analytical results from a flat plate. The latter were corrected to account for the sound refraction through the shear layer [80, 81]. The same correction is applied here to numerical results from CAA simulations, in which the shear layer is not included. Figure 4.11 shows a schematic of the jet shear layer, which is assumed to be parallel to the flow with zero thickness. In the experimental setup, a microphone that is located at (r_0, θ) corresponds to an observer at (r_0, θ_c) in the CAA simulation. According to Amiet [80], the geometric relationships between the different angles are given by

$$\tan\theta_c = \frac{\zeta}{\beta^2 \cos\theta' + M_\infty}, \qquad \cot\theta = \frac{h}{H}\cot\theta_c + \left(1 - \frac{h}{H}\right)\cot\theta', \tag{4.15}$$

where $\zeta = \left[(1 - M_\infty \cos\theta')^2 - \cos^2\theta'\right]^{1/2}$ is defined for brevity. Additionally, an amplitude correction is required to account for potential attenuations or amplifications of the sound. The fluctuating pressure at the microphone location, p', is related to the fluctuating pressure in the absence of a shear layer, p'_c, by [80]

$$\frac{p'_c}{p'} = \left\{\frac{h\csc\theta'}{r_0\zeta^2}\left[\sin\theta' + \left(\frac{H}{h} - 1\right)\zeta\right]^{1/2}\left[\sin^3\theta' + \left(\frac{H}{h} - 1\right)\zeta^3\right]^{1/2}\right\} \times$$

$$\frac{1}{2\sin\theta'}\left[M_\infty^2\left(1 - M_\infty\cos\theta'\right)^2 + \left(1 - M_\infty^2\cos^2\theta'\right)\right]^{1/2}\left[\zeta + \sin\theta'\left(1 - M_\infty\cos\theta'\right)^2\right]. \tag{4.16}$$

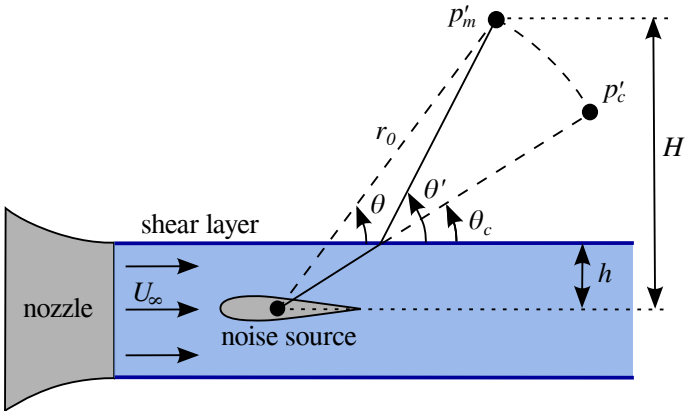

Figure 4.11: Configuration for shear layer correction in an open-jet wind tunnel.

Figure 4.12 shows the amplitude and angle corrections for the shear layer at various jet speeds. These corrections are applied from the aerofoil mid-chord, which is assumed to be the noise source. Table 4.6 summarises the corrections that are considered for the numerical results. For a microphone at $\theta = 90^\circ$, the largest deviation in the observer angle occurs at the highest speed, $\theta - \theta_c = 16^\circ$ for

$U_\infty = 120\,\mathrm{m/s}$. However, the amplitude corrections are less than 1 dB. Therefore, including the shear layer correction is expected to have a small effect in the numerical noise predictions, at least for the tested cases. This might not be the case for acute upstream observer angles, $\theta > 130$, in which the amplitude and angle corrections are particularly strong, as is shown in Figure 4.12. Note that the shear layer correction could have been applied from the aerofoil leading edge instead of the aerofoil mid-chord, however, this would have a small impact for the configurations investigated in this section.

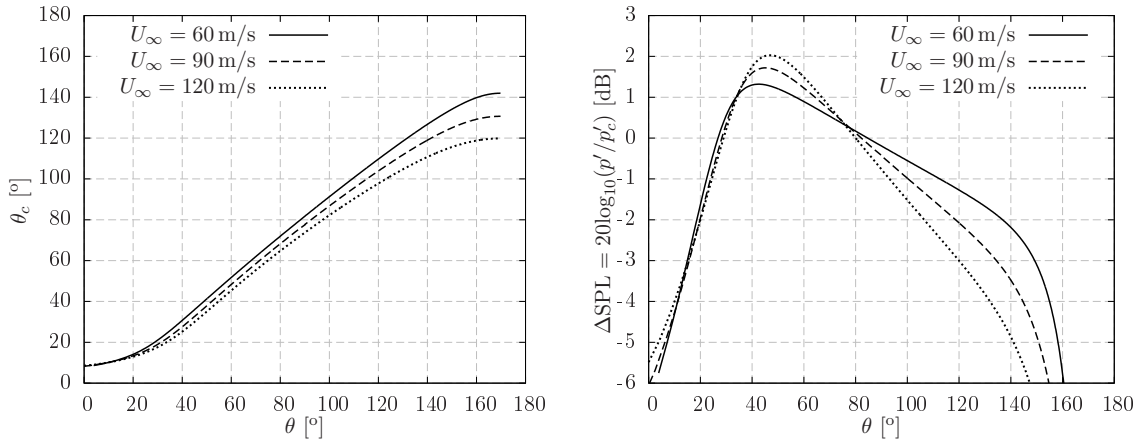

(a) Angle correction.

(b) Amplitude correction for SPL spectra.

Figure 4.12: Shear layer correction at various jet speeds with $r_0 = 2.25\,\mathrm{m}$ and $h/r_0 = 0.177$.

U_∞ [m/s]	θ_c [°]	$\Delta\mathrm{SPL} = 20\log_{10}(p'/p'_c)$ [dB]
60	82	-0.20
90	77	-0.44
120	74	-0.73

Table 4.6: Shear layer corrections for CAA simulations with $r_0 = 2.25\,\mathrm{m}$, $h/r_0 = 0.177$, and $\theta = 90^\mathrm{o}$.

Figure 4.13 shows SPL spectra from numerical simulations and experimental measurements at an observer angle of $\theta = 90^\mathrm{o}$. Both fully and pseudo three-dimensional turbulence predict similar trends and noise levels at all frequencies, with discrepancies between both approaches of less than 2 dB. This indicates that leading edge noise of a three-dimensional aerofoil with realistic geometry can be predicted from the two-dimensional aerofoil response, which is consistent with the results reported by Glegg and Devenport [77] for incompressible flows. Additionally, the agreement between experimental and numerical results is better than 3 dB for the majority of tested frequencies and cases, especially at low speed. This suggests that the isotropic turbulence assumption is sufficiently good to reproduce experimental noise measurements. However, as the tunnel speed increases, numerical

simulations over-predict the experiment. For example, the largest disagreement is about 4.5 dB at frequencies around 2500 Hz for the jet speed of 90 m/s. It should be noted that for frequencies above 2000 Hz, Paterson and Amiet [79] applied amplitude corrections of up to 4 dB to the experimental data. This was due to the wind tunnel background noise, which caused some uncertainty in the experimental data. Additionally, some necessary inputs for the numerical simulations had to be assumed since these were not specified by Paterson and Amiet [79]. For example, the mean flow density was set to $1.2\,\mathrm{kg/m^3}$ for the numerical simulations.

An important assumption of the present methodology is that the FW-H solver considers noise propagation in a uniform mean flow before the shear layer correction is applied to the numerical predictions. This implies that potential distortions in the noise radiation due to mean flow gradients around the aerofoil are not included. Although SPL spectra at more observer locations are required to make further conclusions, the shape of the numerical curves follow the trends predicted experimentally.

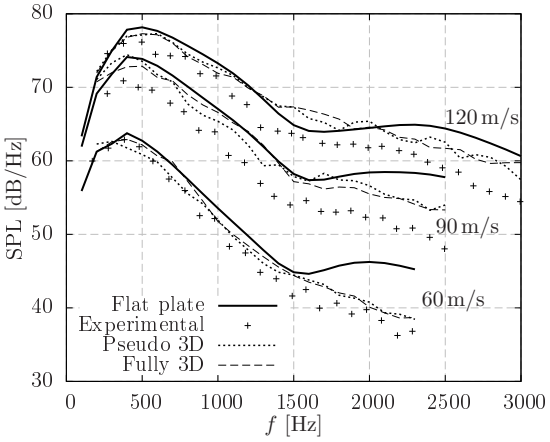

Figure 4.13: Experimental noise measurements and CAA simulations of a NACA 0012 aerofoil at $AoA = 0^{o}$. Experimental data digitised from the work of Paterson and Amiet [79].

In terms of computational cost, the total time divided by the number of time steps, grid points and processors is of the same order of magnitude in both numerical approaches. This result suggests that the computation of fully three-dimensional turbulence is not behind the increased computational cost of three-dimensional simulations. For the same number of time steps and processors, fully three-dimensional simulations are more expensive due to the larger number of grid points (about 22 million) when compared to the two-dimensional mesh (about 0.4 million), and also due to the larger number of governing equations that must be solved. The good agreement between both approaches shows that the pseudo three-dimensional turbulence approach constitutes an accurate low-cost alternative to fully three-dimensional simulations for wings with straight leading edge and constant cross-section.

4.4 Simulations of Symmetric Aerofoils at Zero Angle of Attack

Chaitanya *et al.* [87] measured far-field noise from a number of symmetric aerofoils with thicknesses ranging from $t_A/c = 0.06$ to 0.24. Experimental results showed a good agreement when compared to CAA predictions using synthetic turbulence based on Fourier modes. In this section, this experiment is reproduced using the pseudo three-dimensional turbulence approach, which has been shown to provide similar results to fully three-dimensional simulations at a reduced computational cost in Section 4.3.

4.4.1 Experimental and Numerical Setup

NACA 0006-63, NACA 0012-103, and NACA 0024-63 aerofoils were tested in the ISVR open-jet wind tunnel with $c = 0.15$ m and $d = 0.225$ m. These aerofoils correspond to modified versions of the classic NACA aerofoils to include independent modifications of leading edge radius and chordwise location of maximum thickness. Tested aerofoils are shown in Figure 4.14. Further details on how to generate NACA aerofoils of the 4-digit modified series are given in References [94, 151].

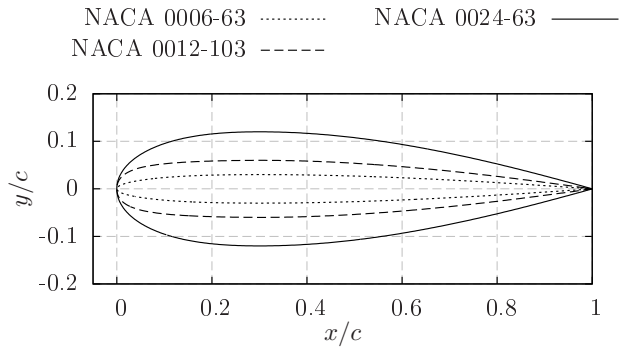

Figure 4.14: Aerofoils tested in the experiment of Chaitanya *et al.* [87].

The jet speed was set to $U_\infty = 60$ m/s and the characteristics of the turbulent flow in the test section were $u'_{rms}/U_\infty = 0.025$ and $\Lambda = 0.008$ m. For these input parameters, the Gaussian superposition technique is used to reproduce the isotropic von Kármán spectrum. Using the pseudo three-dimensional turbulence approach, the parameters for the Gaussian superposition are presented in Table 4.7. For each aerofoil geometry, an inviscid mean flow with no shear layer was used in the CAA simulations. This allows a direct comparison with the experimental results presented by Chaitanya *et al.* [87], in which the effect of the shear layer on the noise was corrected.

ith Gaussian eddy	Λ_i [m]	$u'^2_{rms,i}$ [m^2/s^2]
1	3.618×10^{-2}	7.861×10^{-5}
2	2.029×10^{-2}	4.021×10^{-4}
3	1.091×10^{-2}	3.672×10^{-4}
4	5.524×10^{-3}	2.020×10^{-4}
5	2.199×10^{-3}	1.265×10^{-4}

Table 4.7: Parameters for Gaussian superposition to obtain a two-dimensional fluctuating velocity field with the statistics of the three-dimensional von Kármán spectrum assuming $k_z = 0$, and with $U_\infty = 60\,\text{m/s}$, $u'_{rms}/U_\infty = 0.025$, and $\Lambda = 0.008\,\text{m}$.

An array of 11 microphones was placed in the acoustic far-field at a distance of $r_0 = 1.2\,\text{m}$ from the aerofoil leading edge. The microphones were uniformly distributed from 40$^\text{o}$ to 140$^\text{o}$, relative to the downstream direction. Figure 4.15 shows a schematic representation of the experimental setup.

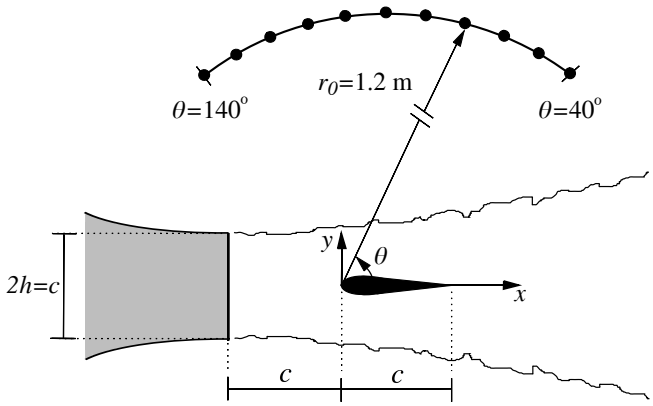

Figure 4.15: Symmetric NACA aerofoil in the experimental setup of Chaitanya *et al.* [87].

4.4.2 Comparison with Experimental Results

Untreated experimental data from an open-jet wind tunnel using grid-generated turbulence usually include jet noise from the nozzle, leading edge noise from the turbulence impinging on the aerofoil, and aerofoil self-noise from the boundary layer passing by the trailing edge. In contrast, CAA simulations in this thesis only include leading edge noise, since turbulence is injected into the CAA domain without producing jet noise, and the turbulent boundary layer is not included in the numerical modelling. Figure 4.16 shows SPL spectra at 90$^\text{o}$ above the aerofoil mid-chord, in which experimental data were treated by Chaitanya *et al.* [87] to remove shear layer effects on the noise propagation. The discrepancy at low frequencies is due to jet noise in the experiment, which is dominant for frequen-

cies below 800 Hz. When leading edge noise is the dominant source of noise, the agreement between numerical and experimental predictions is within 2 dB at most frequencies. However, numerical predictions exhibit a larger disagreement close to the frequency in which aerofoil self-noise is expected to be dominant. This threshold arises at lower frequencies for thicker aerofoils, at approximately $ft_A/U_\infty = 1$ for the tested configurations. It is concluded that the advanced digital filter method using pseudo three-dimensional turbulence is able to reproduce the experimental results with a similar level of accuracy as the Fourier mode method used by Chaitanya *et al.* [87].

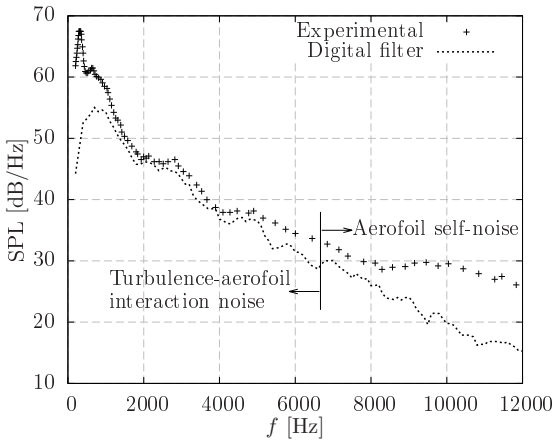

(a) NACA 0006-63 aerofoil.

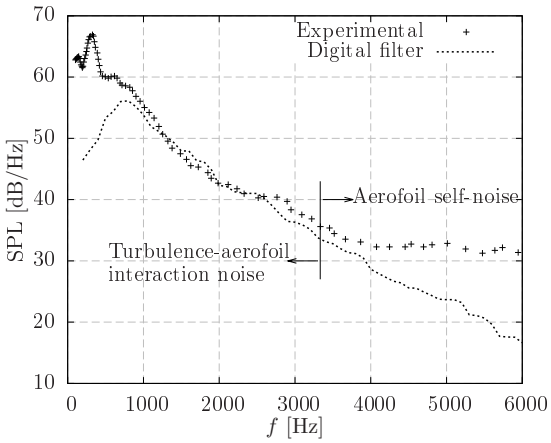

(b) NACA 0012-103 aerofoil.

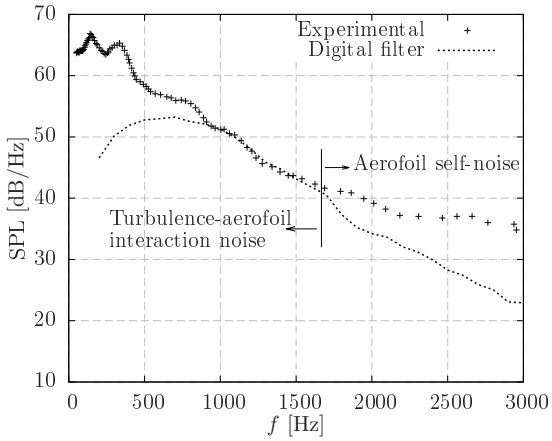

(c) NACA 0024-63 aerofoil.

Figure 4.16: Experimental noise measurements at 90° above the aerofoil mid-chord and CAA simulations of NACA 4-digit aerofoils at $AoA = 0°$. Experimental data digitised from the work of Chaitanya *et al.* [87].

4.5 Simulations of Cambered Aerofoils at Non-Zero Angle of Attack

In the Fan Stage Broadband Noise Benchmarking Programme, an open-jet wind tunnel experiment of a NACA 65(12)-10 aerofoil was proposed as a benchmark case to study turbulence-aerofoil interaction noise [97]. This aerofoil has also been used in previous experimental and numerical studies, such as those by Gruber [85], Deniau *et al.* [96], and Clair *et al.* [38], among others.

In this section, numerical simulations of a NACA 65(12)-10 aerofoil at various angles of attack are presented using various mean flow modelling assumptions. Inviscid mean flows without jet shear layer have been shown to produce accurate noise results for symmetric aerofoils at $AoA = 0^{\circ}$ (see Sections 4.3 and 4.4). In this section, the suitability of the inviscid mean flow assumption is assessed on a cambered NACA 65(12)-10 aerofoil. Additionally, a CAA simulation using a viscous mean flow with the jet shear layer is performed for a high angle of attack configuration. In this case, a gradient term suppression strategy is used to guarantee the stability of the LEEs. Numerical noise predictions are compared to experimental measurements available at various observer angles, which allows a thorough validation of the pseudo three-dimensional turbulence approach.

4.5.1 Experimental and Numerical Setup

Noise measurements of a NACA 65(12)-10 aerofoil at $AoA = 0^{\circ}$ (baseline) were presented by Hainaut *et al.* [97]. The experiment was performed in the same open-jet wind tunnel facility as the symmetric aerofoils presented in Section 4.4, with the experimental setup shown in Figure 4.15. The jet speed was set to 60 m/s, and the turbulence intensity and integral length scale were $u'_{rms}/U_{\infty} = 0.017$ and $\Lambda = 0.008$ m, respectively. Table 4.8 shows the parameters for the Gaussian superposition using the pseudo three-dimensional turbulence approach.

ith Gaussian eddy	Λ_i [m]	$u'^2_{rms,i}$ [m^2/s^2]
1	3.618×10^{-2}	3.637×10^{-5}
2	2.029×10^{-2}	1.859×10^{-4}
3	1.091×10^{-2}	1.699×10^{-4}
4	5.524×10^{-3}	9.335×10^{-5}
5	2.199×10^{-3}	5.847×10^{-5}

Table 4.8: Parameters for Gaussian superposition to obtain a two-dimensional fluctuating velocity field with the statistics of the three-dimensional von Kármán spectrum assuming $k_z = 0$, and with $U_{\infty} = 60$ m/s, $u'_{rms}/U_{\infty} = 0.017$, and $\Lambda = 0.008$ m.

Noise results for the NACA 65(12)-10 aerofoil presented by Gruber [85] showed a 2 dB difference between the baseline and the $AoA = 15^{o}$ configuration at $U_{\infty} = 60\text{m/s}$, i.e., the effect of angle of attack on the noise predictions was found to be small. However, the angle of attack introduces significant variations in the mean flow distribution around the aerofoil. A downwards jet deflection was reported for the $AoA = 15^{o}$ configuration, which reduced the effective angle of attack perceived by the aerofoil. For symmetric aerofoils, Brooks *et al.* [152] defined the effective angle of attack for a two-dimensional wind tunnel as the result of dividing the geometric angle of attack by $[(1 + 2\sigma_e)^2 + \sqrt{12\sigma_e}]$, where $\sigma_e = (\pi^2/48)[c/(2h)]^2$ and $2h$ is the jet vertical length, as shown in Figure 4.15. Assuming that the correction is suitable for cambered aerofoils, the effective angle of attack for a NACA 65(12)-10 aerofoil at $AoA = 15^{o}$ would be of approximately 4.21^{o}, as reported by Gruber [85]. Figure 4.17 shows a NACA 65(12)-10 aerofoil at various angles of attack.

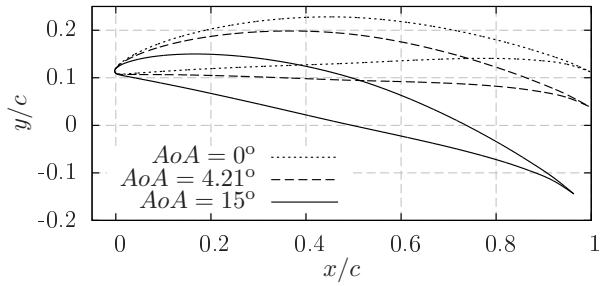

Figure 4.17: NACA 65(12)-10 aerofoil at various angles of attack.

For the CAA simulations, the aerofoil is tested at angles of attack of 0^{o} and 4.21^{o} using an inviscid mean flow without jet, and 15^{o} using a viscous mean flow with jet. The aerofoil is rotated around the leading edge, such that the distance from the leading edge to far-field observers is similar in all configurations. Gruber [85] found a recirculation bubble on the pressure surface near the leading edge for the $AoA = 0^{o}$ configuration. However, such a recirculation bubble cannot be included in the inviscid mean flow solutions without jet. The viscous mean flow with the jet was computed by using the Spalart-Allmaras turbulence model for the RANS equations with zero shear stress on the aerofoil wall. Consequently, the boundary layer on the aerofoil surface and recirculation bubbles are not included in the mean flow solution, which is consistent with the slip-wall boundary condition that is used by the LEEs. The absence of the recirculation bubble in the CAA simulations is expected to have a small effect on the noise results. This is because the distortion of the turbulence spectra, which has been identified as an important contributor to aerofoil geometry effects on the noise, occurs upstream of the leading edge.

Figure 4.18 shows contours of mean flow Mach number and non-dimensional vorticity magnitude around a NACA 65(12)-10 aerofoil. For the $AoA = 4.21^{o}$ configuration in the freestream, there is a

small deviation of the turbulent structures due to the aerofoil camber and angle of attack. However, when the jet of the wind tunnel is modelled, the deflection of the jet mean flow forces the turbulent structures to move downwards. An increase in the vorticity contours can also be observed in the shear layer due to the strong mean flow gradients, which stretch the turbulent structures. In such a case, the LEEs diverge due to the development of Kelvin-Helmholtz instabilities [145]. To avoid this, the simulation using a viscous mean flow with jet was performed by means of a simplified version of the LEEs that removes the term $\partial U_{0,x}/\partial y$ from the governing equations. This numerical simplification was shown to produce stable LEE results without significant loss of accuracy by Bogey *et al.* [153], when studying the sound propagation of a low-frequency monopole in a sheared mean flow.

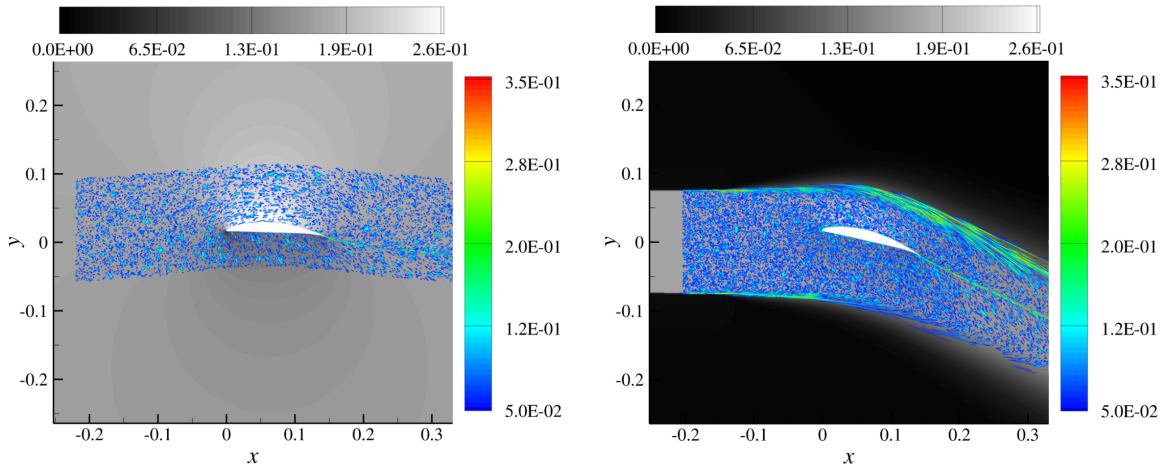

(a) Aerofoil at $AoA = 4.21^{o}$ in an inviscid mean flow without jet (freestream).

(b) Aerofoil at $AoA = 15^{o}$ in a viscous mean flow with jet.

Figure 4.18: Contours of mean flow Mach number (grey scale) and non-dimensional vorticity magnitude ($\|\nabla \times \mathbf{u}'\| L_{ref}/c_{\infty}$, colour scale) around a NACA 65(12)-10 aerofoil.

In the experiment, the separation between the nozzle exit and the leading edge is equal to the aerofoil chord, as shown in Figure 4.15. For the simulation using a viscous mean flow with jet, such a small distance is not sufficient to inject the eddies without truncation and to include a buffer zone. Consequently, the mean flow variables at the plane of the nozzle exit have been copied to all grid points in the CAA domain that are upstream of the nozzle exit.

4.5.2 Comparison with Experimental Results

The pressure coefficient, C_p, of the CFD mean flow simulations is compared to experimental data in Figure 4.19. The amplitude of the C_p on the aerofoil surface is over-predicted for the freestream configurations (no jet), especially on the suction side. It is concluded that the C_p computed by the

aerofoil in the freestream at 4.21° cannot reproduce the experimental pressure distribution around the aerofoil at $AoA = 15°$, and therefore the aerofoil loading is significantly affected by the absence of the jet. This conclusion is supported by the viscous mean flow simulation with the jet, which is able to closely reproduce the trends and levels of the C_p distribution at $AoA = 15°$, despite the fact that shear stress has been neglected on the aerofoil surface. Including the jet of the experimental setup plays an important role in the correct modelling of the mean flow around the aerofoil.

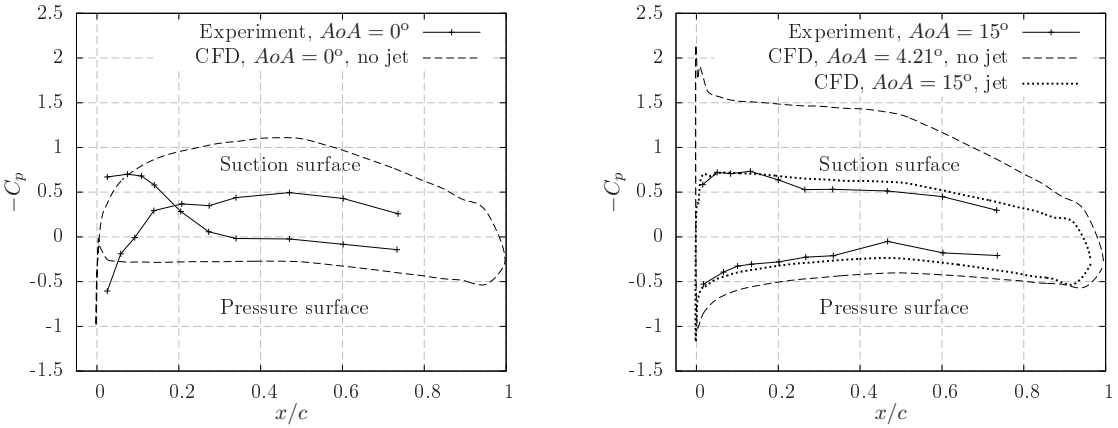

(a) Experimental and numerical data for $AoA = 0°$. Experimental data digitised from the work of Gruber [85].

(b) Experimental and numerical data for $AoA = 15°$. Experimental data digitised from the work of Hainaut *et al.* [97].

Figure 4.19: C_p for a NACA 65(12)-10 aerofoil at $U_\infty = 60$ m/s.

Figure 4.20 shows SPL spectra at several microphone locations measured from the aerofoil leading edge. In this case, experimental and numerical results are presented without applying a shear layer correction. This is because the amplitude and angle corrections are expected to be small for observer angles around 90° at low jet speeds ($U_\infty = 60$ m/s in this experiment). Additionally, applying the shear layer correction might be inaccurate for the aerofoil at $AoA = 15°$ due to the strong deflection of the jet and the shear layer, which is broadened (see Figure 4.18b).

As shown in Figure 4.20, numerical simulations of the aerofoil at $AoA = 15°$ in the jet configuration, and $AoA = 4.21°$ in the freestream, predict noise levels to within 2 dB. This suggests that the aerofoil loading and mean flow modelling assumptions play a small role in the accuracy of the CAA results. The simulation with the aerofoil at $AoA = 0°$ shows consistently higher noise levels at high frequencies than those at non-zero angle of attack, especially at upstream observer angles. Gruber [85] found experimentally a small noise reduction with increasing the angle of attack of a NACA 65(12)-10 aerofoil, which was associated with non-homogeneous turbulence across the test section and potential variations in the leading edge location when changing the angle of attack. Similar trends in the noise results are shown in Figure 4.20 for the CAA simulations, although the aerofoil leading edge was

kept at a fixed location (see Figure 4.17) and completely isotropic turbulence was used. Nevertheless, the differences in noise levels between all numerical computations at different angles of attack are small (less than 4 dB), which suggests that moderate variations in the angle of attack are not necessary to be included in CAA simulations in order to obtain a representative leading edge noise prediction. Finally, the comparison between numerical and experimental noise predictions at $AoA = 0^{o}$ shows an agreement to within 2 dB for the frequency range in which leading edge noise is dominant. The disagreement at low frequencies ($f < 800$ Hz) is due to jet noise from the nozzle in the open-jet wind tunnel.

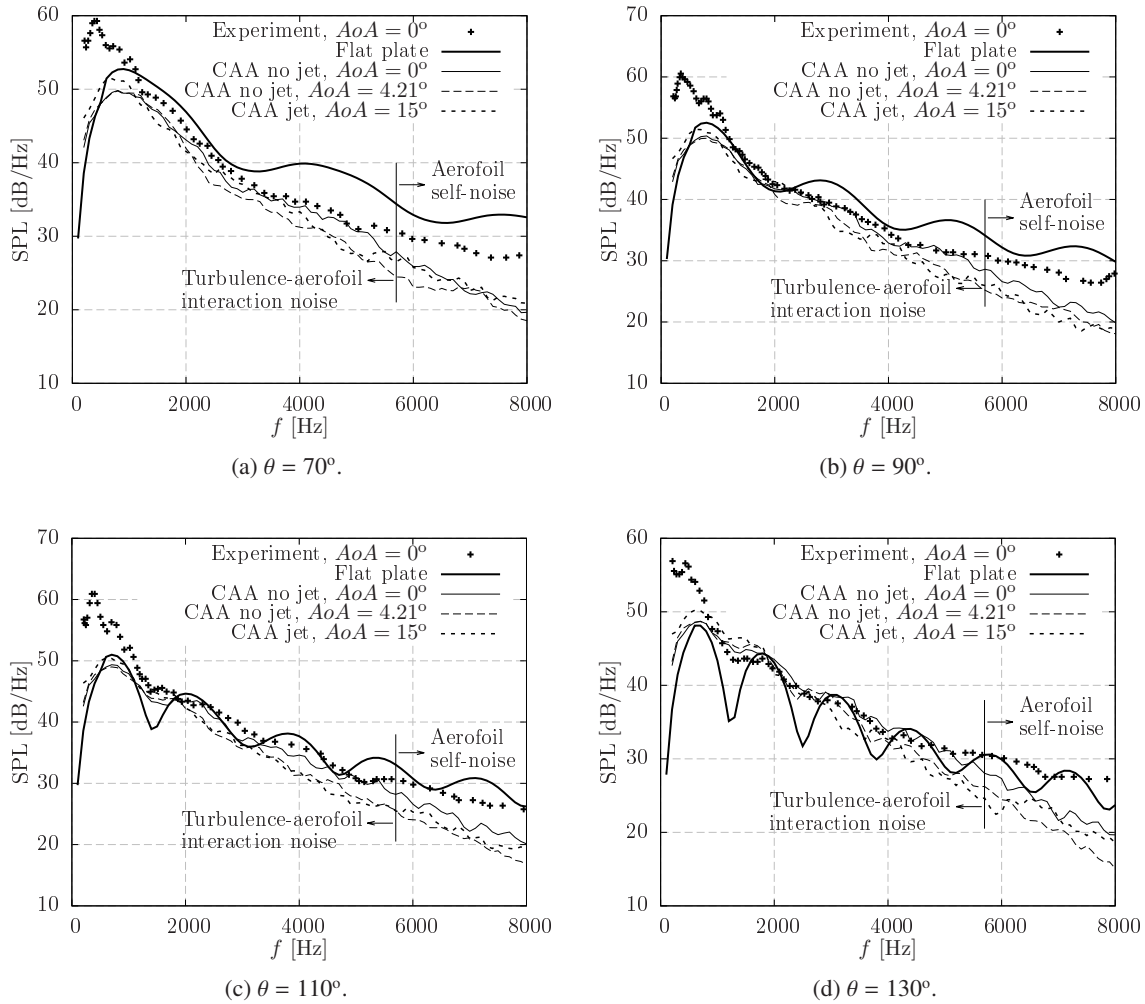

(a) $\theta = 70^{o}$. (b) $\theta = 90^{o}$.

(c) $\theta = 110^{o}$. (d) $\theta = 130^{o}$.

Figure 4.20: SPL spectra for a NACA 65(12)-10 aerofoil at various observer angles. Experimental data digitised from the work of Hainaut *et al.* [97].

4.6 Summary

In this chapter, the advanced digital filter method has been extended to realise a fully three-dimensional turbulent flow. The method is validated to reproduce a target isotropic spectrum through a superposition of three-dimensional Gaussian eddies that define a new eddy shape. Additionally, a pseudo three-dimensional approach has been developed to perform low-cost CAA simulations that can be used to reproduce experimental measurements without applying correction factors for the velocity spectra and the three-dimensional sound propagation in the free field. Firstly, two-dimensional synthetic turbulence with the key statistics of three-dimensional turbulence is generated. This can be achieved if $E^{(2D)}$ is forced to reproduce the shape of $E^{(3D)}/(4k)$ with $k_z = 0$ in the two-dimensional Gaussian superposition. Secondly, unsteady data from a two-dimensional CAA simulation are collected on the aerofoil surface and copied in the spanwise direction to produce a three-dimensional surface. This is used as an input for a three-dimensional FW-H solver that radiates the noise to the far-field. Both fully and pseudo three-dimensional synthetic turbulence approaches have been used to reproduce experimental measurements of leading edge noise from a number of open-jet wind tunnel facilities. The main findings are summarised as follows:

- From a computational perspective, the generation of fully three-dimensional turbulence with the advanced digital filter method does not noticeably slow down the code. Three-dimensional simulations of leading edge noise were found to be more expensive due to the increased number of grid points and governing equations to be solved.

- The pseudo three-dimensional turbulence approach has been successfully validated for a NACA 0001 aerofoil with straight leading edge. The agreement between the analytical prediction of Amiet [39] and the numerical results is better than 1.5 dB, if the numerical spanwise resolution satisfies $d/\Delta z \geq 15$.

- Additionally, the pseudo three-dimensional turbulence approach has been found to be sufficiently generic to reproduce experimental noise measurements from different open-jet wind tunnels to within 3 dB, at least for the tested aerofoil configurations. Consequently, fully three-dimensional CAA simulations are not required to obtain numerical results from aerofoils with straight leading edge that can be compared to experimental results. The pseudo three-dimensional approach constitutes a low-cost numerical methodology that provides satisfactory results.

- Three-dimensional noise predictions of aerofoils with realistic geometry can be obtained by CAA modelling of the two-dimensional aerofoil response.

- The assumption of isotropic turbulence was found to be suitable for reproducing experimental measurements of leading edge noise from single aerofoils in various open-jet wind tunnels.

- The amplitude and angle corrections to account for the shear layer refraction are small for observer angles at around 90^o at low jet speeds. Under these circumstances, shear layer corrections might not be required to compare experimental and numerical leading edge noise predictions from open-jet wind tunnel experiments.

- Realistic mean flows, including viscosity and jet with shear layers, can be modelled in LEE simulations of leading edge noise if $\partial U_{0,x}/\partial y$ gradients are suppressed for numerical stability.

- Important discrepancies were found between numerical and experimental C_p distributions for the freestream and jet configurations. Only the CAA simulation including the open-jet of the wind tunnel was able to closely match the experimental trends in the C_p distribution.

- Numerical noise results have shown a weak dependence on the mean flow modelling assumptions and aerofoil loading. Particularly, inviscid mean flows and aerofoils in the freestream are acceptable mean flow assumptions to reproduce experimental noise measurements from open-jet wind tunnels. For example, numerical noise results showed an agreement with experimental measurements by Chaitanya *et al.* [87] to within 2 dB.

- Numerical noise predictions of a cambered NACA 65(12)-10 aerofoil showed an insensitivity to angle of attack and aerofoil mean loading. This confirms that modelling the angle of attack is not necessary in CAA simulations at the design stage.

Chapter 5

Leading Edge Noise Predictions Using Anisotropic Turbulence

In previous chapters, leading edge noise predictions of single aerofoils were performed by assuming isotropic turbulence. This assumption has been found to be suitable for fundamental studies of turbulence-aerofoil interaction noise (see Chapter 3), and for numerical predictions of open-jet wind tunnel measurements using grid-generated turbulence, which is nearly isotropic (see Chapter 4). However, anisotropic turbulence is present in turbofan engines, as shown in Figure 5.1.

In static test conditions, variations of the order of 10^2 between the streamwise and transverse length scales were reported at the fan intake by Kantola and Warren [16], although the level of anisotropy is notably reduced in flight conditions [15]. Highly anisotropic turbulence can also be found in the boundary layer that interacts with the fan blade tip [154]. Additionally, anisotropic turbulence has been reported in hotwire measurements of fan wakes. For example, the ratios of streamwise-to-transverse integral length scales, $l_{11}^{(1)}/l_{22}^{(1)}$ and $l_{11}^{(1)}/l_{33}^{(1)}$, can range approximately between 1.4 and 4 depending on the radial location, as can be inferred from the experimental data of Podboy *et al.* [18]. Note that $l_{11}^{(1)}/l_{22}^{(1)} = l_{11}^{(1)}/l_{33}^{(1)} = 2$ for isotropic turbulence[6]. Ganz *et al.* [17] found that the isotropic von Kármán spectrum might be sufficient to represent the spectral distribution of the fan wakes in the mid-span. However, modelling the anisotropy in the fan wakes is becoming increasingly important. This is because the next generation of turbofan engines, such as ultra-high bypass ratio turbofan engines, is expected to decrease the separation between the fan blades and the OGVs.

[6] See footnote 2.

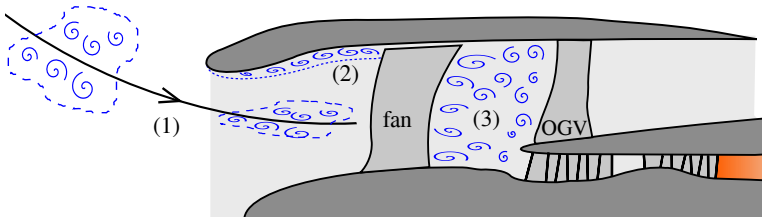

Figure 5.1: Locations where anisotropic turbulence affects leading edge noise in a turbofan engine: intake (1), boundary layer (2), and fan wakes (3).

Anisotropic turbulence at the fan intake [113] and the fan wakes [18] can be modelled as axisymmetric turbulence. This type of turbulence corresponds to a simple representation of an anisotropic flow, in which the root-mean-square velocity and length scale vary in a prevailing direction [155] (such as the engine axis) and remains isotropic in a plane perpendicular to the prevailing direction. Atassi and Logue [156] used an axisymmetric turbulence model that is based on rapid distortion theory of Batchelor and Proudman [146] to study turbulence ingestion noise from the fan intake. Alternatively, Posson *et al.* [112] and Hanson [102] adopted the homogeneous axisymmetric turbulence model of Kerschen and Gliebe [113] in their cascade models for the prediction of fan wake-OGV interaction noise. This turbulence model was also used by Devenport *et al.* [78] to study the effect of angle of attack on the turbulence-aerofoil interaction noise from a NACA 0015 aerofoil.

To date, few works have addressed the effects of anisotropic turbulence on leading edge noise, despite the anisotropic features of turbulence in turbofan engines. For turbulence that is stretched in the axial direction, Atassi and Logue [156] and Posson *et al.* [112] found that the maximum noise level moved to lower frequencies, followed by a decrease in noise in the mid-frequency range. Furthermore, analytical models to predict turbulence ingestion noise and fan-OGV interaction noise have been found to be highly sensitive to input turbulence spectra [112, 114, 156]. Devenport *et al.* [78] reported a significant increase in noise levels with increasing angle of attack for turbulence stretched in the axial direction. However, the study was limited to low frequencies and incompressible Mach numbers.

In light of the above discussion, it is necessary to obtain a more comprehensive insight into the effects of anisotropic turbulence on leading edge noise. This could be useful to improve current understanding of broadband noise from complex fan systems in which anisotropic turbulence is present. In this chapter, an extensive parameter study is presented to assess the effects of anisotropic turbulence on leading edge noise. This CAA study includes simulations using moderately anisotropic turbulence, which is representative of the anisotropy in the fan wakes, and a number of single aerofoil configurations, including variations in aerofoil thickness, mean flow Mach number, and angle of attack, among others.

The present chapter is organised as follows. In Section 5.1, the advanced digital filter method is extended to generate two- and three-dimensional homogeneous anisotropic synthetic turbulence with Gaussian spectra. Then, fully and pseudo three-dimensional anisotropic turbulence are tested for CAA simulations of single aerofoils in Section 5.2. Finally, a parameter study is presented in Section 5.3 to assess the effects of anisotropy on turbulence-aerofoil interaction noise. The homogeneous axisymmetric turbulence model of Kerschen and Gliebe [113] has been adopted for the parameter study.

5.1 Anisotropic Synthetic Turbulence

In this section, further developments in the advanced digital filter method are presented to generate homogeneous anisotropic synthetic turbulence with Gaussian spectra. The assumption of homogeneity allows an explicit control on the resulting velocity spectra, which is convenient for leading edge noise predictions.

5.1.1 Two-Dimensional Anisotropic Turbulence

In the isotropic version of the advanced digital filter method (see Section 2.2), each eddy introduces a fluctuating velocity field around its centre, acting as a spatial filter with a constant length scale (Λ) in all spatial directions. However, the governing equations of a two-dimensional Gaussian eddy can be extended to account for spatial variations in length scales. This is achieved by taking into account the following aspects in Equations 2.14a and 2.14b:

- For isotropic turbulence, $l_{11}^{(1)} = l_{22}^{(2)} = \Lambda$. However, the length scales may vary in each spatial direction for anisotropic turbulence. To simplify the notation, the length scales in the streamwise and transverse directions are written here as $l_x = l_{11}^{(1)}$ and $l_y = l_{22}^{(2)}$, respectively.
- Variations in the filter length in each spatial direction are introduced by taking advantage of the properties of the exponential function, which allows the separation of the exponential term $\exp\left[-\pi r_p^2/(2\Lambda^2)\right]$, where $r_p^2 = (x - x_p)^2 + (y - y_p)^2$, into

$$A_p^{(2D)} = \exp\left[-\frac{\pi\left(x - x_p\right)^2}{2l_x^2}\right]\exp\left[-\frac{\pi\left(y - y_p\right)^2}{2l_y^2}\right]. \tag{5.1}$$

- By imposing the divergence-free condition on the fluctuating velocity field of each eddy, the terms u'_{rms}/Λ^2 are conveniently replaced by u'_0/l_x^2 and u'_0/l_y^2, where u'_0 is a characteristic velocity term that controls the amplitude of the anisotropic eddies.

- The term that controls the eddy density, Δ_e, is substituted by $\sqrt{\Delta_{e,x}\Delta_{e,y}}$, where $\Delta_{e,x}$ and $\Delta_{e,y}$ correspond to the separation between eddy centres in the x- and y-directions, respectively.

Thus, Equations 2.14a and 2.14b can be rewritten for the pth two-dimensional anisotropic Gaussian eddy as

$$u'_{x,p}(\mathbf{x}) = -\sqrt{2\pi\Delta_{e,x}\Delta_{e,y}}\epsilon_p \left(y - y_p\right) \frac{u'_0}{l_y^2} A_p^{(2\mathrm{D})}, \tag{5.2a}$$

$$u'_{y,p}(\mathbf{x}) = \sqrt{2\pi\Delta_{e,x}\Delta_{e,y}}\epsilon_p \left(x - x_p\right) \frac{u'_0}{l_x^2} A_p^{(2\mathrm{D})}. \tag{5.2b}$$

Note that the equations of a two-dimensional isotropic Gaussian eddy are recovered by setting $u'_0 = u'_{rms}$, $l_x = l_y = \Lambda$, and $\Delta_{e,x} = \Delta_{e,y} = \Delta_e$ in Equations 5.2a and 5.2b.

Figure 5.2 shows contours and streamlines of the fluctuating velocity field introduced by an anisotropic Gaussian eddy. This type of eddy introduces streamlines with the shape of an ellipse due to the different length scales involved, i.e., the eddies are stretched in a prevailing direction. In contrast, isotropic Gaussian eddies introduce circular-shaped streamlines with a constant radius, as shown in Figure 2.1.

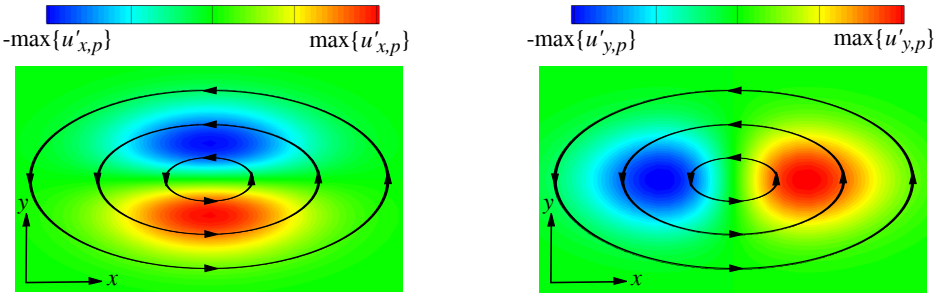

(a) $u'_{x,p}$ contours and streamlines. (b) $u'_{y,p}$ contours and streamlines.

Figure 5.2: Fluctuating velocity field due to a two-dimensional anisotropic eddy with $l_x = 3l_y$.

Following the implementation strategy of the advanced digital filter method for isotropic turbulence, eddies are introduced into the CAA domain through a local injection plane to generate anisotropic turbulence. Figure 5.3 shows a schematic of the numerical implementation. Since the limiting values of the eddy radius and eddy spacing can be expressed as a function of the length scales, the correct statistics of the anisotropic turbulent flow are recovered provided that $r_{e,x} \geq 3l_x/2$, $r_{e,y} \geq 3l_y/2$, $\Delta_{e,x} \leq l_x/2$, and $\Delta_{e,y} \leq l_y/2$. These limiting values are based on those obtained from a parameter study in Appendix B.

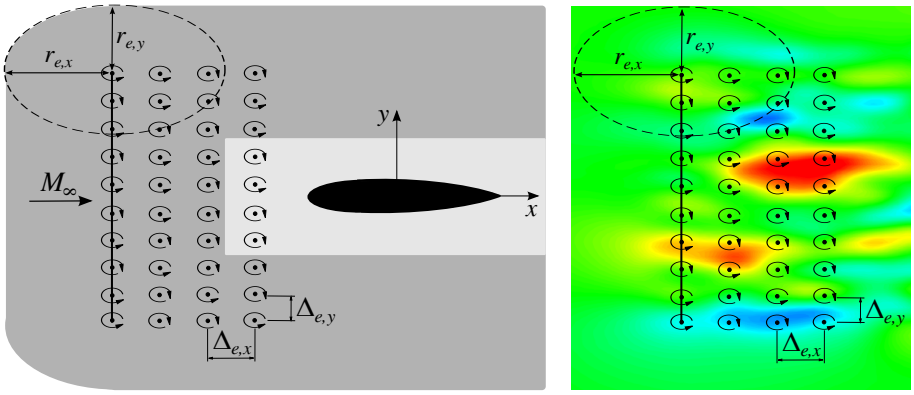

Figure 5.3: Injection plane and parameters to generate anisotropic turbulence. Light grey background represents the region where the desired statistical properties are reproduced.

The spectral content of turbulent flows generated by using two-dimensional anisotropic Gaussian eddies is defined by the streamwise and transverse velocity spectra

$$\Phi_{11}^{(2D)}(k_x, k_y) = \frac{2}{\pi^3} u_0'^2 l_x^2 l_y^2 k_y^2 \exp\left(-\frac{l_x^2 k_x^2}{\pi}\right) \exp\left(-\frac{l_y^2 k_y^2}{\pi}\right), \tag{5.3a}$$

$$\Phi_{22}^{(2D)}(k_x, k_y) = \frac{2}{\pi^3} u_0'^2 l_x^2 l_y^2 k_x^2 \exp\left(-\frac{l_x^2 k_x^2}{\pi}\right) \exp\left(-\frac{l_y^2 k_y^2}{\pi}\right), \tag{5.3b}$$

respectively. The root-mean-square velocities of the anisotropic turbulent flow are obtained through the integration of their corresponding velocity spectrum over all wavenumbers, which gives $u'_{x,rms} = u'_0 \sqrt{l_x/l_y}$ and $u'_{y,rms} = u'_0 \sqrt{l_y/l_x}$. Hence, the ratio of root-mean-square velocity components is proportional to the ratio of length scales, i.e.,

$$u'_{x,rms}/u'_{y,rms} = l_x/l_y. \tag{5.4}$$

This relationship, which is a consequence of the divergence-free condition, implies that it is only possible to take control of 3 of the parameters $u'_{x,rms}$, $u'_{y,rms}$, l_x, and l_y. Furthermore, Equation 5.4 indicates that an increase in a particular length scale is associated with an increase in the velocity fluctuations in the corresponding direction, if the rest of parameters remain constant.

The numerical implementation of the synthetic turbulence method was validated by using turbulence stretched in both streamwise and transverse directions with the same turbulent kinetic energy, $K = (u'^2_{x,rms} + u'^2_{y,rms})/2 = \text{const}$. Figure 5.4 shows analytical and numerical one-dimensional spectra, where an agreement of better than 1.5 dB is found at all frequencies. This level of accuracy, which is similar to that reported for the advanced digital filter method using isotropic turbulence in Section 2.2, validates the numerical implementation.

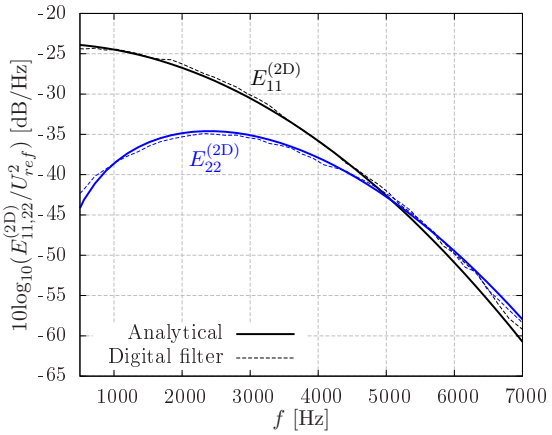

(a) Turbulence stretched in the streamwise direction with $l_x = 3l_y$, $l_y = 0.004$ m.

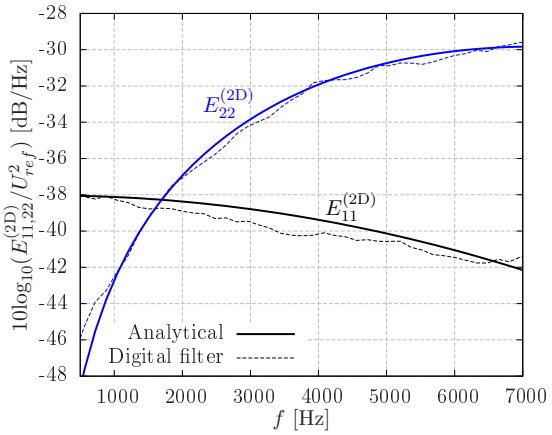

(b) Turbulence stretched in the transverse direction with $l_y = 3l_x$, $l_x = 0.004$ m.

Figure 5.4: One-dimensional spectra of two-dimensional anisotropic Gaussian turbulence with $u_0'^2 = 3\,\mathrm{m}^2/\mathrm{s}^2$. The injection plane parameters are $r_{e,x} = 3l_x/2$, $r_{e,y} = 3l_y/2$, $\Delta_{e,x} = l_x/2$, and $\Delta_{e,y} = l_y/2$. The reference speed is $U_{ref} = 1\,\mathrm{m/s}$.

5.1.2 Three-Dimensional Anisotropic Turbulence

The fluctuating velocity field of a three-dimensional isotropic Gaussian eddy, which is defined by Equations 4.5a-4.5c, can also be extended to account for anisotropy. Following a similar approach as in Section 5.1.1, the fluctuating velocity field introduced by the pth three-dimensional anisotropic Gaussian eddy is given by

$$u'_{x,p}(\mathbf{x}) = \sqrt{\pi\Delta_{e,x}\Delta_{e,y}\Delta_{e,z}}\left[\frac{\epsilon_{2,p}\left(z-z_p\right)}{l_z^2} - \frac{\epsilon_{3,p}\left(y-y_p\right)}{l_y^2}\right]\frac{u'_0}{\left(l_x l_y l_z\right)^{1/6}}A_p^{(3D)}, \tag{5.5a}$$

$$u'_{y,p}(\mathbf{x}) = \sqrt{\pi\Delta_{e,x}\Delta_{e,y}\Delta_{e,z}}\left[\frac{\epsilon_{3,p}\left(x-x_e\right)}{l_x^2} - \frac{\epsilon_{1,p}\left(z-z_e\right)}{l_z^2}\right]\frac{u'_0}{\left(l_x l_y l_z\right)^{1/6}}A_p^{(3D)}, \tag{5.5b}$$

$$u'_{z,p}(\mathbf{x}) = \sqrt{\pi\Delta_{e,x}\Delta_{e,y}\Delta_{e,z}}\left[\frac{\epsilon_{1,p}\left(y-y_e\right)}{l_y^2} - \frac{\epsilon_{2,p}\left(x-x_e\right)}{l_x^2}\right]\frac{u'_0}{\left(l_x l_y l_z\right)^{1/6}}A_p^{(3D)}, \tag{5.5c}$$

where $\epsilon_{i,p}$ are random numbers that can take ± 1 for $i = 1, 2, 3$, and $A_p^{(3D)}$ corresponds to the exponential term

$$A_p^{(3D)} = \exp\left[-\frac{\pi\left(x-x_p\right)^2}{2l_z^2}\right]\exp\left[-\frac{\pi\left(y-y_p\right)^2}{2l_y^2}\right]\exp\left[-\frac{\pi\left(z-z_p\right)^2}{2l_x^2}\right]. \tag{5.6}$$

In order to realise a fully three-dimensional turbulent flow, the injection plane is extended in the spanwise direction as shown in Figure 5.5a. It should be noted that the length of the filters are similar for two- and three-dimensional eddies, since $A_p^{(2D)}$ and $A_p^{(3D)}$ have similar definitions. Therefore, the correct turbulence statistics can be recovered provided that the radius of the eddies satisfies $r_{e,x} \geq 3l_x/2$, $r_{e,y} \geq 3l_y/2$, and $r_{e,z} \geq 3l_z/2$, and the eddy spacing in each spatial direction is $\Delta_{e,x} \leq l_x/2$, $\Delta_{e,y} \leq l_y/2$, and $\Delta_{e,z} \leq l_z/2$. The resulting velocity spectra using three-dimensional anisotropic Gaussian eddies are given by

$$\Phi_{11}^{(3D)}(k_x, k_y, k_z) = \frac{u_0'^2}{\pi^4}\left(l_x l_y l_z\right)^{5/3}\left(k_y^2 + k_z^2\right)\exp\left(-\frac{l_x^2k_x^2 + l_y^2k_y^2 + l_z^2k_z^2}{\pi}\right), \tag{5.7a}$$

$$\Phi_{22}^{(3D)}(k_x, k_y, k_z) = \frac{u_0'^2}{\pi^4}\left(l_x l_y l_z\right)^{5/3}\left(k_x^2 + k_z^2\right)\exp\left(-\frac{l_x^2k_x^2 + l_y^2k_y^2 + l_z^2k_z^2}{\pi}\right), \tag{5.7b}$$

$$\Phi_{33}^{(3D)}(k_x, k_y, k_z) = \frac{u_0'^2}{\pi^4}\left(l_x l_y l_z\right)^{5/3}\left(k_x^2 + k_y^2\right)\exp\left(-\frac{l_x^2k_x^2 + l_y^2k_y^2 + l_z^2k_z^2}{\pi}\right). \tag{5.7c}$$

The numerical implementation is validated in Figure 5.5b, which shows analytical and numerical one-dimensional spectra of three-dimensional anisotropic Gaussian turbulence with $u_0'^2 = 3\,\mathrm{m}^2/\mathrm{s}^2$, $l_x = 0.008\,\mathrm{m}$, $l_y = 2l_x$, and $l_z = 3l_x$. The values of the length scales have been chosen to generate moderately anisotropic turbulence that is stretched in the transverse and spanwise directions. Consequently, the transverse and spanwise one-dimensional spectra, $E_{22}^{(3D)}$ and $E_{33}^{(3D)}$ respectively, do not overlap onto a single curve, as would be expected for isotropic turbulence. Numerical and analytical results exhibit an agreement of better than 1.5 dB.

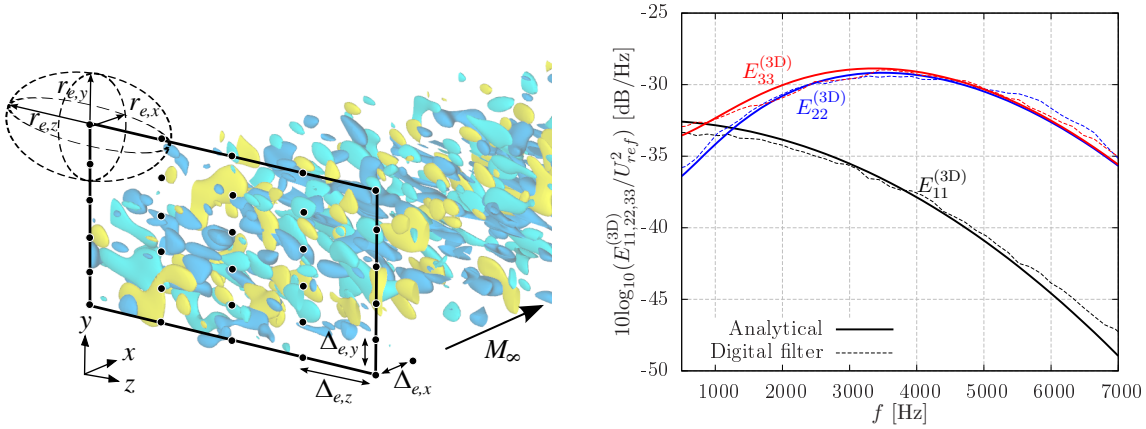

(a) Turbulence injection plane.

(b) One-dimensional spectra, $U_{ref} = 1\,\mathrm{m/s}$.

Figure 5.5: Three-dimensional anisotropic Gaussian turbulence with $u_0'^2 = 3\,\mathrm{m}^2/\mathrm{s}^2$, $l_x = 0.008\,\mathrm{m}$, $l_y = 2l_x$, and $l_z = 3l_x$. The injection plane parameters are $r_{e,x} = 3l_x/2$, $r_{e,y} = 3l_y/2$, $r_{e,z} = 3l_z/2$, $\Delta_{e,x} = l_x/2$, $\Delta_{e,y} = l_y/2$, and $\Delta_{e,z} = l_z/2$.

5.2 Investigation into the Spanwise Wavenumber

In Chapter 4, the pseudo three-dimensional turbulence approach was found to be suitable for leading edge noise predictions of aerofoils with straight leading edge and constant spanwise cross-section. This approach is based on the assumption that only the spanwise wavenumber $k_z = 0$ contributes to the far-field noise at the mid-span plane, due to the symmetry of the flat plate configuration studied by Amiet [39]. However, CAA simulations in Chapter 4 were intended for isotropic turbulence. This section performs leading edge noise predictions using fully and pseudo three-dimensional anisotropic turbulence. The aim is to assess the influence of the spanwise wavenumber on leading edge noise predictions when using anisotropic turbulence. To this end, a NACA 0012 aerofoil at $AoA = 0^{\circ}$ is simulated using an inviscid mean flow with $M_\infty = 0.3$. The aerofoil chord and semi-span were set to $c = 0.15\,\text{m}$ and $d = 0.1125\,\text{m}$, respectively.

5.2.1 Numerical Setup for Fully Three-dimensional Turbulence

Fully three-dimensional anisotropic Gaussian turbulence was injected into the CAA domain with $u_0'^2 = 3\,\text{m}^2/\text{s}^2$, $l_x = 0.008\,\text{m}$, $l_y = 2l_x$, and $l_z = 3l_x$, as shown in Figure 5.6. The turbulent structures are predominantly elongated in the spanwise direction, which is convenient to study possible effects of the spanwise wavenumber on the noise. Note that periodic boundary conditions are set in the spanwise direction, as explained in Section 4.3.2.

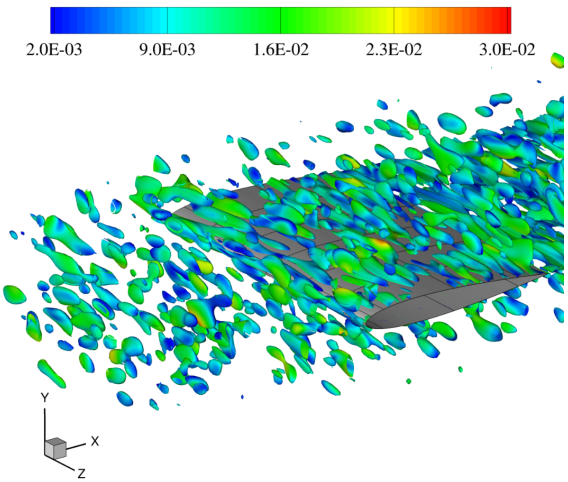

Figure 5.6: Iso-contours of constant Q-criterion coloured by non-dimensional fluctuating velocity magnitude, $\|\mathbf{u}'\|/c_\infty$, interacting with a three-dimensional NACA 0012 aerofoil at $M_\infty = 0.3$ and $AoA = 0^{\circ}$. Three-dimensional anisotropic Gaussian turbulence was generated with $u_0'^2 = 3\,\text{m}^2/\text{s}^2$, $l_x = 0.008\,\text{m}$, $l_y = 2l_x$, and $l_z = 3l_x$.

5.2.2 Numerical Setup for Pseudo Three-dimensional Turbulence

The pseudo three-dimensional turbulence approach (see Section 4.2) is also used here to reduce the computational cost associated with fully three-dimensional simulations. The purpose is to model the aerofoil response from a two-dimensional CAA simulation. Then, a three-dimensional FW-H solver is used for the far-field noise radiation. The CAA simulation of the NACA 0012 aerofoil was performed by using two-dimensional anisotropic turbulence with $u_0'^2 = 0.019\,\mathrm{m}^2/\mathrm{s}^2$, $l_x = 0.008\,\mathrm{m}$, and $l_y = 2l_x$, as described in Section 5.1.1. These input parameters ensure that the resulting two-dimensional velocity spectra from Equations 5.3a and 5.3b are similar in shape and levels to those defined by Equations 5.7a and 5.7b for three-dimensional turbulence, if $k_z = 0$ is assumed.

5.2.3 Influence of Spanwise Wavenumber on Leading Edge Noise

Figure 5.7 shows PWL spectra of NACA 0012 aerofoils from the CAA simulations and the flat plate prediction using the analytical model of Amiet [39] with the upwash velocity spectrum of anisotropic turbulence. Similar noise predictions can be obtained from pseudo and fully three-dimensional simulations, which confirm the validity of the $k_z = 0$ assumption for anisotropic turbulence. Thus, the acoustic response of three-dimensional aerofoils with straight leading edge and constant cross-section can be modelled as two-dimensional, even in the presence of anisotropic turbulence. Overall, the PWL spectra of the NACA 0012 aerofoil show similar trends as reported for thick aerofoils in isotropic turbulence. At low frequencies, $fc/U_\infty < 3$, there is a reasonable agreement between the thick aerofoil and the flat plat prediction. However, a noticeable decay on the noise levels is observed at high frequencies, as a consequence of the aerofoil thickness.

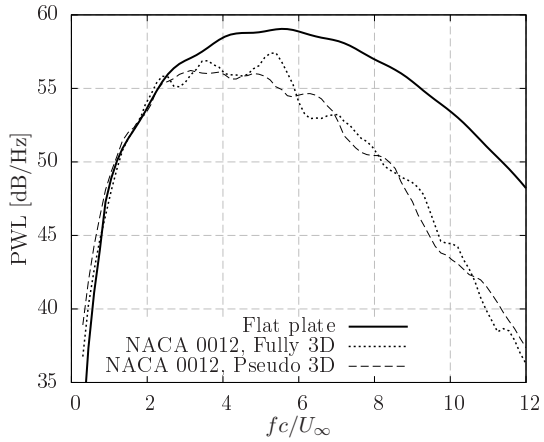

Figure 5.7: PWL spectra of a NACA 0012 aerofoil using fully and pseudo three-dimensional anisotropic Gaussian turbulence in comparison with the flat plate prediction.

5.3 Effects of Anisotropic Turbulence on Leading Edge Noise

In this section, a number of parameters are examined to better understand the effects of anisotropy on turbulence-aerofoil interaction noise, including variations in freestream Mach number, aerofoil thickness, angle of attack, and turbulence length scale-to-chord ratio. To reduce the computational expense, two-dimensional CAA simulations are performed by means of the pseudo three-dimensional turbulence approach. Anisotropic synthetic turbulence with the key statistics of the homogeneous axisymmetric model of Kerschen and Gliebe [113] is generated by superimposing a number of anisotropic Gaussian eddies with various length scales. This allows an extension of the spectral content, which is useful to study the effects of anisotropic turbulence on leading edge noise at high frequencies. CAA simulations were performed for aerofoils with $c = 0.15$ m and $d = 0.225$ m.

5.3.1 Homogeneous Axisymmetric Turbulence

For homogeneous axisymmetric turbulence that is aligned with the mean flow in the x-direction, the axial and transverse velocity spectra are defined according to Kerschen and Gliebe [113] as

$$\Phi_{11}^{(3D)}(k_x, k_y, k_z) = \frac{2 l_a l_t^4 u_a'^2 \left(k_y^2 + k_z^2\right)}{\pi^2 \left[1 + l_a^2 k_x^2 + l_t^2 \left(k_y^2 + k_z^2\right)\right]^3}, \tag{5.8a}$$

$$\Phi_{22}^{(3D)}(k_x, k_y, k_z) = \frac{2 l_a l_t^4 u_a'^2}{\pi^2 \left[1 + l_a^2 k_x^2 + l_t^2 \left(k_y^2 + k_z^2\right)\right]^3} \left[k_x^2 + k_z^2 \left(2\frac{u_t'^2}{u_a'^2} - \frac{l_t^2}{l_a^2}\right)\right], \tag{5.8b}$$

respectively, where u_a', l_a, and u_t', l_t, are the root-mean-square velocity fluctuations and length scales in the axial and transverse directions, respectively. The length scales in the model of Kerschen and Gliebe [113] are related to the longitudinal and transverse integral length scales, $l_{11}^{(1)}$ and $l_{22}^{(1)}$, as follows

$$l_{11}^{(1)} = \frac{\pi}{u_{x,rms}'^2} \int_{-\infty}^{\infty} \int_{-\infty}^{\infty} \Phi_{11}^{(3D)}(k_x = 0, k_y, k_z) \mathrm{d}k_y \mathrm{d}k_z = l_a, \tag{5.9}$$

$$l_{22}^{(1)} = \frac{\pi}{u_{y,rms}'^2} \int_{-\infty}^{\infty} \int_{-\infty}^{\infty} \Phi_{22}^{(3D)}(k_x = 0, k_y, k_z) \mathrm{d}k_y \mathrm{d}k_z = \frac{l_a}{2} \frac{u_a'^2}{u_t'^2} \left(2\frac{u_t'^2}{u_a'^2} - \frac{l_t^2}{l_a^2}\right). \tag{5.10}$$

A constraint of this model is that $2(u_t'/u_a')^2 \geq (l_t/l_a)^2$, which is easily satisfied in typical fan wake experiments. Furthermore, the isotropic turbulence model of Liepmann *et al.* [157] is recovered from Equations 5.8a and 5.8b when $u_a' = u_t' = u_{rms}'$ and $l_a = l_t = \Lambda$. It can additionally be verified that $l_{11}^{(1)}/l_{22}^{(1)} = 2$ is satisfied under these conditions.

The superposition of Gaussian spectra is useful to expand the spectral content of a turbulent flow. The shape of a three-dimensional velocity spectrum $\Phi_{ij}^{(3D)}(k_x, k_y, k_z = 0)$ can be reproduced through a linear summation of N_e two-dimensional anisotropic Gaussian spectra, $\sum_{n=1}^{N_e} \Phi_{ij,n}^{(2D)}(k_x, k_y)$. To this end, anisotropic Gaussian eddies with various $u'_{0,i}$, $l_{x,i}$, and $l_{y,i}$ for $i = 1, ..., N_e$ are introduced simultaneously at each eddy centre along the injection plane. The fluctuating velocity field introduced by the summation of N_e eddies at each eddy centre is given by

$$u'_{x,p}(\mathbf{x}) = -\sqrt{2\pi\Delta_{e,x}\Delta_{e,y}}\left(y - y_p\right)\sum_{i=1}^{N_e}\frac{\epsilon_{p,i}u'_{0,i}}{l_{y,i}^2}\exp\left[-\frac{\pi\left(x - x_p\right)^2}{2l_{x,i}^2}\right]\exp\left[-\frac{\pi\left(y - y_p\right)^2}{2l_{y,i}^2}\right], \tag{5.11a}$$

$$u'_{y,p}(\mathbf{x}) = \sqrt{2\pi\Delta_{e,x}\Delta_{e,y}}\left(x - x_p\right)\sum_{i=1}^{N_e}\frac{\epsilon_{p,i}u'_{0,i}}{l_{x,i}^2}\exp\left[-\frac{\pi\left(x - x_p\right)^2}{2l_{x,i}^2}\right]\exp\left[-\frac{\pi\left(y - y_p\right)^2}{2l_{y,i}^2}\right]. \tag{5.11b}$$

Limiting values for the eddy radius and separation between eddy centres are based on the largest and shortest length scales involved in each spatial direction. Thus, the correct statistics of the turbulent flow are obtained provided that $r_{e,x} \geq 3\max\{l_{x,i}\}/2$, $r_{e,y} \geq 3\max\{l_{y,i}\}/2$, $\Delta_{e,x} \leq \min\{l_{x,i}\}/2$, and $\Delta_{e,y} \leq \min\{l_{y,i}\}/2$ for $i = 1, ..., N_e$.

To study the effects of anisotropy on leading edge noise, the baseline configuration corresponds to the isotropic Liepmann spectrum with $l_a = l_t = 0.008\,\text{m}$, and $u'_a = 0.017U_\infty$. Note that u'_t is not explicitly defined in Equations 5.8a and 5.8b if $k_z = 0$. Nevertheless, u'_t is assumed to take a value that satisfies the constraint $2(u'_t/u'_a)^2 \geq (l_t/l_a)^2$ for the validity of the model.

From the baseline configuration, l_a/l_t is varied between 0.33 and 3 to assess the effects of moderately anisotropic turbulence. In ducted-fan configurations and open-jet wind tunnel experiments, turbulent flows are normally stretched in the axial direction. Therefore, cases with $l_a/l_t > 1$ are particularly relevant for turbofan engine applications. Nevertheless, cases with $l_a/l_t < 1$ are also documented here for completeness of the analysis. Table 5.1 presents values of $u'_{0,i}$, $l_{x,i}$, and $l_{y,i}$ for the superposition of anisotropic Gaussian spectra. These values were found by fitting the analytical spectra with an accuracy better than 1.5 dB for reduced frequencies $fc/U_\infty \leq 12$.

Length scales	ith Gaussian eddy	$l_{x,i}$ [m]	$l_{y,i}$ [m]	$u'^2_{0,i}$ [m^2/s^2] ($M_\infty = 0.3$)	$u'^2_{0,i}$ [m^2/s^2] ($M_\infty = 0.6$)
$l_a/l_t = 3$ $l_t = 0.008$ m	1	7.50×10^{-2}	2.50×10^{-2}	1.40×10^{-4}	6.50×10^{-4}
	2	4.70×10^{-2}	1.65×10^{-2}	4.60×10^{-4}	1.91×10^{-3}
	3	2.80×10^{-2}	9.50×10^{-3}	4.10×10^{-4}	1.45×10^{-3}
	4	1.50×10^{-2}	5.10×10^{-3}	2.20×10^{-4}	8.50×10^{-4}
	5	6.55×10^{-3}	4.00×10^{-3}	1.60×10^{-5}	6.40×10^{-5}
$l_a/l_t = 2$ $l_t = 0.008$ m	1	4.70×10^{-2}	2.35×10^{-2}	3.90×10^{-4}	1.56×10^{-3}
	2	2.60×10^{-2}	1.30×10^{-2}	9.00×10^{-4}	3.60×10^{-3}
	3	1.42×10^{-2}	7.20×10^{-3}	4.20×10^{-4}	1.68×10^{-3}
	4	8.00×10^{-3}	4.00×10^{-3}	1.80×10^{-4}	7.20×10^{-4}
	5	4.40×10^{-3}	8.00×10^{-3}	4.50×10^{-6}	1.80×10^{-5}
$l_a = l_t = 0.008$ m isotropic turbulence	1	2.35×10^{-2}	2.35×10^{-2}	7.38×10^{-4}	3.00×10^{-3}
	2	1.30×10^{-2}	1.30×10^{-2}	1.77×10^{-3}	7.00×10^{-3}
	3	7.20×10^{-3}	7.20×10^{-3}	7.10×10^{-4}	2.50×10^{-3}
	4	5.00×10^{-3}	5.00×10^{-3}	5.00×10^{-4}	2.00×10^{-3}
$l_a/l_t = 0.5$ $l_a = 0.008$ m	1	2.10×10^{-2}	4.10×10^{-2}	4.70×10^{-3}	1.90×10^{-2}
	2	1.05×10^{-2}	2.10×10^{-2}	7.80×10^{-3}	3.00×10^{-2}
	3	4.70×10^{-3}	9.60×10^{-3}	2.50×10^{-3}	1.00×10^{-2}
	4	5.30×10^{-3}	4.90×10^{-3}	1.80×10^{-4}	7.00×10^{-4}
	5	5.00×10^{-3}	1.30×10^{-2}	1.00×10^{-5}	4.00×10^{-5}
$l_a/l_t = 0.33$ $l_a = 0.008$ m	1	2.50×10^{-2}	7.80×10^{-2}	4.00×10^{-3}	1.60×10^{-2}
	2	1.65×10^{-2}	4.70×10^{-2}	1.15×10^{-2}	4.60×10^{-2}
	3	9.50×10^{-3}	2.80×10^{-2}	1.20×10^{-2}	4.80×10^{-2}
	4	5.10×10^{-3}	1.50×10^{-2}	6.00×10^{-3}	2.40×10^{-2}
	5	4.00×10^{-3}	6.55×10^{-3}	4.80×10^{-4}	1.90×10^{-3}

Table 5.1: Parameters for Gaussian superposition to obtain a two-dimensional fluctuating velocity field with the statistics of axisymmetric turbulence as defined by Kerschen and Gliebe [113], assuming $k_z = 0$ with $u'_a/U_\infty = 0.017$.

5.3.2 Flat Plates and Thin Aerofoils at Zero Angle of Attack

CAA simulations of a NACA 0001 aerofoil at $M_\infty = 0.6$ and $AoA = 0^o$ are presented in this section. The aerofoil chord and the semi-span are set to $c = 0.15\,\text{m}$ and $d = 0.225\,\text{m}$, respectively. The mean flow is assumed to be uniform, which is valid for thin aerofoils. To assess that the correct velocity spectra are recovered from the CAA simulations, a monitor point was placed at approximately $0.2c$ upstream of the aerofoil leading edge along the stagnation line. Figure 5.8 shows numerical and analytical one-dimensional spectra of anisotropic turbulence for moderate ratios of l_a/l_t. Results are in good agreement, showing the effectiveness of the anisotropic Gaussian superposition methodology.

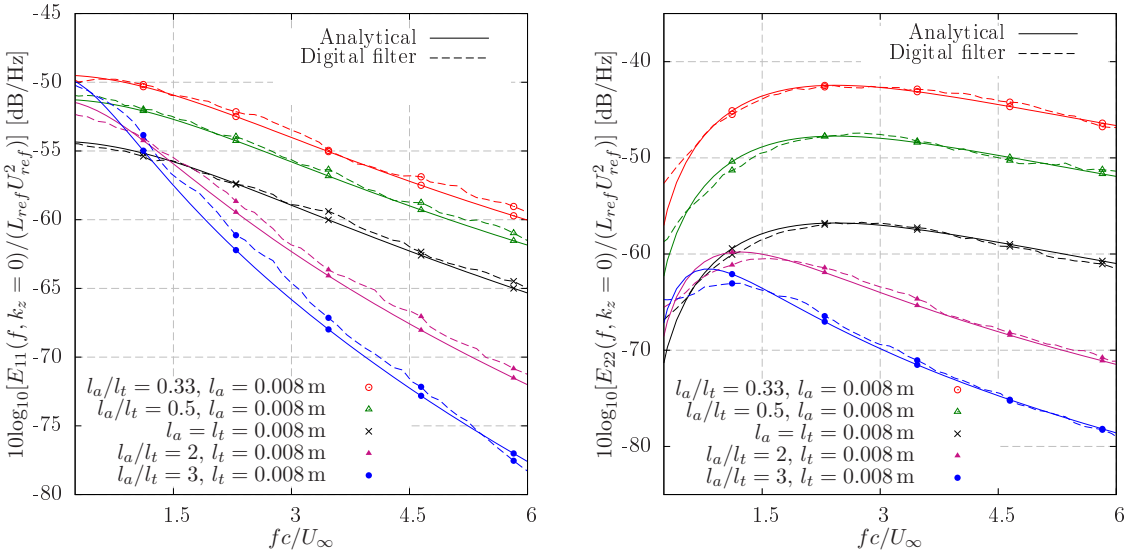

(a) Streamwise. (b) Transverse.

Figure 5.8: One-dimensional spectra of homogeneous axisymmetric turbulence as defined by Kerschen and Gliebe [113], assuming $k_z = 0$ with $M_\infty = 0.6$ and $u'_a/U_\infty = 0.017$. The reference length and speed are $L_{ref} = 1\,\text{m}$ and $U_{ref} = 1\,\text{m/s}$, respectively.

Both E_{11} and E_{22} show similar behaviours with respect to the isotropic turbulence baseline. An increase in the streamwise length scale, $l_a/l_t > 1$, leads to slightly higher amplitudes at low frequencies and a significant reduction at high frequencies. Additionally, the maximum in E_{22} is shifted towards lower frequencies. In contrast, an increase in the transverse length scale ($l_a/l_t < 1$) leads to a nearly constant increase in amplitude at all frequencies. The use of axisymmetric turbulence produces a redistribution of the energy in the velocity spectra when compared to isotropic turbulence with the same turbulent kinetic energy. This redistribution, which is caused by the different length scales involved, changes the amount of energy that could potentially contribute to the leading edge noise. Consequently, two flows with the same turbulent kinetic energy can produce different leading edge

noise depending on the spatial length scales. This is particularly important for analytical models, in which noise predictions are quite sensitive to the input turbulence model, as reported by Posson *et al.* [112]. Grace [114] also highlighted the importance of the turbulence length scales in the power spectrum from a low-order cascade model.

Figure 5.9 shows the numerical PWL and SPL spectra of a NACA 0001 aerofoil. The PWL spectra are computed from the sound power as given in Equation 4.14. Additionally, the analytical flat plate prediction of Amiet [39] has been computed by using the transverse velocity spectrum in Equation 5.8b. The agreement between numerical and analytical predictions is better than 2 dB at all frequencies. In the cascade model of Posson *et al.* [112], a strong decrease in noise levels at high frequencies and a shift of the maximum towards lower frequencies was found when using the axisymmetric turbulence model of Kerschen and Gliebe [113] with $l_a/l_t = 2$ in comparison to the case with $l_a/l_t = 1$ (isotropic turbulence). Similar trends are reported for the PWL spectra of a single flat plate in Figure 5.9, which are also consistent with the findings of Atassi and Logue [156] using rapid distortion theory to model anisotropy at the fan intake.

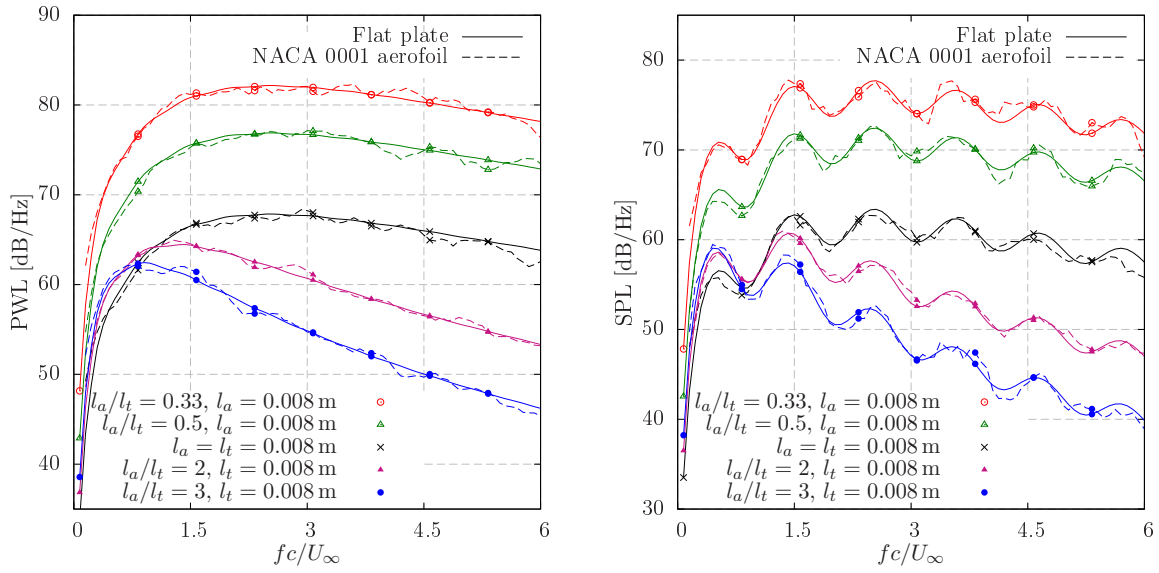

(a) PWL spectra.

(b) SPL spectra at $\theta = 90^o$.

Figure 5.9: PWL and SPL spectra for a NACA 0001 aerofoil in anisotropic turbulence.

The trends of the transverse turbulence spectra in Figure 5.8b closely follow those of the PWL spectra in Figure 5.9a. Thus, E_{22} and PWL spectra present a maximum at the same chord-based reduced frequency for each anisotropic turbulence case. Furthermore, the amplitude separation in dB at a fixed frequency between two particular ratios, l_a/l_t, is similar in E_{22} and PWL spectra. Amiet [39] showed that the broadband noise due to the interaction of isotropic turbulence with a flat plate only

depends on the transverse velocity spectrum ($S_{pp}^{(3D)} \propto \Phi_{22}^{(3D)}(k_x, k_z = 0)$ as can be seen in Equation 4.10). This result remains valid for thin aerofoils in anisotropic turbulence.

Directivity patterns at $fc/U_\infty = 3$ are shown in Figure 5.10 for further validation of the CAA simulations. The agreement of the numerical results with the flat plate model of Amiet [39] is better than 2 dB at the majority of observer angles. The location of the lobes due to the loss of compactness at high frequencies is correctly predicted by the numerical simulations.

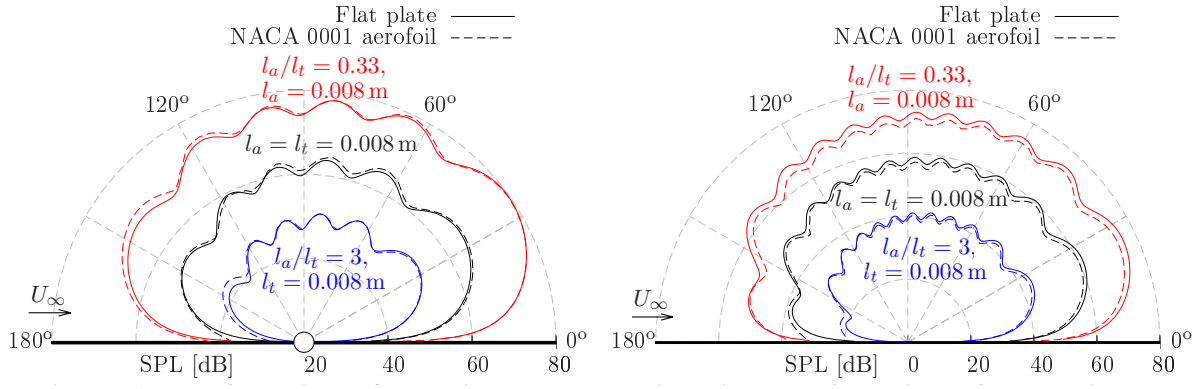

(a) SPL spectra at $fc/U_\infty = 3$.

(b) SPL spectra at $fc/U_\infty = 6$.

Figure 5.10: Noise directivity for a NACA 0001 aerofoil at $M_\infty = 0.6$ using anisotropic turbulence.

5.3.3 Thick Aerofoils at Zero Angle of Attack in Various Mach Number Flows

The effects of aerofoil thickness on the noise are studied for a NACA 0012 aerofoil at $AoA = 0^o$. CAA simulations were performed by assuming inviscid mean flows at two different freestream Mach numbers, $M_\infty = 0.3$ and 0.6, and by using the parameters that are given in Table 5.1 for the anisotropic Gaussian superposition. Figure 5.11 shows instantaneous contours of non-dimensional vorticity magnitude and fluctuating pressure in CAA simulations with eddies stretched in the streamwise and transverse directions. In both cases, acoustic pressure is generated at the aerofoil leading edge and radiated to the far-field with a dipole-like directivity, as occurs with isotropic turbulence (for example, see Figure 3.10). However, pressure contours due to anisotropic turbulence with $l_a/l_t = 0.33$ present a broader frequency content than those with $l_a/l_t = 3$. This observation is related to the shape of the one-dimensional spectra shown in Figure 5.8, in which the small amplitude difference between high and low frequencies in the $l_a/l_t = 0.33$ case makes fluctuating pressure contours to show a wide frequency content. In contrast, most energy in one-dimensional spectra with $l_a/l_t = 3$ concentrates at low frequencies.

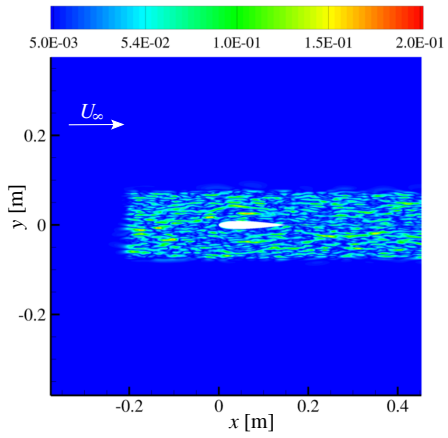

(a) Non-dimensional vorticity magnitude, $\|\nabla \times \mathbf{u}'\| L_{ref}/c_\infty$, of anisotropic turbulence with $l_a/l_t = 3$.

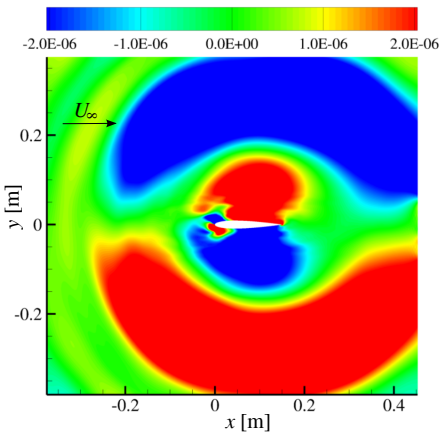

(b) Non-dimensional fluctuating pressure, $p'/(\rho_\infty c_\infty^2)$, of anisotropic turbulence with $l_a/l_t = 3$.

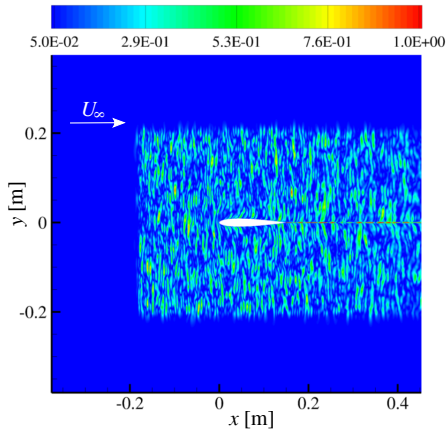

(c) Non-dimensional vorticity magnitude, $\|\nabla \times \mathbf{u}'\| L_{ref}/c_\infty$, of anisotropic turbulence with $l_a/l_t = 0.33$.

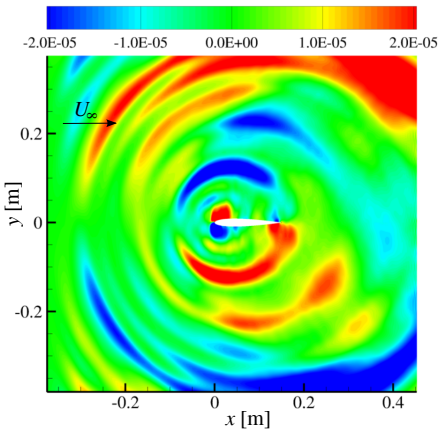

(d) Non-dimensional fluctuating pressure, $p'/(\rho_\infty c_\infty^2)$, of anisotropic turbulence with $l_a/l_t = 0.33$.

Figure 5.11: Instantaneous contour plots of a NACA 0012 aerofoil at $M_\infty = 0.3$ and $AoA = 0^o$ interacting with anisotropic synthetic turbulence.

Figure 5.12 shows the PWL spectra from anisotropic turbulence interacting with a NACA 0012 aerofoil at $M_\infty = 0.3$ compared to analytical predictions for a flat plate. The noise reduction is quantified by plotting the $\Delta\text{PWL} = \text{PWL}|_{\text{flat plate}} - \text{PWL}|_{\text{NACA 0012}}$ spectra as a function of the thickness-based reduced frequency. The good overlap in the ΔPWL spectra indicates that the noise reduction due to aerofoil thickness occurs in all the anisotropic turbulence cases investigated. These cases follow the same trends as in the isotropic turbulence baseline. Therefore, the amount of noise reduction due to thickness at high frequencies is independent of the anisotropy in the flow.

The scaling law of Gershfeld [71] has been included in Figure 5.12b, which shows a consistent over-prediction of the noise reduction effect in comparison with the numerical ΔPWL spectra. The over-prediction is particularly pronounced at high frequencies. Alternatively, Equation 3.4 can provide an improved estimation of the ΔPWL spectra due to aerofoil thickness, even in the presence of moderately anisotropic turbulence.

Paterson and Amiet [79] tested a NACA 0012 aerofoil and found a 5 dB noise reduction at $ft_A/U_\infty = 1$, which was used as a reference value for the breakdown of the flat plate model. An earlier appearance of aerofoil thickness effects on the noise from a NACA 0012 aerofoil has been reported in recent numerical and experimental studies [87, 94]. In Figure 5.12b, the ΔPWL spectra for isotropic turbulence suggests that the breakdown occurs at a slightly lower frequency than predicted by Paterson and Amiet [79]. A 5 dB reduction in PWL due to thickness effect of a NACA 0012 aerofoil is found at approximately $ft_A/U_\infty = 0.9$ for both isotropic and anisotropic turbulence at $M_\infty = 0.3$.

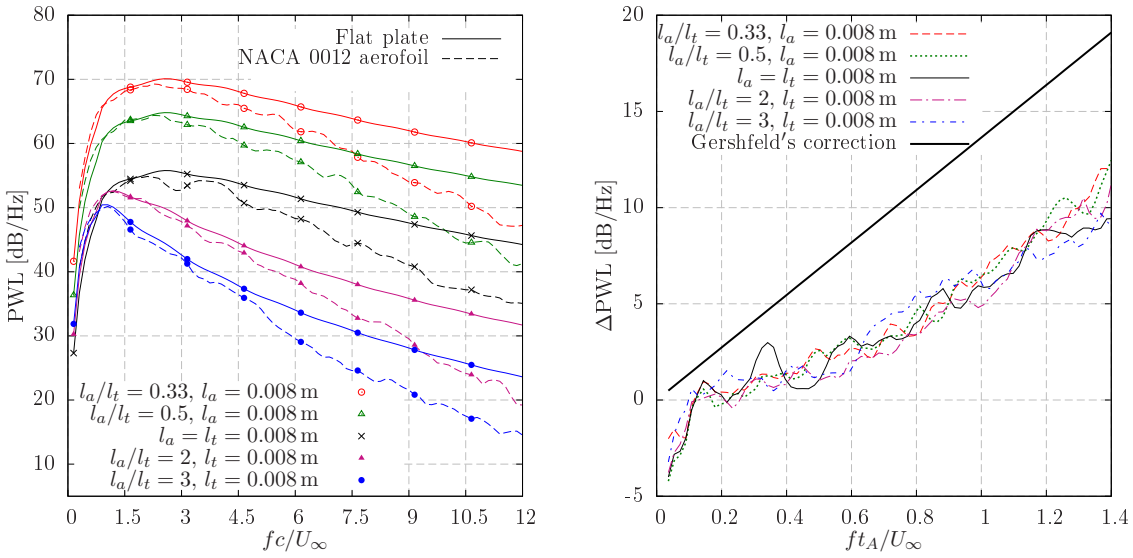

(a) PWL spectra.

(b) ΔPWL = PWL|$_{\text{flat plate}}$ − PWL|$_{\text{NACA 0012}}$.

Figure 5.12: Noise spectra for a NACA 0012 aerofoil at $M_\infty = 0.3$ and $AoA = 0^o$ interacting with anisotropic turbulence.

Figure 5.13 shows a directivity plot at $fc/U_\infty = 9$. ΔSPL = SPL|$_{\text{flat plate}}$ − SPL|$_{\text{NACA 0012}}$ exhibits a more pronounced noise reduction at downstream observer angles, $\theta < 45^o$, for both isotropic and anisotropic turbulence. Furthermore, the directivity pattern at a fixed frequency seems to be independent of the degree of anisotropy in the flow, as the location of the lobes are similar for l_a/l_t ranging between 0.33 and 3.

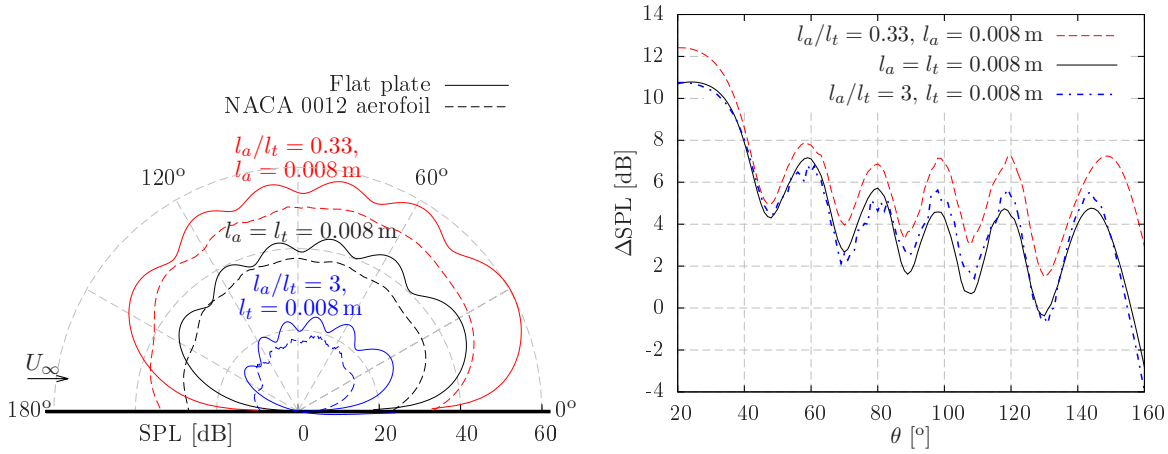

(a) SPL spectra.

(b) $\Delta\text{SPL} = \text{SPL}|_{\text{flat plate}} - \text{SPL}|_{\text{NACA 0012}}$.

Figure 5.13: Noise directivity at $fc/U_\infty = 9$ for a NACA 0012 aerofoil at $M_\infty = 0.3$ and $AoA = 0^o$ interacting with anisotropic turbulence.

The PWL spectra from simulations with a freestream Mach number of $M_\infty = 0.6$ are presented in Figure 5.14. ΔPWL spectra scales linearly with ft_A/U_∞, as found for $M_\infty = 0.3$ in Figure 5.12b. However, the increase in the mean flow Mach number results in a worse overlap of the ΔPWL spectra for different levels of anisotropy, as can be seen in Figure 5.14b. Particularly, $\Delta\text{PWL}|_{l_a/l_t>1}$ is consistently lower than $\Delta\text{PWL}|_{l_a/l_t<1}$. In other words, cases with turbulence stretched in the streamwise direction, $l_a/l_t > 1$, tend to be about $2-3$ dB louder at all frequencies than cases with turbulence stretched in the transverse direction, $l_a/l_t < 1$, when compared to their corresponding flat plate predictions. This difference is significant, since it goes beyond the uncertainty of the current CAA methodology, which is below 2 dB at a discrete frequency. In Chapter 3, it was found that the transverse velocity fluctuations are mainly responsible for the leading edge noise of a thick aerofoil at $AoA = 0^o$ in isotropic turbulence, which is consistent with previous findings of Gill *et al.* [41]. However, the streamwise fluctuating velocity component becomes increasingly important in anisotropic turbulence with $l_a/l_t > 1$, as can be inferred from Equation 5.4. Additionally, Kim *et al.* [95] found that the streamwise velocity fluctuations have a bigger influence on the noise as the Mach number increases. Consequently, it is hypothesised here that a relatively large ratio, l_a/l_t, may delay the onset of aerofoil thickness effects on leading edge noise at high Mach numbers.

Directivity plots at $fc/U_\infty = 9$ are shown in Figure 5.15 for a NACA 0012 aerofoil at $M_\infty = 0.6$. Similar to the directivity plots at $M_\infty = 0.3$ in Figure 5.13, noise reduction at a high frequency mainly occurs at downstream observer angles, $\theta < 45^o$. Furthermore, the location of the lobes occurs at similar radiation angles regardless of the degree of anisotropy in the flow. However, a smaller

$\Delta\text{SPL} = \text{SPL}|_{\text{flat plate}} - \text{SPL}|_{\text{NACA 0012}}$ can be found as l_a/l_t increases, which reinforces the hypothesis of aerofoil thickness effects on leading edge noise being delayed by large l_a/l_t at high Mach numbers.

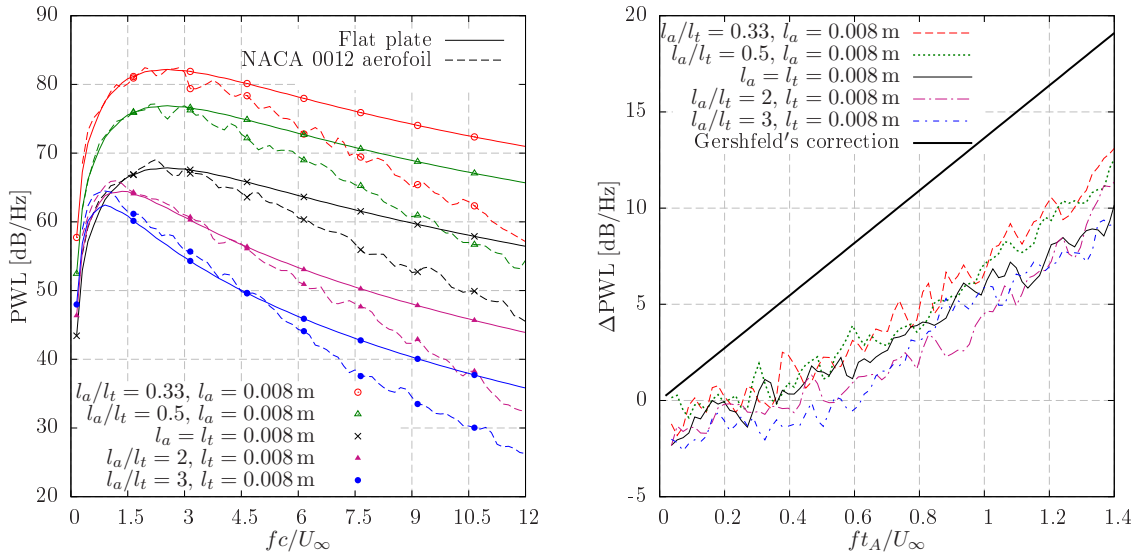

(a) PWL spectra.

(b) $\Delta\text{PWL} = \text{PWL}|_{\text{flat plate}} - \text{PWL}|_{\text{NACA 0012}}$.

Figure 5.14: Noise spectra for a NACA 0012 aerofoil at $M_\infty = 0.6$ and $AoA = 0^\text{o}$ interacting with anisotropic turbulence.

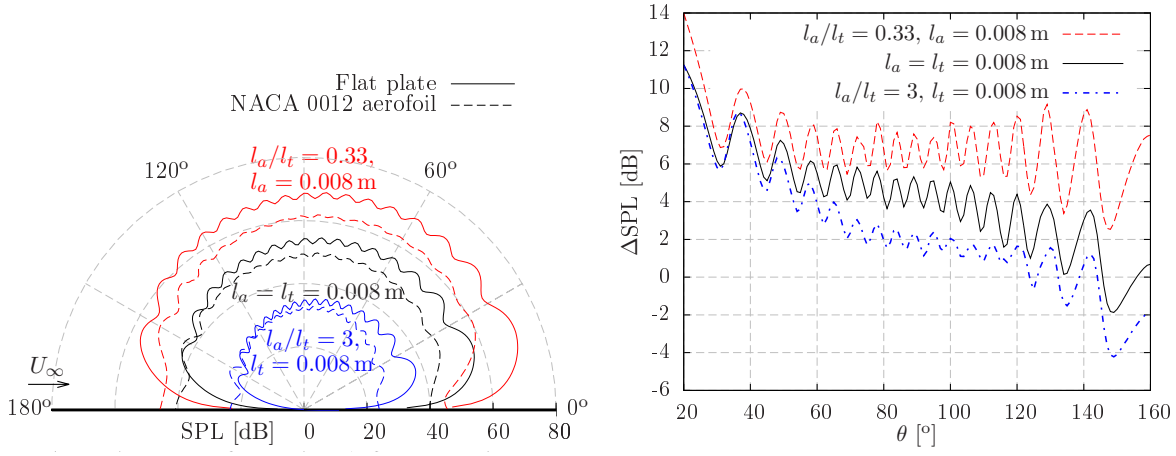

(a) SPL spectra.

(b) $\Delta\text{SPL} = \text{SPL}|_{\text{flat plate}} - \text{SPL}|_{\text{NACA 0012}}$.

Figure 5.15: Noise directivity at $fc/U_\infty = 9$ for a NACA 0012 aerofoil at $M_\infty = 0.6$ and $AoA = 0^\text{o}$ interacting with anisotropic turbulence.

5.3.4 Thick Aerofoils at Non-Zero Angle of Attack

In this section, the NACA 0012 aerofoil is rotated 6° around its leading edge to study the effects of angle of attack on leading edge noise using anisotropic turbulence. An inviscid mean flow with freestream Mach number $M_\infty = 0.3$ is used in CAA simulations. This aerofoil configuration is suitable to study possible effects of angle of attack on the noise, while ensuring a subsonic flow around the aerofoil.

Figure 5.16a presents the PWL spectra of a NACA 0012 aerofoil at $AoA = 6^o$ for various l_a/l_t in comparison to simulations at $AoA = 0^o$ from Section 5.3.3. The PWL spectra show that an increase in the angle of attack tends to reduce the noise of a thick aerofoil in anisotropic turbulence with $l_a/l_t < 1$, especially at high frequencies. Synthetic turbulence methods that only enforce the transverse velocity fluctuations under-predict the leading edge noise of thick aerofoils at non-zero angle of attack, as shown in Section 3.3. In a way, this also occurs in anisotropic turbulence with $l_a/l_t < 1$, since the transverse fluctuating velocity component is larger than the streamwise component, and is thus the dominant component, producing the noise reduction at non-zero angle of attack. Further evidence of the similarity between synthetic turbulence that only models the transverse velocity fluctuations and anisotropic turbulence stretched in the transverse direction can be observed in Figures 3.10a and 5.11c, respectively. In both cases, non-dimensional contours of vorticity magnitude exhibit similar flow features, such as turbulent structures elongated in the transverse direction.

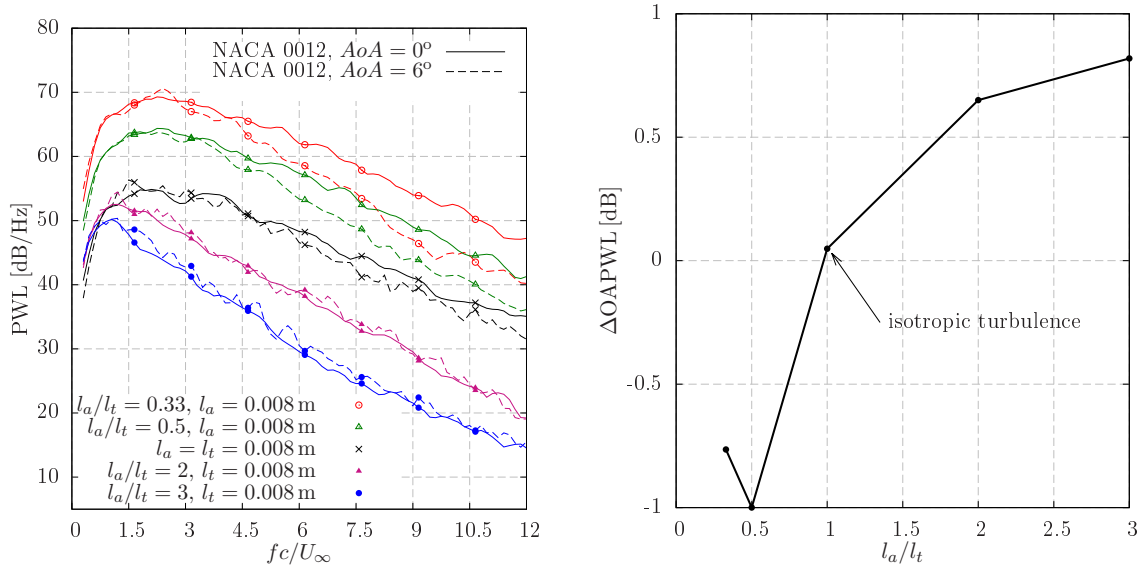

(a) PWL spectra.

(b) $\Delta\text{OAPWL} = \text{OAPWL}|_{AoA=6^o} - \text{OAPWL}|_{AoA=0^o}$.

Figure 5.16: Noise predictions for a NACA 0012 aerofoil at $AoA = 0^o$ and 6^o in a $M_\infty = 0.3$ flow interacting with anisotropic turbulence.

In anisotropic turbulence with $l_a/l_t > 1$, the PWL spectra in Figure 5.16a present a consistent increase of about 1 dB at all frequencies. Although such an increase is within the level of accuracy of the current methodology, the result indicates that a moderate increase in the angle of attack of a thick aerofoil has a small impact on the PWL spectra. In contrast, Devenport *et al.* [78] showed an increase in SPL of about 5 dB for every 4° increment at 800 Hz for a NACA 0015 aerofoil at $M_\infty = 0.08$ with $l_a/l_t = 2$, suggesting a stronger effect of anisotropy on leading edge noise. The results of this thesis, which have been validated by using a flat plate theory in Section 5.3.2, are also consistent with experimental findings. Although turbulence is considered nearly isotropic in open-jet wind tunnel experiments of leading edge noise, a certain degree of anisotropy exists [79, 82, 158]. For example, Paterson and Amiet [150] found that the effect of angle of attack on leading edge noise was negligible for a NACA 0012 aerofoil, despite correcting the von Kármán isotropic spectrum with a contracted spanwise correlation length to account for some anisotropy in the flow. Additionally, the use of isotropic spectra in analytical models for the prediction of fan-OGV interaction noise usually offers an acceptable agreement with experiments [102, 112], in which the fan wakes often present $l_a/l_t > 1$, suggesting that potential anisotropy effects might be negligible.

The discrepancy with the findings reported by Devenport *et al.* [78] may be explained by the different assumptions involved in the numerical methodologies. Devenport *et al.* [78] used a panel method that is valid for leading edge noise predictions of aerofoils in incompressible flows, i.e. low Mach numbers, whereas the LEEs can deal with compressible flows. Additionally, the panel method assumed the aerofoil to be acoustically compact such that the aerofoil chord is significantly smaller than the acoustic wavelength. Consequently, the noise predictions performed by Devenport *et al.* [78] were restricted to frequencies below 1000 Hz. The validity of the results presented in the current work extends to frequencies up to 8160 Hz for $M_\infty = 0.3$, which corresponds to $fc/U_\infty = 12$. Furthermore, the loss of compactness, which causes lobes in directivity plots at high frequencies, is correctly modelled by the LEEs.

Figure 5.16b shows variations in $\Delta\text{OAPWL} = \text{OAPWL}|_{AoA=6^\circ} - \text{OAPWL}|_{AoA=0^\circ}$ with l_a/l_t. The OverAll PWL (OAPWL) for each aerofoil configuration is calculated as

$$\text{OAPWL} = 10\log_{10}\left(\frac{\int \mathcal{P}(f)\mathrm{d}f}{\mathcal{P}_{ref}}\right), \tag{5.12}$$

where the sound power of the aerofoil is calculated as in Equation 4.14, and integrated for frequencies between 204 Hz ($fc/U_\infty = 0.3$) and 8160 Hz ($fc/U_\infty = 12$). The ΔOAPWL calculation shows a nearly negligible effect of angle of attack for aerofoils interacting with isotropic turbulence, $\Delta\text{OAPWL} \approx 0\,\text{dB}$. However, there is a small increase ($< 1\,\text{dB}$) in the noise when turbulence is stretched in the streamwise direction, $l_a/l_t > 1$, and a decrease as turbulence is stretched in the transverse direction, $l_a/l_t < 1$. It should be noted that the OAPWL is mainly dominated by low frequencies

with large sound levels, which may mask differences in the PWL spectra at high frequencies. Overall, the effect of the angle of attack on leading edge noise due to moderately anisotropic turbulence is small, with differences in ΔOAPWL smaller than 1 dB for l_a/l_t ranging from 0.33 to 3.

Figure 5.17 shows directivity plots of NACA 0012 aerofoils at various chord-based reduced frequencies and l_a/l_t. The leading edge noise reduction that was identified for the aerofoil at $AoA = 6^o$ in anisotropic turbulence with $l_a/l_t < 1$ is mainly produced at downstream observer angles. For cases with anisotropic turbulence stretched in the streamwise direction, no significant variations in SPL are observed at a particular observer location due to a change in angle of attack.

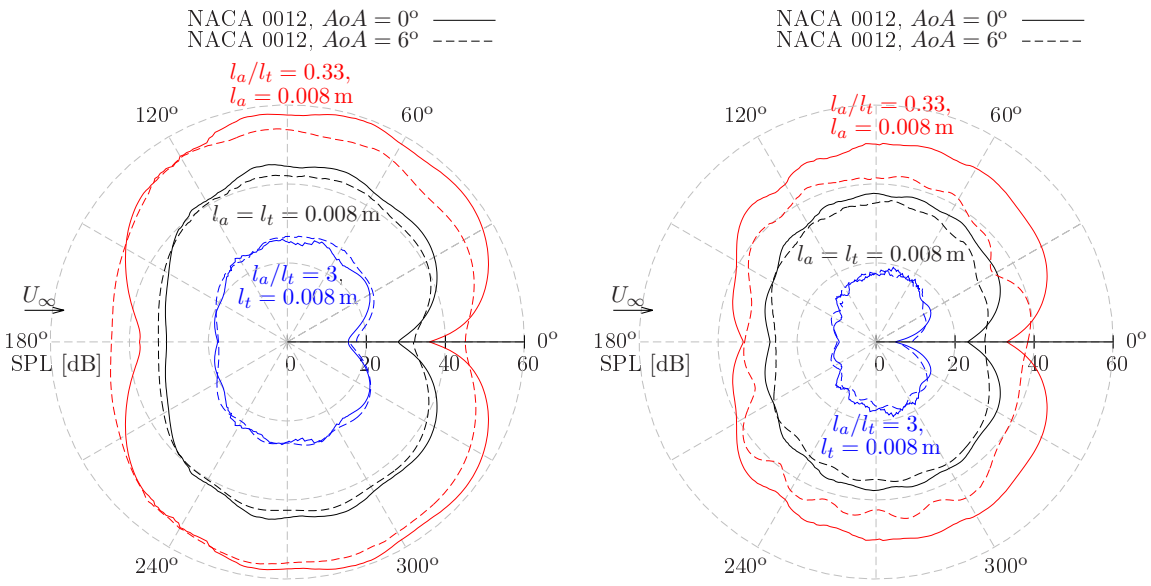

(a) SPL spectra at $fc/U_\infty = 6$.

(b) SPL spectra at $fc/U_\infty = 9$.

Figure 5.17: Directivity plots for a NACA 0012 aerofoil at $AoA = 0^o$ and 6^o in a $M_\infty = 0.3$ flow interacting with anisotropic turbulence.

5.3.5 Turbulence Length Scale-to-Chord Ratio

In this thesis, leading edge noise predictions have been performed for aerofoils in which the chord is significantly larger than the turbulence length scale, as occurs in turbofan engines. While keeping this assumption, this section presents simulations of a NACA 0012 aerofoil in a $M_\infty = 0.3$ flow at $AoA = 0^o$ and 6^o with twice the baseline turbulence length scale (0.016 m instead of 0.008 m). The objective is to assess whether an increase in the ratio between the turbulence length scales and the aerofoil chord can vary the conclusions achieved in previous sections. The configurations studied are

$l_a/l_t = 0.5$ with $l_a = 0.016\,\text{m}$ and $l_a/l_t = 2$ with $l_t = 0.016\,\text{m}$. The parameters for the anisotropic Gaussian superposition are given in Table 5.2. Additionally, Table 5.3 presents a summary of the turbulence length scale-to-chord ratios in this chapter.

Length scales	ith Gaussian eddy	$l_{x,i}$ [m]	$l_{y,i}$ [m]	$u'^2_{0,i}$ [m^2/s^2] ($M_\infty = 0.3$)
$l_a/l_t = 2$ $l_t = 0.016\,\text{m}$	1	9.40×10^{-2}	4.70×10^{-2}	7.80×10^{-4}
	2	5.18×10^{-2}	2.60×10^{-2}	1.80×10^{-3}
	3	2.80×10^{-2}	1.40×10^{-2}	8.38×10^{-4}
	4	1.60×10^{-2}	7.80×10^{-3}	3.20×10^{-4}
	5	8.60×10^{-3}	1.40×10^{-2}	1.02×10^{-5}
	6	1.20×10^{-2}	4.00×10^{-3}	5.00×10^{-5}
	7	4.40×10^{-3}	4.40×10^{-3}	9.00×10^{-6}
$l_a/l_t = 0.5$ $l_a = 0.016\,\text{m}$	1	4.70×10^{-2}	9.40×10^{-2}	6.24×10^{-3}
	2	2.60×10^{-2}	5.18×10^{-2}	1.44×10^{-2}
	3	1.40×10^{-2}	2.80×10^{-2}	6.70×10^{-3}
	4	7.80×10^{-3}	1.60×10^{-2}	2.56×10^{-3}
	5	1.40×10^{-2}	8.60×10^{-3}	8.16×10^{-5}
	6	4.00×10^{-3}	1.20×10^{-2}	4.00×10^{-4}
	7	4.40×10^{-3}	4.40×10^{-3}	7.20×10^{-5}

Table 5.2: Parameters for Gaussian superposition to obtain a two-dimensional fluctuating velocity field with the statistics of axisymmetric turbulence as defined by Kerschen and Gliebe [113], assuming $k_z = 0$ with $u'_a/U_\infty = 0.017$.

	l_a/c	l_t/c
$l_a/l_t = 0.5$ and $l_a = 0.008\,\text{m}$	0.053	0.107
$l_a/l_t = 2$ and $l_t = 0.008\,\text{m}$	0.107	0.053
$l_a/l_t = 0.5$ and $l_a = 0.016\,\text{m}$	0.107	0.213
$l_a/l_t = 2$ and $l_t = 0.016\,\text{m}$	0.213	0.107

Table 5.3: Turbulence length scale-to-chord ratio for cases in Sections 5.3.2, 5.3.3, and 5.3.4 (grey contours) and new values (white contours). Note that the aerofoil chord is $c = 0.15\,\text{m}$.

Figure 5.18 shows the PWL spectra for the CAA simulations with increased length scales. For cases with $l_a/l_t = 2$, a 10 dB noise reduction is found at $fc/U_\infty = 12$ for the NACA 0012 aerofoils at $AoA = 0^\text{o}$ and 6^o in comparison with the flat plate prediction, which is similar to the noise reduction

shown in Figure 5.16a. In this case, the effect of angle of attack on leading edge noise is small. In contrast, a significant noise reduction is found for the angle of attack configuration with l_a/l_t = 0.5. These results suggest that variations in the turbulence length scales do not significantly alter the conclusions of Sections 5.3.3 and 5.3.4 for the effects of anisotropy on leading edge noise, if l_a/l_t is kept constant and turbulence length scales are small in comparison with the aerofoil chord.

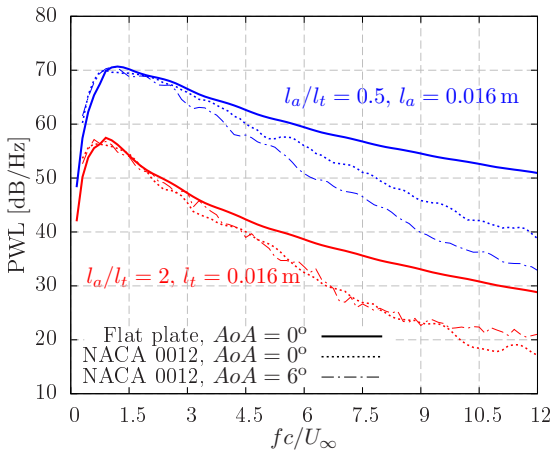

Figure 5.18: Influence of length scale-to-chord ratio on broadband noise using anisotropic turbulence.

5.4 Summary

The advanced digital filter method has been extended and validated to generate two- and three-dimensional homogeneous anisotropic synthetic turbulence with Gaussian spectra. A superposition of anisotropic Gaussian spectra is applied to reproduce homogeneous axisymmetric turbulence as defined by Kerschen and Gliebe [113] with l_a/l_t varying from 0.33 to 3, which is representative of the anisotropy in the fan wakes. Leading edge noise predictions of a number of single aerofoil configurations have been performed using a CAA solver to model the aerofoil response and a FW-H solver for the far-field noise radiation. The CAA methodology has been validated on a NACA 0001 aerofoil at $AoA = 0^o$ in homogeneous axisymmetric turbulence. Noise predictions show an agreement with the analytical flat plate solution of Amiet [39] to within 2 dB. The main findings are summarised as follows:

- If the turbulence length scales are significantly smaller than the aerofoil span, only the spanwise wavenumber $k_z = 0$ of the vortical disturbances contributes to the leading edge noise for observers in the far-field at the mid-span [39]. This assumption is valid for aerofoils interacting with both isotropic and anisotropic turbulence.

- Leading edge noise from thin aerofoils at $AoA = 0^{o}$ mainly depends on the transverse velocity spectrum, regardless of the degree of anisotropy in the turbulent flow.
- The directional dependence of the length scales in anisotropic turbulence allows the energy to be redistributed over the different wavenumber components. This redistribution affects the amount of energy in the turbulent flow that contributes to the leading edge noise.
- CAA simulations of a NACA 0012 aerofoil at $AoA = 0^{o}$ show that the noise reduction due to aerofoil thickness follows similar trends in both isotropic and moderately anisotropic turbulence. For example, a 10 dB noise reduction is observed at $fc/U_{\infty} = 12$ in a $M_{\infty} = 0.3$ flow.
- $\Delta\text{PWL} = \text{PWL}|_{\text{flat plate}} - \text{PWL}|_{\text{NACA 0012}}$ spectra scale linearly with ft_A/U_{∞}, and show a good overlap for the various l_a/l_t investigated at $M_{\infty} = 0.3$. Furthermore, the correction of Gershfeld [71] over-predicts the noise reduction of thick NACA 4-digit aerofoils interacting with both isotropic and anisotropic turbulence.
- As the Mach number is increased ($M_{\infty} = 0.6$), the onset of thickness effects on the noise seems to be slightly delayed for cases with $l_a/l_t > 1$. This is believed to be related to the streamwise velocity fluctuations, which become increasingly important with a larger l_a/l_t.
- Sound directivity is unchanged by anisotropy in the flow. At a fixed frequency, directivity plots show that the location of the lobes occur at the same observer angles for the various l_a/l_t tested.
- An angle of attack increase of 6^{o} does not show significant changes on the PWL spectra of a NACA 0012 aerofoil in anisotropic turbulence with $l_a/l_t > 1$. In contrast, the PWL spectra decay notably faster at high frequencies when $l_a/l_t < 1$ due to a noise reduction at downstream observer angles. Nevertheless, the effect of angle of attack on leading edge noise is small, with differences in $\Delta\text{OAPWL} = \text{OAPWL}|_{AoA=6^{o}} - \text{OAPWL}|_{AoA=0^{o}}$ of less than 1 dB for anisotropic turbulence with l_a/l_t ranging from 0.33 to 3.
- Absolute variations in the turbulence length scale do not change previous conclusions, provided that the ratio between them is kept constant, i.e. $l_a/l_t = \text{const.}$, and the turbulence length scales are small in comparison with the aerofoil chord.

Chapter 6

Fan Wake Modelling for Turbulence-Cascade Interaction Noise

Previous chapters focused on the interaction of isotropic and anisotropic turbulence with single aerofoil configurations. In this chapter, the CAA analysis is extended to study fan wake modelling assumptions and turbulence-cascade interaction noise. Early works in this area modelled the interaction of harmonic gusts with cascades, such as the benchmark configurations proposed by Namba and Schulten (see Category 4 in Reference [124]) and Envia (see Category 3, Problem 2 in Reference [125]). Recently, a harmonic gust decomposition was used by Chaitanya *et al.* [126] to assess the effects of vane geometry on cascade noise using a two-dimensional linearised Navier-Stokes equation solver.

Synthetic turbulence methods have been proposed to overcome the limitations of harmonic gusts to represent the fan wake statistics. For example, Polacsek *et al.* [40] adopted a simplified representation of the fan wakes that modelled the upwash velocity fluctuations by using a Fourier mode method for isotropic turbulence. Based on the RPM method [52], Dieste (see Chapter 6 in Reference [127]) generated two-dimensional fan wakes with Gaussian spectra and cyclostationary variations in the turbulent kinetic energy, such that the resulting turbulent flow was non-homogeneous and non-stationary. Wohlbrandt *et al.* [128] extended Dieste's approach [127] to include cyclostationary variations in the integral length scale of the fan wakes, although their effect on cascade noise was inconclusive.

This chapter presents two-dimensional CAA simulations to study simplified but representative configurations of fan wake-OGV interaction noise. The advanced digital filter method is adapted here to reproduce the turbulence statistics of the fan wakes under various assumptions, including homogeneous isotropic turbulence with the von Kármán spectrum, and non-homogeneous turbulence with cyclostationary variations in turbulent kinetic energy and integral length scale. Synthetic turbulence

with correct statistics of the fan wakes is injected into the CAA domain to model the interaction with a cascade, which radiates broadband noise in the upstream and downstream directions. Noise predictions from cascade simulations are validated against the analytical model of Cheong *et al.* [101]. This analytical model predicts the sound power spectrum from the interaction of isotropic turbulence with an unloaded two-dimensional flat plate cascade using the LEEs. The present work also includes a parameter study of the effects of mean flow Mach number and vane geometry on cascade noise. A modal spectral decomposition is also included to examine the contribution of cut-on modes to the broadband noise.

This chapter is organised as follows. In Section 6.1, the advanced digital filter method is adapted and validated to generate fan wakes with various modelling assumptions. The numerical setup for the cascade simulations is presented in Section 6.2. A cascade of NACA 0001 aerofoils is used in Section 6.3 to validate the CAA methodology against the flat plate model of Cheong *et al.* [101]. The influence of the fan wake modelling assumptions on cascade noise are discussed in Section 6.4. Finally, a parameter study is presented in Section 6.5 to assess the effects of mean flow Mach number, vane count, aerofoil thickness, camber, stagger angle, and inter-vane spacing on broadband noise from cascades interacting with isotropic turbulence.

6.1 Fan Wake Modelling Assumptions

The two-dimensional advanced digital filter method that was presented in Chapter 2 is adapted in this section to account for various fan wake modelling assumptions, such as

- isotropic turbulence with constant turbulent kinetic energy (or turbulence intensity) and integral length scale,
- cyclostationary variations in turbulent kinetic energy with constant integral length scale, and
- cyclostationary variations in both turbulent kinetic energy and integral length scale.

It should be noted that the cyclostationary assumption is valid when the fan wake statistics present periodic variations in time, as shown by Jurdic *et al.* [159]. To reduce the computational cost, the fan wake modelling assumptions are implemented for two-dimensional CAA simulations in this chapter. However, the numerical implementation could potentially be extended to fully three-dimensional simulations.

6.1.1 Isotropic Turbulence

Analytical models for the prediction of fan wake-OGV interaction noise often assume isotropic turbulence to represent the spectral content of the fan wakes. Although the fan wakes always present a certain degree of anisotropy, especially close to the trailing edge of the fan blades [18], Ganz *et al*. [17] found that the isotropic von Kármán spectrum provides a good representation of the spectral distribution at mid-span locations.

In this section, the advanced digital filter method is adapted to inject two-dimensional isotropic turbulence into the CAA domain all along the circumferential direction, i.e., from the top edge of the CAA domain to the bottom edge, where periodic boundary conditions are applied. As shown in Figure 6.1, the periodic boundary condition in the transverse direction is implemented by creating ghost eddies with the same characteristics as their corresponding eddies in the physical domain that cannot be fully injected without truncation. Such a numerical implementation ensures the continuity of the fluctuating velocity field across the circumferential edges. The fluctuating velocity field of a two-dimensional eddy from the Gaussian superposition is defined by Equations 2.21a and 2.21b for isotropic turbulence.

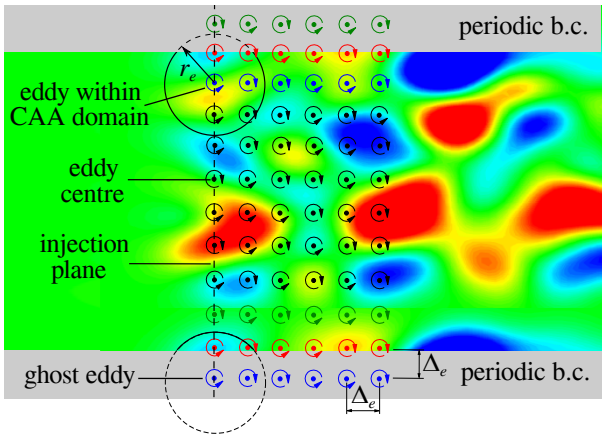

Figure 6.1: Injection plane with periodic boundary conditions (abbreviated as b.c.) in the circumferential direction.

The current numerical implementation is particularly useful to study cascade noise, since all vanes would interact with the oncoming turbulence. This represents an advantage in comparison with previous CAA studies on fan wake modelling, in which the fan wakes interacted with a single flat plate [127] or were injected locally to interact with a few vanes [128]. In such a case, further assumptions should be made for the computation of cascade noise with the total vane count, such as considering that the vanes are uncorrelated noise sources [128].

6.1.2 Cyclostationary Variations in Turbulent Kinetic Energy

Various analytical and numerical studies have proposed to split the turbulence downstream of the fan stage into background and wake turbulence [105, 112]. Background turbulence is typically modelled as having a constant turbulent kinetic energy and integral length scale. Wake turbulence includes spatio-temporal variations in the turbulent kinetic energy, but the integral length scale takes a constant value. Dieste [127] used the cyclostationary analysis of Jurdic *et al.* [159] to model periodic variations in the turbulent kinetic energy from two-dimensional fan wakes as

$$K_w(y,t) = u'^2_{rms,b} + u'^2_{rms,w} \sum_{i=-\infty}^{i=+\infty} \exp\left[-\frac{\ln 2}{h_w^2}\Big(y - \Omega R(t + iT_w)\Big)^2\right], \tag{6.1}$$

where $u'_{rms,b}$ is the root-mean-square fluctuating velocity of the background turbulence, $u'_{rms,w}$ is the maximum root-mean-square of the fluctuating velocity of the wake turbulence, h_w is the semi-wake width, Ω is the angular speed of the fan wakes, R is the radius of the wrapped cascade, and $T_w = 2\pi/(n_w\Omega)$ is the period of the fan wakes, with n_w being the number of wakes along the circumferential direction, y. Figure 6.2 shows cyclostationary variations in the turbulent kinetic energy of the fan wakes, which are modelled by a train of Gaussian functions. Although the fan wakes usually present a certain degree of skewness, and are not perfectly symmetric, Gaussian functions are considered a good approximation for the distribution of the turbulent kinetic energy of the fan wakes [103, 105].

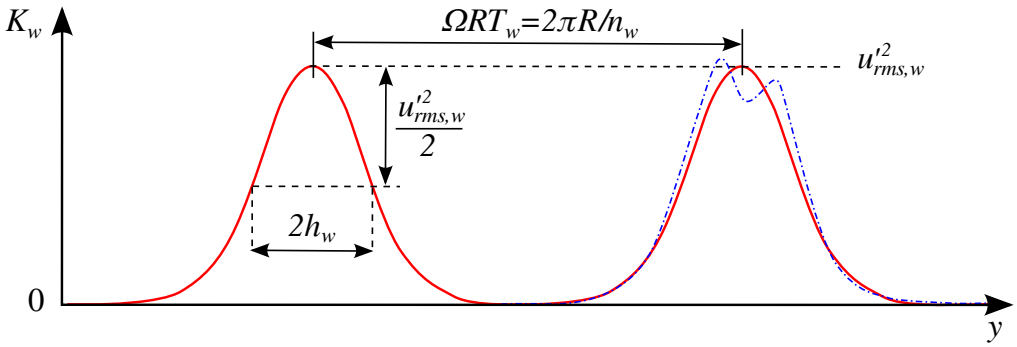

Figure 6.2: Schematic of variations in the turbulent kinetic energy of the fan wakes modelled by a Gaussian profile (solid line in red) and typical distribution from experiments (dash-dot line in blue) in the circumferential direction. Background turbulence has been neglected, $u'_{rms,b} = 0\,\mathrm{m/s}$.

Due to the absence of accurate information, and to simplify the analysis, the integral length scales of the background and wake turbulence are often assumed to take the same value [105, 127]. However, Ju *et al.* [115] showed non-negligible variations in the shape of the noise spectra when using different integral length scales for the background and wake turbulence. In the current work, Equation 6.1 is adopted to define cyclostationary variations in the turbulent kinetic energy, in which the background

turbulence is neglected, i.e., $u'_{rms,b} = 0\,\mathrm{m/s}$. This assumption is suitable to assess the influence of the wake turbulence on cascade noise, since $u'_{rms,w}$ is between 7.4 and 14.8 times larger than $u'_{rms,b}$ in experimental tests [159].

By assuming that the statistics of the fan wakes can be locally defined at the eddy centre, (x_p, y_p), the fluctuating velocity field of the pth eddy that is injected into the CAA domain takes the form

$$u'_{x,p}(\mathbf{x}) = -A_w \sqrt{2\pi}\Delta_e \epsilon_p \left(y - y_p\right) \sum_{i=1}^{N_e} \frac{u'_{rms,i}}{\Lambda_i^2} \exp\left(-\frac{\pi r_p^2}{2\Lambda_i^2}\right), \tag{6.2a}$$

$$u'_{y,p}(\mathbf{x}) = A_w \sqrt{2\pi}\Delta_e \epsilon_p \left(x - x_p\right) \sum_{i=1}^{N_e} \frac{u'_{rms,i}}{\Lambda_i^2} \exp\left(-\frac{\pi r_p^2}{2\Lambda_i^2}\right), \tag{6.2b}$$

which correspond to Equations 2.21a and 2.21b for an isotropic eddy multiplied by an amplitude scaling factor, A_w, to include cyclostationary variations as defined by Equation 6.1, i.e.,

$$A_w(y_p, t) = \sum_{i=-\infty}^{i=+\infty} \left\{ \exp\left[-\frac{\ln 2}{h_w^2} \left(y_p - \Omega R(t + iT_w)\right)^2 \right] \right\}^{1/2}. \tag{6.3}$$

The assumption of defining the fan wake statistics at the eddy centre was found to be suitable for reproducing the correct turbulence statistics by Dieste [127] (see *Implementation 1* in Chapter 6), who also examined alternative implementations. In the numerical implementation used in this thesis, $A_w(y_p, t)$ acts as a scaling factor for the amplitude of the eddies that are injected into the CAA domain. Therefore, the resulting turbulent flow is locally isotropic and contains eddies with similar size throughout the CAA domain. Since $A_w(y_p, t) \in [0, 1]$ and the maximum K_w contained in the fan wakes occurs at $A_w(y_p, t) = 1$, the Gaussian superposition must be performed to match the target isotropic energy spectrum with $u'_{rms,w}$. It should also be noted that streamwise and transverse velocity fluctuations present similar levels of turbulence intensity in the current implementation, which is consistent with experimental findings of fan wake statistics at the mid-span [17, 160]. Since the eddies are convected as frozen turbulence, the current CAA methodology cannot account for the wake spreading and increased overlapping that occurs as the wakes are convected downstream of the fan stage.

6.1.3 Cyclostationary Variations in Integral Length Scale

To date, few works have studied the circumferential distribution of the integral length scale within the fan wakes [128, 160]. Wohlbrandt *et al.* [128] performed unsteady RANS simulations of a fan stage and reported that the smallest turbulence length scales occur at approximately the wake centre, where the turbulent kinetic energy presents a maximum. In contrast, Maunus *et al.* [160] examined

experimental data from the SDT fan rig and found that the largest length scales occur around the wake centre at the mid-span. Furthermore, RANS simulations using two-equation turbulence models showed unclear trends for the circumferential distribution of the integral length scale.

In order to assess the effects on cascade noise due to cyclostationary variations in integral length scale, two circumferential distributions with opposite trends are proposed in this section:

$$\Lambda_{w,1}(y_p,t) = \Lambda_{min} + (\Lambda_{max} - \Lambda_{min})\left[1 - \frac{A_w(y_p,t) - \min\{A_w(y_p,t)\}}{\max\{A_w(y_p,t)\} - \min\{A_w(y_p,t)\}}\right], \tag{6.4}$$

where the minimum integral length scale, Λ_{min}, is found at maximum turbulent kinetic energy in the fan wakes, and

$$\Lambda_{w,2}(y_p,t) = \Lambda_{max} - (\Lambda_{max} - \Lambda_{min})\left[1 - \frac{A_w(y_p,t) - \min\{A_w(y_p,t)\}}{\max\{A_w(y_p,t)\} - \min\{A_w(y_p,t)\}}\right], \tag{6.5}$$

where the maximum integral length scale, Λ_{max}, corresponds to the maximum turbulent kinetic energy in the fan wakes. Figure 6.3 shows a schematic of the proposed distributions for the integral length scale of the fan wakes. The ratio $\Lambda_{max}/\Lambda_{min}$ ranges between 4 and 2.4 approximately in previous works of Wohlbrandt *et al.* [128] and Maunus *et al.* [160], which give an indication of the circumferential variations expected for the integral length scales of the fan wakes.

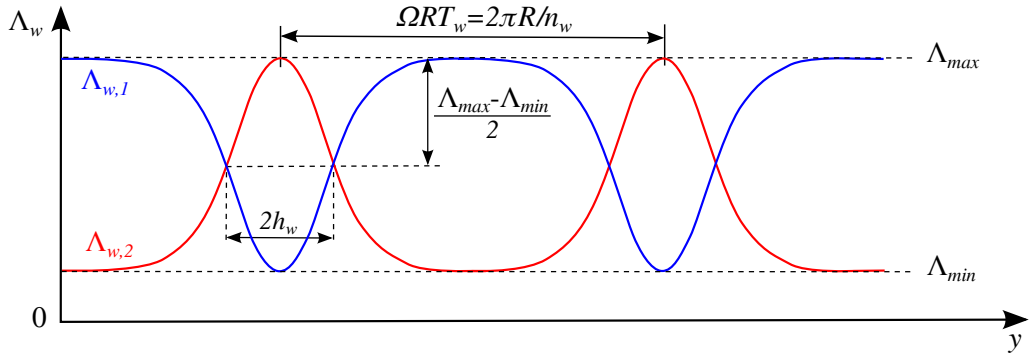

Figure 6.3: Schematic of variations in the integral length scale of the fan wakes modelled by a Equation 6.4 ($\Lambda_{w,1}$, solid line in blue) and Equation 6.5 ($\Lambda_{w,2}$, solid line in red) in the circumferential direction.

Assuming that the fan wake statistics are defined at each eddy centre, Equations 6.2a and 6.2b can be modified to account for cyclostationary variations in both turbulent kinetic energy and integral length scale as follows

$$u'_{x,p}(\mathbf{x}) = -A_w\sqrt{2\pi}\Delta_e\epsilon_p\left(y - y_p\right)\sum_{i=1}^{N_e}\frac{u'_{rms,i}}{\Lambda_i^2\frac{\Lambda_w^2}{\Lambda_{max}^2}}\exp\left(-\frac{\pi r_p^2}{2\Lambda_i^2\frac{\Lambda_w^2}{\Lambda_{max}^2}}\right), \tag{6.6a}$$

$$u'_{y,p}(\mathbf{x}) = A_w \sqrt{2\pi}\Delta_e \epsilon_p \left(x - x_p\right) \sum_{i=1}^{N_e} \frac{u'_{rms,i}}{\Lambda_i^2 \frac{\Lambda_w^2}{\Lambda_{max}^2}} \exp\left(-\frac{\pi r_p^2}{2\Lambda_i^2 \frac{\Lambda_w^2}{\Lambda_{max}^2}}\right), \tag{6.6b}$$

where Λ_w is the circumferential distribution of the integral length scale in the fan wakes, such as those proposed by Equations 6.4 and 6.5. Thus, the integral length scales in the Gaussian superposition, Λ_i for $i = 1, ..., N_e$, are locally scaled by a factor of Λ_w/Λ_{max} for each eddy along the injection plane.

6.1.4 Validation of Numerical Implementation for Gaussian Spectra

Previous works used Gaussian spectra to generate synthetic turbulence as a simplified approach for the spectral content in the fan wakes [127, 128]. In this section, the numerical implementation of the previous fan wake modelling assumptions is validated for Gaussian spectra.

The baseline configuration corresponds to isotropic turbulence that follows the two-dimensional Gaussian spectrum defined in Equation 2.12 with $M_\infty = 0.3$, $u'_{rms}/U_\infty = 0.017$, and $\Lambda_w\,(= \Lambda) = 0.008\,\text{m}$. In order to include variations in the turbulent kinetic energy using Equation 6.3, the semi-wake width is set to $h_w = \Lambda_w/0.42$ according to Jurdic *et al.* [159]. A total number of $n_w = 2$ wakes are injected into the CAA domain. To simplify the post-processing of the fan wake statistics, the rotational speed is set to zero ($\Omega = 0\,\text{rad/s}$), such that the resulting turbulent flow is homogeneous in the x-direction. Variations in the integral length scale using Equations 6.4 and 6.5 are performed by setting $\Lambda_{min} = 0.004\,\text{m}$ and $\Lambda_{max}/\Lambda_{min} = 4$.

For validation purposes, synthetic turbulence is injected into an empty CAA domain with uniform grid spacing $1.1\times10^{-4}\,\text{m}$, whose dimensions are $x/L_{ref} \in [-0.096, 0.16]$ and $y/L_{ref} \in [-0.125, 0.125]$ with $L_{ref} = 1\,\text{m}$. Figure 6.4 shows the CAA domain for the validation case with cyclostationary variations in the turbulent kinetic energy. All simulations were run for 4.8×10^6 iterations using a non-dimensional time step of $\Delta t c_\infty/L_{ref} = 5 \times 10^{-4}$. Velocity samples were collected at 100 monitor points uniformly distributed along the circumferential direction, y, downstream of the injection plane.

Figure 6.5 shows analytical and numerical one-dimensional spectra averaged in the circumferential direction, where an agreement of better than 1 dB is found at all frequencies. All cases with cyclostationary variations in $K_w(y)$ have the same total turbulent kinetic energy. Therefore, differences in the shape of streamwise and transverse spectra are caused by different distributions of Λ_w. For example, the spectra are dominated by the low frequencies when using the $\Lambda_{w,2}(y)$ distribution, since the maximum turbulent kinetic energy occurs at the largest integral length scale.

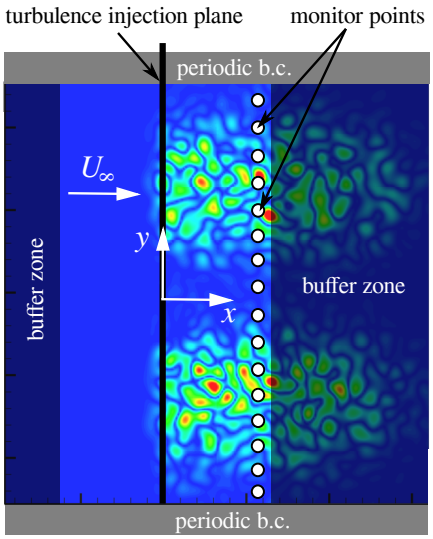

Figure 6.4: CAA domain for validation of the fan wake statistics and contours of fluctuating vorticity magnitude, assuming $K_w(y)$ and Λ_w = const.

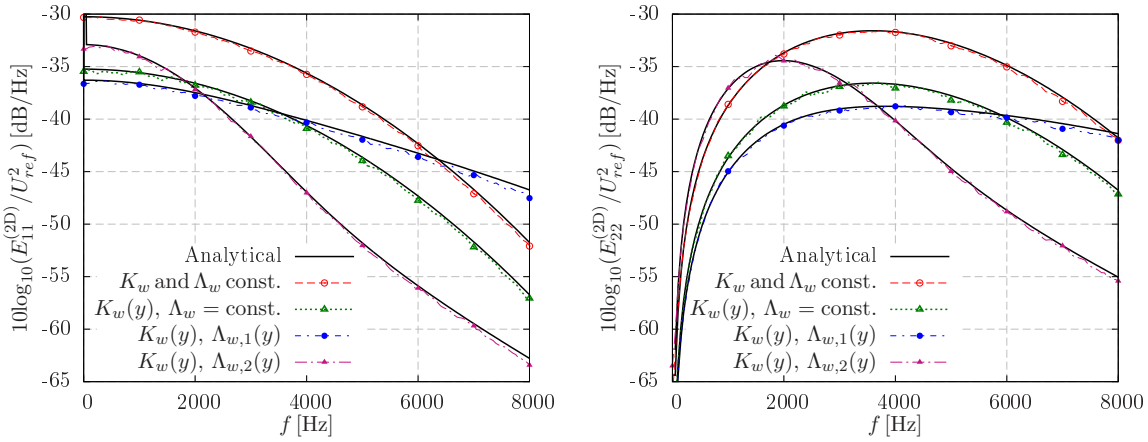

(a) Streamwise, U_{ref} = 1 m/s.

(b) Transverse, U_{ref} = 1 m/s.

Figure 6.5: One-dimensional Gaussian spectra averaged in the circumferential direction for different fan wake modelling assumptions.

Figure 6.6a shows variations in $K_w = (u'^2_{x,rms} + u'^2_{y,rms})/2$ for the different fan wake modelling assumptions. A good agreement is found between analytical and numerical results, giving validation to the numerical method to inject fan wakes with periodic boundary conditions in the circumferential direction. The maximum turbulent kinetic energy from the different numerical implementations is slightly lower than the analytical predictions at location A. This is likely to be caused by the finite mesh

resolution, which cannot convect the smallest vortical structures without dissipation. Additionally, no significant wake overlapping is found at location B, where $K_w \approx 0\,\mathrm{m}^2/\mathrm{s}^2$.

The integral length scale distribution can be obtained from the streamwise one-dimensional spectrum at each monitor point by using [88]

$$\Lambda_w = \lim_{f \to 0} \frac{U_\infty E_{11}^{(2\mathrm{D})}(f)}{4u_{x,rms}'^2}. \tag{6.7}$$

Taking advantage of the flatness of $E_{11}^{(2\mathrm{D})}(f)$ at low frequencies, $\lim_{f\to 0} E_{11}^{(2\mathrm{D})}(f)$ can be approximated by taking the averaged value of the spectrum for $f < 250\,\mathrm{Hz}$. This strategy is similar to that used by Ganz *et al.* [17] to compute the integral length scale from experimental hotwire measurements of the fan wakes. Figure 6.6b shows the circumferential distribution of the integral length scale, in which a good agreement is observed between analytical and numerical predictions.

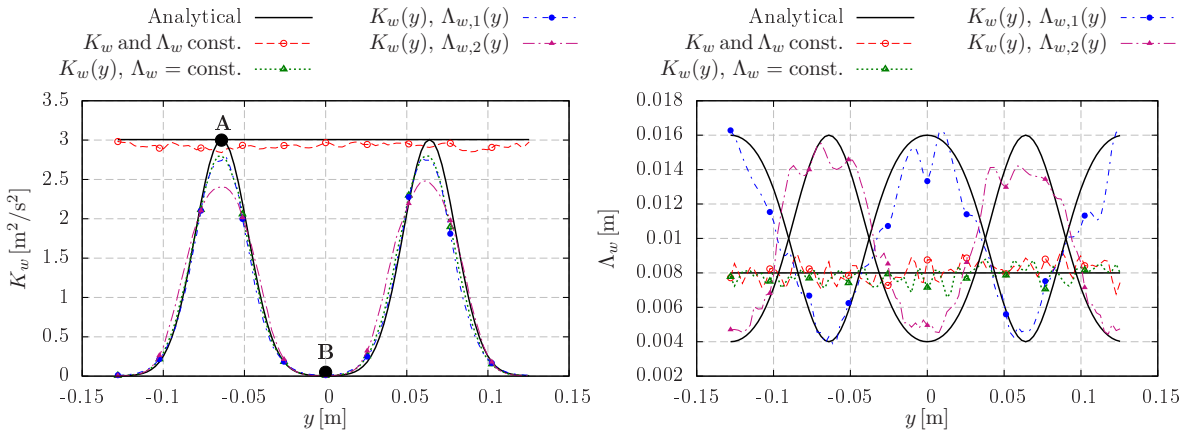

(a) Turbulent kinetic energy.

(b) Integral length scale.

Figure 6.6: Circumferential distribution of turbulent kinetic energy and integral length scale for different fan wake modelling assumptions.

6.1.5 Validation of Numerical Implementation for von Kármán Spectra

Following a similar methodology as described in Section 6.1.4, the numerical implementation is also validated for the von Kármán spectrum in Equation 2.22 with $M_\infty = 0.3$, $u_{rms}'/U_\infty = 0.017$, and $\Lambda_w\,(=\Lambda) = 0.008\,\mathrm{m}$. Since the von Kármán spectrum presents a broader spectral content than a Gaussian spectrum, the CAA mesh has been refined to ensure that small vortical structures are convected without significant dissipation. Thus, the uniform grid spacing is now set to $2.1 \times 10^{-4}\,\mathrm{m}$.

Isotropic turbulence with the von Kármán spectrum is generated from a superposition of Gaussian eddies using Equations 2.21a and 2.21b with the values that are given in Table 2.1. The amplitude of the isotropic turbulent flow is modulated by using Equation 6.3 with $n_w = 2$, $\Omega = 0\,\mathrm{rad/s}$, and $h_w = \Lambda_w/0.42$, such that the width of the wakes is similar to that of the Gaussian validation in Section 6.1.4. In order to include variations in the integral length scale between $\Lambda_{min} = 0.004\,\mathrm{m}$ and $\Lambda_{max}/\Lambda_{min} = 4$, Equations 6.6a and 6.6b are used with the values given in Table 6.1.

ith Gaussian eddy	Λ_i [m]	$u'^2_{rms,i}$ [m^2/s^2]
1	5.048×10^{-2}	5.176×10^{-2}
2	2.801×10^{-2}	2.180×10^{-1}
3	1.457×10^{-2}	2.759×10^{-1}
4	7.117×10^{-3}	2.522×10^{-1}
5	2.801×10^{-3}	3.721×10^{-1}

Table 6.1: Parameters for Gaussian superposition to obtain the two-dimensional von Kármán spectrum with $M_\infty = 0.3$, $u'_{rms}/U_\infty = 0.017$, and $\Lambda\,(=\Lambda_{max}) = 0.016\,\mathrm{m}$.

The numerical implementation is validated by comparison of analytical and numerical one-dimensional spectra averaged in the circumferential direction, as shown in Figure 6.7. A good agreement is found at all frequencies for the different fan wake modelling assumptions examined.

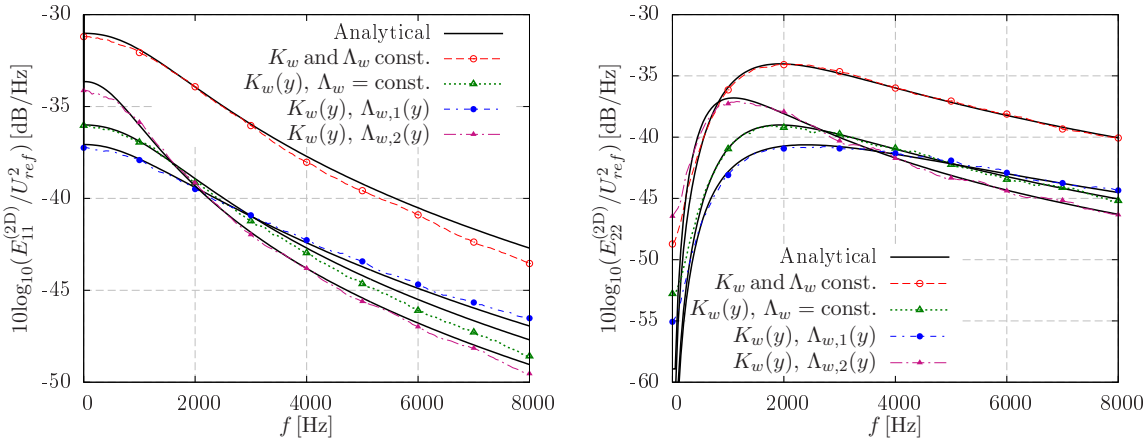

(a) Streamwise, $U_{ref} = 1\,\mathrm{m/s}$.

(b) Transverse, $U_{ref} = 1\,\mathrm{m/s}$.

Figure 6.7: One-dimensional von Kármán spectra averaged in the circumferential direction for different fan wake modelling assumptions.

Figure 6.8 shows contours of non-dimensional fluctuating vorticity magnitude using different fan wake modelling assumptions. When comparing Figures 6.8a and 6.8b, the amplitude of the turbulent structures decay away from the wake centreline as a consequence of modelling variations in the turbulent kinetic energy. However, the size of the turbulent structures remain approximately constant throughout the domain. In contrast, Figure 6.8c shows small turbulent structures at the wake centreline, as expected from the $\Lambda_{w,1}$ distribution. Opposite trends are observed when using $\Lambda_{w,2}$ in Figure 6.8d, where the largest turbulent structures are located at the wake centreline.

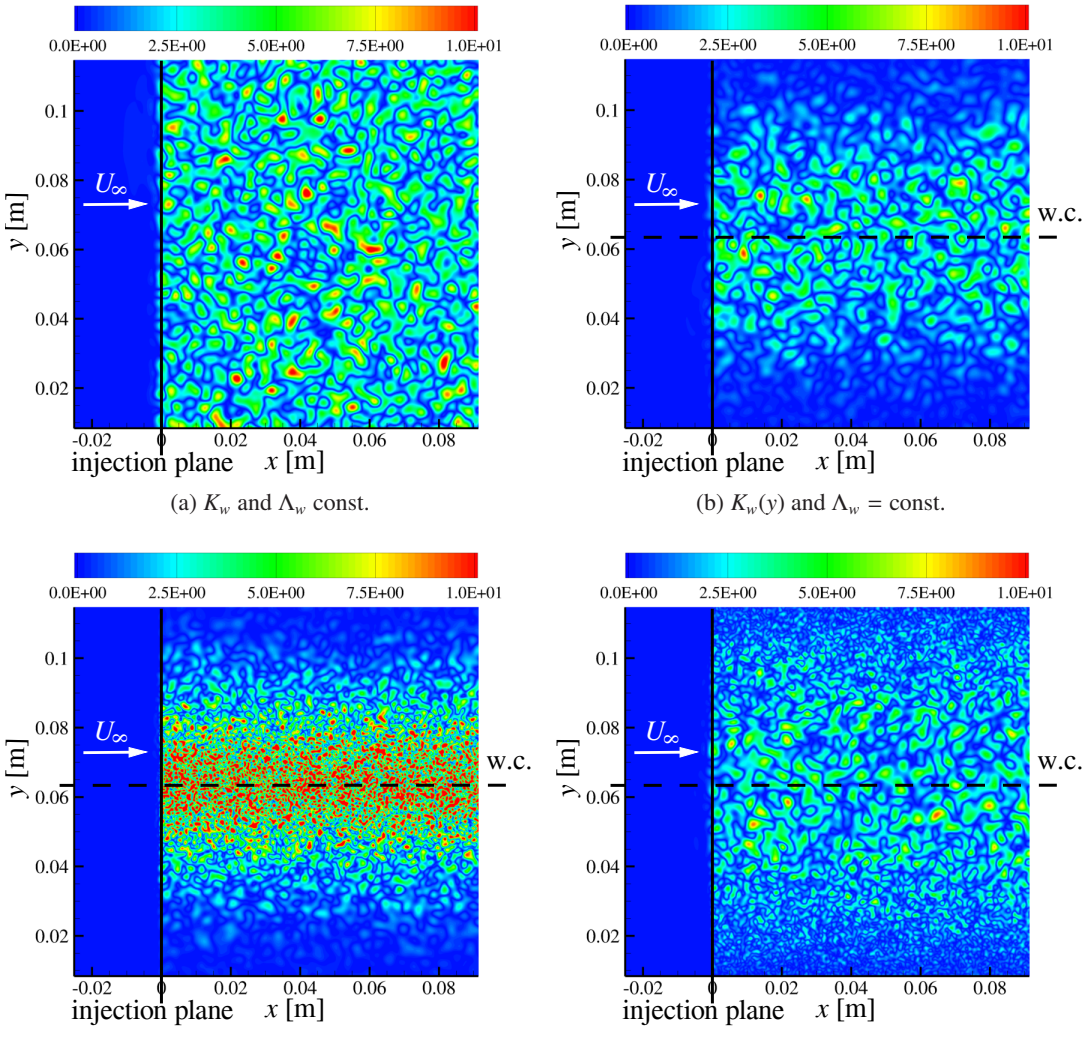

(a) K_w and Λ_w const.

(b) $K_w(y)$ and Λ_w = const.

(c) $K_w(y)$ and $\Lambda_{w,1}(y)$.

(d) $K_w(y)$ and $\Lambda_{w,2}(y)$.

Figure 6.8: Instantaneous contours of non-dimensional vorticity magnitude, $\|\nabla \times \mathbf{u}'\| L_{ref}/c_\infty$, using different fan wake modelling assumptions. Dashed lines represent the wake centreline (abbreviated as w.c.).

6.2 Cascade Configurations

A schematic of the two-dimensional cascade configuration that is investigated in this chapter is shown in Figure 6.9, where $M_x^{\pm} = U_{0,x}^{\pm}/c_\infty$ and $M_y^{\pm} = U_{0,y}^{\pm}/c_\infty$ are the mean flow Mach numbers in the axial and circumferential directions respectively, the superscript '+' denotes upstream and '−' denotes downstream, α is the stagger angle, s is the inter-vane spacing, and c is the vane chord. Such a configuration allows the study of stagger angle effects on cascade noise, whereas sweep and lean angles cannot be included in the present analysis. The reader is referred to Figure 1.6 for a schematic of the OGV angles.

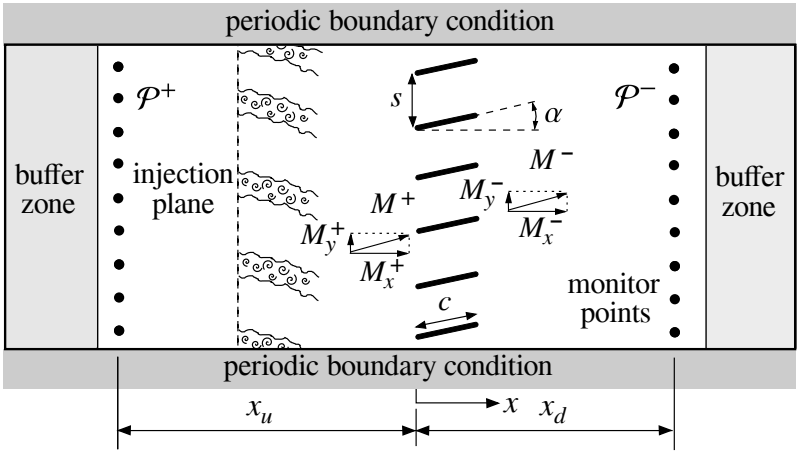

Figure 6.9: Computational setup for two-dimensional CAA simulations of turbulence-cascade interaction noise.

Numerical noise predictions are obtained from arrays of monitor points upstream, x_u, and downstream, x_d, of the cascade. Following previous work of Kim *et al.* [62], numerical sound power spectra for a unit span cascade can be computed as

$$\mathcal{P}^{\pm}(\omega) = \sum_{l=-\infty}^{\infty} \mathcal{P}_l^{\pm}(\omega) \tag{6.8}$$

where l is the order of the acoustic mode in the circumferential direction (or 'duct mode'), which is related to the acoustic wavenumber in the circumferential direction, $\kappa_{y,l} = 2\pi l/(Bs)$. The modal sound power is defined as

$$\mathcal{P}_l^{\pm}(\omega) = \frac{BsL_{ref}}{\rho_\infty} \mathrm{Re}\left\{ \left|\hat{p}_l'(\omega)\right|^2 \frac{\omega}{\left|\omega + U_{0,x}^{\pm}\kappa_{x,l}^{\pm} + U_{0,y}^{\pm}\kappa_{y,l}^{\pm}\right|^2} \left[-\kappa_{x,l}^{\pm *} + \frac{U_{0,x}^{\pm}}{c_\infty^2}\left(\omega + U_{0,x}^{\pm}\kappa_{x,l}^{\pm} + U_{0,y}^{\pm}\kappa_{y,l}\right)\right]\right\} \tag{6.9}$$

where $()^*$ represents the complex conjugate, Re{} is the real part operator, B is the number of vanes, $\hat{p}'_l(\omega)$ is the amplitude of the fluctuating pressure from a spatio-temporal Fourier transform, and the acoustic wavenumber in the axial direction is

$$\kappa^{\pm}_{x,l} = \frac{M^{\pm}_x(\omega/c_\infty + M^{\pm}_y\kappa_{y,l}) \pm \sqrt{(\omega/c_\infty + M^{\pm}_y\kappa_{y,l})^2 - \left[1-(M^{\pm}_x)^2\right]\kappa^2_{y,l}}}{1-(M^{\pm}_x)^2}. \tag{6.10}$$

It should be noted that Equation 6.9 constitutes an extension of that proposed by Kim *et al.* [62] for cascades with zero stagger angle and without variations in the direction of the mean flow across the cascade. A complete derivation of Equation 6.9 is presented in Appendix D. Although the summation in Equation 6.8 extends to an infinite number of circumferential modes, in practice only cut-on modes contribute to the sound power spectra. The limit for the cut-on modes can be computed by solving the discriminant in Equation 6.10, which leads to

$$l^{\pm}_{max}(\omega) = \frac{Bs\omega}{2\pi c_\infty}\frac{M^{\pm}_y + \sqrt{1-(M^{\pm}_x)^2}}{1-(M^{\pm})^2}, \qquad l^{\pm}_{min}(\omega) = \frac{Bs\omega}{2\pi c_\infty}\frac{M^{\pm}_y - \sqrt{1-(M^{\pm}_x)^2}}{1-(M^{\pm})^2}. \tag{6.11}$$

Since the cascade radiates noise into the free field, the upstream and downstream Mach numbers are similar away from the cascade, i.e., $M^+ = M^- = M_\infty$. Due to the absence of the fan stage in the CAA simulations, potential shielding effects on upstream-travelling acoustic waves cannot be included in the sound power spectra.

6.3 Validation Case: Two-Dimensional NACA 0001 Cascade

In order to validate the CAA methodology for the computation of the sound power spectra, a cascade of NACA 0001 aerofoils with a reduced vane count of $B = 4$ is used in this section. The aerofoil chord and the gap-to-chord ratio are set to $c = 0.15\,\text{m}$ and $s/c = 0.75$, respectively, which are representative values for OGVs in turbofan engines. The mean flow is assumed to be uniform and aligned with the aerofoil chord at $M_\infty = 0.6$. Two configurations with stagger angles of $\alpha = 0^\text{o}$ and 30^o are investigated using purely two-dimensional isotropic turbulence. To this end, the advanced digital filter method is used to reproduce the von Kármán spectrum in Equation 2.22 with $u'_{rms}/U_\infty = 0.017$, $\Lambda = 0.008\,\text{m}$, using the values in Table 2.2 for the Gaussian superposition.

6.3.1 Analytical Cascade Model

The analytical model of Cheong *et al.* [101], which was developed for isotropic turbulence interacting with a flat plate cascade in a uniform mean flow, gives upstream and downstream sound power spectra. Therefore, this analytical model is used in the present chapter for validation and analysis of cascade noise from CAA simulations. Sound power spectra for a unit span cascade can be written as

$$\mathcal{P}^{\pm}(\omega) = \frac{2\pi\rho_{\infty}M_{\infty}L_{ref}}{\cos(\alpha)} \sum_{l=l_{min}}^{l_{max}} Q_l^{\pm}(k_x) \sum_{r=-\infty}^{\infty} \Phi_{22}^{(2\mathrm{D})}(k_x, k_{y,l+Br}), \tag{6.12}$$

where $Q_l^{\pm}$ is the non-dimensional modal power response function defined as

$$Q_l^{\pm}(k_x) = \left|R_l^{\pm}(k_x, k_{y,\mathrm{mod}(l,B)})\right|^2 \frac{\omega \mathrm{Re}\{-c_{\infty}\kappa_{x,l}^{\pm} + M_x(\omega + U_{0,x}\kappa_{x,l}^{\pm} + U_{0,y}\kappa_{y,l})\}}{\left|\omega + U_{0,x}\kappa_{x,l}^{\pm} + U_{0,y}\kappa_{y,l}\right|^2}. \tag{6.13}$$

In Equation 6.13, $\mathrm{mod}(l, B)$ corresponds to the reminder of l/B, and the cascade response function, $R_l^{\pm}$, can be obtained from the LINSUB code of Whitehead [161].

6.3.2 Mesh Generation and Numerical Setup

Initially, the CAA mesh of a single vane passage was designed for each cascade configuration. The CAA mesh extends to 5 chord lengths upstream and downstream of the cascade and contains 3.5×10^5 grid points for a single vane passage. Then, the cascade mesh with the total vane count was obtained by copying the mesh of a single vane passage B times in the transverse direction. Periodic boundary conditions were used in the top and bottom edges of the cascade mesh. It should be noted that CAA meshes for cascade simulations were designed by following a similar strategy as detailed in Section 2.4.3 for single aerofoils, and further details are given in Appendix C. Figure 6.10 shows the cascade mesh of a single passage using a NACA 0001 aerofoil with the stagger angle set to $\alpha = 30^{\mathrm{o}}$.

Cut-off modes in the acoustic pressure field are expected to be damped before reaching the monitor points such that cut-off modes do not contribute to the sound power spectra. However, Kim and Cheong [162] suggested that time-domain computations of cascade noise could be affected by unattenuated cut-off modes. In order to assess the dependency of the noise predictions on the location of the monitor points, arrays of 225 monitor points were placed at $x_u = -3c$ and $-1.5c$ upstream of the cascade, and at $x_d = 2.5c$ and $4c$ downstream of the cascade. For the numerical calculation of $\mathcal{P}^{\pm}$, a total number of 3.18×10^4 fluctuating pressure samples are collected every 566 non-dimensional time steps $\Delta t c_{\infty}/L_{ref} = 4 \times 10^{-6}$.

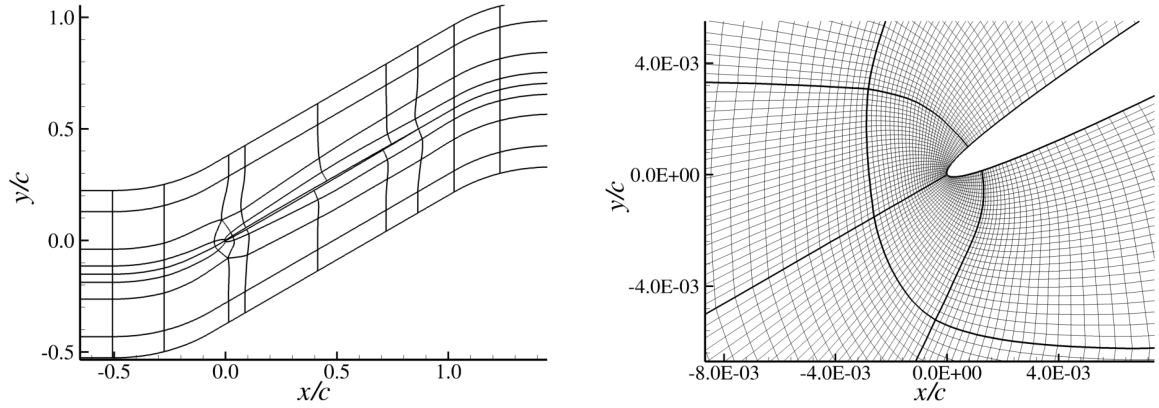

(a) Block topology around the aerofoil.

(b) Mesh in the leading edge region.

Figure 6.10: Cascade mesh of a single vane passage with a NACA 0001 aerofoil at $\alpha = 30^{o}$.

A double FFT is performed from fluctuating pressure samples to compute $\hat{p}'_l(\omega)$ in Equation 6.9. In order to reduce high-frequency oscillations in the $\hat{p}'_l(\omega)$ calculation, the result from the FFT is smoothed by using a moving average filter with a span of 22 elements. The reference power for the PWL spectra is $\mathcal{P}_{ref} = 1 \times 10^{-12}$ W.

6.3.3 Noise Results

Sound power spectra at various upstream and downstream locations are shown in Figure 6.11 for the cascade of NACA 0001 aerofoils at $\alpha = 0^{o}$. The good agreement between noise predictions at the locations examined indicates that the arrays of monitor points can be placed at $x_u \leq -1.5c$ and $x_d \geq 2.5c$, where sound power spectra are not significantly affected by cut-off modes.

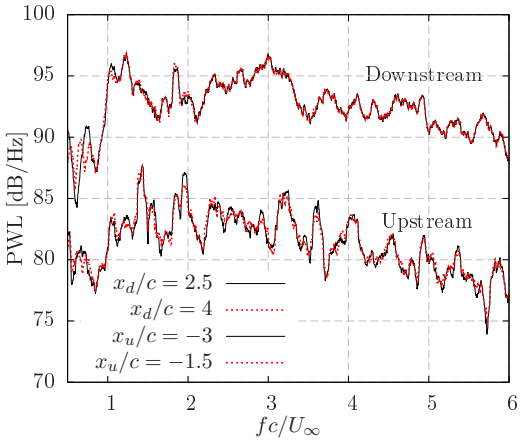

Figure 6.11: Influence of the monitor array location on the PWL spectra from a cascade of NACA 0001 aerofoils at $M_\infty = 0.6$ with $B = 4$, $s/c = 0.75$, and $\alpha = 0^{o}$.

Figure 6.12 shows a comparison between the PWL spectra from the cascade of NACA 0001 aerofoils at $\alpha = 0^{\circ}$ and 30°, and their corresponding flat plate prediction using the analytical model of Cheong *et al.* [101]. Numerical noise predictions are able to reproduce the correct shape of peaks and valleys in the spectra due to the interference of several cut-on modes propagating upstream and downstream of the cascade. Overall, the numerical PWL spectra show an agreement within $2-3$ dB of the analytical prediction at most frequencies, which validates the current CAA methodology.

Additionally, the sound power spectrum from a single flat plate using Amiet's model [39] was calculated and scaled by the number of vanes, $B = 4$, as shown in Figure 6.12. Cheong *et al.* [101] reported that sound power spectra have a high sensitivity on the vane count at low frequencies, in which the interaction between neighbouring vanes is important. In contrast, at high frequencies, cascade effects on the noise are negligible, and the sound power spectra scale with the number of vanes. The comparison between the cascade and single flat plate predictions in Figure 6.12 shows a good agreement, especially at high frequencies. Similar results were also shown by Blandeau *et al.* [70]. However, the predictions for a single flat plate cannot reproduce the correct shape of peaks and valleys in the cascade spectra.

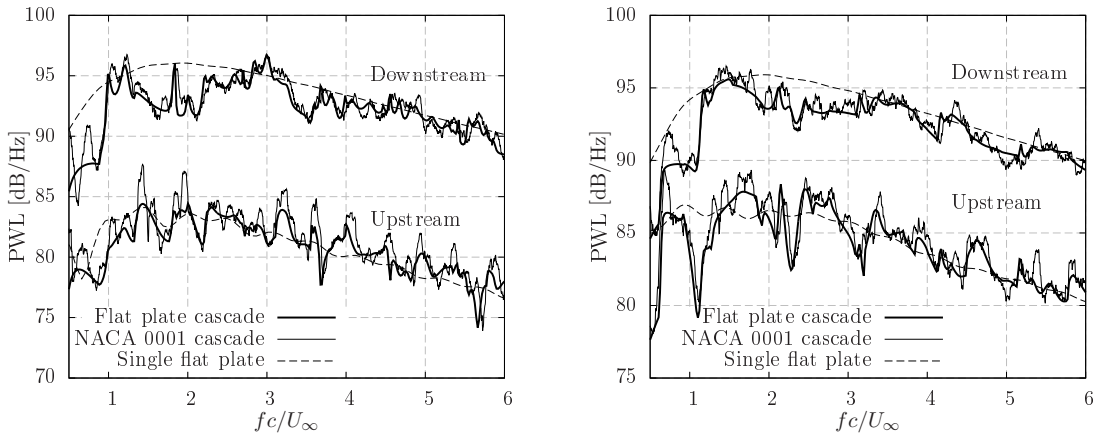

(a) $\alpha = 0^{\circ}$. (b) $\alpha = 30^{\circ}$.

Figure 6.12: PWL spectra from a cascade of NACA 0001 aerofoils at $M_\infty = 0.6$ with $B = 4$ and $s/c = 0.75$.

For further validation, mode-frequency maps of $\mathcal{P}_l^{\pm}$ are shown in Figure 6.13 for the cascade with $\alpha = 0^{\circ}$. A reasonably good agreement is found between analytical and numerical modal power distributions. Numerical predictions are able to correctly identify the circumferential modes that contribute to the sound power spectra, i.e., the 'cut-on triangle'.

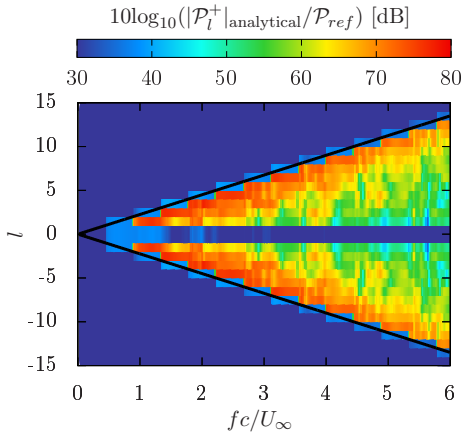

(a) $\mathcal{P}_l^+$ upstream of flat plate cascade.

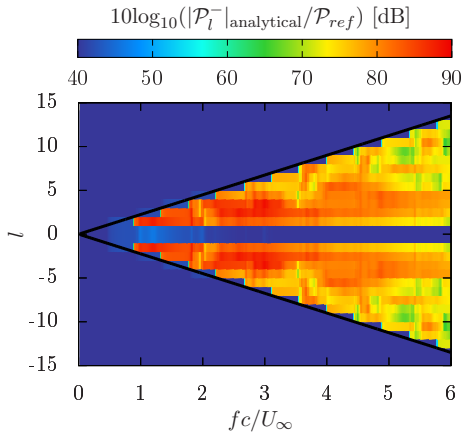

(b) $\mathcal{P}_l^-$ downstream of flat plate cascade.

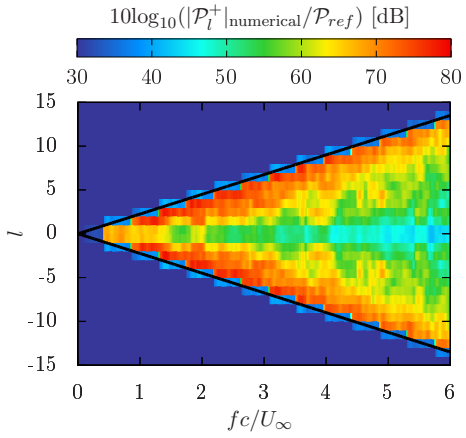

(c) $\mathcal{P}_l^+$ upstream of NACA 0001 cascade.

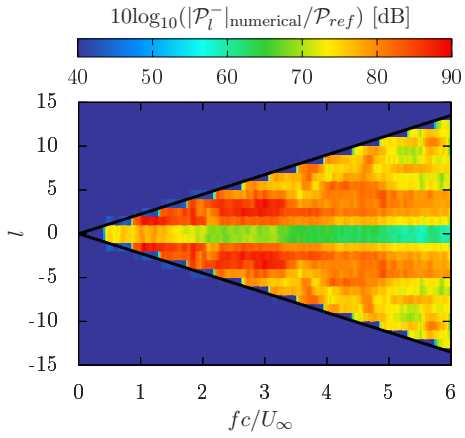

(d) $\mathcal{P}_l^-$ downstream of NACA 0001 cascade.

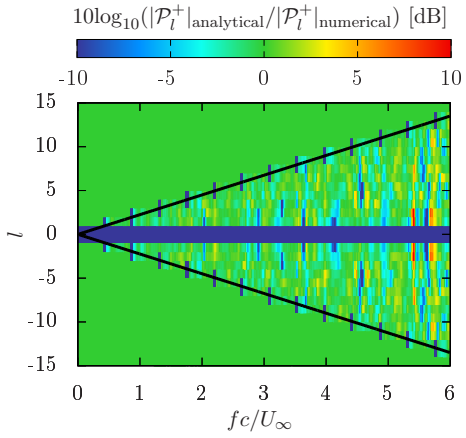

(e) Differences in $\mathcal{P}_l^+$ upstream.

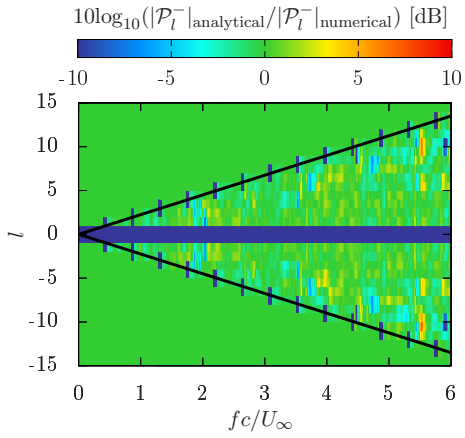

(f) Differences in $\mathcal{P}_l^-$ downstream.

Figure 6.13: Modal spectral decomposition for a cascade of flat plates (analytical) and NACA 0001 aerofoils (numerical) at $M_\infty = 0.6$ with $B = 4$, $s/c = 0.75$ and $\alpha = 0^o$. A thick black line is used to highlight the cut-off lines.

The largest discrepancies between analytical and numerical mode-frequency maps in Figure 6.13 are observed on the line of minimum modal power, which corresponds to $l = 0$. This is not believed to be caused by numerical error, but due to the thickness of the NACA 0001 aerofoils in the numerical simulations. In the upstream direction, circumferential modes near the cut-off lines defined by Equation 6.11 present a larger amplitude than the modes away from the cut-off lines. However, opposite trends are found in the downstream direction. These observations, which were previously highlighted by Cheong *et al.* [163] for flat plates, remain true for a cascade of thin aerofoils.

6.4 Influence of Fan Wake Modelling on Cascade Noise

Potential effects of fan wake modelling assumptions on cascade noise are assessed using a 4-vane cascade of NACA 0001 aerofoils at $M_\infty = 0.6$ with $c = 0.15\,\text{m}$, $s/c = 0.75$, and $\alpha = 0^\text{o}$. To this end, numerical sound power spectra are compared to analytical predictions using the flat plate model for two-dimensional cascades of Cheong *et al.* [101]. The analytical predictions were obtained by using the circumferentially-averaged transverse velocity spectrum, which is a common practice to reproduce experimental noise measurements using analytical models [102, 114]. Unlike CAA simulations, the fan wake modelling is not included in the analytical model.

6.4.1 Effect of Turbulent Kinetic Energy Modelling

Cyclostationary variations in the turbulent kinetic energy are modelled by using the von Kármán spectrum with $u'_{rms}/U_\infty = 0.017$ and $\Lambda_w\,(=\Lambda) = 0.008\,\text{m}$, which is achieved from Gaussian superposition with the parameters in Table 2.2. In this case, the amplitude of the eddies is modulated by Equation 6.3 using $n_w = 4$, $\Omega = 2640\,\text{rad/s}$, $R = Bs/(2\pi)$, and $h_w = \Lambda_w/0.42$. Figure 6.14 shows instantaneous contours of non-dimensional fluctuating vorticity magnitude and fluctuating pressure in the simulation with cyclostationary variations in the turbulent kinetic energy. The effectiveness of the periodic boundary condition in the circumferential direction can be observed in the fluctuating pressure contours, which also show a number of upstream- and downstream-travelling cut-on modes. These are radiated from the leading edge of the aerofoils, following a dipole-like pattern as occurs in single aerofoil configurations.

Figure 6.15 shows the PWL spectra radiated by the cascade of NACA 0001 aerofoils when modelling cyclostationary variations in the turbulent kinetic energy ($K_w(y,t)$, $\Lambda_w = \text{const.}$). The absence of fan wake modelling in the analytical flat plate model does not impact the good agreement between numerical and analytical results, which is better than 2 dB for most frequencies. When comparing the noise predictions in Figure 6.15 with those in Figure 6.12a for isotropic turbulence, it can be observed

that cyclostationary variations in the turbulent kinetic energy of the fan wakes modify the amplitude of the PWL spectra. Particularly, the PWL spectra are scaled down by approximately 4.4 dB at all frequencies, which corresponds to $10\log_{10}(A^2_{w,rms})$. This conclusion is not expected to be altered by variations in the input parameters that define the distribution of turbulent kinetic energy in the fan wakes, such as n_w, Ω, and R. For example, Dieste [127] showed that an increase in the separation between fan wakes that interact with a single flat plate scales down the noise levels, but maintains the shape of the noise spectra, and Wohlbrandt *et al.* [128] reported unaffected cascade noise when increasing the rotation speed of the fan wakes. Ju *et al.* [115] recently concluded that modelling variations in the turbulent kinetic energy of the fan wakes might not be necessary for analytical models, if a constant integral length scale is assumed.

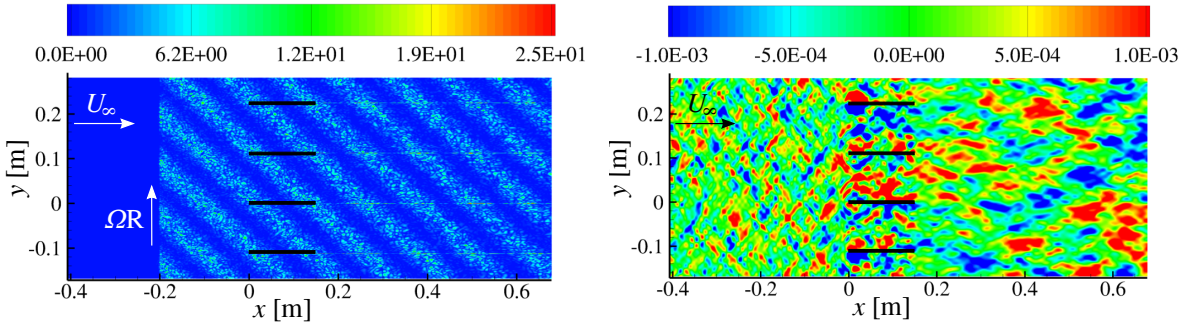

(a) Non-dimensional vorticity magnitude, $\|\nabla \times \mathbf{u}'\|L_{ref}/c_\infty$.

(b) Non-dimensional fluctuating pressure, $p'/(\rho_\infty c_\infty^2)$.

Figure 6.14: Instantaneous contour plots of a cascade with NACA 0001 aerofoils at $M_\infty = 0.6$ with $B = 4$, $s/c = 0.75$, and $\alpha = 0^o$. The fan wakes include cyclostationary variations in the turbulent kinetic energy. A thick black line is used to highlight the location of the aerofoils.

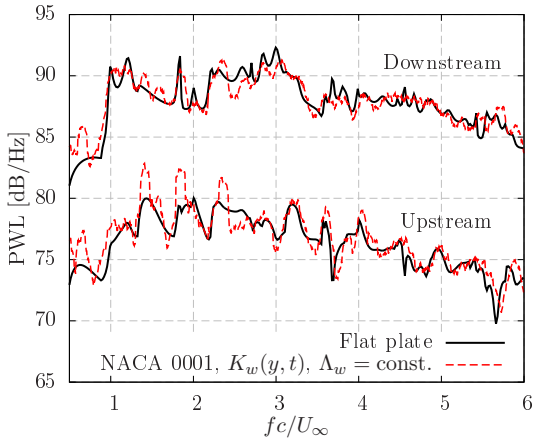

Figure 6.15: PWL spectra from a cascade of NACA 0001 aerofoils at $M_\infty = 0.6$ with $B = 4$, $s/c = 0.75$, and $\alpha = 0^o$. The CAA simulation includes fan wakes with cyclostationary variations in the turbulent kinetic energy.

6.4.2 Effect of Integral Length Scale Modelling

Cyclostationary variations in the integral length scale are modelled by Equations 6.4 and 6.5 for the $\Lambda_{w,1}$ and $\Lambda_{w,2}$ distributions with $\Lambda_{min} = 0.004\,\text{m}$ and $\Lambda_{max}/\Lambda_{min} = 4$. In this case, the Gaussian superposition is done by using Equations 6.6a and 6.6b with the parameters given in Table 6.2.

ith Gaussian eddy	Λ_i [m]	$u'^2_{rms,i}$ [m^2/s^2]
1	5.048×10^{-2}	2.070×10^{-1}
2	2.801×10^{-2}	8.721×10^{-1}
3	1.457×10^{-2}	1.104
4	7.117×10^{-3}	1.009
5	2.801×10^{-3}	1.488

Table 6.2: Parameters for Gaussian superposition to obtain the two-dimensional von Kármán spectrum with $M_\infty = 0.6$, $u'_{rms}/U_\infty = 0.017$, and $\Lambda\,(= \Lambda_{max}) = 0.016\,\text{m}$.

Figure 6.16 shows the PWL spectra from simulations including cyclostationary variations in the integral length scale of the fan wakes. The slope of the PWL spectra is altered by variations in the integral length scales, which produce a redistribution of the energy over the whole frequency range.

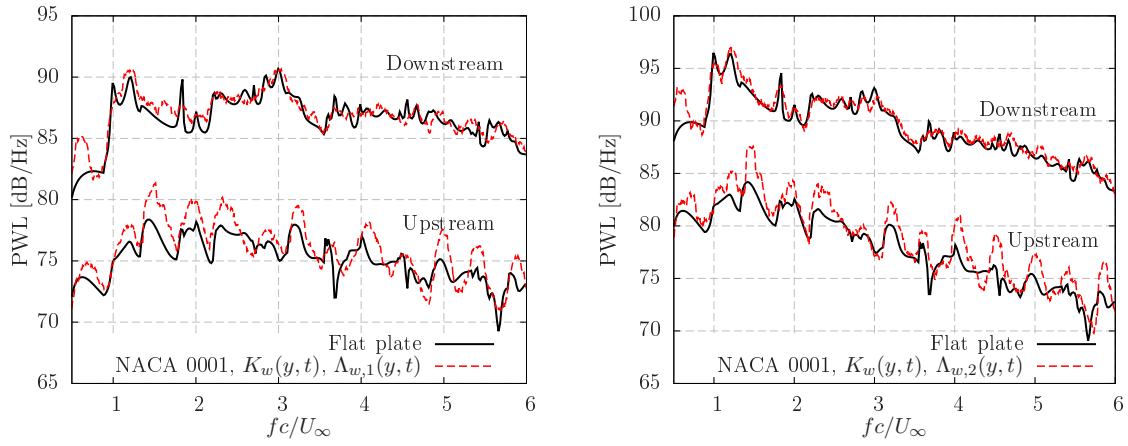

(a) $K_w(y,t)$ and $\Lambda_{w,1}(y,t)$.

(b) $K_w(y,t)$ and $\Lambda_{w,2}(y,t)$.

Figure 6.16: PWL spectra from cascades of NACA 0001 aerofoils at $M_\infty = 0.6$ with $B = 4$, $s/c = 0.75$, and $\alpha = 0^o$. CAA simulations include fan wakes with cyclostationary variations in both the turbulent kinetic energy and integral length scale.

When using the $\Lambda_{w,1}(y,t)$ distribution, the smallest turbulent structures in the fan wakes present high levels of turbulent kinetic energy. Therefore, noise levels are decreased at low frequencies ($\sim$ 2 dB for $fc/U < 4$ in comparison with Figure 6.15) and the PWL spectra are flattened, as shown in Figure 6.16a. In contrast, the role of the low frequencies is reinforced when using the $\Lambda_{w,2}(y,t)$ distribution, in which the turbulent kinetic energy is mainly contained by large turbulent structures. Thus, Figure 6.16b shows a noticeable increase in noise levels at low frequencies of about 5 dB. It should be noted that variations in the shape of the PWL spectra follow similar trends to those experienced by the transverse one-dimensional spectrum averaged in the circumferential direction, as shown in Figure 6.7b.

6.4.3 Summary of fan wake modelling assumptions

For all the fan wake modelling assumptions that have been examined, the PWL spectra show similar distributions of peaks and valleys. This suggests that acoustic cut-on modes excited by the cascade response due to vortical disturbances are pre-determined by a given cascade configuration and Mach number. Therefore, the role of the oncoming turbulence from the fan wakes is to modulate the amplitude of the cut-on modes that contribute to the sound power spectra, as indicated by Cheong *et al.* [163] for isotropic turbulence. For the frequency range investigated, the lowest noise levels are found when modelling the fan wake statistics with the $\Lambda_{w,1}(y,t)$ distribution. This result indicates that significant noise reductions can be achieved by reducing the turbulent kinetic energy of large turbulent structures and energy containing eddies in the fan wakes.

Overall, a good agreement is found between analytical predictions using the circumferentially-averaged transverse spectrum and numerical simulations including fan wake modelling. Broadband noise mainly relies on the averaged spectrum that is perceived by the cascade, and not in the instantaneous statistics of the fan wakes. A more realistic description of the fan wakes leads to an increase in modelling complexity and computational cost, however, it does not produce more accurate broadband noise predictions. This conclusion is valid for the cases with small Λ_w/c, as occurs in turbofan engines. For example, Λ_w/c is approximately 0.05 in the cases examined in this section, and about 0.1 in the fan rig experiment of Ganz *et al.* [17]. For large values of Λ_w/c, the size of the eddies is increased and vane-to-vane correlations might be relevant, particularly for cases with an eddy radius larger than the inter-vane spacing. Overall, numerical results indicate that OGV noise can be predicted accurately by using isotropic turbulence with the circumferentially-averaged spectrum of the fan wakes.

6.5 Parameter Study on Turbulence-Cascade Interaction Noise

In this section, a parameter study on turbulence-cascade interaction noise is presented using the isotropic von Kármán spectrum with $u'_{rms}/U_\infty = 0.017$ and $\Lambda = 0.008$ m. The assumption of isotropic turbulence is adopted here to reduce the computational expense of CAA simulations in comparison to those modelling the fan wake statistics. The baseline configuration is a 4-vane cascade of NACA 0012 aerofoils in an inviscid mean flow at $M_\infty = 0.3$ with $c = 0.15$ m, $s/c = 0.75$, and $\alpha = 0^o$. Figure 6.17 shows instantaneous contours of non-dimensional fluctuating vorticity and pressure for the baseline configuration. The present parameter study includes variations in the vane count, aerofoil thickness, mean flow Mach number, camber, stagger angle, and inter-vane spacing on cascade noise.

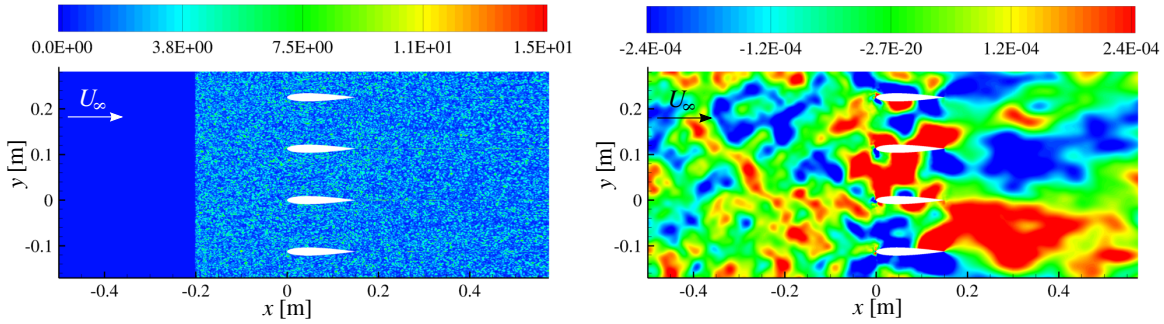

(a) Non-dimensional vorticity magnitude, $\|\nabla \times \mathbf{u}'\| L_{ref}/c_\infty$. (b) Non-dimensional fluctuating pressure, $p'/(\rho_\infty c_\infty^2)$.

Figure 6.17: Instantaneous contour plots of a cascade with NACA 0012 aerofoils at $M_\infty = 0.3$ with $B = 4$, $s/c = 0.75$, and $\alpha = 0^o$ interacting with isotropic turbulence.

6.5.1 Vane Count

Broadband noise predictions of turbulence-cascade interaction normally require the inclusion of a full annulus in order to account for refraction effects and the correct cut-on acoustic modes that can propagate in the duct. However, single OGV passages have been used in previous numerical studies to reduce the size of the mesh, and therefore the computational expense [20, 40].

In order to assess the effect of vane count on the noise, cascades of NACA 0012 aerofoils with $B = 1$, 4, and 20 vanes are simulated in the CAA solver. Figure 6.18 shows the PWL spectra per vane upstream and downstream of the cascade, respectively. Noise predictions from CAA simulations were compared with the flat plate model of Cheong *et al.* [101]. Results show a significant noise reduction due to aerofoil thickness at high frequencies, as occurs in single aerofoil configurations (see Chapter 3), which is discussed in Section 6.5.2.

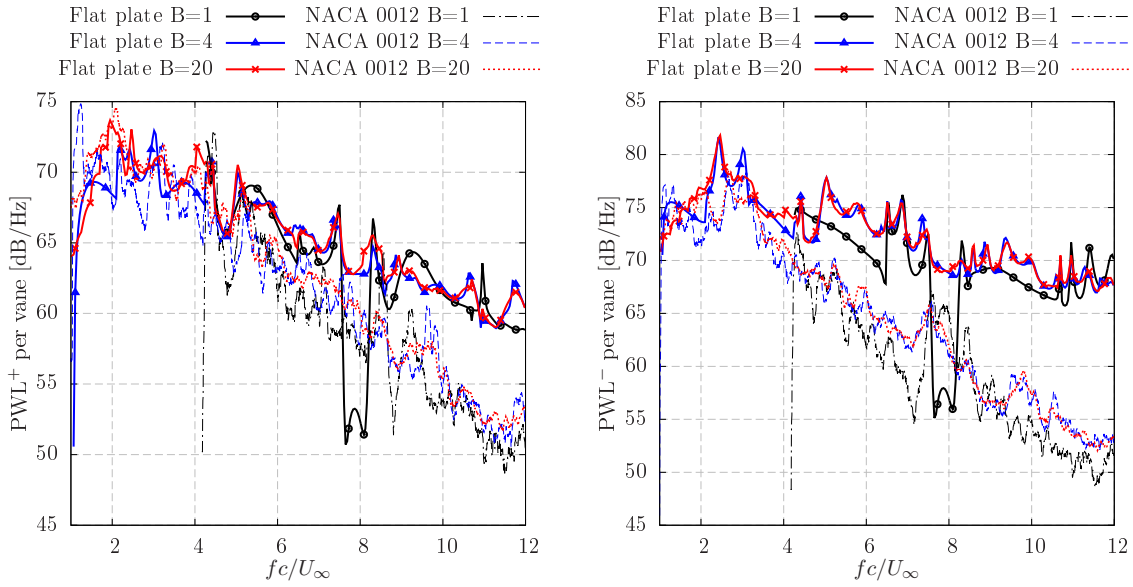

(a) Upstream.

(b) Downstream.

Figure 6.18: PWL spectra for different vane counts in cascades at $M_\infty = 0.3$ with $s/c = 0.75$ and $\alpha = 0^o$.

Simulations with a single vane passage cannot give accurate noise predictions for low frequencies due to the small width of the CAA domain, which limits the cut-on modes that can propagate. Based on the analytical model of Cheong *et al.* [101], the minimum frequency that can propagate for a cascade of flat plates at $\alpha = 0^o$ is given by

$$f_{min} = \frac{c_\infty \sqrt{1 - M_\infty^2}}{Bs}, \tag{6.14}$$

which corresponds to $fc/U_\infty = 4.2$ for the cascade simulation with $B = 1$, as can be seen in Figure 6.18. Chaitanya *et al.* [126] highlighted that the reduced frequency range of interest for fan broadband noise applications is around $fc/U_\infty = 2$, which corresponds to the third harmonic of the BPF for a conventional turbofan engine at approach conditions. Thus, at least $B = 4$ vanes should be used to cover the reduced frequency range of interest. However, discrepancies of up to 4 dB can be found in the PWL spectra at low frequencies ($fc/U_\infty < 4$). This highlights the importance of taking into account the total number of vanes for correct broadband noise predictions in the frequency range of interest for fan noise applications.

At high frequencies, there is a good collapse in the shape and trends of the PWL spectra per vane, especially for $B \geq 4$. Thus, it is possible to reduce the number of vanes computed when investigating high frequencies, since the PWL spectra increase with the number of vanes at high frequencies as

$10\log_{10}(B)$ [102]. Therefore, thick aerofoils seem to behave as uncorrelated noise sources at high frequencies, as found in previous studies for flat plates [70, 101].

6.5.2 Aerofoil Thickness

A typical OGV thickness in turbofan engines is about $t_A/c \approx 0.06$. For example, Ganz *et al.* [17] performed noise measurements of a 18-inch fan rig using stators with $t_A/c = 0.05$ and 0.07 at the hub and tip, respectively. In this section, cascades of NACA 0006 and NACA 0012 aerofoils are used to assess thickness effects on cascade noise. Figure 6.19 shows the numerical PWL spectra and their corresponding analytical predictions for a cascade of flat plates. For the various cases examined, the downstream PWL spectra are about 5dB louder than the upstream spectra. This result indicates that OGV broadband noise mainly contributes to the exhaust noise from the bypass duct, regardless of the vane thickness.

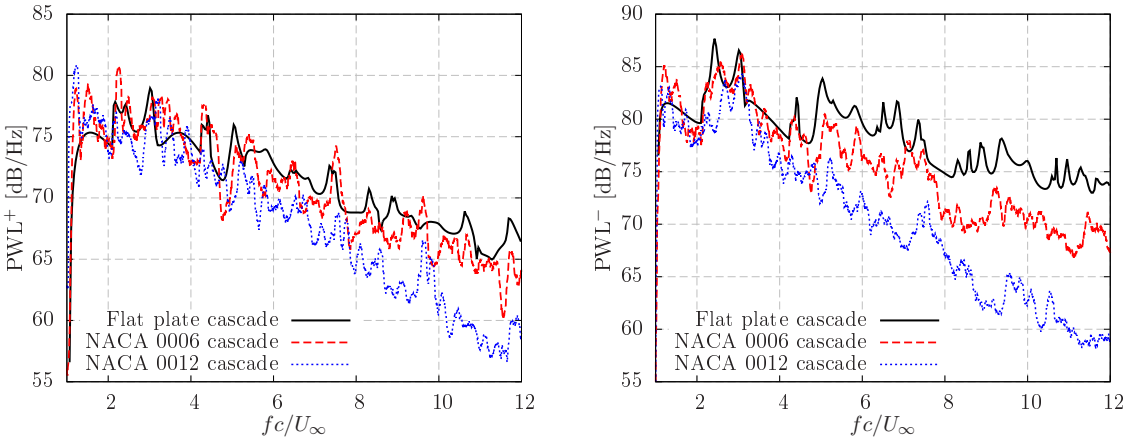

(a) Upstream.

(b) Downstream.

Figure 6.19: PWL spectra from cascades of NACA 0006 and NACA 0012 aerofoils at $M_\infty = 0.3$ with $B = 4$, $s/c = 0.75$, and $\alpha = 0^o$.

At low frequencies ($fc/U_\infty < 3$), the PWL spectra from thick vanes present similar noise levels than flat plates, with small discrepancies of less than 3 dB on average. Consequently, increasing the vane thickness is unlikely to reduce broadband noise in the frequency range of interest for turbofan engines. For the cascade of NACA 0006 aerofoils, the PWL spectra resemble those of flat plate predictions over a large portion of the frequency spectrum. This result reinforces the validity of the flat plate assumption for OGV noise predictions, as recently suggested by Grace [120] and Chaitanya *et al.* [126] using a low-order analytical model and harmonic gust simulations, respectively.

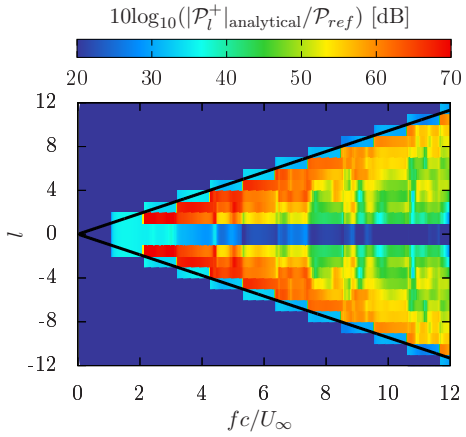

(a) $\mathcal{P}_l^+$ upstream of flat plate cascade.

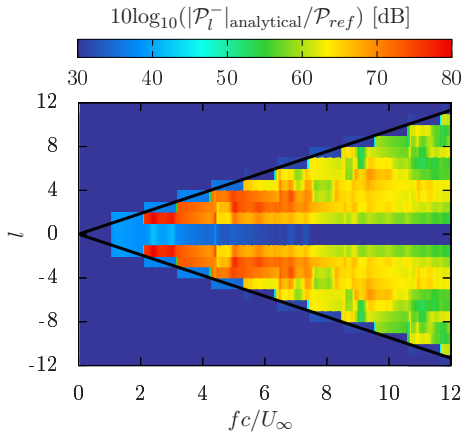

(b) $\mathcal{P}_l^-$ downstream of flat plate cascade.

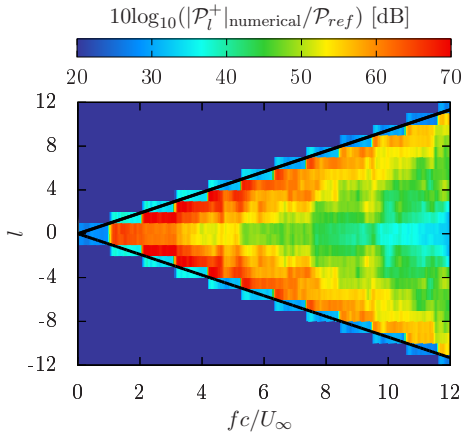

(c) $\mathcal{P}_l^+$ upstream of NACA 0006 cascade.

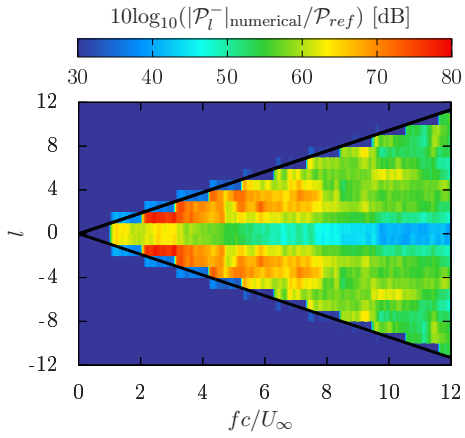

(d) $\mathcal{P}_l^-$ downstream of NACA 0006 cascade.

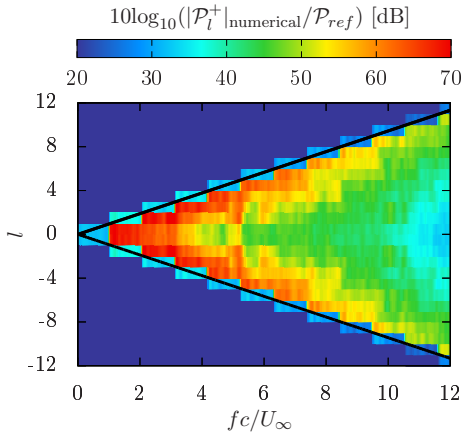

(e) $\mathcal{P}_l^+$ upstream of NACA 0012 cascade.

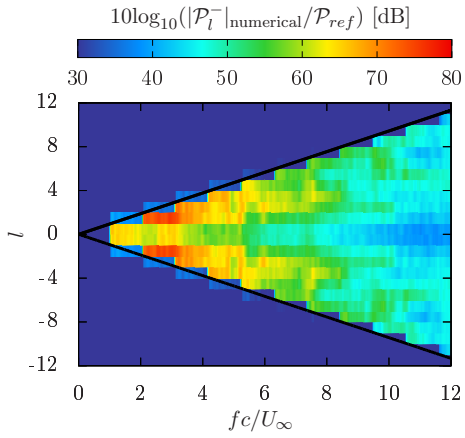

(f) $\mathcal{P}_l^-$ downstream of NACA 0012 cascade.

Figure 6.20: Modal spectral decomposition for cascades at $M_\infty = 0.3$ with $B = 4$, $s/c = 0.75$, and $\alpha = 0^o$. A thick black line is used to highlight the cut-off lines.

A significant noise reduction due to aerofoil thickness is found at high frequencies in Figure 6.19, as occurs in single aerofoil configurations. This noise reduction is especially pronounced for thicker vanes in the downstream direction. For example, the cascade of NACA 0012 aerofoils presents a 7.5 dB noise reduction at $fc/U_\infty = 12$ in the upstream direction, whereas the noise reduction is about 15 dB downstream. These findings are consistent with sound directivity plots in Chapter 3 (for example, see Figure 3.14b), where noise reduction due to aerofoil thickness is larger at downstream observer angles.

A modal decomposition was performed to study the contribution of acoustic modes in the circumferential direction, $l = \kappa_y Bs/(2\pi)$, to the sound power spectra of thick aerofoils. Figure 6.20 shows mode-frequency maps of $\mathcal{P}_l^{\pm}$ for cascades with different vane thickness. At low frequencies, the width of the CAA domain, Bs, limits the number of duct modes that can contribute to the sound power spectrum, which is restricted to a few modes within the cut-off lines. The aerofoil thickness produces an amplitude increase in the circumferential modes close to the line of minimum modal power, $l = 0$, which is particularly pronounced in the upstream direction. This mechanism produces a slight increase in the PWL spectra of cascades with thick vanes at low frequencies, especially in the upstream direction (see Figure 6.19a).

To highlight further thickness effects on cascade noise, Figure 6.21 shows the difference between $\mathcal{P}_l^{\pm}$ from cascades with flat plates and NACA 0012 aerofoils. The modal sound power of cascades with thick vanes resembles that of a cascade with flat plates for $fc/U_\infty < 4$. This justifies the similarities in the PWL spectra from cascades with various vane thicknesses at low frequencies. However, the modal sound power decreases quickly for modes that are away from the cut-off lines at high frequencies. For $fc/U_\infty > 8$, the noise reduction is mainly caused by duct modes with $|l| \in [1, 8]$.

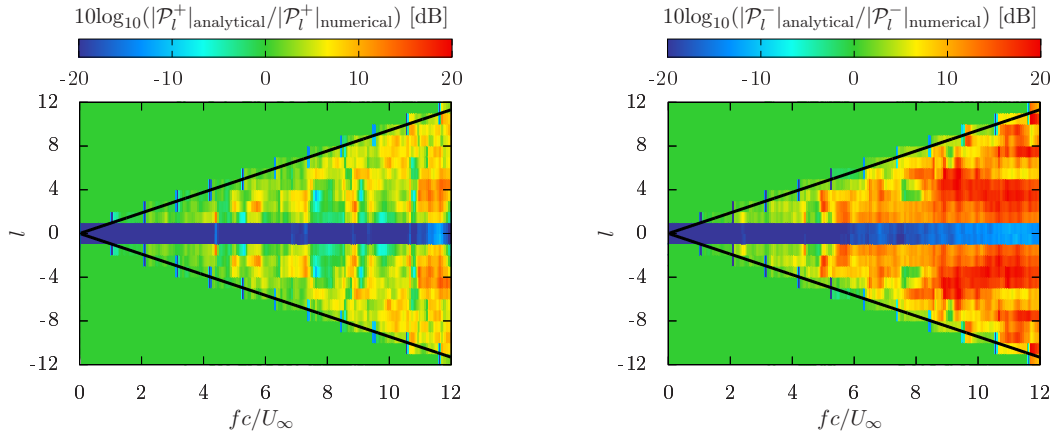

(a) Upstream.

(b) Downstream.

Figure 6.21: Differences in the modal spectral decomposition from cascades of flat plates (analytical) and NACA 0012 aerofoils (numerical) at $M_\infty = 0.3$ with $B = 4$, $s/c = 0.75$, and $\alpha = 0^o$. A thick black line is used to highlight the cut-off lines.

6.5.3 Mach Number

Cascade simulations of NACA 0006 and NACA 0012 aerofoils were performed at $M_\infty = 0.5$. This Mach number is sufficiently high to investigate potential Mach number effects on cascade noise while preventing the formation of shocks between vanes. Note that the inter-vane spacing behaves as a convergent-divergent nozzle. Additionally, noise results are compared to those from cascades at $M_\infty = 0.3$ that were presented in Section 6.5.2.

Figure 6.22 shows the $\Delta\text{PWL} = \text{PWL}|_{\text{flat plate}} - \text{PWL}|_{\text{NACA aerofoil}}$ spectra as a function of fc/U_∞ for different mean flow Mach numbers. There are large oscillations in the ΔPWL spectra, which are due to a mismatch between cut-on modes that contribute to the noise of cascades with thick aerofoils and flat plates. Nevertheless, the ΔPWL spectra show similar trends for each aerofoil geometry at both $M = 0.3$ and 0.5. The collapse is slightly worse for the cascade of NACA 0012 aerofoils at high frequencies, $fc/U_\infty > 5$, where discrepancies of about 3 dB can be observed in both upstream and downstream directions. For a given frequency, slightly larger noise reductions occur at low Mach numbers for thick aerofoils, as reported by Gill [98] and Kim *et al.* [95] for single aerofoils. Nevertheless, it is concluded here that the ΔPWL spectra in cascades scale linearly with fc/U_∞, as occurs in single aerofoil configurations.

Additionally, Figure 6.22 indicates that noise reduction at high frequencies due to aerofoil thickness is significantly smaller for cascades of NACA 0006 aerofoils than for NACA 0012 aerofoils. For the various Mach number investigated, cascades of thin aerofoils and flat plates present similar noise levels ($\Delta\text{PWL} < 3$ dB) for $fc/U_\infty < 4$.

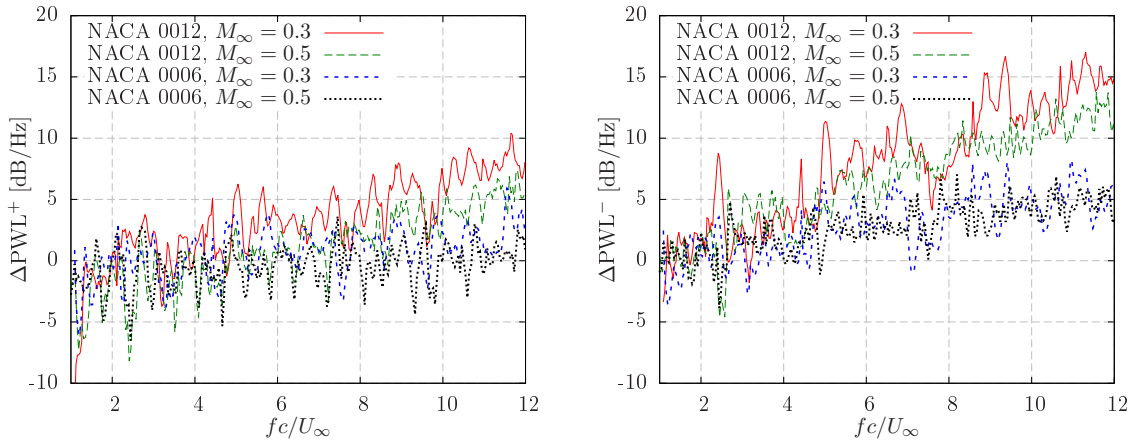

(a) Upstream.

(b) Downstream.

Figure 6.22: $\Delta\text{PWL} = \text{PWL}|_{\text{flat plate}} - \text{PWL}|_{\text{NACA aerofoil}}$ spectra as a function of fc/U_∞ for cascades of NACA 0006 and NACA 0012 aerofoils at $M_\infty = 0.3$ and 0.5 with $B = 4$, $s/c = 0.75$, and $\alpha = 0^\text{o}$.

The thickness-based reduced frequency, ft_A/U_∞, has been highlighted as an important parameter to estimate the noise reduction of thick aerofoils at high frequencies [87, 98]. The importance of this parameter is also found in Figure 6.23 for cascades. A good collapse is found in the ΔPWL spectra of cascades with different vane thicknesses and mean flow Mach numbers. It can also be seen that aerofoil thickness produces larger noise reductions in the downstream direction. Gershfeld's correction [71] (to account for the aerofoil thickness effects on leading edge noise) could be adapted to estimate the noise from cascades with real geometries. This can be done by using a different scaling factor to ft_A/U_∞ for the upstream and downstream spectra in Equation 3.3. Alternatively, the linear least squares method can be used to fit the CAA predictions, as shown in Figure 6.23. The best fit lines for the upstream and downstream estimations of the ΔPWL spectra in dB are given by

$$\Delta\text{PWL}^+ = -2.4579 + 5.6077\frac{ft_A}{U_\infty}, \qquad \Delta\text{PWL}^- = -0.7704 + 9.4340\frac{ft_A}{U_\infty}, \tag{6.15}$$

respectively. It should be noted that the estimated ΔPWL^- spectrum has a greater slope than the ΔPWL^+ spectrum to account for a larger noise reduction at high frequencies in the downstream direction.

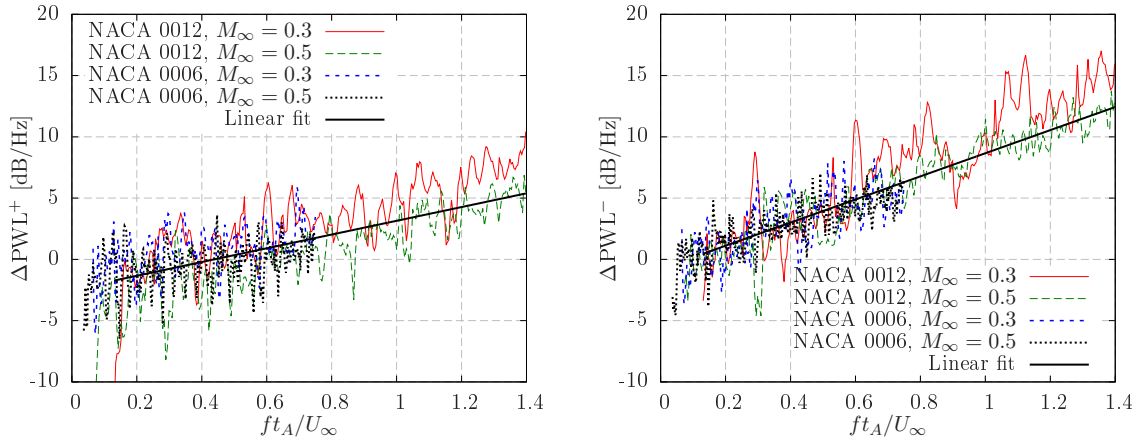

(a) Upstream.

(b) Downstream.

Figure 6.23: $\Delta\text{PWL} = \text{PWL}|_{\text{flat plate}} - \text{PWL}|_{\text{NACA aerofoil}}$ spectra as a function of ft_A/U_∞ for cascades of NACA 0006 and NACA 0012 aerofoils at $M_\infty = 0.3$ and 0.5 with $B = 4$, $s/c = 0.75$, and $\alpha = 0^o$.

6.5.4 Camber

The effects of camber are studied in cascades of NACA 0006, NACA 3406, and NACA 6406 aerofoils, which present a camber of 0%, 3%, and 6% of the chord, respectively. The majority of analytical models for cascade noise assume unloaded flat plates with a constant stagger angle. Therefore, the

mean flow is aligned in the chordwise direction upstream and downstream of the cascade. In contrast, CAA simulations can account for variations in the mean flow direction across the cascade to compute sound power spectra using Equation 6.9. This is particularly relevant when dealing with cambered aerofoils, which may vary the direction of the mean flow, adding or removing swirl.

As shown in Figure 6.24, the mean flow around the cascades is significantly affected by the aerofoil camber. Although the stagger angle is kept to zero, the camber of the NACA 6406 aerofoil induces a change in the direction of the mean flow downstream of the cascade (swirl, $M_y^- < 0$). Additionally, the stagnation region shifts towards the suction side, which varies the angle of attack that is perceived by the aerofoils.

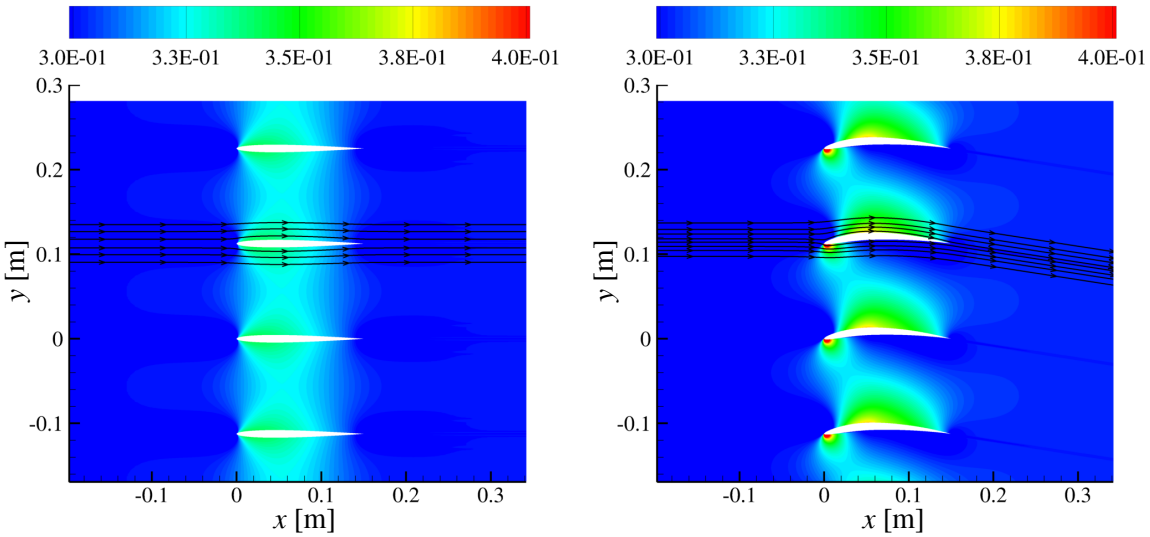

(a) Symmetric NACA 0006 aerofoils.

(b) Cambered NACA 6406 aerofoils.

Figure 6.24: Contours of Mach number around cascades at $M_\infty = 0.3$ with $B = 4$, $s/c = 0.75$, and $\alpha = 0^o$.

The upstream and downstream PWL spectra are shown in Figure 6.25 for various cascades of cambered aerofoils. Despite the significant change in the mean flow distribution around the cascade, there is a good overlap in the PWL spectra for different degrees of camber. This result indicates a small effect of camber and aerofoil mean loading on the cascade noise. For the 6% cambered aerofoil, a consistent increase in the upstream PWL spectrum of only 1 dB is found at most frequencies with respect to low-cambered aerofoils. These findings agree with previous works of Chaitanya *et al.* [126] and Evers and Peake [119], in which variations in the total radiated power within $1 - 2$ dB were reported for cascades of cambered aerofoils.

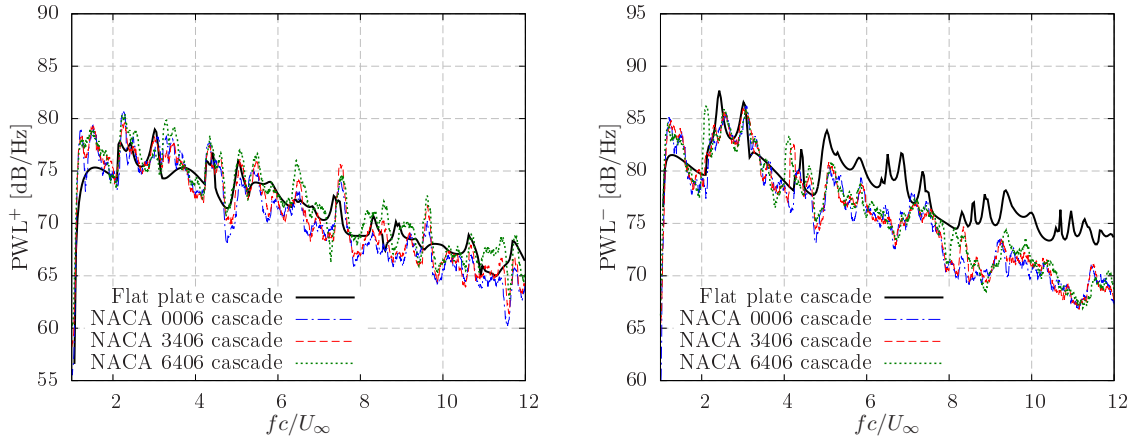

(a) Upstream. (b) Downstream.

Figure 6.25: PWL spectra from cascades of cambered aerofoils at $M_\infty = 0.3$ with $B = 4$, $s/c = 0.75$, and $\alpha = 0^o$.

Figure 6.26 shows mode-frequency maps of $\mathcal{P}_l^\pm$ for the cascade of NACA 6406 aerofoils. The camber of the aerofoils produces a redistribution of the modal sound power, which breaks down the symmetry reported in Figures 6.20c and 6.20d for NACA 0006 aerofoils. This redistribution is related to the swirl generated by the cambered aerofoils, which produce a mean flow deviation of 9° in the downstream direction. The swirl also leads to a small variation in the downstream cut-off lines, which produce a certain skewness in the cut-on triangle of $\mathcal{P}_l^-$. These effects are expected to be aggravated by stronger swirling mean flows. Although camber introduces variations in the modal power distribution, such variations are not reflected in the resulting PWL spectra from the summation of all cut-on modes. This conclusion, which is valid for broadband noise spectra at low and high frequencies, is consistent with results of Evers and Peake [119] and Chaitanya *et al.* [126] using harmonic gusts.

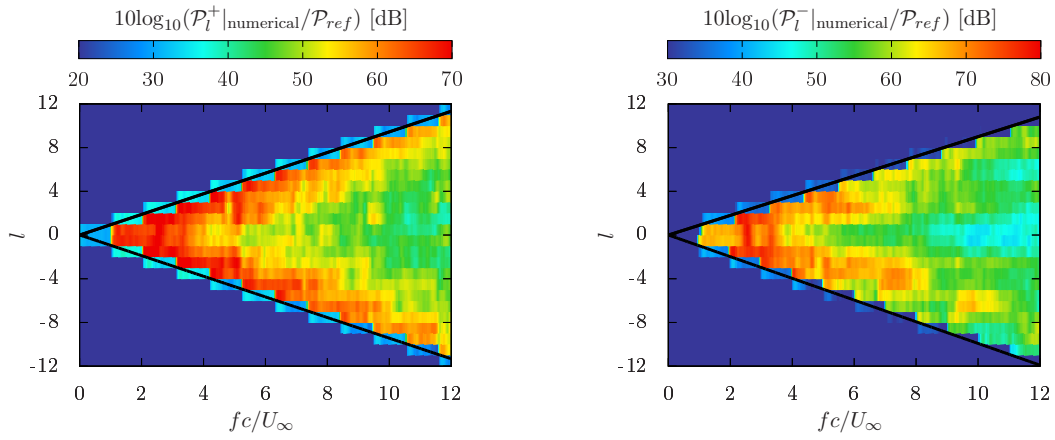

(a) $\mathcal{P}_l^+$ upstream. (b) $\mathcal{P}_l^-$ downstream.

Figure 6.26: Modal spectral decomposition for a cascade of NACA 6406 aerofoils (numerical) at $M_\infty = 0.3$ with $B = 4$, $s/c = 0.75$, and $\alpha = 0^o$. A thick black line is used to highlight the cut-off lines.

6.5.5 Stagger Angle

The stagger angle is now set to $\alpha = 30^{o}$ in the baseline cascade configuration of NACA 0012 aerofoils. This stagger angle is similar to that used by Hanson [102] and Cheong *et al.* [101] when comparing their analytical methods with experimental data from a NASA fan rig. In this configuration, the absence of camber makes the mean flow aligned with the aerofoil chord. Note that the stagger angle and aerofoil camber are usually combined in OGV designs to remove the swirl in the downstream direction.

Figure 6.27 shows the upstream and downstream PWL spectra for staggered and non-staggered cascade configurations. In the upstream direction, the increase in the stagger angle leads to an increase in the noise levels of about $2-3$ dB for cascades of flat plates and NACA 0012 aerofoils, which is particularly pronounced at low frequencies. However, similar noise levels are found in the downstream direction for each configuration when the stagger angle is changed. These results suggest that variations in the stagger angle of cascades with thick aerofoils have a limited effect on the broadband noise.

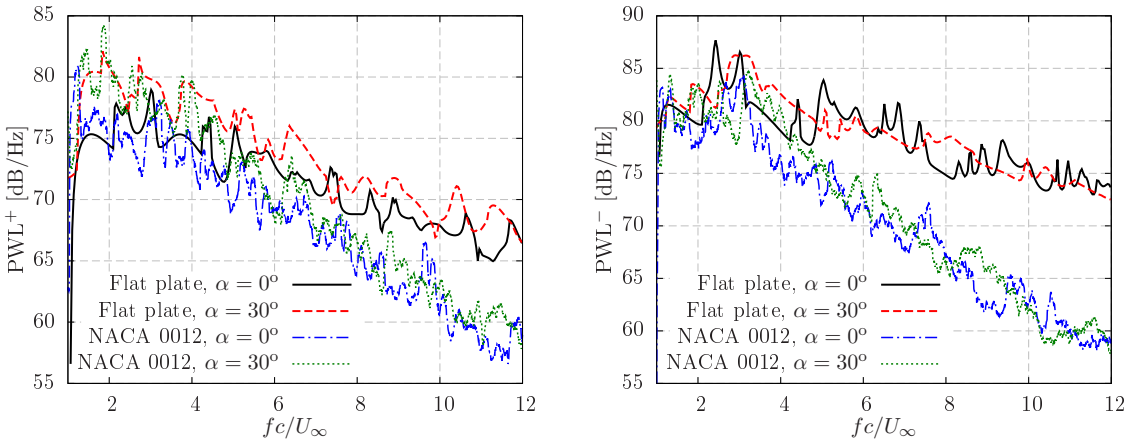

(a) Upstream. (b) Downstream.

Figure 6.27: PWL spectra from cascades of flat plates and NACA 0012 aerofoils at $M_{\infty} = 0.3$ with $B = 4$, $s/c = 0.75$, and $\alpha = 0^{o} - 30^{o}$.

The change in stagger angle leads to a modification of the peaks and valleys in the PWL spectra. This is caused by the redistribution of the cut-on modes that contribute to the modal sound power, as shown in Figure 6.28 using mode-frequency maps of $\mathcal{P}_{l}^{\pm}$. As a consequence of the swirling mean flow ($M_{y}^{\pm} > 0$), the cut-on triangle is now skewed with $\left|l_{max}^{\pm}\right| > \left|l_{min}^{\pm}\right|$ at all frequencies. In the upstream direction, cut-on modes with $l < 0$ are the main contributors to the sound power, whereas sound power is dominated by cut-on modes with $l > 0$ in the downstream direction. These observations were also

discussed by Cheong *et al.* [163] and Jenkins [103] for flat plate cascades. Adding thick vanes to a staggered cascade does not alter significantly the distribution of cut-on modes at low frequecies, but decreases the modal sound power at high frequencies.

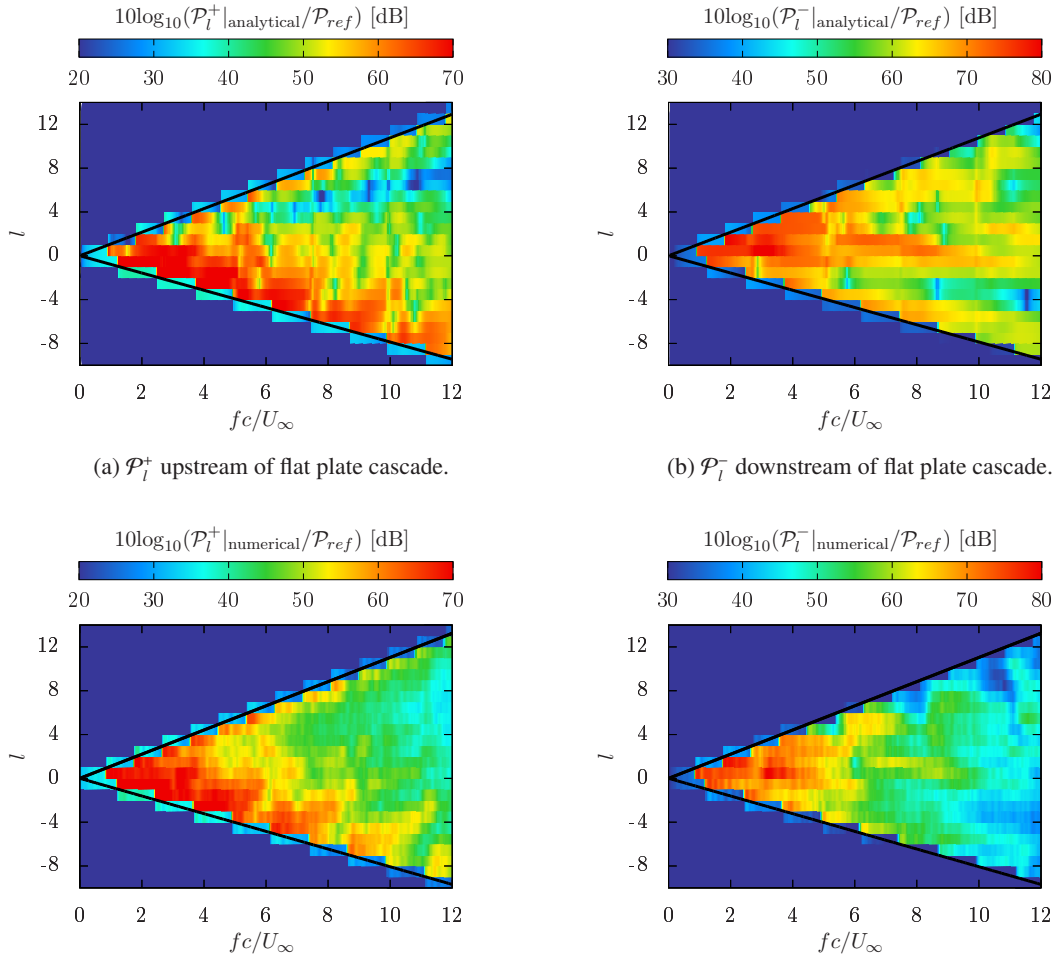

(a) $\mathcal{P}_l^+$ upstream of flat plate cascade.

(b) $\mathcal{P}_l^-$ downstream of flat plate cascade.

(c) $\mathcal{P}_l^+$ upstream NACA 0012 cascade.

(d) $\mathcal{P}_l^-$ downstream of NACA 0012 cascade.

Figure 6.28: Modal spectral decomposition for a cascade of flat plates (analytical) and NACA 0012 aerofoils (numerical) at $M_\infty = 0.3$ with $B = 4$, $s/c = 0.75$, and $\alpha = 30^\text{o}$. A thick black line is used to highlight the cut-off lines.

6.5.6 Inter-Vane Spacing

The effect of variations in the gap-to-chord ratio (or reciprocal of solidity) is assessed by increasing the separation between vanes in the baseline cascade configuration. Thus, s/c is now set to 1.5, while keeping the chord fixed to $c = 0.15\,\text{m}$. An increased gap-to-chord ratio is more representative of

CRORs, in which the separation between consecutive rotor blades is larger than the separation between OGVs in conventional turbofan engines.

Figure 6.29 shows the upstream and downstream PWL spectra for a gap-to-chord ratio of $s/c = 1.5$ in cascades of flat plates and NACA 0012 aerofoils. Results are compared to the baseline configuration with $s/c = 0.75$. The increase in s/c produces a slight increase in noise levels at low frequencies and similar noise levels at high frequencies. It should be noted that as the s/c ratio increases, cascade effects on broadband noise become less important at high frequencies [70, 103]. Thus, the PWL spectrum of the cascade with NACA 0012 aerofoils is expected to become closer to that of the single aerofoil response, scaled by the number of vanes.

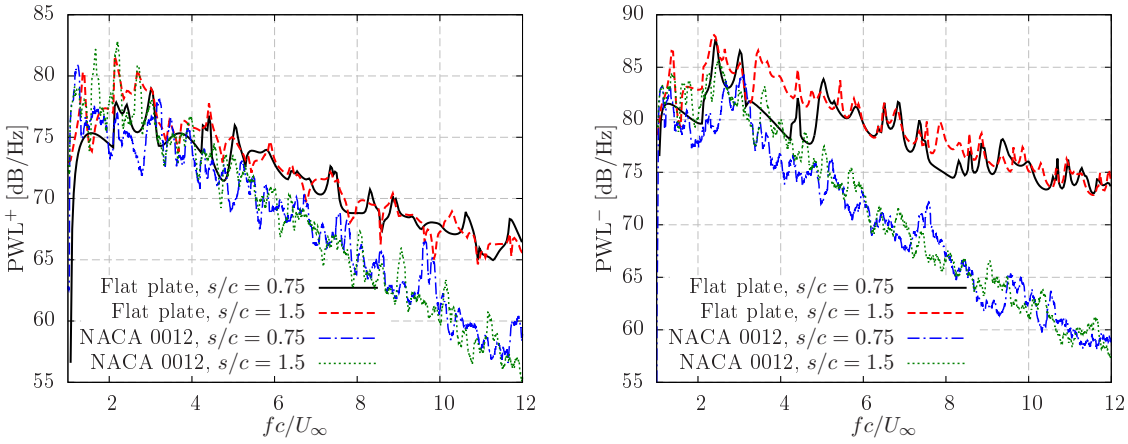

(a) Upstream.

(b) Downstream.

Figure 6.29: PWL spectra from cascades of flat plates and NACA 0012 aerofoils at $M_\infty = 0.3$ with $B = 4$, $s/c = 0.75 - 1.5$, and $\alpha = 0^o$.

6.6 Summary

In this chapter, the advanced digital filter method has been adapted and validated to reproduce the statistics of two-dimensional fan wakes. Three different fan wake modelling assumptions have been proposed: (a) isotropic turbulence with von Kármán spectra, (b) cyclostationary variations in turbulent kinetic energy with a constant integral length scale, and (c) cyclostationary variations in both turbulent kinetic energy and integral length scale. These assumptions have been used to predict turbulence-cascade interaction noise in CAA simulations. Numerical noise results were compared with the analytical cascade model of Cheong *et al.* [101]. Additionally, several cascade configurations have been studied to assess potential OGV geometry effects on cascade noise, including variations in

the vane count, aerofoil thickness, Mach number, camber, stagger angle, and inter-vane spacing. The main findings are summarised as follows:

- When modelling cyclostationary variations in the turbulent kinetic energy of the fan wakes, the PWL spectra upstream and downstream of the cascade are uniformly shifted at all frequencies by $10\log_{10}(A^2_{w,rms})$.

- Cyclostationary variations in the integral length scale of the fan wakes produce a redistribution of the energy in the circumferentially-averaged turbulence spectra. As a consequence, the slope of the PWL spectra is altered upstream and downstream of the cascade. For example, if the largest integral length scale occurs at the maximum turbulent kinetic energy, the resulting PWL spectra will be dominated by low frequencies.

- The location of peaks and valleys in the PWL spectra remains unchanged by the fan wake modelling. This suggests that the same cut-on modes are activated when using isotropic turbulence and when modelling the fan wakes. Therefore, the main effect of the turbulent fan wakes is to modulate the cascade response function.

- The comparison between the analytical and numerical PWL spectra shows that broadband noise mainly depends on the circumferentially-averaged turbulence spectra that interact with the cascade. A realistic description of the fan wakes, with cyclostationary variations in both turbulent kinetic energy and integral length scale, does not lead to a significant improvement of broadband noise predictions. Thus, the isotropic turbulence assumption provides the best compromise between computational cost and simulation accuracy.

- When using a single passage, the minimum frequency that can be solved is normally larger than the frequency range of interest for fan broadband noise applications, $fc/U_\infty \approx 2$, due to the limited width of the CAA domain. By increasing the vane count, the PWL spectra per vane overlap at high frequencies, but there are still some discrepancies in the shape of the spectra at low frequencies. This suggests the need for the total vane count to be used for high-fidelity noise predictions.

- Cascades of thick aerofoils have been found to reduce noise levels at sufficiently high frequencies, $fc/U_\infty > 4$, as occurs for single aerofoils. The noise reduction is particularly pronounced downstream of the cascade, which is caused by a reduction in the modal sound power of duct modes away from the cut-off lines. Additionally, aerofoil thickness has been found to increase the modal sound power along the line of minimum modal power.

- The PWL spectra from 6% thick aerofoils, which are representative of the typical thickness of OGVs, match satisfactorily the analytical flat plate results over a large portion of the frequency

range ($fc/U_\infty < 4$). This reinforces the use of the flat plate assumption for the prediction of OGV broadband noise.

- Noise reduction due to aerofoil thickness in cascades, $\Delta\text{PWL} = \text{PWL}|_{\text{flat plate}} - \text{PWL}|_{\text{NACA aerofoil}}$, scales linearly with fc/U_∞ and ft_A/U_∞, as reported for single aerofoil configurations. However, the slope of the ΔPWL spectra is different in the upstream and downstream directions, since larger noise reductions due to aerofoil thickness occur in the downstream direction. Best fit lines have been calculated to estimate the upstream and downstream ΔPWL spectra as a function of ft_A/U_∞ using the least squares method.

- For cascades of aerofoils with $t_A/c = 0.06$, the PWL spectra are not significantly affected ($\sim$ 1 dB) by a 6% camber increase, despite the noticeable variations in the mean flow around the cascade. This is consistent with the small effect of the aerofoil mean loading on leading edge noise that was discussed in Chapter 4. Nevertheless, modifications to the mean flow, such as adding or removing swirl, break down the symmetry of the cut-on triangle in the mode-frequency maps.

- The PWL spectra present similar noise levels after a significant variation in the stagger angle ($\alpha = 30^\text{o}$) and in the inter-vane spacing ($s/c = 1.5$). However, the distribution of the peaks and valleys in the PWL spectra was significantly altered. This is because variations in α and s/c modify the cut-on modes that contribute to the PWL spectra. For example, the mode-frequency maps of $\mathcal{P}_l^{\pm}$ for the staggered cascade showed a highly skewed cut-on triangle due to the swirling mean flow.

According to the previous conclusions, small improvements in broadband noise reduction from fan wake-OGV interaction can be achieved by independent variations in the vane thickness, camber, stagger angle, and inter-vane spacing. This reduces the number of design parameters that can effectively be optimised to reduce engine fan broadband noise. However, the PWL spectra scale with the number of vanes at high frequencies. Therefore, fan wake-OGV interaction noise can be reduced by decreasing the vane count in turbofan engines. Note that this could introduce variations in the BPF and its harmonics. Additionally, it can be concluded from the present CAA study that the turbulent kinetic energy of the fan wakes is one of the main contributors to the cascade noise. To reduce this potential source of noise: (a) the number of fan blades could also be reduced, (b) the blade design could be further optimised to reduce the boundary layer and wake turbulence, and (c) the separation between the fan stage and OGVs could be increased to allow for the decay of the turbulence intensity in the fan wakes. Alternative OGV designs that use passive noise control technologies, such as wavy leading edges, could also be further investigated [164, 165]. The challenge is to reduce the fan wake-OGV interaction noise without significantly affecting the aerodynamic performance of the engine.

Chapter 7

Conclusions and Future Work

This chapter summarises the work presented throughout this thesis. The key findings and contributions are highlighted, and recommendations for future work are also provided.

7.1 Summary and Conclusions

CAA simulations using the LEEs and synthetic turbulence have been performed to study leading edge noise from single aerofoils and cascades. The conclusions of this thesis have been classified into three different categories: synthetic turbulence methods (see Section 7.1.1), turbulence-aerofoil interaction noise (see Section 7.1.2), and turbulence-cascade interaction noise (see Section 7.1.3).

7.1.1 Synthetic Turbulence Methods

In this thesis, an advanced digital filter method has been developed to generate two- and three-dimensional synthetic turbulence with well-defined isotropic and anisotropic turbulence spectra. The method is based on the RPM method [52, 60], for the mathematical background, and synthetic eddy methods [43, 47, 48], for the numerical implementation. The resulting turbulent flow is divergence-free, as required for leading edge noise predictions, and has a broadband frequency content, in contrast with methods based on Fourier mode methods. The main properties of the advanced digital filter method are summarised as follows:

- The advanced digital filter method reduces the number of parameters and random numbers that are necessary to calculate in recent synthetic eddy methods [48], and avoids the generation and filtering of white noise signals in comparison with the RPM method [52].

- A new eddy profile is defined from a superposition of Gaussian eddies in order to recover a target isotropic energy spectrum, such as von Kármán or Liepmann. In practical cases, $N_e = 5$ Gaussian eddies are sufficient to reproduce a target isotropic energy spectrum.

- All eddies injected into the CAA domain have the same profile and amplitude, and the only difference between them is their direction of rotation, which simplifies the implementation and accelerates the convergence of the turbulence statistics.

- For two- and three-dimensional isotropic turbulence, the correct turbulence statistics are recovered provided that the eddy radius and the eddy spacing in the injection plane satisfy $r_e \geq 3\Lambda/2$ and $\Delta_e \leq \Lambda/2$, respectively. These are optimised values obtained by evaluating the averaged error in the resulting turbulence spectra from a parameter study.

- For leading edge noise predictions, the injection plane can be placed at a distance equivalent to the eddy radius, r_e, upstream of the aerofoil leading edge.

- The advanced digital filter method can be used to generate pseudo three-dimensional turbulence, i.e., two-dimensional synthetic turbulence with the key statistics of three-dimensional turbulence. This type of turbulence is useful to reproduce experimental results from single aerofoils in open-jet wind tunnel experiments at a reduced computational cost. Numerical noise predictions show an agreement with experimental measurements of better than 3 dB for the majority of tested configurations.

- Homogeneous anisotropic turbulence is realised by modifying the length scales of the Gaussian eddies in different spatial directions, while preserving the divergence-free condition. Furthermore, a superposition of anisotropic Gaussian eddies has been used to generate homogeneous axisymmetric turbulence as defined by Kerschen and Gliebe [113].

- The advanced digital filter method can accurately reproduce cyclostationary variations in the turbulent kinetic energy and integral length scale of the fan wakes.

The advantages and limitations of the advanced digital filter method have been compared to Fourier mode methods with one and two fluctuating velocity components. The main conclusions from this comparison are listed below.

- The one-component Fourier mode method is the simplest and fastest synthetic turbulence method among those analysed in this thesis. This method is suitable for studying leading edge noise from aerofoils with moderate thickness ($t_A/c \leq 0.06$) at zero angle of attack. However, the one-component Fourier mode method fails to correctly predict leading edge noise from aerofoils with large thickness at high frequencies and aerofoils at non-zero angle of attack, as indicated by Gill *et al.* [41].

- The advance digital filter method and the two-component Fourier mode method give similar leading edge noise predictions for all the aerofoil configurations examined. This implies that the choice of synthetic turbulence method has no significant influence on the resulting noise prediction. However, the advanced digital filter method provides savings in computational cost, since it is up to 3.9 times faster than the two-component Fourier mode method for two-dimensional simulations.

7.1.2 Turbulence-Aerofoil Interaction Noise

Isotropic turbulence interacting with single aerofoils has been studied to improve current understanding of leading edge noise. The main conclusions are listed below.

- Synthetic turbulence methods based on digital filters and Fourier mode methods have been used to study the effects of freestream Mach number, aerofoil thickness, and angle of attack on leading edge noise. Numerical far-field noise predictions show similar trends as reported in previous experimental, analytical, and numerical works on leading edge noise using isotropic turbulence. Noise is reduced at high frequencies as the aerofoil thickness increases, whereas the angle of attack has a small effect on the noise.

- The $\Delta\text{PWL} = \text{PWL}|_{\text{flat plate}} - \text{PWL}|_{\text{NACA aerofoil}}$ spectra (in dB) scale linearly with fc/U_∞ for the various configurations investigated using isotropic turbulence. For NACA 0006 and NACA 0012 aerofoils, there is a good overlap in the ΔPWL spectra as a function of the thickness-based reduced frequency for $ft_A/U_\infty \leq 0.6$. A best fit line based on the least squares method has been proposed to estimate the ΔPWL spectra as a function of ft_A/U_∞.

- Turbulent structures are distorted in a small region confined within $0.02c$ from the aerofoil leading edge. In the stagnation region, $u'_{x,rms}/U_\infty$ is reduced, and $u'_{y,rms}/U_\infty$ is increased. These trends are also observed in the one-dimensional spectra of the fluctuating velocity, which are distorted in the vicinity of thick aerofoils. Particularly, $E_{11}^{(2D)}$ decays uniformly at all frequencies, whereas $E_{22}^{(2D)}$ is increased at low frequencies and decreased at high frequencies. Additionally, it has been found that the trends and levels of the distorted $E_{22}^{(2D)}$ can be estimated by using a modified von Kármán spectrum that is based on rapid distortion theory.

- One-dimensional spectra $E_{11}^{(2D)}$ and $E_{22}^{(2D)}$ present similar distortions in the leading edge region as a function of fc/U_∞ for a given aerofoil geometry. This result indicates a weak effect of the freestream speed on the distorted spectra. Furthermore, the distortion of the turbulence spectra shows similar trends for aerofoils at zero and non-zero angles of attack, which justifies the insensitivity of the noise predictions to variations in the angle of attack.

- A spectral analysis of the fluctuating pressure on the surface of NACA 0006 and NACA 0012 aerofoils indicates a reduction in the strength of the unsteady pressure response as the aerofoil thickness increases, especially at high frequencies. This finding is consistent with the far-field noise reduction due to aerofoil thickness at high frequencies. Additionally, the maximum p'_{rms}, which is found in the leading edge region, is mainly caused by low frequencies.

- Unlike aerofoils in the free field, simulations including the jet and strong shear layers can reproduce the trends of the experimental C_p. In this case, a simplified version of the LEEs with $\partial U_{0,x}/\partial y$ terms neglected can be used to guarantee the stability of the simulations. Nevertheless, numerical results showed a weak dependence on the mean flow modelling assumptions and aerofoil mean loading, with variations of less than 3 dB for jet and freestream configurations. At a design stage, simulations of aerofoils in the freestream at zero angle of attack should be sufficiently accurate to estimate the leading edge noise of more challenging configurations.

Moderately anisotropic turbulence has been reported experimentally in the fan wakes [18]. However, few works have discussed the effects of anisotropy until now, and the majority of prediction tools for fan broadband noise assume isotropic turbulence. In this thesis, the effects of anisotropic turbulence on leading edge noise have been addressed by means of homogeneous axisymmetric turbulence as defined by Kerschen and Gliebe [113]. CAA simulations were performed using anisotropic synthetic turbulence with the streamwise-to-transverse length scale ratio, l_a/l_t, ranging between 0.33 and 3. The main conclusions are summarised as follows:

- Anisotropic turbulence produces a redistribution of the energy in the velocity spectra, which affects the amount of energy that contributes to the leading edge noise. This highlights the need for noise prediction tools that can account for anisotropy in the fan wakes.

- The upwash velocity spectrum remains the main contributor to the leading edge noise of aerofoils interacting with moderately anisotropic turbulence, as occurs for isotropic turbulence. However, the streamwise velocity fluctuations become increasingly important for cases with $l_a/l_t > 1$.

- When using anisotropic turbulence, the spanwise wavenumber $k_z = 0$ is the main contributor to the leading edge noise from wings with constant cross-section for far-field observers in the mid-span plan. This extends the validity of the $k_z = 0$ assumption, previously stated by Amiet [39] for isotropic turbulence.

- Noise reduction due to aerofoil thickness, $\Delta\text{PWL} = \text{PWL}|_{\text{flat plate}} - \text{PWL}|_{\text{NACA 0012}}$, scales linearly (in dB) with fc/U_∞ for anisotropic turbulence, following similar trends as for isotropic turbulence. Furthermore, a good overlap in the ΔPWL spectra is found for the various l_a/l_t

investigated. The correction of Gershfeld [71] over-predicts the noise reduction due to aerofoil thickness in both isotropic and anisotropic turbulence.

- A moderate angle of attack variation ($AoA = 6^{o}$) has a small effect (ΔOAPWL < 1 dB) on the leading edge noise from single aerofoils interacting with anisotropic turbulence. Nevertheless, cases with $l_a/l_t < 1$ present a significant noise reduction at high frequencies.

7.1.3 Turbulence-Cascade Interaction Noise

In this thesis, the influence of the fan wake modelling assumptions on cascade noise has been assessed in two-dimensional CAA simulations. The main conclusions are summarised as follows:

- Cyclostationary variations in the turbulent kinetic energy uniformly scale the amplitude of the PWL spectrum, whereas cyclostationary variations in the integral length scale modify the slope of the PWL spectrum.

- Broadband noise mainly depends on the circumferentially-averaged turbulence spectra that are perceived by the cascade. Therefore, isotropic turbulence could be used to fit the circumferentially-averaged statistics of the fan wakes without significant loss of accuracy in the broadband noise results.

- Fan wake modelling assumptions do not alter the distribution of peaks and valleys in the PWL spectra, suggesting that the oncoming turbulence only modulates the amplitude of the cut-on modes from the cascade response.

Additionally, a parameter study was performed to assess the effects of OGV geometry on turbulence-cascade interaction noise. This CAA study provides PWL spectra and modal spectral decompositions upstream and downstream of the cascades for representative configurations. The key conclusions are summarised as follows:

- A good overlap is found between the PWL spectra for cascades with $B \geq 4$ using flat plates and 12% thick aerofoils, especially at high frequencies. Using a reduced vane count at low frequencies could provide an estimation of the noise levels, but variations of up to 4 dB in the PWL spectra have been reported at low frequencies.

- Vane thickness effects on cascade noise are small for $fc/U_{\infty} < 4$. The PWL spectra from 6% thick aerofoils, which are representative of the typical OGV thickness, match satisfactorily the analytical flat plate results over a large portion of the frequency range. This confirms that the flat plate assumption is suitable for the prediction of OGV broadband noise.

- Mode-frequency maps of $\mathcal{P}_l^{\pm}$ show that vane thickness increases the amplitude of the duct modes along the line of minimum modal power. The reduction of cascade noise at high frequencies, $fc/U_\infty > 4$, is caused by a decrease in the amplitude of duct modes away from the cut-off lines.
- The PWL spectra show a negligible effect of camber on the noise levels ($\sim$ 1 dB), despite the significant variation that camber causes in the mean flow. This reinforces the fact that aerofoil mean loading has a small effect on leading edge noise.
- Overall, noise levels are weakly affected by a 30^o variation in the stagger angle and a significant increase in the inter-vane spacing. However, peaks and valleys in the PWL spectra were redistributed across the spectra due to a change in the cut-on modes that contribute to the PWL spectra upstream and downstream of the cascade.
- Swirling mean flows, which are related to cascades with cambered or staggered vanes, produce some skewness in the cut-on triangle of the mode-frequency maps. Nevertheless, significant variations in the modal spectra distribution are smoothed out when computing the PWL spectra.

7.2 Recommendations for Future Work

This section presents suggestions for future work in the area of leading edge noise predictions from single aerofoils and cascades.

- **Turbulence-aerofoil interaction noise in transonic flows**. Leading edge noise predictions using the LEEs are restricted to configurations in which the flow remains subsonic. Regions with local supersonic flows and shocks may appear on the suction side of thick aerofoils at transonic Mach numbers or aerofoils at a moderate angle of attack. These cases could be studied by using the full Euler equations, which include the effect of non-linear terms. Initial work in this area has recently been presented for harmonic gusts interacting with single aerofoils in transonic flows [148]. In future works, these configurations could be studied by using realistic turbulent flows, such as those generated by the advanced digital filter method.
- **Aerofoils with wavy leading edge interacting with anisotropic turbulence**. The use of shorter nacelles in the next generation of turbofan engines will reduce the separation between the fan blades and OGVs. Consequently, it will be necessary to account for the anisotropic turbulence in fan wakes for accurate noise predictions. New designs of low-noise OGVs have been proposed for turbofan engines, including aerofoils with wavy leading edge. Experimental works using nearly isotropic turbulence have recently highlighted the importance of the integral length scale on the noise reduction from aerofoils with wavy leading edge [164]. Therefore, it would be interesting to investigate the impact of anisotropic turbulence with various length

scales on aerofoils with wavy leading edge. This could be done by using the three-dimensional advanced digital filter method for anisotropic turbulence that has been presented in Chapter 5.

- **Unsteady mean flows for the prediction of cascade noise**. In Chapter 6, simulations of turbulence-cascade interaction noise were performed by assuming steady mean flows in the LEEs. This was useful to compare results with the analytical model of Cheong *et al.* [101], which assumes a uniform mean flow. However, the use of unsteady mean flows in the LEEs might be useful to model more realistic cases of turbulence-cascade interaction noise. Unsteady mean flows could potentially affect the convection speed of the turbulent flow, and the propagation of acoustic cut-on modes in the bypass duct. Although unsteady mean flows might increase the computational cost and memory requirements of the computations, it seems a step forward towards more realistic CAA computations of fan wake-OGV interaction noise. Initial works on this subject have been recently presented by Wohlbrandt *et al*. [128]. However, an extensive study on the suitability of unsteady mean flows and their effects on cascade noise is still required.

- **Moving/sliding meshes to include the fan/rotor stage in CAA simulations**. Unsteady mean flows could be combined with moving meshes in LEE solvers to include the fan stage in the simulations. Including a row of fan blades might be useful to study the effect of fan shielding on upstream-travelling acoustic waves from the OGVs. There are analytical models in the literature to account for the loss of sound power transmitted across the fan stage that could be used for validation of numerical results using the LEEs. For example, Jenkins (see Chapter 5 in Reference [103]) developed a model based on the previous works of Smith [100] and Whitehead [161] for two-dimensional configurations. Additionally, the interaction between anisotropic turbulence stretched in the axial direction and rotating fan blades could be studied to assess the effects of anisotropy on turbulence ingestion noise at the fan intake.

- **Strip theory in CAA simulations of cascade noise**. The strip theory is used by several analytical models to compute cascade noise at various radial locations. However, analytical models often assume isotropic turbulence and flat plates. The strip theory could be applied in two-dimensional cascade simulations, such as those in Chapter 6, to account for vane geometry effects and fan wake modelling on the predictions of cascade noise. This approach represents an alternative to fully three-dimensional simulations, and would potentially improve the accuracy of cascade noise predictions and the comparison with experimental data.

- **Fully three-dimensional CAA simulations of cascade noise**. In this thesis, cascade simulations were restricted to two-dimensional configurations in order to improve the current understanding of fan wake-OGV interaction noise. However, the effects of sweep and lean angles in OGV noise should be addressed by fully three-dimensional simulations. Until now, few

works have performed three-dimensional simulations of OGVs using the LEEs, and often involve several assumptions to reduce the complexity and computational cost of the simulations. For example, Polacsek *et al.* [40] used a single vane passage with a flat plate, and isotropic turbulence with only the upwash component to model the fan wakes. Next steps in the area of cascade noise using the LEEs should focus on reproducing more realistic cases at a reduced computational cost. Alternatively, Lattice Boltzmann solvers could be used for the computation of turbofan engine noise in highly realistic cases [22, 23, 129].

- **In-duct divergence-free turbulence injection**. The use of in-duct synthetic turbulence to study fan wake-OGV interaction noise in three-dimensional simulations is a challenging problem. This is because the fluctuating velocity field may interact with the duct walls, producing an additional noise source that can contaminate leading edge noise from the OGVs. Thus, it would be useful for three-dimensional cascade noise predictions to develop a method or a boundary condition to inject realistic synthetic turbulence within a duct. By including the bypass duct in the CAA simulations, it could also be possible to study the performance of different liners on broadband duct mode propagation.

- **Effects of heterogeneous OGVs on broadband noise**. Recent developments in turbofan engines show heterogeneous OGVs in which some stator vanes present a modified geometry, such as an increased aerofoil chord or thickness. To date, current analytical models for the prediction of fan wake-OGV interaction noise are not suitable to study the effects of OGV heterogeneity on cascade noise. However, the CAA methodology presented in Chapter 6, which was applied to study broadband noise from homogeneous cascades, can also be used to analyse the effects of OGV heterogeneity on cascade noise.

Appendix A

Random Particle-Mesh

This Appendix presents a derivation of the governing equations for three-dimensional isotropic synthetic turbulence based on the Random Particle-Mesh method [52, 53]. A complete derivation was presented by Dieste (see Appendices A and B in Reference [127]). This derivation is reproduced here, including additional intermediate steps. Although the derivation has been performed for three-dimensional turbulence, the two-dimensional derivation follows the same steps and its main results are also included here.

This Appendix is organised as follows. General equations for the definition of the turbulent velocity field, which is derived from a vector potential, are presented in Section A.1. It should be noted that the vector potential is obtained by filtering white noise signals. In Section A.2, the two-point correlation tensor of the vector potential is linked to the filter in wavenumber space. Assuming homogeneous and isotropic turbulence, it is possible to find a relationship between the longitudinal and transverse correlation functions and the two-point correlation of the vector potential, as shown in Section A.3. Then, the trace of two-point velocity correlation is linked to the filter in wavenumber space in Section A.4. Finally, the energy spectrum of a turbulent flow is linked to the filter in wavenumber space in Section A.5.

A.1 General Equations

To ensure the divergence-free condition, the fluctuating velocity field is derived from the curl of the perturbation vector potential

$$\mathbf{u}'(\mathbf{x},t) = \nabla \times \boldsymbol{\eta}(\mathbf{x},t) = \varepsilon_{ijk}\frac{\partial}{\partial x_j}\eta_k \mathbf{e}_i, \tag{A.1}$$

where $\mathbf{x}$ represents a point in the flow field at time t and ε_{ijk} is the Levi-Civita symbol. Thus, it is straightforward to verify that $\nabla \cdot \mathbf{u}' = \nabla \cdot (\nabla \times \boldsymbol{\eta}) = 0$.

The perturbation vector potential is defined as

$$\eta_i(\mathbf{x}, t) = \int_{V_s} G(\mathbf{x} - \mathbf{x}_e)\mathcal{U}_i(\mathbf{x}_e, t)\mathrm{d}\mathbf{x}_e, \tag{A.2}$$

where $G(\mathbf{x} - \mathbf{x}_e)$ is the spatial filter, $\mathcal{U}_i(\mathbf{x}_e, t)$ is the spatio-temporal white noise signal for the ith-component, and $\mathbf{x}_e$ is a point within the source region, V_s, where the filters are applied. Note that only one white noise term is required for a two-dimensional case, since the turbulent velocity field is derived using only one component of the vector potential, which is reduced to a single streamfunction. The random signal has the following properties:

$$\langle \mathcal{U}_i(\mathbf{x}, t) \rangle = 0, \tag{A.3a}$$

$$\left\langle \mathcal{U}_i(\mathbf{x}_1, t)\mathcal{U}_j(\mathbf{x}_2, t) \right\rangle = \delta(\mathbf{r})\delta_{ij}, \tag{A.3b}$$

$$\frac{D\mathcal{U}_i}{Dt} = 0, \tag{A.3c}$$

where $\mathbf{r} = \mathbf{x}_2 - \mathbf{x}_1$ is the separation between two points and $\langle . \rangle$ represents the ensemble average operator. Note that the process is assumed to be statistically stationary and thus, ensemble average and time average operators are equivalents. Equation A.3c only holds under frozen turbulence assumption, and can be combined with Equation A.3b to give

$$\left\langle \mathcal{U}_i(\mathbf{x}_1, t_1)\mathcal{U}_j(\mathbf{x}_2, t_2) \right\rangle = \delta(\mathbf{r} - \tau\mathbf{U}_0)\delta_{ij}, \tag{A.4}$$

where $\mathbf{U}_0$ is the convection velocity and $\tau = t_2 - t_1$ is the separation between two instants.

A.2 Two-Point Correlation of the Vector Potential in Wavenumber Space

In this Section, the two-point correlation of the vector potential is related to the digital filter in wavenumber space. For a statistically homogeneous process, the two-point correlation of the vector potential is defined as

$$C_{ij}(\mathbf{r}) = \left\langle \eta_i(\mathbf{x}_1, t)\eta_j(\mathbf{x}_2, t) \right\rangle. \tag{A.5}$$

Introducing Equation A.2 into Equation A.5 leads to

$$C_{ij}(\mathbf{r}) = \left\langle \int_{V_{s1}} G(\mathbf{x}_1 - \mathbf{x}_{e1}) \mathcal{U}_i(\mathbf{x}_{e1}, t) \mathrm{d}\mathbf{x}_{e1} \int_{V_{s2}} G(\mathbf{x}_2 - \mathbf{x}_{e2}) \mathcal{U}_j(\mathbf{x}_{e2}, t) \mathrm{d}\mathbf{x}_{e2} \right\rangle. \tag{A.6}$$

Applying the ensemble average operator to the stochastic term, i.e., to the white noise term, gives

$$C_{ij}(\mathbf{r}) = \int_{V_{s1}} \int_{V_{s2}} G(\mathbf{x}_1 - \mathbf{x}_{e1}) G(\mathbf{x}_2 - \mathbf{x}_{e2}) \left\langle \mathcal{U}_i(\mathbf{x}_{e1}, t) \mathcal{U}_j(\mathbf{x}_{e2}, t) \right\rangle \mathrm{d}\mathbf{x}_{e1} \mathrm{d}\mathbf{x}_{e2}. \tag{A.7}$$

Using the property of the white noise term defined by Equation A.3b and taking into account that $\mathbf{x}_1 = \mathbf{x}_2 - \mathbf{r}$, gives

$$C_{ij}(\mathbf{r}) = \delta_{ij} \int_{V_{s2}} G(\mathbf{x}_2 - \mathbf{x}_{e2}) G(\mathbf{x}_2 - \mathbf{x}_{e2} - \mathbf{r}) \mathrm{d}\mathbf{x}_{e2}, \tag{A.8}$$

which is the convolution of the digital filter, and therefore

$$C_{ij}(\mathbf{r}) = (G \otimes G)(\mathbf{r}) \delta_{ij}. \tag{A.9}$$

If the Fourier transform for $C_{ij}(\mathbf{r})$ is defined as

$$\hat{C}_{ij}(\mathbf{k}) = \frac{1}{(2\pi)^3} \int_{-\infty}^{+\infty} C_{ij}(\mathbf{r}) \exp\left(-i\mathbf{k}\cdot\mathbf{r}\right) \mathrm{d}\mathbf{r}, \tag{A.10}$$

the one-dimensional convolution of two functions in physical space corresponds to the multiplication of 2π and the Fourier transforms in wavenumber space, hence

$$\hat{C}_{ij}(\mathbf{k}) = \delta_{ij} 8\pi^3 \hat{G}^2(\mathbf{k}). \tag{A.11}$$

For a purely two-dimensional turbulent flow, Equation A.11 can be rewritten as $\hat{C}(\mathbf{k}) = 4\pi^2 \hat{G}^2(\mathbf{k})$, since the vector potential is defined by a unique streamfunction.

A.3 Longitudinal and transverse Correlation Functions

In this Section, the two-point velocity correlation

$$R_{ij}(\mathbf{r}) = \left\langle u_i(\mathbf{x}_1) u_j(\mathbf{x}_2) \right\rangle, \tag{A.12}$$

is related to the two-point correlation of the vector potential

$$C_{ij}(\mathbf{r}) = C(r)\delta_{ij} = \left\langle \eta_i(\mathbf{x}_1) \eta_j(\mathbf{x}_2) \right\rangle, \tag{A.13}$$

by assuming that the turbulent flow is homogeneous and isotropic. In this case, the two-point velocity correlation can be defined by means of the non-dimensional longitudinal and transverse correlation functions, $f(r)$ and $g(r)$, respectively,

$$R_{ij}(r) = u'^2_{rms}\left\{\left[f(r) - g(r)\right] n_i n_j + g(r)\delta_{ij}\right\}. \tag{A.14}$$

Introducing Equation A.1 into Equation A.12 gives

$$R_{ij}(\mathbf{r}) = \left\langle u_i(\mathbf{x}) u_j(\mathbf{x}+\mathbf{r})\right\rangle = \left\langle \varepsilon_{ilm}\frac{\partial}{\partial x_l}\eta_m(\mathbf{x})\varepsilon_{jpq}\frac{\partial}{\partial x_p}\eta_q(\mathbf{x}+\mathbf{r})\right\rangle. \tag{A.15}$$

The Levi-Civita symbols can be taken out of the ensemble average operator, and using the property of the partial derivatives $\partial/\partial x_p \eta_q(\mathbf{x}+\mathbf{r}) = \partial/\partial r_p \eta_q(\mathbf{x}+\mathbf{r})$, Equation A.15 can be rewritten as

$$R_{ij}(\mathbf{r}) = \varepsilon_{ilm}\varepsilon_{jpq}\left\langle \frac{\partial}{\partial x_l}\eta_m(\mathbf{x})\frac{\partial}{\partial r_p}\eta_q(\mathbf{x}+\mathbf{r})\right\rangle = \varepsilon_{ilm}\varepsilon_{jpq}\frac{\partial}{\partial r_p}\left\langle \eta_q(\mathbf{x}+\mathbf{r})\frac{\partial}{\partial x_l}\eta_m(\mathbf{x})\right\rangle. \tag{A.16}$$

Since $\left\langle \eta_m(\mathbf{x})\eta_q(\mathbf{x}+\mathbf{r})\right\rangle$ only depends on $\mathbf{r}$, using the chain rule for derivatives

$$\frac{\partial}{\partial x_l}\left\langle \eta_m(\mathbf{x})\eta_q(\mathbf{x}+\mathbf{r})\right\rangle = \left\langle \eta_q(\mathbf{x}+\mathbf{r})\frac{\partial}{\partial x_l}\eta_m(\mathbf{x})\right\rangle + \left\langle \eta_m(\mathbf{x})\frac{\partial}{\partial x_l}\eta_q(\mathbf{x}+\mathbf{r})\right\rangle = 0. \tag{A.17}$$

This allows to rewrite Equation A.16 as

$$R_{ij}(\mathbf{r}) = -\varepsilon_{ilm}\varepsilon_{jpq}\frac{\partial}{\partial r_p}\left\langle \eta_m(\mathbf{x})\frac{\partial}{\partial x_l}\eta_q(\mathbf{x}+\mathbf{r})\right\rangle. \tag{A.18}$$

Again, using the property of the partial derivatives as above

$$R_{ij}(\mathbf{r}) = -\varepsilon_{ilm}\varepsilon_{jpq}\frac{\partial}{\partial r_p}\left\langle \eta_m(\mathbf{x})\frac{\partial}{\partial r_l}\eta_q(\mathbf{x}+\mathbf{r})\right\rangle, \tag{A.19}$$

and taking the derivative $\partial/\partial r_l$ out of the ensemble average operator, leads to

$$R_{ij}(\mathbf{r}) = -\varepsilon_{ilm}\varepsilon_{jpq}\frac{\partial^2}{\partial r_p \partial r_l}\left\langle \eta_m(\mathbf{x})\eta_q(\mathbf{x}+\mathbf{r})\right\rangle = -\varepsilon_{ilm}\varepsilon_{jpq}\frac{\partial^2}{\partial r_p \partial r_l}C(r)\delta_{mq}. \tag{A.20}$$

The second order partial derivative can be developed by using the chain rule and taking into account that $\partial r/\partial r_p = r_p/r$, which gives

$$\frac{\partial^2}{\partial r_p \partial r_l}C(r) = \frac{1}{r}\frac{\mathrm{d}}{\mathrm{d}r}C(r)\delta_{pl} - \frac{r_l r_p}{r^3}\frac{\mathrm{d}}{\mathrm{d}r}C(r) + \frac{r_l r_p}{r^2}\frac{\mathrm{d}^2}{\mathrm{d}r^2}C(r). \tag{A.21}$$

Introducing Equation A.21 into Equation A.20, the two-point velocity correlation takes the form

$$R_{ij}(\mathbf{r}) = -\varepsilon_{ilm}\varepsilon_{jpq}\delta_{mq}\delta_{pl}\frac{1}{r}\frac{\mathrm{d}}{\mathrm{d}r}C(r) - \varepsilon_{ilm}\varepsilon_{jpq}\delta_{mq}\left(\frac{\mathrm{d}^2}{\mathrm{d}r^2}C(r) - \frac{1}{r}\frac{\mathrm{d}}{\mathrm{d}r}C(r)\right)\frac{r_m r_p}{r^2}, \tag{A.22}$$

Straightforward algebra shows that $\varepsilon_{ilm}\varepsilon_{jpq}\delta_{mq} = \delta_{lp}\delta_{ij} - \delta_{ip}\delta_{jl}$ and $\varepsilon_{ilm}\varepsilon_{jpq}\delta_{mq}\delta_{pl} = 2\delta_{ij}$, which leads to

$$R_{ij}(\mathbf{r}) = -2\frac{1}{r}\frac{\mathrm{d}}{\mathrm{d}r}C(r)\delta_{ij} - \left(\frac{\mathrm{d}^2}{\mathrm{d}r^2}C(r) - \frac{1}{r}\frac{\mathrm{d}}{\mathrm{d}r}C(r)\right)\frac{r_l r_p}{r^2}\delta_{lp}\delta_{ij} + \left(\frac{\mathrm{d}^2}{\mathrm{d}r^2}C(r) - \frac{1}{r}\frac{\mathrm{d}}{\mathrm{d}r}C(r)\right)\frac{r_l r_p}{r^2}\delta_{ip}\delta_{jl}. \tag{A.23}$$

Rearranging terms in Equation A.23, the two-point velocity correlation takes the form

$$R_{ij}(\mathbf{r}) = \underbrace{\left(\frac{\mathrm{d}^2}{\mathrm{d}r^2}C(r) - \frac{1}{r}\frac{\mathrm{d}}{\mathrm{d}r}C(r)\right)}_{\{f(r)-g(r)\}u'^2_{rms}}\frac{r_i r_j}{r^2} + \underbrace{\left(-\frac{\mathrm{d}^2}{\mathrm{d}r^2}C(r) - \frac{1}{r}\frac{\mathrm{d}}{\mathrm{d}r}C(r)\right)}_{g(r)u'^2_{rms}}\delta_{ij}. \tag{A.24}$$

Thus, Equation A.24 can be compared to Equation A.14 to find the longitudinal and transverse correlation functions in terms of the two-point correlation of the vector potential, which gives

$$u'^2_{rms}f(r) = -\frac{2}{r}\frac{\mathrm{d}}{\mathrm{d}r}C(r), \tag{A.25a}$$

$$u'^2_{rms}g(r) = -\frac{\mathrm{d}^2}{\mathrm{d}r^2}C(r) - \frac{1}{r}\frac{\mathrm{d}}{\mathrm{d}r}C(r), \tag{A.25b}$$

respectively. It should be noted that Equations A.25a and A.25b satisfy the relation between $f(r)$ and $g(r)$ for three-dimensional isotropic turbulence

$$g(r) = f(r) + \frac{r}{2}\frac{\mathrm{d}f(r)}{\mathrm{d}r}. \tag{A.26}$$

For a two-dimensional flow field, these equations are

$$u'^2_{rms}f(r) = -\frac{1}{r}\frac{\mathrm{d}}{\mathrm{d}r}C(r), \tag{A.27a}$$

$$u'^2_{rms}g(r) = -\frac{\mathrm{d}^2}{\mathrm{d}r^2}C(r), \tag{A.27b}$$

since the relation between the longitudinal and the transverse correlation functions differs from the three-dimensional expression and it is given by

$$g(r) = f(r) + r\frac{\mathrm{d}f(r)}{\mathrm{d}r}. \tag{A.28}$$

A.4 Trace of the Two-Point Velocity Correlation and Spatial Filter in Wavenumber Space

The objective of this section is to find a relationship between the half trace of the two-point velocity correlation and the digital filter in wavenumber space. To this end, the first step is to defined the two-point correlation of the vector potential by means of the inverse Fourier transform

$$C(\mathbf{r}) = \int_{-\infty}^{\infty} \hat{C}(k) \exp\left[\mathrm{i}\mathbf{k}\cdot\mathbf{r}\right] \mathrm{d}\mathbf{k}, \tag{A.29}$$

which can also be expressed in spherical co-ordinates. Thus, the separation distance is determined by $\mathbf{r} = (r\cos\varphi_r\cos\theta_r,\ r\cos\varphi_r\sin\theta_r, r\sin\varphi_r)$ and the wave vector is $\mathbf{k} = (r\cos\varphi_k\cos\theta_k,\ r\cos\varphi_k\sin\theta_k,\ r\sin\varphi_k)$. The dot product of these vectors gives

$$\mathbf{r}\cdot\mathbf{k} = kr\left[\cos\varphi_r\cos\varphi_k\cos\theta_r\cos\theta_k + \cos\varphi_r\cos\varphi_k\sin\theta_r\sin\theta_k + \cos\varphi_r\cos\varphi_k + \sin\varphi_r\sin\varphi_k\right], \tag{A.30}$$

and, since the turbulence is isotropic, the statistics only depend on the distance (r) and are independent of the direction (θ_r, φ_r). For example, it is possible to set $\theta_r = \varphi_r = 0$, which leads to $\mathbf{r}\cdot\mathbf{k} = kr\cos\varphi_k\cos\theta_k$. If this variable change is applied, Equation A.29 takes the form

$$C(r) = \int_0^{\infty}\int_{-\pi/2}^{\pi/2}\int_0^{2\pi} \hat{C}(k)\exp\left[\mathrm{i}kr\cos\varphi_k\cos\theta_k\right] k\cos\varphi_k \mathrm{d}\theta_k\mathrm{d}\varphi_k\mathrm{d}k. \tag{A.31}$$

The second step consists of relating $C(r)$ to the spherical Bessel function of the first kind. Note that the Bessel function of the first kind can be defined as

$$J_n(z) = \frac{1}{2\pi i^n}\int_0^{2\pi} \exp\left[iz\cos\phi\right]\exp\left[in\phi\right]\mathrm{d}\phi, \tag{A.32}$$

and for order $n = 0$ it takes the form

$$J_0(z) = \frac{1}{2\pi}\int_0^{2\pi} \exp\left[iz\cos\phi\right]\mathrm{d}\phi. \tag{A.33}$$

Therefore, Equation A.31 can be expressed as

$$C(r) = 2\pi \int_0^{\infty} \int_{-\pi/2}^{\pi/2} \hat{C}(k) k \cos\varphi_k J_0(kr\cos\varphi_k) \mathrm{d}\varphi_k \mathrm{d}k. \tag{A.34}$$

Since

$$\int_{-\pi/2}^{\pi/2} k\cos\varphi_k J_0(kr\cos\varphi_k)\mathrm{d}\varphi_k = 2\frac{\sin(kr)}{kr}, \tag{A.35}$$

and the spherical Bessel function for $n = 0$ can be defined by the sinc function, $j_0(z) = \mathrm{sinc}(z) = \sin(z)/z$, the two-point correlation of the vector potential can be written as

$$C(r) = 2\pi \int_0^{\infty} \hat{C}(k) j_0(kr)\mathrm{d}k. \tag{A.36}$$

Note that Equation A.36 is an alternative form to define the inverse Fourier transform. For a purely two-dimensional approach, the use of spherical Bessel functions is not required, since $\mathbf{r}\cdot\mathbf{k} = kr\cos\varphi_k$ and Equation A.36 is replaced by

$$C(r) = 2\pi \int_0^{\infty} \hat{C}(k) k J_0(kr)\mathrm{d}k. \tag{A.37}$$

On the other hand, half the trace of the two-point velocity correlation tensor is defined as

$$R(r) = \frac{1}{2}R_{ii}(r) = \frac{1}{2}\left[R_{11}(r) + R_{22}(r) + R_{33}(r)\right], \tag{A.38}$$

where, using Equation A.14, the diagonal components of the tensor are

$$R_{11}(r) = \left\{\left[f(r) - g(r)\right]\frac{r_1^2}{r^2} + g(r)\right\} u_{rms}'^2, \tag{A.39a}$$

$$R_{22}(r) = \left\{\left[f(r) - g(r)\right]\frac{r_2^2}{r^2} + g(r)\right\} u_{rms}'^2, \tag{A.39b}$$

$$R_{33}(r) = \left\{\left[f(r) - g(r)\right]\frac{r_3^2}{r^2} + g(r)\right\} u_{rms}'^2. \tag{A.39c}$$

Thus, introducing Equations A.39a-A.39c into Equation A.38 leads to

$$R(r) = \left\{\frac{f(r)}{2} + g(r)\right\} u_{rms}'^2, \tag{A.40}$$

which can be easily related to $C(r)$ using Equations A.27a and A.27b

$$R(r) = -\left[\frac{2}{r}\frac{\mathrm{d}}{\mathrm{d}r}C(r) + \frac{\mathrm{d}^2}{\mathrm{d}r^2}C(r)\right]. \tag{A.41}$$

Now, using the properties of the spherical Bessel functions

$$\frac{\mathrm{d}}{\mathrm{d}z}j_n(z) = \frac{n}{z}j_n(z) - j_{n+1}(z), \qquad j_n(z) = \frac{2n+3}{z}j_{n+1}(z) - j_{n+2}(z), \tag{A.42}$$

and Equation A.36, the trace of the two-point velocity correlation tensor takes the form

$$R(r) = -\left\{-\frac{4\pi}{r}\int_0^\infty \hat{C}(k)k\,j_1(kr)\mathrm{d}k + 2\pi\int_0^\infty \hat{C}(k)\left[-k^2\left(\frac{1}{kr}j_1(kr) - j_2(kr)\right)\right]\mathrm{d}k\right\} =$$

$$= 2\pi\int_0^\infty \hat{C}(k)k^2\left[\frac{3}{kr}j_1(kr) - j_2(kr)\right]\mathrm{d}k = 2\pi\int_0^\infty \hat{C}(k)k^2 j_0(kr)\mathrm{d}k. \tag{A.43}$$

Since $\hat{C}(k)$ is related to $\hat{G}(k)$ by Equation A.11, then

$$R(r) = 2\pi\int_0^\infty \underbrace{8\pi^3\hat{G}^2(k)k^2}_{\hat{R}(k)} j_0(kr)\mathrm{d}k, \tag{A.44}$$

and therefore

$$\hat{R}(k) = 8\pi^3 k^2\hat{G}^2(k). \tag{A.45}$$

For a purely two-dimensional velocity field, Equation A.45 takes the form $\hat{R}(k) = 2\pi^2 k^2\hat{G}^2(k)$, where $k = \sqrt{k_1^2 + k_2^2}$ instead of $k = \sqrt{k_1^2 + k_2^2 + k_3^2}$.

A.5 Energy Spectrum and Spatial Filter in Wavenumber Space

In this Section, the digital filter in wavenumber space is associated to any energy spectrum. Thus, the filter includes both the amplitude and the shape that are required to obtain the target statistical properties of the isotropic turbulent flow.

The trace of the two-point velocity correlation tensor in wavenumber space is related to the velocity spectra as

$$\hat{R}(k) = \frac{1}{2}\Phi_{ii}^{(3\mathrm{D})}(\mathbf{k}) = \frac{1}{2}\left[\Phi_{11}^{(3\mathrm{D})}(\mathbf{k}) + \Phi_{22}^{(3\mathrm{D})}(\mathbf{k}) + \Phi_{33}^{(3\mathrm{D})}(\mathbf{k})\right], \tag{A.46}$$

where introducing Equation A.45 leads to

$$\Phi_{ii}^{(3D)}(\mathbf{k}) = 16\pi^3 k^2 \hat{G}^2(k). \tag{A.47}$$

The energy spectrum can be obtained by integrating the trace of the velocity spectrum tensor over spheres with constant radius

$$E^{(3D)}(k) = \frac{1}{2} \oint_{k=\|\mathbf{k}\|} \Phi_{ii}^{(3D)}(\mathbf{k}) \mathrm{d}S(\mathbf{k}). \tag{A.48}$$

Using Equation A.48 and considering that $S(\mathbf{k})$ is a sphere of radius k in wavenumber space, the energy spectrum is related to the velocity spectra by

$$E^{(3D)}(k) = 2\pi k^2 \Phi_{ii}^{(3D)}(\mathbf{k}), \tag{A.49}$$

where Equation A.47 can be used to obtain

$$E^{(3D)}(k) = 32\pi^4 k^4 \hat{G}^2(k). \tag{A.50}$$

Considering a purely two-dimensional velocity field, Equation A.50 takes the form $E^{(2D)}(k) = 4\pi^3 k^3 \hat{G}^2(k)$. It should be noted that the energy spectrum has the same units in both two-dimensional and three-dimensional approaches, i.e., $\mathrm{m}^3/\mathrm{s}^2$. This means that the filter has different units depending on the number of dimensions involved in the flow field realisation. The same occurs with the white noise term in Equation A.2.

Appendix B

Parameter Study for Advanced Digital Filter Method

This appendix presents a parameter study to determine the eddy radius, r_e, and the separation between eddy centres, Δ_e, that are required to recover the correct turbulence statistics when using the advanced digital filter method. This synthetic turbulence method is used here to reproduce purely two-dimensional Gaussian turbulence, as explained in Section 2.2.1, with turbulence intensity $u'_{rms}/U_\infty = 0.017$ and integral length scale $\Lambda = 0.008\,\text{m}$. To this end, synthetic turbulence is injected into an empty CAA domain with uniform Mach number $M_\infty = 0.3$. The grid spacing is set to $\Delta x = \Delta y = 1.1 \times 10^{-3}\,\text{m}$, and the non-dimensional time step is $\Delta t c_\infty / L_{ref} = 4 \times 10^{-4}$ with $L_{ref} = 1\,\text{m}$. Samples of velocity fluctuations are collected every 9 time steps downstream of the injection plane up to a total number of 1.1×10^4. These are used to compute the streamwise and transverse one-dimensional spectra, $E_{11}^{(2D)}$ and $E_{22}^{(2D)}$, respectively. A comparison between analytical and numerical spectra is performed to quantify the accuracy of the resulting turbulence for various combinations of $r_e \in [\Lambda,\, 5\Lambda/2]$ and $\Delta_e \in [\Lambda,\, \Lambda/6]$.

Figures B.1 and B.2 show streamwise and transverse one-dimensional spectra, respectively. The spectra are calculated using the multitaper spectral analysis of Thomson [138] over a frequency range from $f = 80\,\text{Hz}$ to $10\,\text{kHz}$ with $\Delta f = 100\,\text{Hz}$. The results are summarised in Table B.1, in which the averaged error of the numerical spectra is calculated as

$$\text{Averaged error} = \left(\sum_{n=1}^{N_f} \left| 10\log_{10} \left(\frac{E_{ij}^{(2D)}(f_n)|_{\text{digital filter}}}{E_{ij}^{(2D)}(f_n)|_{\text{analytical}}} \right) \right| \right) / N_f,$$

where N_f corresponds to the total number of frequencies in which the spectra have been calculated. Cases with an averaged error lower than 1 dB (approximately) in both $E_{11}^{(2D)}$ and $E_{22}^{(2D)}$ are highlighted

with a green background colour in Table B.1. Thus, it is concluded that cases with $r_e \geq 3\Lambda/2$ and $\Delta_e \leq \Lambda/2$ can reproduce the correct turbulence statistics.

		Averaged error in [dB]	
r_e [m]	Δ_e [m]	$E_{11}^{(2D)}$	$E_{22}^{(2D)}$
Λ	Λ	11.47	2.81
$3\Lambda/2$	Λ	3.65	0.73
2Λ	Λ	2.58	0.47
$5\Lambda/2$	Λ	2.64	0.68
Λ	$\Lambda/2$	2.75	3.67
$3\Lambda/2$	$\Lambda/2$	0.59	0.85
2Λ	$\Lambda/2$	0.31	0.63
$5\Lambda/2$	$\Lambda/2$	0.35	0.49
Λ	$\Lambda/4$	3.83	3.70
$3\Lambda/2$	$\Lambda/4$	0.62	1.08
2Λ	$\Lambda/4$	0.62	0.67
$5\Lambda/2$	$\Lambda/4$	0.70	0.87
Λ	$\Lambda/6$	3.33	3.72
$3\Lambda/2$	$\Lambda/6$	0.37	0.92
2Λ	$\Lambda/6$	0.36	0.45
$5\Lambda/2$	$\Lambda/6$	0.36	0.59

Table B.1: Parameters for r_e with Δ_e using the advanced digital filter method and averaged numerical error.

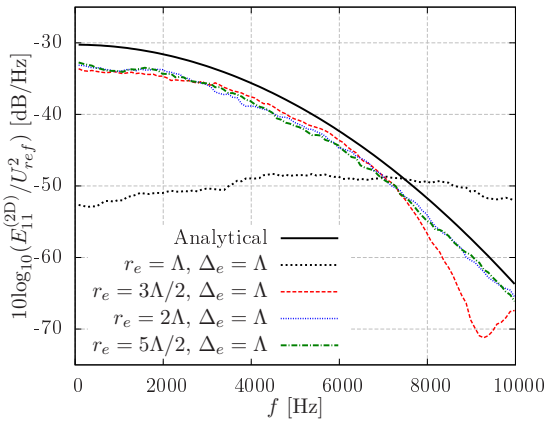

(a) Variations in r_e with $\Delta_e = \Lambda$.

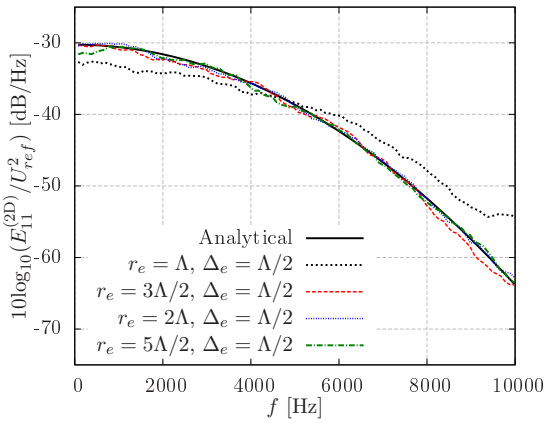

(b) Variations in r_e with $\Delta_e = \Lambda/2$.

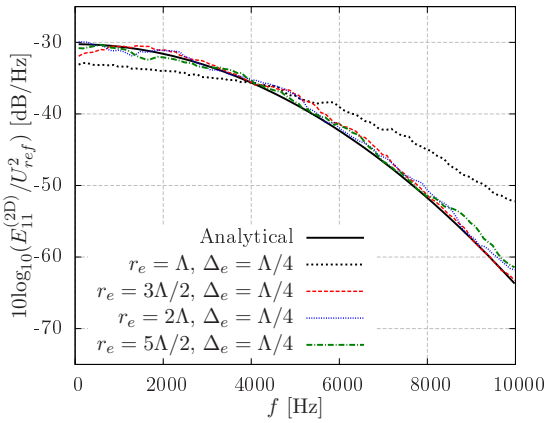

(c) Variations in r_e with $\Delta_e = \Lambda/4$.

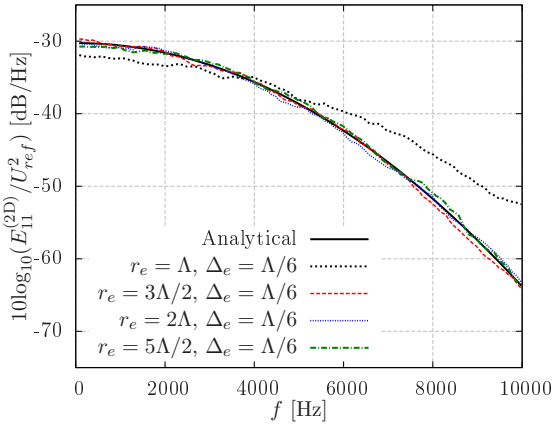

(d) Variations in r_e with $\Delta_e = \Lambda/6$.

Figure B.1: Streamwise one-dimensional spectra, $E_{11}^{(2D)}$, obtained from various combinations of r_e and Δ_e using the advanced digital filter method. The reference speed is $U_{ref} = 1$ m/s.

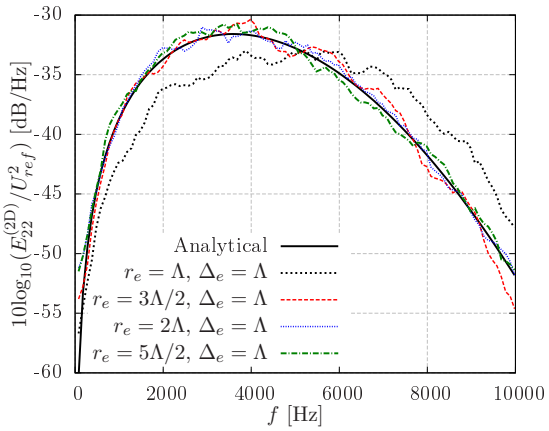

(a) Variations in r_e with $\Delta_e = \Lambda$.

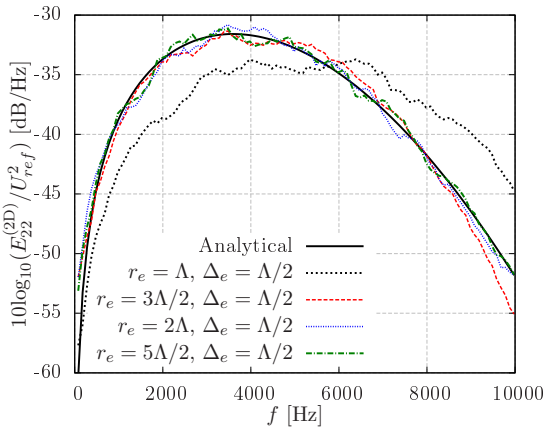

(b) Variations in r_e with $\Delta_e = \Lambda/2$.

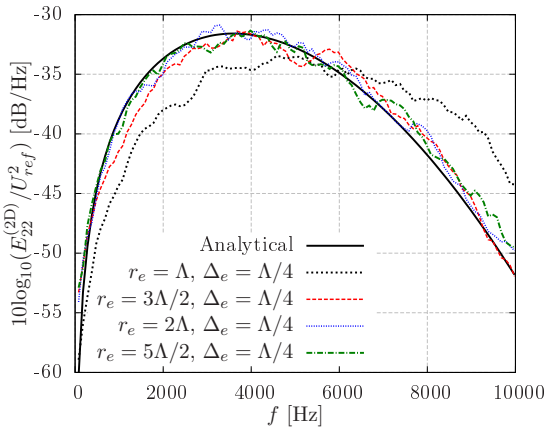

(c) Variations in r_e with $\Delta_e = \Lambda/4$.

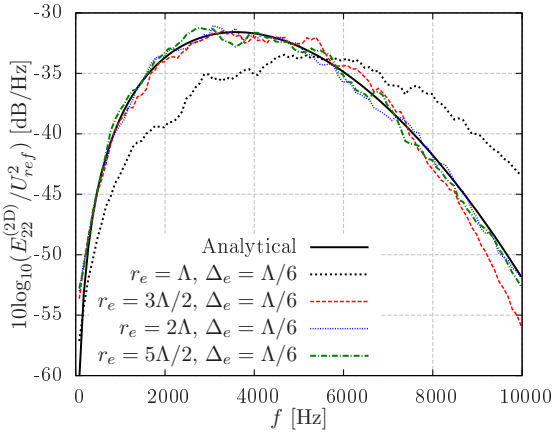

(d) Variations in r_e with $\Delta_e = \Lambda/6$.

Figure B.2: Transverse one-dimensional spectra, $E_{22}^{(2D)}$, obtained from various combinations of r_e and Δ_e using the advanced digital filter method. The reference speed is $U_{ref} = 1$ m/s.

Appendix C

Additional Mesh Information

This appendix presents further details on the meshes that have been designed for CAA simulations of leading edge noise in this thesis. Representative aerofoil and cascade configurations have been selected to better illustrate the key characteristics of the CAA meshes, such as the cell count, the minimum cell size in the leading edge region, $\Delta_{LE} = \min\{\Delta x, \Delta y, \Delta z\}$, and mesh skewness. The latter is defined for equiangular skew as

$$S_k = \max\left\{\frac{\psi_{max} - \psi_e}{\psi_e}, \frac{\psi_e - \psi_{min}}{\psi_e}\right\},$$

where $\psi_e = 90^o$ represents the ideal inner angle for a square cell in the CAA mesh, and ψ_{max} and ψ_{min} are the maximum and minimum inner angles in a cell, respectively. The CAA meshes have been designed in compliance with the indications given by Fattah *et al.* [166] for structured grids in finite different solvers. The aim is to minimise the zones of the mesh that could potentially affect the quality of the numerical solution, such as strong changes in skewness, grid stretching, and sudden variations in the grid metrics. In CAA meshes of thin aerofoils, the maximum skewness normally occurs in the leading edge region, as shown in Figure C.1a. The mesh in this region is often over-resolved in order to capture the curvature of the aerofoil leading edge. Other critical regions are block interfaces, in which sudden changes in the grid lines and metrics may occur, as can be appreciated in Figure C.1b. Tables C.1 and C.2 present additional mesh information for representative cases. In this thesis, CAA meshes usually extend to 4 chord lengths in all directions around a single aerofoil, and the smallest vortical disturbances are propagated with 8 PPW.

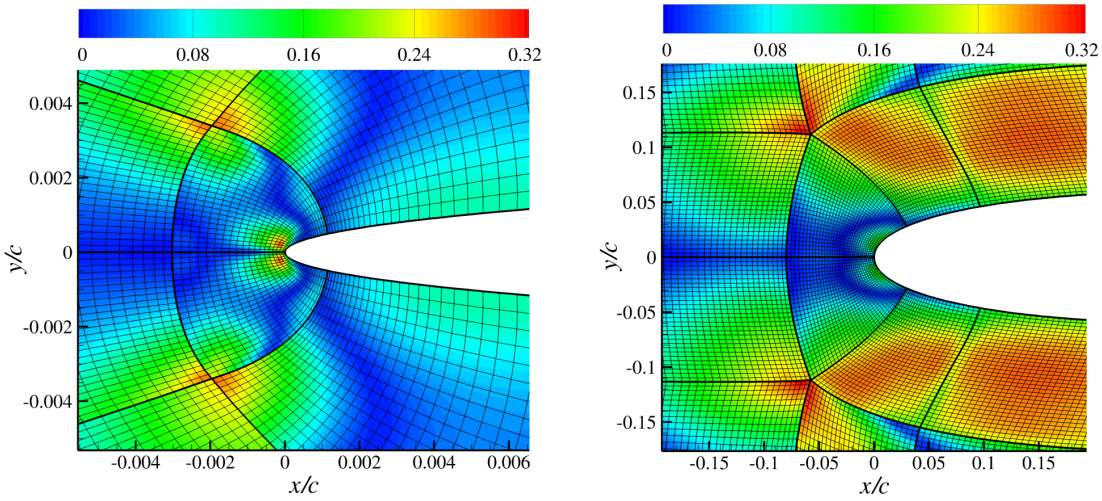

(a) NACA 0001 aerofoil at $AoA = 0^{o}$.

(b) NACA 0012 aerofoil at $AoA = 0^{o}$.

Figure C.1: Contours of skewness, S_k. CAA mesh and block interfaces around the leading edge.

					Leading edge region		
Aerofoil	AoA [°]	Dim.	$\Delta t c_\infty / L_{ref}$	No. cells	Δ_{LE}/c	Max. S_k	Avg. S_k
NACA 0001	0	2D	4.0×10^{-6}	318,890	7.0×10^{-5}	2.9×10^{-1}	1.4×10^{-2}
NACA 65(12)-10	0	2D	4.5×10^{-5}	1,904,014	1.2×10^{-3}	2.1×10^{-1}	7.8×10^{-3}
NACA 65(12)-10	4.21	2D	4.5×10^{-5}	1,898,084	1.3×10^{-3}	2.6×10^{-1}	5.9×10^{-3}
NACA 65(12)-10	15	2D	4.5×10^{-5}	2,106,125	6.7×10^{-4}	3.5×10^{-1}	1.4×10^{-2}
NACA 0012	0	3D	1.8×10^{-4}	21,776,800	3.0×10^{-3}	2.1×10^{-1}	1.5×10^{-2}

Table C.1: Mesh information for representative simulations of single aerofoils in Chapter 4.

					Leading edge region		
Aerofoil	α [°]	s/c	$\Delta t c_\infty / L_{ref}$	No. cells	Δ_{LE}/c	Max. S_k	Avg. S_k
NACA 0001	0	0.75	4×10^{-6}	351,386	7.0×10^{-5}	3.4×10^{-1}	2.0×10^{-2}
NACA 0006	0	0.75	6×10^{-5}	182,250	8.0×10^{-4}	2.7×10^{-1}	2.0×10^{-2}
NACA 0012	30	0.75	8×10^{-5}	237,590	1.2×10^{-3}	3.3×10^{-1}	8.4×10^{-2}
NACA 6406	0	0.75	6×10^{-5}	182,250	8.0×10^{-4}	3.6×10^{-1}	2.5×10^{-2}

Table C.2: Mesh information for representative simulations of cascades in Chapter 6. Mesh data are given for a single passage of simulations using isotropic turbulence.

Appendix D

Derivation of Sound Power for Acoustic Waves

This appendix presents the derivation of Equation 6.9 for the modal sound power in cascade simulations. To this end, the sound power of a harmonic acoustic wave is derived. Using the two-dimensional LEEs, the momentum equations with uniform mean flow can be written as

$$\frac{\partial u'_x}{\partial t} + U_{0,x}\frac{\partial u'_x}{\partial x} + U_{0,y}\frac{\partial u'_x}{\partial y} + \frac{1}{\rho_0}\frac{\partial p'}{\partial x} = 0, \tag{D.1}$$

$$\frac{\partial u'_y}{\partial t} + U_{0,x}\frac{\partial u'_y}{\partial x} + U_{0,y}\frac{\partial u'_y}{\partial y} + \frac{1}{\rho_0}\frac{\partial p'}{\partial y} = 0, \tag{D.2}$$

where $\mathbf{U}_0 = (U_{0,x}, U_{0,y})$ is the mean flow velocity, $\mathbf{u}' = (u'_x, u'_y)$ is the fluctuating acoustic velocity, p' is the fluctuating acoustic pressure, and ρ_0 is the mean flow density. Note that in the absence of vortical and entropy waves, fluctuating variables only contain acoustic waves, which introduce both pressure and velocity disturbances. For a harmonic acoustic wave, the fluctuating variables are given by

$$\begin{vmatrix} p' \\ u'_x \\ u'_y \end{vmatrix} = \begin{vmatrix} \hat{p}' \\ \hat{u}'_x \\ \hat{u}'_y \end{vmatrix} \exp\left[\mathrm{i}\left(\omega t + \kappa_x x + \kappa_y y\right)\right], \tag{D.3}$$

where $\hat{p}'$, $\hat{u}'_x$, and $\hat{u}'_y$ are constant amplitudes, (κ_x, κ_y) are the acoustic wavenumber components in the $x-$ and $y-$directions, respectively, and the imaginary unit satisfies $\mathrm{i}^2 = -1$. As shown by Smith [100], the amplitude of the fluctuating acoustic velocity can be written as a function of the fluctuating

acoustic pressure by introducing Equation D.3 into Equations D.1 and D.2. Hence,

$$\hat{u}'_x = -\frac{\kappa_x \hat{p}'}{\rho_0 \left(\omega + U_{0,x}\kappa_x + U_{0,y}\kappa_y\right)}, \qquad \hat{u}'_y = -\frac{\kappa_y \hat{p}'}{\rho_0 \left(\omega + U_{0,x}\kappa_x + U_{0,y}\kappa_y\right)}. \tag{D.4}$$

Assuming a uniform mean flow, the acoustic intensity in the axial direction can be written as proposed by Morfey [167]

$$\bar{I}_x(\mathbf{x}, t) = \overline{p' u'^*_x} + \frac{U_{0,x}}{\rho_0 c_\infty^2}\overline{p' p'^*} + \rho_0 U_{0,x}\overline{u'_x u'^*_x} + \rho_0 U_{0,y}\overline{u'_y u'^*_x} + \frac{U_{0,x}^2}{c_\infty^2}\overline{u'_x p'^*} + \frac{U_{0,x}U_{0,y}}{c_\infty^2}\overline{u'_y p'^*}, \tag{D.5}$$

where $()^*$ represents the complex conjugate, $\overline{()}$ indicates the time average, and c_∞ is the speed of sound. Introducing Equation D.4 into Equation D.5, and taking the real part gives

$$\bar{I}_x(\mathbf{x}) = \mathrm{Re}\left\{\frac{|\hat{p}'|^2\,\omega}{\rho_0\left|\omega + U_{0,x}\kappa_x + U_{0,y}\kappa_y\right|^2}\left[-\kappa_x^* + \frac{U_{0,x}}{c_\infty^2}\left(\omega + U_{0,x}\kappa_x + U_{0,y}\kappa_y\right)\right]\right\}, \tag{D.6}$$

where $|\hat{p}'|^2 = \hat{p}'\hat{p}'^*$. The sound power (per unit span) can be calculated by integrating the acoustic intensity along the circumferential direction (y), i.e.,

$$\hat{\mathcal{P}} = \int_0^L \bar{I}_x(\mathbf{x})\mathrm{d}y, \tag{D.7}$$

where L corresponds to the circumferential extent. Introducing Equation D.6 into Equation D.7, the sound power of a harmonic acoustic wave takes the form

$$\hat{\mathcal{P}} = \frac{L}{\rho_0}\mathrm{Re}\left\{\frac{|\hat{p}'|^2\,\omega}{\left|\omega + U_{0,x}\kappa_x + U_{0,y}\kappa_y\right|^2}\left[-\kappa_x^* + \frac{U_{0,x}}{c_\infty^2}\left(\omega + U_{0,x}\kappa_x + U_{0,y}\kappa_y\right)\right]\right\}. \tag{D.8}$$

Bibliography

[1] "Global Market Forecast, Flying by Numbers 2015-2034," Airbus, Tech. Rep., 2015.

[2] H. H. Hubbard, "Aeroacoustics of Flight Vehicles: Theory and Practice. Volume 2: Noise Control," NASA, Tech. Rep. RP-1258, 1991.

[3] L. C. de Boer and A. Schroten, "Traffic Noise Reduction in Europe," CE Delft, Tech. Rep., 2007.

[4] "Aeronautics and Air Transport: Beyond Vision 2020 (Towards 2050)," The Advisory Council for Aeronautics Research in Europe (ACARE), Tech. Rep., 2010.

[5] "ICAO's Policies on Charges for Airports and Air Navigation Services," International Civil Aviation Organization (ICAO), Tech. Rep. 9082/6, 2001.

[6] S. White, J. B. Ollerhead, R. E. Cadoux, and M. J. T. Smith, "Quota Count Validation Study: Noise Measurements and Analysis," Civil Aviation Authority, Environmental Research and Consultancy Department, Tech. Rep. 0205, 2003.

[7] R. J. Astley, A. Agarwal, K. R. Holland, P. F. Joseph, R. H. Self, M. G. Smith, R. Sugimoto, and B. J. Tester, "Predicting and Reducing Aircraft Noise," in *14th International Congress on Sound and Vibration*, Cairns, Australia, 2007.

[8] "Part 36 - Noise Standards: Aircraft Type and Airworthiness Certification," Federal Aviation Administration (FAA), Department of Transportation, Tech. Rep., 2011.

[9] "Environmental Protection, Volume I - Aircraft Noise," International Civil Aviation Organization (ICAO), Tech. Rep., 2008.

[10] R. J. Astley, *Chapter 2: Propulsion System Noise - Turbomachinery*. Encyclopedia of Aerospace Engineering, 2010. [Online]. Available: http://dx.doi.org/10.1002/9780470686652.eae336

[11] H. A. Kumasaka, M. M. Martinez, and D. S. Weir, "Definition of 1992 Technology Aircraft Noise Levels and the Methodology for Assessing Airplane Noise Impact of Component Noise Reduction Concepts," NASA, Tech. Rep. CR-198298, 1996.

[12] A. McAlpine, P. J. G. Schwaller, M. J. Fisher, and B. J. Tester, "'Buzz-Saw' Noise: Prediction of the Rotor-Alone Pressure Field," *Journal of Sound and Vibration*, vol. 331, no. 22, pp. 4901–4918, 2012. [Online]. Available: http://dx.doi.org/10.1016/j.jsv.2012.06.009

[13] J. M. Tyler and T. G. Sofrin, "Axial Flow Compressor Noise Studies," *SAE Technical Paper*, no. 620532, 1962. [Online]. Available: http://dx.doi.org/10.4271/620532

[14] T. F. Brooks, D. S. Pope, and M. A. Marcolini, "Airfoil Self-Noise and Prediction," NASA, Tech. Rep. RP-1218, 1989.

[15] R. Mani and K. Bekofske, "Experimental and Theoretical Studies of Subsonic Fan Noise," NASA, Tech. Rep. CR-2660, 1976.

[16] R. A. Kantola and R. E. Warren, "Reduction of Rotor-Turbulence Interaction Noise in Static Fan Noise Testing," in *AIAA 5th Aeroacoustics Conference*, no. AIAA 79-0656, Seattle, Washington, 1979. [Online]. Available: http://dx.doi.org/10.2514/6.1979-656

[17] U. W. Ganz, P. D. Joppa, T. J. Patten, and D. F. Scharpf, "Boeing 18-Inch Fan Rig Broadband Noise Test," NASA, Tech. Rep. CR-1998-208704, 1998.

[18] G. G. Podboy, M. J. Krupar, S. M. Helland, and C. E. Hughes, "Steady and Unsteady Flow Field Measurements within a NASA 22-Inch Fan Model," in *40th AIAA Aerospace Sciences Meeting and Exhibit*, no. AIAA 2002-1033, Reno, Nevada, 2002. [Online]. Available: http://dx.doi.org/10.2514/6.2002-1033

[19] R. D. Sandberg and L. E. Jones, "Direct Numerical Simulations of Airfoil Self-Noise," *Procedia Engineering*, vol. 6, pp. 274–282, 2010. [Online]. Available: http://dx.doi.org/10.1016/j.proeng.2010.09.029

[20] B. Greschner and F. Thiele, "Broadband Noise Analysis of a Rotor-Stator-Cascade Using Wall Modeled LES Simulation," in *18th AIAA/CEAS Aeroacoustics Conference*, no. AIAA 2012-2308, Colorado Springs, Colorado, 2012. [Online]. Available: http://dx.doi.org/10.2514/6.2012-2308

[21] C. K. W. Tam, "Computational Aeroacoustics: Issues and Methods," *AIAA Journal*, vol. 33, no. 10, pp. 1788–1796, 1995. [Online]. Available: http://dx.doi.org/10.2514/3.12728

[22] D. Casalino, A. Hazir, and A. Mann, "Turbofan Broadband Noise Prediction Using the Lattice Boltzmann Method," in *22nd AIAA/CEAS Aeroacoustics Conference*, no. AIAA 2016-2945, Lyon, France, 2016. [Online]. Available: http://dx.doi.org/10.2514/6.2016-2945

[23] D. Casalino and A. Hazir, "Lattice Boltzmann Based Aeroacoustic Simulation of Turbofan Noise Installation Effects," in *23rd International Congress on Sound and Vibration*, Athens, Greece, 2016.

[24] R. H. Kraichnan, "Diffusion by a Random Velocity Field," *Physics of Fluids*, vol. 13, no. 1, pp. 22–31, 1970. [Online]. Available: http://dx.doi.org/10.1063/1.1692799

[25] M. Karweit, P. Blanc-Benon, D. Juvé, and G. Comte-Bellot, "Simulation of the Propagation of an Acoustic Wave through a Turbulent Velocity Field: A Study of Phase Variance," *The Journal of the Acoustical Society of America*, vol. 89, no. 1, pp. 52–62, 1991. [Online]. Available: http://dx.doi.org/10.1121/1.400415

[26] A. Smirnov, S. Shi, and I. Celik, "Random Flow Generation Technique for Large Eddy Simulations and Particle-Dynamics Modeling," *Journal of Fluids Engineering*, vol. 123, no. 2, pp. 359–371, 2001. [Online]. Available: http://dx.doi.org/10.1115/1.1369598

[27] S. H. Huang, Q. S. Li, and J. R. Wu, "A General Inflow Turbulence Generator for Large Eddy Simulation," *Journal of Wind Engineering and Industrial Aerodynamics*, vol. 98, no. 10-11, pp. 600–617, 2010. [Online]. Available: http://dx.doi.org/10.1016/j.jweia.2010.06.002

[28] H. G. Castro and R. R. Paz, "A Time and Space Correlated Turbulence Synthesis Method for Large Eddy Simulations," *Journal of Computational Physics*, vol. 235, pp. 742–763, 2013. [Online]. Available: http://dx.doi.org/10.1016/j.jcp.2012.10.035

[29] P. Batten, U. Goldberg, and S. Chakravarthy, "Interfacing Statistical Turbulence Closures with Large-Eddy Simulation," *AIAA Journal*, vol. 42, no. 3, pp. 485–492, 2004. [Online]. Available: http://dx.doi.org/10.2514/1.3496

[30] R. Yu and X.-S. Bai, "A Fully Divergence-free Method for Generation of Inhomogeneous and Anisotropic Turbulence with Large Spatial Variation," *Journal of Computational Physics*, vol. 256, pp. 234–253, 2014. [Online]. Available: http://dx.doi.org/10.1016/j.jcp.2013.08.055

[31] L. Patruno and M. Ricci, "On the Generation of Synthetic Divergence-Free Homogeneous Anisotropic Turbulence," *Computer Methods in Applied Mechanics and Engineering*, vol. 315, pp. 396–417, 2017. [Online]. Available: http://dx.doi.org/10.1016/j.cma.2016.11.005

[32] G. I. Taylor, "The Spectrum of Turbulence," *Proceedings of the Royal Society of London. Series A, Mathematical and Physical Sciences*, vol. 164, no. 919, pp. 476–490, 1938. [Online]. Available: http://dx.doi.org/10.1098/rspa.1938.0032

[33] W. Béchara, C. Bailly, P. Lafon, and S. M. Candel, "Stochastic Approach to Noise Modeling for Free Turbulent Flows," *AIAA Journal*, vol. 32, no. 3, pp. 455–463, 1994. [Online]. Available: http://dx.doi.org/10.2514/3.12008

[34] C. Bailly, P. Lafon, and S. Candel, "Computation of Noise Generation and Propagation for Free and Confined Turbulent Flows," in *2nd AIAA/CEAS Aeroacoustics Conference*, no. AIAA 96-1732, State College, Pennsylvania, 1996. [Online]. Available: http://dx.doi.org/10.2514/6.1996-1732

[35] C. Bailly and D. Juvé, "A Stochastic Approach to Compute Subsonic Noise Using Linearized Euler's Equations," in *5th AIAA/CEAS Aeroacoustics Conference and Exhibit*, no. AIAA 99-1872, Bellevue, Washington, 1999. [Online]. Available: http://dx.doi.org/10.2514/6.1999-1872

[36] M. Billson, L.-E. Eriksson, and L. Davidson, "Jet Noise Prediction Using Stochastic Turbulence Modeling," in *9th AIAA/CEAS Aeroacoustics Conference and Exhibit*, no. AIAA 2003-3282, Hilton Head, South Carolina, 2003. [Online]. Available: http://dx.doi.org/10.2514/6.2003-3282

[37] M. Billson, L.-E. Eriksson, L. Davidson, and P. Jordan, "Modeling of Synthetic Anisotropic Turbulence and its Sound Emission," in *10th AIAA/CEAS Aeroacoustics Conference*, no. AIAA 2004-2857, Manchester, Great Britain, 2004. [Online]. Available: http://dx.doi.org/10.2514/6.2004-2857

[38] V. Clair, C. Polacsek, T. Le Garrec, G. Reboul, M. Gruber, and P. Joseph, "Experimental and Numerical Investigation of Turbulence-Airfoil Noise Reduction Using Wavy Edges," *AIAA Journal*, vol. 51, no. 11, pp. 2695–2713, 2013. [Online]. Available: http://dx.doi.org/10.2514/1.J052394

[39] R. K. Amiet, "Acoustic Radiation from an Airfoil in a Turbulent Stream," *Journal of Sound and Vibration*, vol. 41, no. 4, pp. 407–420, 1975. [Online]. Available: http://dx.doi.org/10.1016/S0022-460X(75)80105-2

[40] C. Polacsek, V. Clair, T. Le Garrec, G. Reboul, and M. C. Jacob, "Numerical Predictions of Turbulence/Cascade-Interaction Noise Using Computational Aeroacoustics with a Stochastic Model," *AIAA Journal*, vol. 53, no. 12, pp. 3551–3566, 2015. [Online]. Available: http://dx.doi.org/10.2514/1.J053896

[41] J. Gill, X. Zhang, and P. Joseph, "Single Velocity-Component Modeling of Leading Edge Turbulence Interaction Noise." *The Journal of the Acoustical Society of America*, vol. 137, no. 6, pp. 3209–3220, 2015. [Online]. Available: http://dx.doi.org/10.1121/1.4921547

[42] E. Sergent, "Vers une Méthodologie de Couplage entre la Simulation des Grandes Échelles et les Modèles Statistiques," Ph.D. dissertation, École Centrale de Lyon, 2002.

[43] N. Jarrin, S. Benhamadouche, D. Laurence, and R. Prosser, "A Synthetic-Eddy-Method for Generating Inflow Conditions for Large-Eddy Simulations," *International Journal of Heat and Fluid Flow*, vol. 27, no. 4, pp. 585–593, 2006. [Online]. Available: http://dx.doi.org/10.1016/j.ijheatfluidflow.2006.02.006

[44] N. Jarrin, R. Prosser, J.-C. Uribe, S. Benhamadouche, and D. Laurence, "Reconstruction of Turbulent Fluctuations for Hybrid RANS/LES Simulations Using a Synthetic-Eddy Method," *International Journal of Heat and Fluid Flow*, vol. 30, no. 3, pp. 435–442, 2009. [Online]. Available: http://dx.doi.org/10.1016/j.ijheatfluidflow.2009.02.016

[45] T. S. Lund, X. Wu, and K. D. Squires, "Generation of Turbulent Inflow Data for Spatially-Developing Boundary Layer Simulations," *Journal of Computational Physics*, vol. 140, no. 2, pp. 233–258, 1998. [Online]. Available: http://dx.doi.org/10.1006/jcph.1998.5882

[46] R. Poletto, T. Craft, and A. Revell, "A New Divergence Free Synthetic Eddy Method for the Reproduction of Inlet Flow Conditions for LES," *Flow, Turbulence and Combustion*, vol. 91, no. 3, pp. 519–539, 2013. [Online]. Available: http://dx.doi.org/10.1007/s10494-013-9488-2

[47] A. Sescu and R. Hixon, "Toward Low-Noise Synthetic Turbulent Inflow Conditions for Aeroacoustic Calculations," *International Journal for Numerical Methods in Fluids*, vol. 73, no. 12, pp. 1001–1010, 2013. [Online]. Available: http://dx.doi.org/10.1002/fld.3833

[48] J. W. Kim and S. Haeri, "An Advanced Synthetic Eddy Method for the Computation of Aerofoil-Turbulence Interaction Noise," *Journal of Computational Physics*, vol. 287, pp. 1–17, 2015. [Online]. Available: http://dx.doi.org/10.1016/j.jcp.2015.01.039

[49] A. Careta, F. Sagués, and J. M. Sancho, "Stochastic Generation of Homogeneous Isotropic Turbulence with Well-Defined Spectra," *Physical Review E*, vol. 48, no. 3, pp. 2279–2287, 1993. [Online]. Available: http://dx.doi.org/10.1103/PhysRevE.48.2279

[50] M. Klein, A. Sadiki, and J. Janicka, "A Digital Filter Based Generation of Inflow Data for Spatially Developing Direct Numerical or Large Eddy Simulations," *Journal of Computational Physics*, vol. 186, no. 2, pp. 652–665, 2003. [Online]. Available: http://dx.doi.org/10.1016/S0021-9991(03)00090-1

[51] L. di Mare, M. Klein, W. P. Jones, and J. Janicka, "Synthetic Turbulence Inflow Conditions for Large-Eddy Simulation," *Physics of Fluids*, vol. 18, no. 2, p. 025107, 2006. [Online]. Available: http://dx.doi.org/10.1063/1.2130744

[52] R. Ewert, "Broadband Slat Noise Prediction Based on CAA and Stochastic Sound Sources from a Fast Random Particle-Mesh (RPM) Method," *Computers and Fluids*, vol. 37, no. 4, pp. 369–387, 2008. [Online]. Available: http://dx.doi.org/10.1016/j.compfluid.2007.02.003

[53] R. Ewert, J. Dierke, J. Siebert, A. Neifeld, C. Appel, M. Siefert, and O. Kornow, "CAA Broadband Noise Prediction for Aeroacoustic Design," *Journal of Sound and Vibration*, vol. 330, no. 17, pp. 4139–4160, 2011. [Online]. Available: http://dx.doi.org/10.1016/j.jsv.2011.04.014

[54] M. Siefert and R. Ewert, "Sweeping Sound Generation in Jets Realized with a Random Particle-Mesh Method," in *15th AIAA/CEAS Aeroacoustics Conference*, no. AIAA 2009-3369, Miami, Florida, 2009. [Online]. Available: http://dx.doi.org/10.2514/6.2009-3369

[55] A. Wohlbrandt, N. Hu, S. Guérin, and R. Ewert, "Analytical Reconstruction of Isotropic Turbulence Spectra Based on the Gaussian Transform," *Computers and Fluids*, vol. 132, pp. 46–50, 2016. [Online]. Available: http://dx.doi.org/10.1016/j.compfluid.2016.03.023

[56] R. Ewert and W. Schröder, "Acoustic Perturbation Equations Based on Flow Decomposition via Source Filtering," *Journal of Computational Physics*, vol. 188, no. 2, pp. 365–398, 2003. [Online]. Available: http://dx.doi.org/10.1016/S0021-9991(03)00168-2

[57] R. Ewert, C. Appel, J. Dierke, and M. Herr, "RANS/CAA Based Prediction of NACA 0012 Broadband Trailing Edge Noise and Experimental Validation," in *15th AIAA/CEAS Aeroacoustics Conference*, no. AIAA 2009-3269, Miami, Florida, 2009. [Online]. Available: http://dx.doi.org/10.2514/6.2009-3269

[58] I. F. Cozza, A. Iob, and R. Arina, "Broadband Trailing-Edge Noise Prediction with a Stochastic Source Model," *Computers and Fluids*, vol. 57, pp. 98–109, 2012. [Online]. Available: http://dx.doi.org/10.1016/j.compfluid.2011.12.011

[59] M. Mesbah, "Flow Noise Prediction Using the Stochastic Noise Generation and Radiation Approach," Ph.D. dissertation, Katholieke Universiteit Leuven, 2006.

[60] M. Dieste and G. Gabard, "Random Particle Methods Applied to Broadband Fan Interaction Noise," *Journal of Computational Physics*, vol. 231, no. 24, pp. 8133–8151, 2012. [Online]. Available: http://dx.doi.org/10.1016/j.jcp.2012.07.044

[61] A. M. Wohlbrandt, S. Guérin, and R. Ewert, "Simultaneous Computation of Surface and Volume Sources for Fan Broadband Noise with the Random-Particle-Mesh Method," in *19th AIAA/CEAS Aeroacoustics Conference*, no. AIAA 2013-2119, Berlin, Germany, 2013. [Online]. Available: http://dx.doi.org/10.2514/6.2013-2119

[62] D. Kim, S. Heo, and C. Cheong, "Time-Domain Inflow Boundary Condition for Turbulence-Airfoil Interaction Noise Prediction Using Synthetic Turbulence Modeling," *Journal of Sound and Vibration*, vol. 340, pp. 138–151, 2015. [Online]. Available: http://dx.doi.org/10.1016/j.jsv.2014.11.036

[63] C. K. W. Tam and Z. Dong, "Radiation and Outflow Boundary Conditions for Direct Computation of Acoustic and Flow Disturbances in a Nonuniform Mean Flow," *Journal of Computational Acoustics*, vol. 4, no. 2, pp. 175–201, 1996. [Online]. Available: http://dx.doi.org/10.1142/S0218396X96000040

[64] M. B. Giles, "Nonreflecting Boundary Conditions for Euler Equation Calculations," *AIAA Journal*, vol. 28, no. 12, pp. 2050–2058, 1990. [Online]. Available: http://dx.doi.org/10.2514/3.10521

[65] W. R. Sears, "Some Aspects of Non-Stationary Airfoil Theory and its Practical Application," *Journal of the Aeronautical Sciences*, vol. 8, no. 3, pp. 104–108, 1941. [Online]. Available: http://dx.doi.org/10.2514/8.10655

[66] L. T. Filotas, "Oblique Compressible Sears Function," *AIAA Journal*, vol. 12, no. 11, pp. 1601–1603, 1974. [Online]. Available: http://dx.doi.org/10.2514/3.49556

[67] R. K. Amiet, "Compressibility Effects in Unsteady Thin-Airfoil Theory," *AIAA Journal*, vol. 12, no. 2, pp. 252–255, 1974. [Online]. Available: http://dx.doi.org/10.2514/3.49212

[68] J. M. R. Graham, "Similarity Rules for Thin Aerofoils in Non-Stationary Subsonic Flows," *Journal of Fluid Mechanics*, vol. 43, no. 4, pp. 753–766, 1970. [Online]. Available: http://dx.doi.org/10.1017/S0022112070002719

[69] R. K. Amiet, "High Frequency Thin-Airfoil Theory for Subsonic Flow," *AIAA Journal*, vol. 14, no. 8, pp. 1076–1082, 1976. [Online]. Available: http://dx.doi.org/10.2514/3.7187

[70] V. P. Blandeau, P. F. Joseph, G. Jenkins, and C. J. Powles, "Comparison of Sound Power Radiation from Isolated Airfoils and Cascades in a Turbulent Flow," *The Journal of the Acoustical Society of America*, vol. 129, no. 6, pp. 3521–3530, 2011. [Online]. Available: http://dx.doi.org/10.1121/1.3569706

[71] J. Gershfeld, "Leading Edge Noise from Thick Foils in Turbulent Flows," *The Journal of the Acoustical Society of America*, vol. 116, no. 3, pp. 1416–1426, 2004. [Online]. Available: http://dx.doi.org/10.1121/1.1780575

[72] S. Moreau, M. Roger, and V. Jurdic, "Effect of Angle of Attack and Airfoil Shape on Turbulence-Interaction Noise," in *11th AIAA/CEAS Aeroacoustics Conference*, no. AIAA 2005-2973, Monterey, California, 2005. [Online]. Available: http://dx.doi.org/10.2514/6.2005-2973

[73] L. D. Santana, J. Christophe, C. Schram, and W. Desmet, "A Rapid Distortion Theory Modified Turbulence Spectra for Semi-Analytical Airfoil Noise Prediction," *Journal of Sound and Vibration*, vol. 383, pp. 349–363, 2016. [Online]. Available: http://dx.doi.org/10.1016/j.jsv.2016.07.026

[74] L. J. Ayton and N. Peake, "On High-Frequency Noise Scattering by Aerofoils in Flow," *Journal of Fluid Mechanics*, vol. 734, pp. 144–182, 2013. [Online]. Available: http://dx.doi.org/10.1017/jfm.2013.477

[75] J. C. R. Hunt, "A Theory of Turbulent Flow Round Two-Dimensional Bluff Bodies," *Journal of Fluid Mechanics*, vol. 61, no. 4, pp. 625–706, 1973. [Online]. Available: http://dx.doi.org/10.1017/S0022112073000893

[76] M. Roger and S. Moreau, "Extensions and Limitations of Analytical Airfoil Broadband Noise Models," *International Journal of Aeroacoustics*, vol. 9, no. 3, pp. 273–306, 2010. [Online]. Available: http://dx.doi.org/10.1260/1475-472X.9.3.273

[77] S. A. L. Glegg and W. J. Devenport, "Panel Methods for Airfoils in Turbulent Flow," *Journal of Sound and Vibration*, vol. 329, no. 18, pp. 3709–3720, 2010. [Online]. Available: http://dx.doi.org/10.1016/j.jsv.2010.03.007

[78] W. J. Devenport, J. K. Staubs, and S. A. L. Glegg, "Sound Radiation from Real Airfoils in Turbulence," *Journal of Sound and Vibration*, vol. 329, no. 17, pp. 3470–3483, 2010. [Online]. Available: http://dx.doi.org/10.1016/j.jsv.2010.02.022

[79] R. W. Paterson and R. K. Amiet, "Acoustic Radiation and Surface Pressure Characteristics of an Airfoil due to Incident Turbulence," NASA, Tech. Rep. CR-2733, 1976.

[80] R. K. Amiet, "Correction of Open Jet Wind Tunnel Measurements for Shear Layer Refraction," in *2nd AIAA Aeroacoustics Conference*, no. AIAA 75-532, Hampton, Virginia, 1975. [Online]. Available: http://dx.doi.org/10.2514/6.1975-532

[81] R. K. Amiet, "Refraction of Sound by a Shear Layer," *Journal of Sound and Vibration*, vol. 58, no. 4, pp. 467–482, 1978. [Online]. Available: http://dx.doi.org/10.1016/0022-460X(78)90353-X

[82] S. Moreau and M. Roger, "Competing Broadband Noise Mechanisms in Low-Speed Axial Fans," *AIAA Journal*, vol. 45, no. 1, pp. 48–57, 2007. [Online]. Available: http://dx.doi.org/10.2514/1.14583

[83] J. K. Staubs, "Real Airfoil Effects on Leading Edge Noise," Ph.D. dissertation, Virginia Polytechnic Institute and State University, 2008.

[84] F. V. Hutcheson, T. F. Brooks, C. L. Burley, and D. J. Stead, "Measurement of the Noise Resulting from the Interaction of Turbulence with a Lifting Surface," in *17th AIAA/CEAS Aeroacoustics Conference*, no. AIAA 2011-2907, Portland, Oregon, 2011. [Online]. Available: http://dx.doi.org/10.2514/6.2011-2907

[85] M. Gruber, "Airfoil Noise Reduction by Edge Treatments," Ph.D. dissertation, University of Southampton, Institute of Sound and Vibration Research (ISVR), 2012.

[86] T. P. Chong, P. F. Joseph, and P. O. A. L. Davies, "Design and Performance of an Open Jet Wind Tunnel for Aero-Acoustic Measurement," *Applied Acoustics*, vol. 70, no. 4, pp. 605–614, 2009. [Online]. Available: http://dx.doi.org/10.1016/j.apacoust.2008.06.011

[87] P. Chaitanya, J. Gill, S. Narayanan, P. Joseph, C. Vanderwel, X. Zhang, and B. Ganapathisubramani, "Aerofoil Geometry Effects on Turbulence Interaction Noise," in *21st AIAA/CEAS Aeroacoustics Conference*, no. AIAA 2015-2830, Dallas, Texas, 2015. [Online]. Available: http://dx.doi.org/10.2514/6.2015-2830

[88] S. B. Pope, *Turbulent Flows*, 6th ed. Cambridge University Press, 2000.

[89] W. Olsen and J. Wagner, "Effect of Thickness on Airfoil Surface Noise," *AIAA Journal*, vol. 20, no. 3, pp. 437–439, 1982. [Online]. Available: http://dx.doi.org/10.2514/3.7922

[90] A. M. Hall, O. V. Atassi, J. Gilson, R. Reba, and D. Shannon, "Effect of Leading-Edge Thickness on High-Speed Airfoil-Turbulence Interaction Noise," in *17th AIAA/CEAS Aeroacoustics Conference*, no. AIAA 2011-2861, Portland, Oregon, 2011. [Online]. Available: http://dx.doi.org/10.2514/6.2011-2861

[91] T. F. Geyer, E. Sarradj, and M. Hobracht, "Noise Generated by a Leading Edge in Anisotropic Turbulence," in *Inter-Noise*, Hamburg, Germany, 2016, pp. 6067–6078.

[92] H. Atassi, S. Subramaniam, and J. Scott, "Acoustic Radiation from Lifting Airfoils in Compressible Subsonic Flow," in *13th Aeroacoustics Conference*, no. AIAA 90-3911, Tallahassee, Florida, 1990. [Online]. Available: http://dx.doi.org/10.2514/6.1990-3911

[93] D. P. Lockard and P. J. Morris, "Radiated Noise from Airfoils in Realistic Mean Flows," *AIAA Journal*, vol. 36, no. 6, pp. 907–914, 1998. [Online]. Available: http://dx.doi.org/10.2514/2.494

[94] J. Gill, X. Zhang, and P. Joseph, "Symmetric Airfoil Geometry Effects on Leading Edge Noise," *The Journal of the Acoustical Society of America*, vol. 134, no. 4, pp. 2669–2680, 2013. [Online]. Available: http://dx.doi.org/10.1121/1.4818769

[95] D. Kim, G.-S. Lee, and C. Cheong, "Inflow Broadband Noise from an Isolated Symmetric Airfoil Interacting with Incident Turbulence," *Journal of Fluids and Structures*, vol. 55, pp. 428–450, 2015. [Online]. Available: http://dx.doi.org/10.1016/j.jfluidstructs.2015.03.015

[96] H. Deniau, G. Dufour, C. Polacsek, and S. Moreau, "Affordable Compressible LES of Airfoil-Turbulence Interaction in a Free Jet," in *17th AIAA/CEAS Aeroacoustics*

Conference, no. AIAA 2011-2707, Portland, Oregon, 2011. [Online]. Available: http://dx.doi.org/10.2514/6.2011-2707

[97] T. Hainaut, G. Gabard, and V. Clair, "CAA Study of Airfoil Broadband Interaction Noise Using Stochastic Turbulent Vorticity Sources," in *21st AIAA/CEAS Aeroacoustics Conference*, no. AIAA 2015-2222, Dallas, Texas, 2015. [Online]. Available: http://dx.doi.org/10.2514/6.2015-2222

[98] J. R. Gill, "Broadband Noise Generation of a Contra-Rotating Open Rotor Blade," Ph.D. dissertation, University of Southampton, Airbus Noise Technology Centre (ANTC), 2015.

[99] T. Hainaut, G. Gabard, and V. Clair, "A CAA Study of Turbulence Distortion in Broadband Fan Interaction Noise," in *22nd AIAA/CEAS Aeroacoustics Conference*, no. AIAA 2016-2839, Lyon, France, 2016. [Online]. Available: http://dx.doi.org/10.2514/6.2016-2839

[100] S. N. Smith, "Discrete Frequency Sound Generation in Axial Flow Turbomachines," Aeronautical Reseach Council, Tech. Rep. 3709, 1973.

[101] C. Cheong, P. Joseph, and S. Lee, "High Frequency Formulation for the Acoustic Power Spectrum due to Cascade-Turbulence Interaction," *The Journal of the Acoustical Society of America*, vol. 119, no. 1, pp. 108–122, 2006. [Online]. Available: http://dx.doi.org/10.1121/1.2139626

[102] D. B. Hanson, "Theory for Broadband Noise of Rotor and Stator Cascades with Inhomogeneous Inflow Turbulence Including Effects of Lean and Sweep," NASA, Tech. Rep. CP-2001-210762, 2001.

[103] G. Jenkins, "Models for the Prediction of Rear-Arc and Forward-Arc Fan Broadband Noise in Turbofan Engines," Ph.D. dissertation, University of Southampton, Institute of Sound and Vibration Research (ISVR), 2013.

[104] C. S. Ventres, M. A. Theobald, and W. D. Mark, "Turbofan Noise Generation, Volume 1: Analysis," NASA, Tech. Rep. CR-167952, 1982.

[105] M. Nallasamy and E. Envia, "Computation of Rotor Wake Turbulence Noise," *Journal of Sound and Vibration*, vol. 282, no. 3-5, pp. 649–678, 2005. [Online]. Available: http://dx.doi.org/10.1016/j.jsv.2004.03.062

[106] G. G. Podboy, M. J. Krupar, C. E. Hughes, and R. P. Woodward, "Fan Noise Source Diagnostic Test - LDV Measured Flow Field Results," in *8th AIAA/CEAS Aeroacoustics Conference and Exhibit*, no. AIAA 2002-2431, Breckenridge, Colorado, 2002. [Online]. Available: http://dx.doi.org/10.2514/6.2002-2431

[107] R. P. Woodward, C. E. Hughes, R. J. Jeracki, and C. J. Miller, "Fan Noise Source Diagnostic Test, Far-Field Acoustic Results," in *8th AIAA/CEAS Aeroacoustics Conference and Exhibit*, no. AIAA 2002-2427, Breckenridge, Colorado, 2002. [Online]. Available: http://dx.doi.org/10.2514/6.2002-2427

[108] M. Nallasamy, E. Envia, S. A. Thorp, and A. Shabbir, "Fan Noise Source Diagnostic Test - Computation of Rotor Wake Turbulence Noise," in *8th AIAA/CEAS Aeroacoustics Conference and Exhibit*, no. AIAA 2002-2489, Breckenridge, Colorado, 2002. [Online]. Available: http://dx.doi.org/10.2514/6.2002-2489

[109] L. J. Heidelberg, "Fan Noise Source Diagnostic Test - Tone Modal Structure Results," in *8th AIAA/CEAS Aeroacoustics Conference and Exhibit*, no. AIAA 2002-2428, Breckenridge, Colorado, 2002. [Online]. Available: http://dx.doi.org/10.2514/6.2002-2428

[110] D. B. Hanson and K. P. Horan, "Turbulence/Cascade Interaction: Spectra of Inflow, Cascade Response, and Noise," in *4th AIAA/CEAS Aeroacoustics Conference*, no. AIAA 98-2319, Toulouse, France, 1998. [Online]. Available: http://dx.doi.org/10.2514/6.1998-2319

[111] S. A. L. Glegg, "The Response of a Swept Blade Row to a Three-Dimensional Gust," *Journal of Sound and Vibration*, vol. 227, no. 1, pp. 29–64, 1999. [Online]. Available: http://dx.doi.org/10.1006/jsvi.1999.2327

[112] H. Posson, S. Moreau, and M. Roger, "Broadband Noise Prediction of Fan Outlet Guide Vane Using a Cascade Response Function," *Journal of Sound and Vibration*, vol. 330, no. 25, pp. 6153–6183, 2011. [Online]. Available: http://dx.doi.org/10.1016/j.jsv.2011.07.040

[113] E. J. Kerschen and P. R. Gliebe, "Noise Caused by the Interaction of a Rotor with Anisotropic Turbulence," *AIAA Journal*, vol. 19, no. 6, pp. 717–723, 1981. [Online]. Available: http://dx.doi.org/10.2514/3.50995

[114] S. M. Grace, "Fan Broadband Interaction Noise Modeling Using a Low-Order Method," *Journal of Sound and Vibration*, vol. 346, pp. 402–423, 2015. [Online]. Available: http://dx.doi.org/10.1016/j.jsv.2015.02.013

[115] H. Ju, R. Mani, M. Vysohlid, and A. Sharma, "Investigation of Fan-Wake/Outlet-Guide-Vane Interaction Broadband Noise," *AIAA Journal*, vol. 53, no. 12, pp. 3534–3550, 2015. [Online]. Available: http://dx.doi.org/10.2514/1.J053167

[116] H. M. Atassi and I. V. Vinogradov, "A Model for Fan Broadband Interaction Noise in Nonuniform Flow," in *11th AIAA/CEAS Aeroacoustics Conference*, no. AIAA 2005-2880, Monterey, California, 2005. [Online]. Available: http://dx.doi.org/10.2514/6.2005-2880

[117] H. M. Atassi and I. V. Vinogradov, "Modelling Broadband Fan Noise and Comparison with Experiments," in *13th AIAA/CEAS Aeroacoustics Conference*, no. AIAA 2007-3691, Rome, Italy, 2007. [Online]. Available: http://dx.doi.org/10.2514/6.2007-3691

[118] H. M. Atassi and M. M. Logue, "Effect of Turbulence Structure on Broadband Fan Noise," in *14th AIAA/CEAS Aeroacoustics Conference*, no. AIAA 2008-2842, Vancouver, Canada, 2008. [Online]. Available: http://dx.doi.org/10.2514/6.2008-2842

[119] I. Evers and N. Peake, "On Sound Generation by the Interaction between Turbulence and a Cascade of Airfoils with Non-Uniform Mean Flow," *Journal of Fluid Mechanics*, vol. 463, no. 1, pp. 25–52, 2002. [Online]. Available: http://dx.doi.org/10.1017/S0022112002008698

[120] S. M. Grace, "Influence of Model Parameters and the Vane Response Method on a Low-Order Prediction of Fan Broadband Noise," *International Journal of Aeroacoustics*, vol. 15, no. 1-2, pp. 131–143, 2016. [Online]. Available: http://dx.doi.org/10.1177/1475472X15627407

[121] H. Posson and M. Roger, "Experimental Validation of a Cascade Response Function for Fan Broadband Noise Predictions," *AIAA Journal*, vol. 49, no. 9, pp. 1907–1918, 2011. [Online]. Available: http://dx.doi.org/10.2514/1.J050728

[122] A. Sescu, "Towards Computations Aeroacoustics Prediction of Realistic Turbofan Broadband Noise Using Synthetic Turbulence Modeling," Ph.D. dissertation, The University of Toledo, 2011.

[123] M. Olausson and L.-E. Eriksson, "Rotor Wake/Stator Broadband Noise Calculations Using Hybrid RANS/LES and Chorochronic Buffer Zones," in *15th AIAA/CEAS Aeroacoustics Conference*, no. AIAA 2009-3338, Miami, Florida, 2009. [Online]. Available: http://dx.doi.org/10.2514/6.2009-3338

[124] "Third Computational Aeroacoustics (CAA) Workshop on Benchmark Problems," NASA, Tech. Rep. CP-2000-209790, 2000.

[125] "Fourth Computational Aeroacoustics (CAA) Workshop on Benchmark Problems," NASA, Tech. Rep. CP-2004-212954, 2004.

[126] P. Chaitanya, J. Coupland, and P. Joseph, "Airfoil Geometry Effects on Turbulence Interaction Noise in Cascades," in *22nd AIAA/CEAS Aeroacoustics Conference*, no. AIAA 2016-2738, Lyon, France, 2016. [Online]. Available: http://dx.doi.org/10.2514/6.2016-2738

[127] M. Dieste, "Random-Vortex-Particle Methods Applied to Broadband Fan Interaction Noise," Ph.D. dissertation, University of Southampton, Institute of Sound and Vibration Research (ISVR), 2011.

[128] A. M. Wohlbrandt, S. Guérin, and R. Ewert, "Extension of the Random Particle Mesh Method to Periodic Turbulent Flows for Fan Broadband Noise Prediction," in *21st AIAA/CEAS Aeroacoustics Conference*, no. AIAA 2015-2383, Dallas, Texas, 2015. [Online]. Available: http://dx.doi.org/10.2514/6.2015-2383

[129] D. Casalino, A. F. P. Ribeiro, E. Fares, S. Nölting, A. Mann, F. Perot, Y. Li, P.-T. Lew, C. Sun, P. Gopalakrishnan, R. Zhang, H. Chen, and K. Habibi, "Towards Lattice-Boltzmann Prediction of Turbofan Engine Noise," in *20th AIAA/CEAS Aeroacoustics Conference*, no. AIAA 2014-3101, Atlanta, Georgia, 2014. [Online]. Available: http://dx.doi.org/10.2514/6.2014-3101

[130] L. J. Heidelberg, D. G. Hall, J. E. Bridges, and M. Nallasamy, "A Unique Ducted Fan Test Bed for Active Noise Control and Aeroacoustics Research," in *2nd AIAA/CEAS Aeroacoustics Conference*, no. AIAA 96-1740, State College, Pennsylvania, 1996. [Online]. Available: http://dx.doi.org/10.2514/6.1996-1740

[131] X. Zhang, X. X. Chen, C. L. Morfey, and P. A. Nelson, "Computation of Spinning Modal Radiation from an Unflanged Duct," *AIAA Journal*, vol. 42, no. 9, pp. 1795–1801, 2004. [Online]. Available: http://dx.doi.org/10.2514/1.890

[132] X. Wang, Z. Hu, and X. Zhang, "Aeroacoustic Effects of High-Lift Wing Slat Track and Cut-out System," *International Journal of Aeroacoustics*, vol. 12, no. 3, pp. 283–308, 2013. [Online]. Available: http://dx.doi.org/10.1260/1475-472X.12.3.283

[133] W. Liu, J. W. Kim, X. Zhang, D. Angland, and B. Caruelle, "Landing-Gear Noise Prediction Using High-Order Finite Difference Schemes," *Journal of Sound and Vibration*, vol. 332, no. 14, pp. 3517–3534, 2013. [Online]. Available: http://dx.doi.org/10.1016/j.jsv.2013.01.035

[134] J. W. Kim, "Optimised Boundary Compact Finite Difference Schemes for Computational Aeroacoustics," *Journal of Computational Physics*, vol. 225, no. 1, pp. 995–1019, 2007. [Online]. Available: http://dx.doi.org/10.1016/j.jcp.2007.01.008

[135] F. Q. Hu, M. Y. Hussaini, and J. L. Manthey, "Low-Dissipation and Low-Dispersion Runge-Kutta Schemes for Computational Acoustics," *Journal of Computational Physics*, vol. 124, no. 1, pp. 177–191, 1996. [Online]. Available: http://dx.doi.org/10.1006/jcph.1996.0052

[136] J. W. Kim, "High-Order Compact Filters with Variable Cut-Off Wavenumber and Stable Boundary Treatment," *Computers and Fluids*, vol. 39, no. 7, pp. 1168–1182, 2010. [Online]. Available: http://dx.doi.org/10.1016/j.compfluid.2010.02.007

[137] J. Gill, R. Fattah, and X. Zhang, "Evaluation and Development of Non-Reflective Boundary Conditions for Aeroacoustic Simulations," in *21st AIAA/CEAS Aeroacoustics*

Conference, no. AIAA 2015-2677, Dallas, Texas, 2015. [Online]. Available: http://dx.doi.org/10.2514/6.2015-2677

[138] D. J. Thomson, "Spectrum Estimation and Harmonic Analysis," *Proceedings of the Institute of Electrical and Electronics Engineers (IEEE)*, vol. 70, no. 9, pp. 1055–1096, 1982. [Online]. Available: http://dx.doi.org/10.1109/PROC.1982.12433

[139] C. K. Tam, "Advances in Numerical Boundary Conditions for Computational Aeroacoustics," *Journal of Computational Acoustics*, vol. 6, no. 4, pp. 377–402, 1998. [Online]. Available: http://dx.doi.org/10.1142/S0218396X98000259

[140] J. W. Kim, A. S. H. Lau, and N. D. Sandham, "Proposed Boundary Conditions for Gust-Airfoil Interaction Noise," *AIAA Journal*, vol. 48, no. 11, pp. 2705–2709, 2010. [Online]. Available: http://dx.doi.org/10.2514/1.J050428

[141] F. Farassat and G. P. Succi, "The Prediction of Helicopter Discrete Frequency Noise," *Vertica*, vol. 7, no. 4, pp. 309–320, 1983.

[142] F. Farassat, "Derivation of Formulations 1 and 1A of Farassat," NASA, Tech. Rep. TM-2007-214853, 2007.

[143] M. C. M. Wright and C. L. Morfey, "On the Extrapolation of Acoustic Waves from Flow Simulations with Vortical Out Flow," *International Journal of Aeroacoustics*, vol. 14, no. 1-2, pp. 217–227, 2015. [Online]. Available: http://dx.doi.org/10.1260/1475-472X.14.1-2.217

[144] V. Clair, "Calcul Numérique de la Réponse Acoustique d'un Aubage Soumis à un Sillage Turbulent," Ph.D. dissertation, Université Claude Bernard, 2013.

[145] X. Zhang, X. Chen, J. Gill, and X. Huang, "Gradient Term Filtering for Stable Sound Propagation with Linearized Euler Equations," in *20th AIAA/CEAS Aeroacoustics Conference*, no. AIAA 2014-3306, Atlanta, Georgia, 2014. [Online]. Available: http://dx.doi.org/10.2514/6.2014-3306

[146] G. K. Batchelor and I. Proudman, "The Effect of Rapid Distortion of a Fluid in Turbulent Motion," *The Quarterly Journal of Mechanics and Applied Mathematics*, vol. 7, no. 1, pp. 83–103, 1954. [Online]. Available: http://dx.doi.org/10.1093/qjmam/7.1.83

[147] L. J. Ayton, J. Gill, and N. Peake, "Comparison of Analytical, Numerical, and Experimental Results for Unsteady Aerofoil Interaction Noise," in *21st AIAA/CEAS Aeroacoustics Conference*, no. AIAA 2015-3265, Dallas, Texas, 2015. [Online]. Available: http://dx.doi.org/10.2514/6.2015-3265

[148] J. Gill, X. Zhang, S. Zhong, R. Fattah, and D. Angland, "Airfoil-Gust Interactions in Transonic Flow," in *22nd AIAA/CEAS Aeroacoustics Conference*, no. AIAA 2016-2872, Lyon, France, 2016. [Online]. Available: http://dx.doi.org/10.2514/6.2016-2872

[149] P. A. Davidson, *Turbulence, An Introduction For Scientists and Engineers*, 1st ed. Oxford University Press, 2004.

[150] R. W. Paterson and R. K. Amiet, "Noise and Surface Pressure Response of an Airfoil to Incident Turbulence," *Journal of Aircraft*, vol. 14, no. 8, pp. 729–736, 1977. [Online]. Available: http://dx.doi.org/10.2514/3.58845

[151] C. L. Ladson, C. W. Brooks, A. S. Hill, and D. W. Sproles, "Computer Program to Obtain Ordinates for NACA Airfoils," NACA, Tech. Rep. TM-4741, 1996.

[152] T. F. Brooks, M. A. Marcolini, and D. S. Pope, "Airfoil Trailing-Edge Flow Measurements," *AIAA Journal*, vol. 24, no. 8, pp. 1245–1251, 1986. [Online]. Available: http://dx.doi.org/10.2514/3.9426

[153] C. Bogey, C. Bailly, and D. Juvé, "Computation of Flow Noise Using Source Terms in Linearized Euler's Equations," *AIAA Journal*, vol. 40, no. 2, pp. 235–243, 2002. [Online]. Available: http://dx.doi.org/10.2514/2.1665

[154] S. Glegg and N. Walker, "Fan Noise from Blades Moving Through Boundary Layer Turbulence," in *5th AIAA/CEAS Aeroacoustics Conference and Exhibit*, no. AIAA 99-1888, Bellevue, Washington, 1999. [Online]. Available: http://dx.doi.org/10.2514/6.1999-1888

[155] S. Chandrasekhar, "The Theory of Axisymmetric Turbulence," *Philosophical Transactions of the Royal Society of London. Series A, Mathematical and Physical Sciences*, vol. 242, no. 855, pp. 557–577, 1950. [Online]. Available: http://dx.doi.org/10.1098/rsta.1950.0010

[156] H. M. Atassi and M. M. Logue, "Fan Broadband Noise in Anisotropic Turbulence," in *15th AIAA/CEAS Aeroacoustics Conference*, no. AIAA 2009-3148, Miami, Florida, 2009. [Online]. Available: http://dx.doi.org/10.2514/6.2009-3148

[157] H. W. Liepmann, J. Laufer, and K. Liepmann, "On The Spectrum of Isotropic Turbulence," NACA, Tech. Rep. TN-2473, 1951.

[158] T. Sjögren and A. V. Johansson, "Measurement and Modelling of Homogeneous Axisymmetric Turbulence," *Journal of Fluid Mechanics*, vol. 374, no. 1, pp. 59–90, 1998. [Online]. Available: http://dx.doi.org/10.1017/S0022112098002511

[159] V. Jurdic, P. Joseph, and J. Antoni, "Investigation of Rotor Wake Turbulence Through Cyclostationary Spectral Analysis," *AIAA Journal*, vol. 47, no. 9, pp. 2022–2030, 2009. [Online]. Available: http://dx.doi.org/10.2514/1.36728

[160] J. Maunus, S. Grace, D. Sondak, and V. Yakhot, "Characteristics of Turbulence in a Turbofan Stage," *Journal of Turbomachinery*, vol. 135, no. 2, p. 021024, 2013. [Online]. Available: http://dx.doi.org/10.1115/1.4006774

[161] D. S. Whitehead, "AGARD Manual on Aeroelasticity in Axial-Flow Turbomachines, Volume 1 Unsteady Turbomachinery Aerodynamics, Classical Two-Dimensional Methods," Advisory Group for Aerospace Research and Development (AGARD), Tech. Rep. AG-298, 1987.

[162] D. Kim and C. Cheong, "Time- and Frequency-Domain Computations of Broadband Noise due to Interaction between Incident Turbulence and Rectilinear Cascade of Flat Plates," *Journal of Sound and Vibration*, vol. 331, no. 21, pp. 4729–4753, 2012. [Online]. Available: http://dx.doi.org/10.1016/j.jsv.2012.05.013

[163] C. Cheong, V. Jurdic, and P. Joseph, "Decomposition of Modal Acoustic Power due to Cascade-Turbulence Interaction," *Journal of Sound and Vibration*, vol. 324, no. 1-2, pp. 57–73, 2009. [Online]. Available: http://dx.doi.org/10.1016/j.jsv.2009.01.059

[164] P. Chaitanya, S. Narayanan, P. Joseph, C. Vanderwel, J. Turner, J. W. Kim, and B. Ganapathisubramani, "Broadband Noise Reduction Through Leading Edge Serrations on Realistic Aerofoils," in *21st AIAA/CEAS Aeroacoustics Conference*, no. AIAA 2015-2202, Dallas, Texas, 2015. [Online]. Available: http://dx.doi.org/10.2514/6.2015-2202

[165] P. Chaitanya, S. Narayanan, P. Joseph, and J. W. Kim, "Leading Edge Serration Geometries for Significantly Enhanced Leading Edge Noise Reductions," in *22nd AIAA/CEAS Aeroacoustics Conference*, no. AIAA 2016-2736, Lyon, France, 2016. [Online]. Available: http://dx.doi.org/10.2514/6.2016-2736

[166] R. Fattah, D. Angland, and X. Zhang, "A Priori Grid Quality Estimation for High-Order Finite Differencing," *Journal of Computational Physics*, vol. 315, pp. 629–643, 2016. [Online]. Available: http://dx.doi.org/10.1016/j.jcp.2016.03.063

[167] C. L. Morfey, "Acoustic Energy in Non-Uniform Flows," *Journal of Sound and Vibration*, vol. 14, no. 2, pp. 159–170, 1971. [Online]. Available: http://dx.doi.org/10.1016/0022-460X(71)90381-6